**Republic of Iraq**

**Ministry of Higher Education**

**and Scientific Research**

**University of Babylon**

**College of Engineering**

**Civil Engineering Department**

# Behavior of Composite Steel Corrugated Plate-Concrete Deck Mechanically Connected with Steel Floor Beams Exposed to Fire

A Thesis

Submitted to the College of Engineering / University of Babylon in Partial Fulfillment of the Requirements for the Degree of Doctor of Philosophy in Engineering/ Civil Engineering/ Structures

By

**Mays Abdulridha Hamad Mousa**

Supervised by

**Prof. Dr. Haitham H. Muteb**

2023 A.D 1445 A.H

# قالوا سبحانك لا علم لنا إلا ما علمتنا إنك أنت العليم الحكيم

**صدق الله العلي العظيم**

**سورة البقرة (الآية 32)**

## DEDICATION

*For person who supports me, is like my soul who prays to me with all my steps, to that one who gives her help to pass the difficulties... For my lovely mother.*

*For my pacemaker of my life, the one who I can't describe by written words on paper... My great father.*

*For my darling husband, without his support, I can't get this much of knowledge, thanks from the core of my heart.*

*For my brothers and sister, my pillars of support and constant encouragement.*

*For my esteemed supervisor, the messenger of knowledge, Prof. Dr. Haitham H. Muteb Al-Daami*

*For the friends who gave birth by situation those who support and never harm*

# ACKNOWLEDGEMENT

First and foremost, I am immensely grateful to Allah for His blessings and abundant generosity. He has provided me with those who have extended a helping hand and support to complete my studies. I send my prayers and greetings to the noblest of prophets and messengers, our master Muhammad, and to his pure and virtuous family.

I would like to express my sincere thanks and deep gratitude to Prof. Dr. Haitham H. Muteb for his gracious supervision of this thesis. His valuable guidance, encouragement, and support went far beyond research related matters. His expert knowledge, creativity, and passion were a great inspiration.

I am grateful to my family for enduring my mood swings and inconvenience throughout my study period. I appreciate their understanding and patience with me. I pray that Allah honors them and grants them all goodness.

I am deeply grateful to my husband, Dr. Mustafa Salah Shaker, for his unwavering love, encouragement, and patience. His belief in my abilities, even in times of self-doubt, has motivated me to overcome obstacles.

I am grateful to the professors under whose guidance I studied at the Faculty of Engineering, Civil Engineering Department. Without their knowledge, guidance, and support, I would not have reached this stage. May Allah reward them with the best of rewards. I am also grateful to the staff of the Structural Engineering Laboratory for their assistance and expertise.

I am incredibly grateful to Hilti Company for their invaluable support in providing the X-HVB shear connector and its accessories. Their contribution played a vital role in the successful completion of my project. I am truly thankful for their assistance.

I would like to thank everyone who has helped me along the way. I could not have done this without your support.

**Mays Abdulridha Hamad**

**2023**

# ABSTRACT

Due to the large increase of use of composite beams in buildings and the rising incidence of fire accidents, it has become essential to understand their behavior when exposed to fire. The behavior of shear connectors plays an important part in sustaining the required strength of a composite beam. Composite beams, as far as this research is concerned, are made with a bare or insulated steel section connected to a concrete or a composite slab with corrugated steel plate. This slab is attached to the upper flange of the beam by shear connectors.

Various types of shear connectors are employed in the construction industry based on their intended use. The evolving demands for rapid and sustainable construction have led to the development of different types of composite slabs and shear connectors. The X-HVB represents a new shear connector, offering a viable alternative to conventional shear stud connectors. Notably, it excels in environmental friendliness and is adaptable for use in cold or hot-formed profiles, as well as rehabilitation projects. The connectors have been tested under different types of loading at ambient temperature; however, the behavior of these connectors during the fire has not been studied. In this dissertation, design limitations are presented to investigate the strength of such types of shear connectors under fire, which are newly used in the composite steel-concrete structure.

The study was divided into three main parts. In the first part, pushout tests were conducted to experimentally investigate the behavior of X-HVB shear connectors in fire. These tests aimed to examine the shear strength, ductility, stiffness, and shear-slipping relationships. Various parameters were investigated, such as exposure to different temperature levels (350, 450, and 550ºC), the direction of the corrugated steel plate (parallel or transverse to the beam's axis), the degree of composite action, and the orientation of the shear connector (backward or forward) in relation to the shear force direction.

Moving on to the second part, the focus shifted to experimentally investigating the fire behavior of simply supported composite beams with different orientations of corrugated steel plates, either parallel or transverse to the beam's length. This was done under different fire exposure directions, either from the top of the concrete slab or from the bottom of the steel beam, and at different temperature exposure levels (350, 450,

and 550ºC). Lastly, the third part involved the validation of a numerical model using ABAQUS Standard/Explicit 2017.

The results obtained from the pushout test indicate that the forward orientation of the shear connector, relative to the shear force direction, exhibits greater fire resistance compared to the backward orientation under fire exposure conditions. Furthermore, it was observed that the ductility of the shear connector varies depending on the direction of the corrugated steel plate (parallel or transverse) to the steel beam. For specimens with parallel corrugated steel plates, an increased degree of shear connection results in increased stiffness and ductility. However, this is not the case for specimens with transverse corrugated steel plates, as the ductility actually decreased and stiffness increase in those instances.

While from beam test, the results showed that the load carrying capacity of specimens that exposed to fire from top of concrete slab is slightly decreased after burning at 400ºC no matter the sheeting orientation. While it is decreased significantly after exposure to fire temperatures of (350, 450 and 550ºC) from bottom of steel beam by about (20%, 29% and 30%), respectively for specimens with parallel sheeting and the loss increased to about (23%, 33% and 40), respectively for specimens with transverse sheeting.

The finite element model results show good agreement with the experimental results. In this thesis, a parametric analysis is performed to investigate the effect of size of steel beam profile and the effect of exposure to fire from both top of concrete slab and bottom of steel beam. It is concluded that using IPE200 steel beams instead of IPE160 steel sections significantly improved performance, with a 19.82% and 14% increase in ultimate load at ambient temperature and a more pronounced 30.35% and 15.37% increase under fire conditions from bottom of steel beam for parallel and transverse corrugated steel plate specimens, respectively. Also, the reduction in ultimate load for specimens that exposed to fire from both top and bottom faces was 15.5% and 16.25% compared with specimens exposed to fire form bottom and 35.7% and 36.5% compared with specimens exposed to fire from top for parallel and transverse corrugated steel plates, respectively.

# TABLE OF CONTENTS

**Subject**.....**Page No.**

DEDICATION.....i

ACKNOWLEDGEMENT.....I

ABSTRACT.....II

TABLE OF CONTENTS.....IV

LIST OF TABLES.....VII

LIST OF FIGURES.....VIII

NOTATION.....XIV

ABBREVIATIONS.....XVI

## CHAPTER ONE: INTRODUCTION

1.1 GENERAL…….....1

1.2 BEHAVIOR AND DESIGN ASPECTS OF COMPOSITE SLAB.....2

1.3 SHEAR CONNECTORS.....5

1.4 HILTI X-HVB SHEAR CONNECTOR.....8

1.4.1 Advantages of Hilti X-HVB Shear Connecter…….....9

1.4.2 Disadvantages of Hilti X-HVB Shear Connecter…….....10

1.5 BEHAVIOR OF COMPOSITE STEEL – CONCRETE IN FIRE.....10

1.6 RESEARCH SIGNIFICANCE.....11

1.7 RESEARCH OBJECTIVES.....12

1.8 LAYOUT OF THESIS.....13

## CHAPTER TWO: LITERATURE REVIEW

2.1 GENERAL……. .....15

2.2 COMPOSITE CONSTRUCTION.....15

2.3.1. Composite Slab…….....15

2.3.2. Composite Beam with Solid Slab…….....24

2.3.3. Composite Beam with Composite Slab…….....29

2.3.4. Composite Beam Under Fire Effect…….....33

2.4 CONCLUDING REMARK…….....50

## CHAPTER THREE: EXPERIMENTAL WORK

3.1 INTRODUCTION ..... 53
3.2 METHODOLOGY ..... 53
3.3 DETAILS OF TEST SPECIMENS ..... 54
3.4 MATERIAL PROPERTIES ..... 58
3.4.1 Steel Beam ..... 58
3.4.2 X-HVB Shear Connecter ..... 60
3.4.3 Corrugated Steel Plate ..... 61
3.4.4 Steel Reinforcement of Concrete ..... 63
3.4.5 Cement ..... 65
3.4.6 Coarse Aggregate ..... 66
3.4.7 Fine Aggregate ..... 67
3.4.8 Water ..... 68
3.4.9 Crack Width Ruler ..... 68
3.5 PUSHOUT TEST ..... 69
3.6 CONCRETING AND CURING PROCEDURES OF THE SPECIMENS ..... 73
3.7 BURNING PROCESS ..... 78
3.8 INSTRUMENTATION AND TEST PROCEDURES ..... 82

## CHAPTER FOUR: EXPERIMENTAL WORK

4.1 INTRODUCTION ..... 85
4.2 TEST RESULTS FOR PUSH-OUT SPECIMENS ..... 85
4.2.1 Effect of Temperature ..... 87
4.2.2 Effect of Degree of Shear Connection ..... 89
4.2.3 Effect of Orientation of X-HVB Shear Connecter ..... 90
4.2.4 Effect of Direction of Corrugated Steel Plate ..... 91
4.2.5 Failure Mode ..... 95
4.2.6 Stiffness and Ductility ..... 100
4.3 TEST RESULTS FOR COMPOSITE BEAM SPECIMENS ..... 102
4.3.1 Load–defection Response ..... 103
4.3.2 Load-slip Response ..... 110
4.3.3 Failure Mode ..... 114
4.3.4 Stiffness and Ductility ..... 120

4.3.5 Energy Absorption Capacity……122
4.4 DIGITAL IMAGE CORRELATION METHOD……..124
4.4.1 Distribution of Normal Strain……127

## CHAPTER FIVE: NUMERICAL ANALYSIS BY FINITE ELEMENT

5.1 INTRODUCTION……146
5.2 FINITE ELEMENT MODELING……146
5.3 MATERIAL PROPERTIES……147
5.4 MODELING OF SPECIMENS……147
5.3.1 Parts and Assembly……147
5.3.2 Finite Element Modeling Interaction……150
5.3.3 Loading and Boundary Conditions……151
5.5 CONVERGENCE STUDY……152
5.6 RESULTS OF FINITE ELEMENT ANALYSIS……154
5.3.1 Specimens with Parallel Corrugated Steel Plate…155
5.3.2 Specimens with Transverse Corrugated Steel Plate……161
5.7 PARAMETRIC STUDY……167
5.3.1 Effect of Fire Exposure from Bottom and Top Sides……168
5.3.2 Effect of Size of Steel Beam Profile……176

## CHAPTER SIX: CONCLUSIONS AND RECOMMENDATIONS

6.1 INTRODUCTION……183
6.2 KEY FINDINGS……183
6.2.1 Conclusions Based on Experimental Pushout Test……183
6.2.2 Conclusions Based on The Composite Beam Specimens……184
6.3 RECOMMENDATIONS……187
**REFERENCES……188**
APPENDIX A: DESIGN OF THE TESTED COMPOSITE BEAM SPECIMENS……A-1
APPENDIX B: MODELING OF MATERIAL PROPERTIES……B-1
APPENDIX C: MODELING OF MATERIAL PROPERTIES FOR ELEVATED TEMPERATURE……C-1

# LIST OF TABLES

Table 2.1: Geometrical properties of push-out specimens. ..... 27
Table 3.1: Composite beam specimens' details. ..... 58
Table 3.2: Results of tested steel coupons. ..... 60
Table 3.3: Properties of corrugated steel plate. ..... 63
Table 3.4: Tests results of steel reinforcement specimens. ..... 64
Table 3.5: Mechanical properties of cement. ..... 65
Table 3.6: Chemical analysis of cement. ..... 65
Table 3.7: Mechanical and chemical properties of coarse aggregate. ..... 66
Table 3.8: Grading of coarse aggregate. ..... 66
Table 3.9: Chemical and mechanical properties of fine aggregate. ..... 67
Table 3.10: Grading of fine aggregate. ..... 67
Table 3.11: Pushout specimens' details. ..... 70
Table 3.12: Test values of cube compressive strengths of samples before and after exposure to fire flame. ..... 75
Table 4.1: Results of the tested push-out specimens……..….86
Table 4.2: Summary of the results of composite girders. ..... 103
Table 5.1: Comparison of experimental and numerical results…… ...154
Table 5.2: The details of the studied variables. ..... 167
Table 5.3: Results of the parametric study. ..... 168

# LIST OF FIGURES

Figure 1.1: Typical layout of composite secondary beam and slab structure ..... 3
Figure 1.2: Composite beams with different types of steel decks, a) Re-entrant deck; b) trapezoidal deck . ..... 4
Figure 1.3: Corrugated profile steel with embossment ..... 5
Figure 1.4: Shear connectors types . ..... 6
Figure 1.5: Hilti X-HVB System. ..... 9
Figure 2. 1: Components of composite construction system …… ……16
Figure 2. 2: The two systems and the corresponding cross-sections proposed by Daphne and Euripidis: (a) simply supported system, (b) the continuous system …..…….. 18
Figure 2. 3: Load - deflection at mid span …..……... 19
Figure 2. 4: Load - end slip ……. 19
Figure 2. 5 : Profiled steel sheet details: (a) with V-Notch ,(b) without Notch……..20
Figure 2. 6: Load–Deflection curve for specimen with thickness of profiled sheet (a) 0.8mm, (b) 1.2mm……... 20
Figure 2. 7: Load–slip curve for specimen with thickness of profiled sheet (a) 0.8mm, (b) 1.2mm…… 20
Figure 2. 8: The temperature histories of composite slabs with different convective heat transfer coefficients ($h_c$) on the fire-exposed surface: (a) the thicker section of a slab, (b) the thicker section of a slab…… 21
Figure 2. 9: Corrugation sheet types: (a) trapezoidal steel deck, (b) triangle steel deck, (c) T-shapes steel deck…… 23
Figure 2. 10: Detachment of the corrugated steel deck from the concrete……..24
Figure 2. 11: layout for push-out specimens……... 28
Figure 2. 12: Test Samples of Nie et. al. Research Work……30
Figure 2. 13: Different locations of the shear stud within a sheeting rib…… 31
Figure 2. 14: Finite element model adopted for parametric study showing parts of push test……31
Figure 2. 15: General test arrangement for push test…… 33
Figure 2. 16: Details of mesh position and T16 reinforcing bar…… 33
Figure 2. 17: Schematic figure of the composite steel-concrete beam under fire……... 34
Figure 2. 18: Finite element mesh and boundary condition of the [3]: (a) solid slab model, (b) profiled steel sheeting slab model……..37
Figure 2. 19: Slip at different load levels according to time for [3]: (a) solid slab, (b) profiled steel sheeting slab model……38
Figure 2. 20: Details and Dimensions of push test specimens proposed by Mirza et al. 39
Figure 2. 21: Composite castellated beam predicted by Ellobody…… 41
Figure 2. 22: Composite noncastellated beam predicted by Ellobody…….. 42
Figure 2. 23: Details of specimens (unit: mm)…… 42
Figure 2. 24: Experimental program: (a) specimen restraining scheme, (b) details of restraints, (c) test setup, and (d) composite beam specimen……. 46

Figure 2. 25: The temperature profile of steel beam due to protected by (a)one-layer intumescent coating, (b) four layers intumescent coating under (ISO 834) Standard fire, (c) one-layer intumescent coating under Fast fire and (d) four layers intumescent coating under Fast fire…… 48
Figure 2. 26: Comparison of protected and unprotected steel beam temperature results under standard (ISO) and fast fires……..49
Figure 3. 1: Details of the experimental program……..……..54
Figure 3. 2: Composite beam specimens' details with parallel corrugated steel plate (all dimensions in cm)……55
Figure 3. 3: Composite beam specimens' details with transverse corrugated steel plate (all dimensions in cm)…… 56
Figure 3. 4: The specimen nomination system…… 57
Figure 3. 5: IPE 160 steel beam…….. 59
Figure 3. 6: Configuration of standard coupons specimens according to ASTM……...59
Figure 3. 7: X-HVB95 Shear Connector: (a) Detailed Geometry [75]; (b)Installation. 61
Figure 3. 8: Trapezoidal corrugated steel plate……... 62
Figure 3. 9: The tension test set-up to obtain the tensile strength of steel deck……..63
Figure 3. 10: The tension test set-up to obtain the material data from the reinforcement……...64
Figure 3. 11: Crack width ruler……68
Figure 3. 17: The specimen nomination system……..70
Figure 3. 12: The dimensions and arrangement for pushout specimens for forward orientation of the shear connecter with parallel corrugated steel plate……... 71
Figure 3. 13: The dimensions and arrangement for pushout specimens for forward orientation of the shear connecter with transverse corrugated steel plate……... 72
Figure 3. 14: The dimensions and arrangement for pushout specimens for backward orientation of the shear connecter with parallel corrugated steel plate……... 72
Figure 3. 15: The dimensions and arrangement for pushout specimens for backward orientation of the shear connecter with transverse corrugated steel plate……... 73
Figure 3. 16: X-HVB shear connecter' layout relative to shear force: (a) Forward, (b) Backward…… 73
Figure 3. 18: Compressive strength testing machine……...75
Figure 3. 19: Composite beam specimens before concrete casting……76
Figure 3. 20: Pushout specimens before concrete casting……... 77
Figure 3. 21: Pouring concrete into the steel mold……..77
Figure 3. 22: Curing procedures for column specimens and samples…… 78
Figure 3. 23: Top and Front view of the furnace and equipment…… 79
Figure 3. 24: The full details of the burning process and stove with the connections….80
Figure 3. 25: Methods used for temperature measure: (a) Digital thermocouple gage, (b) infrared thermometer……... 81
Figure 3.26: The instrumentation and test setup of the specimens……..83
Figure 3. 27: Details of the testing machine used in this study……...83
Figure 3. 28: Details on the testing machine utilized in this study…… 84

Figure 4.1: The key parameters of push-out tests, corresponding to EC4 [83]..... … 87
Figure 4.2: Effect of temperature levels on the shear resistance of X-HVB shear connectors with parallel profiled steel plate to the steel beam. ..... 88
Figure 4.3: Effect of temperature levels on the shear resistance of X-HVB shear connectors with transverse profiled steel plate to the steel beam. ..... 89
Figure 4.4: Influence of degree of shear connection on the shear resistance of X-HVB shear connectors. ..... 90
Figure 4.5: Influence of temperature levels on the shear resistance of X-HVB shear connectors with transverse profiled steel plate to the steel beam. ..... 91
Figure 4. 6: Influence of direction of profiled steel plate on the shear resistance of X-HVB shear connectors at ambient temperature. ..... 92
Figure 4.7: Influence of direction of profiled steel plate on the shear resistance of X-HVB shear connectors at 350 °C ..... 92
Figure 4.8: Influence of direction of profiled steel plate on the shear resistance of X-HVB shear connectors at 450 °C ..... 93
Figure 4.9: Influence of direction of profiled steel plate on the shear resistance of X-HVB shear connectors at 550 °C ..... 93
Figure 4.10: Influence of direction of profiled steel plate on the shear resistance with double X-HVB shear connectors. ..... 94
Figure 4.11: Influence of direction of profiled steel plate on the shear resistance of X-HVB shear connectors with backward orientation. ..... 94
Figure 4.12: detachment of the profiled steel sheet. ..... 97
Figure 4.13: The failure mode of specimens PD1 and PD2. ..... 97
Figure 4.14: The failure mode of specimens after exposed to fire before testing. ..... 98
Figure 4.15: Failure mechanism for specimens $PFD_1SO_1$ and $PFD_1dO_1$. ..... 98
Figure 4.16: Failure mechanism for specimens PFD1SO2 ..... 99
Figure 4.17: The failure mode of specimens PFD2SO1 and PFD2SO2. ..... 99
Figure 4.18: Failure mechanism for specimen PD2dO1R2. ..... 100
Figure 4.19: Ductility response for all the tested specimens. ..... 102
Figure 4.20: Load versus deflection curve at mid-span of composite beam with parallel corrugated plate ..... 106
Figure 4.21: Load versus deflection curve at mid-span of composite beam with transverse corrugated plate. ..... 107

Figure 4.22: Load versus deflection curve at mid-span of composite beam at ambient temperature. ..... 107
Figure 4.23: Load versus deflection curve at mid-span of composite beam at 350°C. 108
Figure 4.24: Load versus deflection curve at mid-span of composite beam at 450°C. 108
Figure 4.25: Load versus deflection curve at mid-span of composite beam at 550°C. 109
Figure 4.26: Effect of fire exposed direction on Load-Deflection Curve of composite beam with transverse corrugated plate..... 109
Figure 4.27: Load versus deflection curve at mid-span of composite beam with transverse corrugated plate. ..... 110
Figure 4.28: Influence of direction of corrugated steel plate to the steel beam (parallel or transverse) on the shear resistance of X-HVB shear connectors at ambient temperature. ..... 111
Figure 4.29: Influence of exposure to fire on the shear resistance of X-HVB shear connectors with parallel corrugated plate to the steel beam. ..... 112
Figure 4.30: Influence of exposure to fire on the shear resistance of X-HVB shear connectors with transverse corrugated plate to the steel beam. ..... 112
Figure 4.31: Effect of direction of fire exposure on Load Slip curve of composite beam under fire exposure for specimens with parallel profiled plate. ..... 113
Figure 4.32: Effect of direction of fire exposure on Load Slip curve of composite beam under fire exposure for specimens with transverse profiled plate. ..... 114
Figure 4.33: Formation of transverse cracks due to the effects of fire during the fire process. ..... 115
Figure 4.34: Failure mode in specimen CD1. ..... 116
Figure 4.35: Failure mode in specimen CD2. ..... 117
Figure 4.36: Thermal and longitudinal cracking in specimen CD1BR1. ..... 118
Figure 4.37: Thermal and longitudinal cracking of composite slab in composite beam CD1BR3..... 118
Figure 4.38: Thermal and longitudinal cracking of composite beam CD2BR1. ..... 119
Figure 4.39: shear connecter failure. ..... 119
Figure 4.40: Cracking and separation of composite slab in composite beam CD2TR2. ..... 119
Figure 4.41: Cracking and separation of composite slab in composite beam CD1TR2. ..... 120
Figure 4.42: Stiffness and Ductility index response for all the tested specimens. ..... 122

Figure 4.43: The results of energy absorption capacity for all tested specimens. ..... 123
Figure 4.44: Digital Image Correlation method set-up. ..... 125
Figure 4.45: A Comparative Analysis of Load-Deflection Behavior: Experimental vs. DIC Methods..... 126
Figure 5. 1: Concrete slab and corrugated steel plate for both direction…….…….148
Figure 5. 2: Parts used in the modeling of specimens…… 149
Figure 5. 3: The Assembled Parts of Composite beam for direction 1……..149
Figure 5. 4: The Assembled parts of composite beam for direction 2……...150
Figure 5. 5: Boundary conditions of modeled composite beam…… 151
Figure 5. 6: The convergence study results……... 152
Figure 5. 7: Finite Element Mesh of composite beam……...153
Figure 5. 8: Load-deflection curve for specimen CD1……..156
Figure 5. 9: Von-Mises equivalent stress distribution of specimen CD1……..156
Figure 5. 10: Load-deflection curve for specimen CD1BR1…….157
Figure 5. 11: Von-Mises equivalent stress distribution of specimen CD1BR2…….157
Figure 5. 12: Load-deflection curve for specimen CD1TR1…….158
Figure 5. 13: Von-Mises equivalent stress distribution of specimen CD1TR2…….158
Figure 5. 14: Temperature distribution in specimens CD1BR2 and CD1TR2 after 60-minutes of burning at 450°C……..159
Figure 5. 15: Heat transfer with time for specimens CD1BR2 and CD1TR2 burned at 450°C…….160
Figure 5. 16: Load-deflection curve for specimen CD2……161
Figure 5. 17: Von-Mises equivalent stress distribution of specimen CD2……162
Figure 5. 18 : Load-deflection curve for specimen CD2BR2……162
Figure 5. 19: Von-Mises equivalent stress distribution of specimen CD2BR2…….163
Figure 5. 20: Load-deflection curve for specimen CD2TR2…….163
Figure 5. 21: Von-Mises equivalent stress distribution of specimen CD2TR2…….164
Figure 5. 22: Temperature distribution in specimens CD1BR2 and CD1TR2 after 60-minutes of burning at 450°C……..165
Figure 5. 23: Heat transfer with time for specimens CD1BR2 and CD1TR2 burned at 450°C…….166
Figure 5. 24: Cases of fire exposure in multi-story buildings……... 170
Figure 5. 25: Load-deflection curve for specimen CD1BTR2…….. 170
Figure 5. 26: Load-deflection curve for specimen CD2BTR2…….. 171

Figure 5. 27: Von-Mises equivalent stress distribution of specimens CD1BTR2 and CD2BTR2……..172
Figure 5. 28: Temperature distribution in specimens CD1BTR2 and CD2BTR2 after 60-minutes of burning at 450°C……..173
Figure 5. 29: Heat transfer with time for specimen CD1BTR2 burned at 450°C……. 174
Figure 5. 30: Heat transfer with time for specimen CD2BTR2 burned at 450°C……. 175
Figure 5. 31: Load-deflection curve for specimens with steel beam section IPE200 and parallel-corrugated steel plate……176
Figure 5. 32: Von-Mises equivalent stress distribution of specimens CD1$d_{200}$ and CD1BTR2$d_{200}$……178
Figure 5. 33: Heat transfer with time for specimen CD1BR2$d_{200}$ burned at 450°C…..179
Figure 5. 34: Load-deflection curve for specimens with steel beam section IPE200 and transversely -corrugated steel plate……... 180
Figure 5. 35: Von-Mises equivalent stress distribution of specimens CD2$d_{200}$ and CD2BTR2$d_{200}$……181
Figure 5. 36: Heat transfer with time for specimen CD2BR2$d_{200}$ burned at 450°C…..182

# NOTATION

The major symbols used in the text are listed below; others are indicated with their equations where they first appear.

| Symbol | Definition | Unit |
|---|---|---|
| $b_e$ | Effective slab width | mm |
| $b_f$ | Flange width of beam | mm |
| **C/C** | From center to center of dimensions | mm |
| **d** | Depth of steel beam | mm |
| **E** | Young's modulus | Mpa |
| $f'_c$ | Cylinder uniaxial compressive strength of concrete | MPa |
| $f_{cu}$ | Cube uniaxial compressive strength of concrete | MPa |
| $f_u$ | Ultimate strength | MPa |
| **Fy** | Yielding stress | MPa |
| **h** | Overall depth of composite deck | mm |
| $h_r$ | Overall depth of corrugated steel plate | mm |
| $h_s$ | Overall height of X-HVB shear connecter | mm |
| $I_{tr}$ | The second moment of inertia of a composite beam | $m^4$ |
| **M** | Flexural strength | kN.m |
| $M_p$ | Plastic moment of beam | kN.m |
| $P_u$ | Ultimate load | kN |
| $W_r$ | Average width of concrete rib | mm |
| $W_{rb}$ | Width of bottom rib of corrugated steel plate | mm |
| $W_{rt}$ | Width of top rib of corrugated steel plate | mm |

| | | |
|---|---|---|
| $\boldsymbol{\Delta u}$ | Ultimate displacement | mm |
| $\boldsymbol{K_{SC}}$ | Stiffness | kN/mm |
| $\boldsymbol{Q_n}$ | Connector shear capacity | kN |
| $\boldsymbol{\delta_{peak}}$ | Peak slip | mm |
| $\boldsymbol{\delta_u}$ | Ultimate slip | mm |

# ABBREVIATIONS

| Abbreviations | Definition |
|---|---|
| **AASHTO** | American Association of State Highway and Transportation Officials |
| **ACI** | American Concrete Institute |
| **AISC** | American Institute of Steel Construction |
| **ASTM** | American Society for Testing and Materials |
| **BS** | British Standard |
| **C3D8R** | 8 node brick elements, reduced integration |
| **CDP** | Concrete Damage Plasticity |
| **CSP** | Corrugated Steel Plate |
| **D.C. A** | Degree of Composite Action |
| **DIC** | Digital Image Correlation |
| **EC3** | Eurocode 3 |
| **EC4** | Eurocode 4 |
| **Exp.** | Experimental |
| **FEM** | Finite Element Method |
| **FEA** | Finite Element Analysis |
| **IQ. S** | Iraqi Specification |
| **ISO** | International Organization for Standardization |

| | |
|---|---|
| **Max.** | Maximum |
| **Min.** | Minimum |
| **MPa** | Mega Pascal ($MN/m_2$) |
| **N/A** | Not available |
| **Num.** | Numerical |
| **T3D2** | 2 nodes 3 D truss element |

# CHAPTER ONE
# INTRODUCTION

## 1.1 GENERAL

Steel-concrete composite structures are commonly used in construction, as they enable the most efficient use of each material. By connecting a steel and a concrete part, the composite action is realized, increasing the bearing capacities of the structural element. The most common steel-concrete composite system is a downstand composite beam (T-beam) that consists of a steel profile and a concrete slab placed over it. The concrete slab is implemented in one of two ways: as a solid slab or as a composite slab cast in Corrugated Steel Plate (CSP). The most important feature of composite slab with CSP is its ability to enable the construction of steel-framed building systems with effortless, rapid, lightweight, and cost-effective construction. Due to its numerous advantages over other types of floor systems, this construction method is widely accepted and embraced by the construction industry [1], [2].

To join the steel beam and the concrete slab and to prevent vertical separation and enable shear force transfer, shear connectors need to be used [3]. The most extensively used and known shear connector is welded stud connector; this connector's popularity is due to its strength being the same in all directions and that it is easy to fabricate by semi-automatic welding through the CSP. However, contractors do not always recognize this advantage, especially in countries where the atmospheric conditions are unfavorable. Poor-quality welding through the CSP has driven some contractors to give up this procedure and return to manual welding with electrodes. The difficulties of welding shear studs through CSP on site, and the increasing emphasis on environmental preservation and sustainable

development in all sectors of industry, have led to the development of a new non-welded shear connector called X-HVB by Hilti company [4].

A composite structure requires the consideration of the design process under risk conditions, given that the behavior of a composite structural system under fire is outstandingly different from its behavior at ambient temperatures. However, in recent years, the frequent occurrence of building fires has brought a serious threat to the safety of building structures and human safety. The research on the fire resistance performance of composite structures or members has become the main direction of fire resistance research of building structures, but there are no relevant fire-resistant design provisions for composite beam with X-HVB shear connecter type in current codes, which brings great risks to the application of composite members. Therefore, the research on the fire resistance of composite beams with X-HVB shear connecter is forward-looking and has important theoretical value.

## 1.2 BEHAVIOR AND DESIGN ASPECTS OF COMPOSITE SLAB

In modern floor construction, metal decking is increasingly replacing the conventional solid reinforced concrete slab, as illustrated in Figure 1.1. The metal decking, typically made of corrugated steel sheets with additional indentations or embossments, serves a dual purpose: acting as permanent formwork during the pouring of concrete and providing tension reinforcement once the concrete has cured. This composite slab comprises a corrugated steel sheet and an upper concrete topping, interconnected in a way that effectively resists horizontal shear forces at the steel-concrete interface [5].

The corrugated steel sheeting can have a trapezoidal or re-entrant profile, as depicted in Figure 1.2. It is commonly oriented perpendicular or

parallel to the steel beam axis and is typically joined using shear studs [6]. The corrugated steel sheeting exhibits the following general characteristics [7]:

- Thickness ranging between 0.75 mm and 1.5 mm.
- Depth between 40 mm and 80 mm.
- Standard protection against corrosion with a thin layer of galvanizing on both faces.

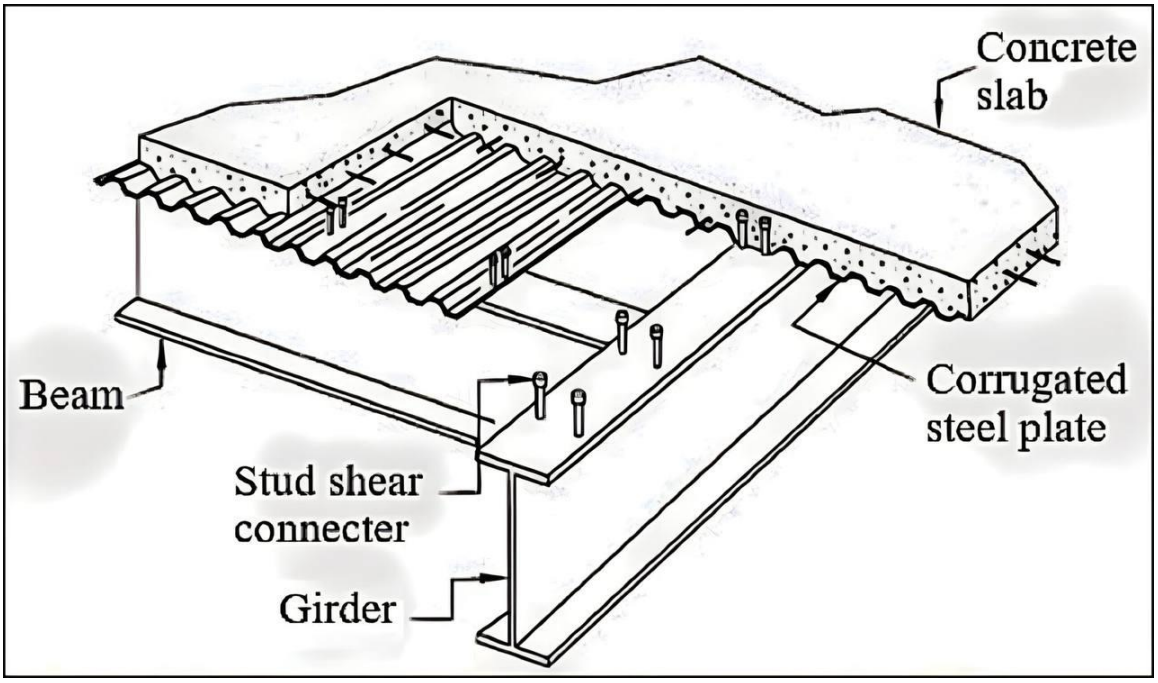


**Figure 1. 1: Typical layout of composite secondary beam and slab structure** [8]**.**


**Figure 1. 2: Composite beams with different types of steel decks, a) Re-entrant deck; b) trapezoidal deck** [9]**.**

Figure 1.3 shows that embossments (deformed surfaces) are usually present on the web and top flanges of the corrugated steel sheeting [10]. These embossments play a vital role in establishing a mechanical interlock between the corrugated steel sheet and the concrete interface. Additionally, the corrugated steel sheeting contributes to resisting horizontal slippage, which may occur when the shear force on the shear connectors reaches its ultimate strength. This slippage happens between the contact surface of the profiled deck and the concrete while facilitating the transfer of shear stresses from the concrete slab to the steel deck [11], [12].

By leveraging the benefits of corrugated steel sheeting, modern floor construction achieves cost-effectiveness, reduced structural weight, and enhanced construction efficiency. The composite slab's durability and resilience are improved, making it a favorable choice for contemporary construction projects. Adherence to proper design, detailing, and installation methods is crucial to ensure a successful composite floor that meets safety, performance, and sustainability requirements [1].


**Figure 1. 3: Corrugated steel plate with embossment** [13]**.**

## 1.3 SHEAR CONNECTORS

Shear connectors serve the important purpose of establishing strong bonding and facilitating the transfer of horizontal shear forces that arise between a steel beam and a concrete slab. Their efficient transmission of shear forces enables the composite beam to act as a single, unified structural element, significantly improving its overall performance and load-carrying capacity. Figure 1.4 illustrates the different types of shear connectors that have been used over time to achieve composite action between steel profiles and concrete decks.

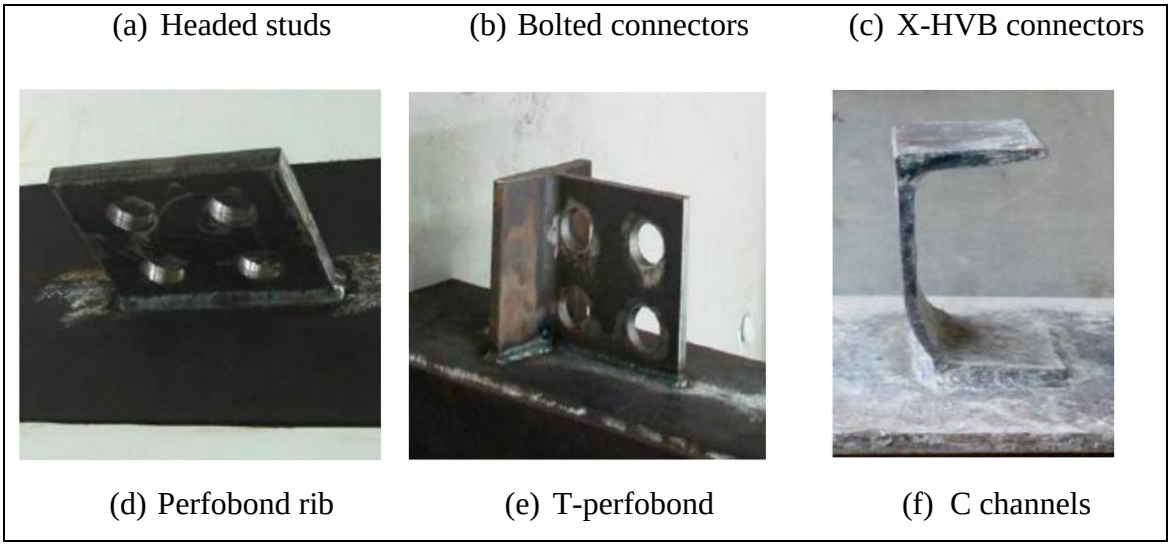


**Figure 1. 4: Some types of shear connectors** [14]**.**

The selection of shear connection types for composite constructions is influenced by significant variations in installation workload, base material preparation method, and the preferred installation environment. Moreover, each shear connector type exhibits unique characteristics in terms of shear resistance, ductility, and stiffness, which must be considered when incorporating shear connectors into composite constructions

[14].

A variety of shear connectors have been employed to achieve composite action between steel profiles and concrete decks in building and bridge construction. Headed studs are the shear connectors commonly adopted in industries (Figure 1.4 (a)); headed studs provide steel shank resisting longitudinal shear forces and have an anchorage head to prevent the vertical movement of slabs in composite structures [15]. Generally, to install a headed stud in the prefabricated steel girder beam, special welding equipment are essential. The weld strength should be higher than the stud strength. However, these welds generally face fatigue problems under repeated loadings [16], [17].

Bolted shear connectors, including friction grip bolts and bolts with single or double embedded nuts (Figure 1.4 (b)). They are usually fabricated in a workshop and assembled on site. Bolted connections are easy to install, inspect, and maintain. They also allow for flexibility and adjustability in design and erection. However, bolted connections also have some drawbacks, such as requiring more material, creating holes and stress concentrations in the steel, and needing extra protection against corrosion and vibration [18].

The X-HVB shear connector (Figure 1.4 (c)) utilizes powder-actuated fasteners to achieve composite action between steel profile sheets and composite decks. This type of shear connector will be further explained in the next section and will serve as the primary focus of study in this thesis.

The perfobond rib connectors (Figure 1.4 (d)) necessitate the use of perforated rectangular steel plates with circular holes that are more prominent than the diameter of transverse reinforcement and perforating rebars. Perfobond rib plates are conventionally welded at the top flange of steel girders [19], [20].

T-perfobond connectors (Figure 1.4 (e)) were created by attaching a flange to the perfobond rib plate to combine the high strength of a block type connector with some ductility and uplift resistance resulting from the holes in the perfobond rib connector. T-perfobond connectors are more resistant and stiffer than perfobond rib connectors for equivalent longitudinal plate designs [14].

Chanel shear connectors (Figure 1.4 (f)) offer greater shear resistance due to their substantial concrete contact area. Standard welding techniques are sufficient for the installation of this type of connector, with push-out tests demonstrating that factors such as flange thickness, web thickness,

and channel length can influence the resistance of the composite structure [21], [22].

## 1.4 HILTI X-HVB SHEAR CONNECTOR

The X-HVB shear connector is a type of mechanical connector used to provide a shear connection between a steel beam and a concrete slab in composite steel and concrete structures [14]. The connector adopted by Hilti Company is more user-friendly than conventional types, and it is named after its shape, which resembles the letter X. Additionally, they have another variant called HVB, which stands for “Headed and Vertical Bent” [23].

The X-HVB shear connector is designed and tested in accordance with various international standards and codes, such as the American Institute of Steel Construction (AISC) [24] and the European Standard EN 1994-1-1 [25]. These standards provide guidelines for the design, fabrication, and installation of the connectors, ensuring that they meet the required performance criteria and are safe and reliable. The use of standard connectors also helps to facilitate the construction process, reducing the need for custom-designed connectors and simplifying the fabrication and installation process [23].

Hilti X-HVB shear connectors are cold formed angle shear connectors, fixed by two powder-actuated fasteners (XENP-21 HVB) driven with a powder-actuated tool (Hilti DX 76 or DX 76 PTR), placed on one leg of the angle, all these parts are shown in Figure 1.5. It is possible to use one, two or three connectors in each steel decking rib, depending on the requirements [14].


(a) X-HVB shear connector with two X-ENP-21 HVB nails [26]

(b) DX 76 PTR tool, equipped for X-HVB installation [27]

(c) cartridges [27]

**Figure 1. 5: Hilti X-HVB System.**

### 1.4.1 Advantages of Hilti X-HVB Shear Connecter

The difficulties of welding shear studs through corrugated sheeting on site has led to development of a new non-welded shear connector which have some advantages, such as [28]:

- Quick and convenient installation: The X-HVB shear connections can be installed rapidly using a portable, hand-held, powder-actuated fastening tool. Two X-ENP-21 HVB nails are used to directly fix the shear connectors to the steel profile. No welding or electricity is required, making the installation process efficient.
- Compatibility with various conditions: The installation of X-HVB shear connections is not affected by base material coatings, such as zinc coatings, or paints. It is also largely unaffected by weather conditions, ensuring consistent performance regardless of the environment.
- No additional preparation required: Unlike traditional headed studs, the installation of X-HVB shear connectors does not necessitate further preparation of the steel sheeting or pre-drilling of holes. This eliminates

the need for interrupting the profiled sheeting or creating additional openings.

- Easy quality checks: The quality of installation can be easily assessed by visually examining the standoff of the nails over the surface of the fastened material. For fasteners that do not allow for accurate visual checks, the use of a stand-off template is recommended to ensure proper installation.

### 1.4.2 Disadvantages of Hilti X-HVB Shear Connecter

There are some disadvantages associated with the use of the X-HVB shear connector. One significant disadvantage is its lower capacity compared to traditional welded shear connectors, which requires a correspondingly larger number of connectors to achieve the same level of strength. Additionally, the X-HVB shear connector is a proprietary system from Hilti, which may limit the availability and increase the cost of the connector [29].

## 1.5 BEHAVIOR OF COMPOSITE STEEL – CONCRETE IN FIRE

The behavior of composite steel-concrete structures in fire conditions is influenced by the interaction between their steel and concrete components when subjected to high temperatures. When exposed to fire, the steel in the composite structure undergoes a loss in strength and stiffness, while the concrete experiences a decrease in load-bearing capacity due to the decomposition of cement paste and the release of moisture. This composite structure exhibits unique characteristics during fire events, with its overall performance being affected by the properties of both materials and the degree of their composite action [30], [31].

Thermal gradients play a crucial role in the behavior of composite steel-concrete in fire. Steel elements heat up faster than concrete, creating

temperature differences between the two materials. This temperature gradient induces stress and potential cracking in the concrete, particularly at the steel-concrete interface, known as spalling. Spalling can compromise the structural integrity [32], [33].

Fire protection measures are implemented to mitigate the effects of fire on composite steel-concrete structures. These measures include applying fire-resistant coatings to steel members to delay their temperature rise and adding concrete cover to protect steel reinforcement from direct exposure to high temperatures. These protective measures aim to extend the time it takes for the steel to reach critical temperatures, allowing more time for evacuation and firefighting [34].

Building codes and standards, such as the American Institute of Steel Construction (AISC) [35] and the European Standard EN 1994-1-2 [36], provide guidelines for the design and testing of composite structures to ensure their fire resistance. For example, AISC requires composite structures to be designed to meet specific fire resistance criteria, based on the expected fire exposure and the performance of the individual components [37]. Similarly, EN 1994-1-2 provides guidelines for the design of composite structures under fire conditions, including requirements for fire protection, structural analysis, and testing [38].

## 1.6 RESEARCH SIGNIFICANCE

The significance of this research lies in its specific investigation of the structural behavior of composite beams with X-HVB shear connectors when exposed to fire flames. While previous studies have explored the effects of fire on composite beams with various types of shear connectors, none have focused on the behavior of composite beams with the novel X-HVB shear connectors in fire conditions. Therefore, this thesis fills an important

knowledge gap regarding the behavior of composite beams with X-HVB shear connectors during fire exposure. The findings of this research contribute to improving safety and promoting the wider application of this innovative shear connector type.

Understanding how composite systems perform under fire is crucial for promoting sustainable construction practices. By optimizing fire-resistant design, this research can encourage the use of composite materials known for their high strength-to-weight ratio and eco-friendly properties.

## 1.7 RESEARCH OBJECTIVES

The main objectives of this study are:

1. Understand how the novel type of shear connector (X-HVB) affects the behavior of composite beams under fire conditions.
2. To examine the behavior and failure mechanisms of X-HVB shear connectors in the composite beam system under different levels of fire exposure and setups of corrugated sheets.
3. Studying the effect of degree of shear connection and the orientation of the shear connecter (backward or forward) to the shear force direction on the shear resistance of the X-HVB shear connecter, cracking behavior, deformation characteristics and load versus slip.
4. Conducting an experimental program to investigate the impact of fire flames on the load-carrying capacity of composite beam specimens with corrugated sheets oriented in different directions (parallel or transverse to the steel beam).
5. Investigating experimentally the influence of direction of fire exposure (either from top of concrete slab or bottom of steel beam).
6. Carrying out a finite element models to simulate the behavior of the tested specimens utilizing BAQUS computer program and study many variables by providing a useful parametric study.

## 1.8 LAYOUT OF THESIS

The thesis is presented in six chapters, as follows:

**Chapter 1 (Introduction):** contains a general description of the whole thesis.

**Chapter 2 (Literature Review):** This chapter reviews a number of studies and scientific researches which have been published on the impact of fire on composite slab and composite beam by accredited scholars and researchers.

**Chapter 3 (Experimental Program):** This chapter determines the basic properties of materials used, details of the tested specimens, burning process, devices and test of samples after burning.

**Chapter 4 (Results and Discussion):** deals with presentation, discussion and evaluation of the experimental results of specimens tested in the present study.

**Chapter 5 (Numerical Study):** includes a brief introduction to the finite elements method and details of the chosen models as well as meshing and analysis of specimens using ABAQUS 2017 computer program.

**Chapter 6 (Conclusions and Recommendations):** This chapter shows conclusions and offers some suggestions for future studies.

# CHAPTER TWO
# LITERATURE REVIEW

## 2.1 GENERAL

This chapter presents a literature review that is relevant to the research project. The review includes previous experimental and numerical investigations related to composite slabs, composite beams with solid slabs or with composite corrugated slabs, the effect of fire on composite beams and composite slabs, as well as the behavior of various types of shear connectors before and after exposure to fire.

## 2.2 COMPOSITE CONSTRUCTION

The term "composite construction" typically refers to the integration of steel and concrete into a single component in building and civil engineering structures. The purpose is to achieve a higher level of performance than what would be possible if the two materials were used separately. In composite construction, the design must acknowledge the inherent differences in properties between steel and concrete and ensure that the structural system effectively accommodates these differences. Consequently, some form of interconnection is necessary to ensure the proper functioning of the composite structure [5].

### 2.2.1 Composite Slab

Composite slabs, consisting of corrugated steel decking and reinforced concrete topping, have seen an increasing usage in Portugal. This approach offers a favorable alternative to traditional concrete slabs due to its simple and efficient assembly process at construction sites. Once the corrugated sheeting is installed and supported by beams, it acts as both a platform and formwork during the concrete pouring process. This method eliminates the

need for additional reinforcement, struts, formwork, and requires less storage space, resulting in cost reductions. The use of composite slab allows for simultaneous construction of multiple building levels [39].

Typically, composite slabs with corrugated sheeting incorporate a reinforcement mesh placed on the top face (see Figure 2.1). This mesh serves as the primary reinforcement for resisting hogging moments, enhancing slab strength in the event of a fire and distributing point loads. The Figure also illustrates the presence of shear studs as a shear connecter, which ensure a strong connection between the beam and the steel sheeting. Other construction details depicted include an end edge trim used to cover openings during concreting, and a restrain strap [40].

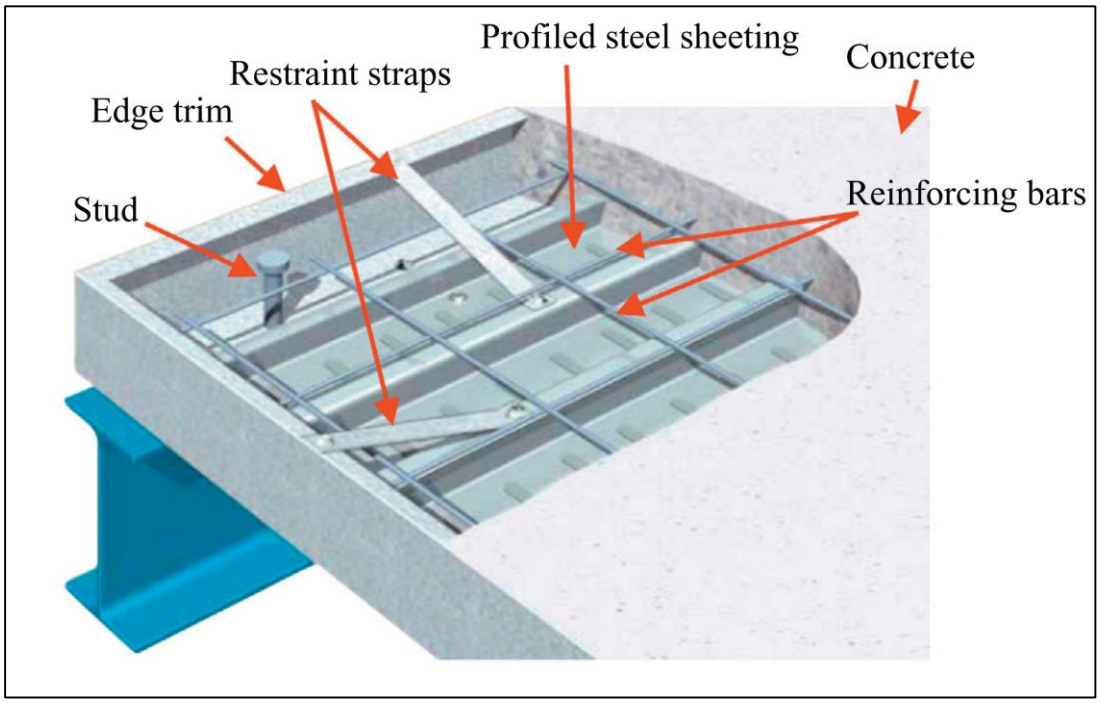


**Figure 2. 1: Components of composite construction system** [40].

**Rustin and Venkatesh (2011)** [41]**;** traced the effect of steel fibre in enhancing the behavior of composite floor structure towards fire resistance through experimental and numerical study. The researchers compared the behavior and fire resistance of traditional composite floor assemblies with those incorporating steel fibre reinforced concrete.

The results showed that the inclusion of steel fibres in the concrete significantly enhanced load-carrying capacity and reduced deflection during fire exposure compared to traditional composite floors. Furthermore, the study examined the influence of various parameters on the fire performance of steel fibre reinforced concrete composite floor assemblies, such as the volume fraction and aspect ratio of steel fibres. The researchers observed that an optimized combination of steel fibre content and geometry could maximize the fire resistance and performance of the composite floor assemblies.

**Guo (2012)** [42]**;** presented a numerical study to investigate the influence of the steel deck thickness, strength of concrete and mesh size on the behavior of composite slabs in fire. A total of six composite slabs were tested under different fire scenarios, with different load ratios. It was proven that the thickness of the steel deck had a significant influence on the fire resistance of the composite slab. However, the strength of the concrete and the mesh size only played a minor role.

**Daphne and Euripidis (2013)** [43]**;** presented a numerical study to clarify the performance of composite slabs in two structural systems: a simply supported and a 2-span continuous one at elevated temperatures, using the standard ISO fire curve to estimate the effect of static indeterminacy on the fire resistance of composite slabs, with specimen details shown in Figure 2.2. At ambient temperature, the two systems are designed to have the same load-bearing capacity. It was determined that the continuous slab appears to have significantly better behavior at estimated temperatures than the simply supported one.

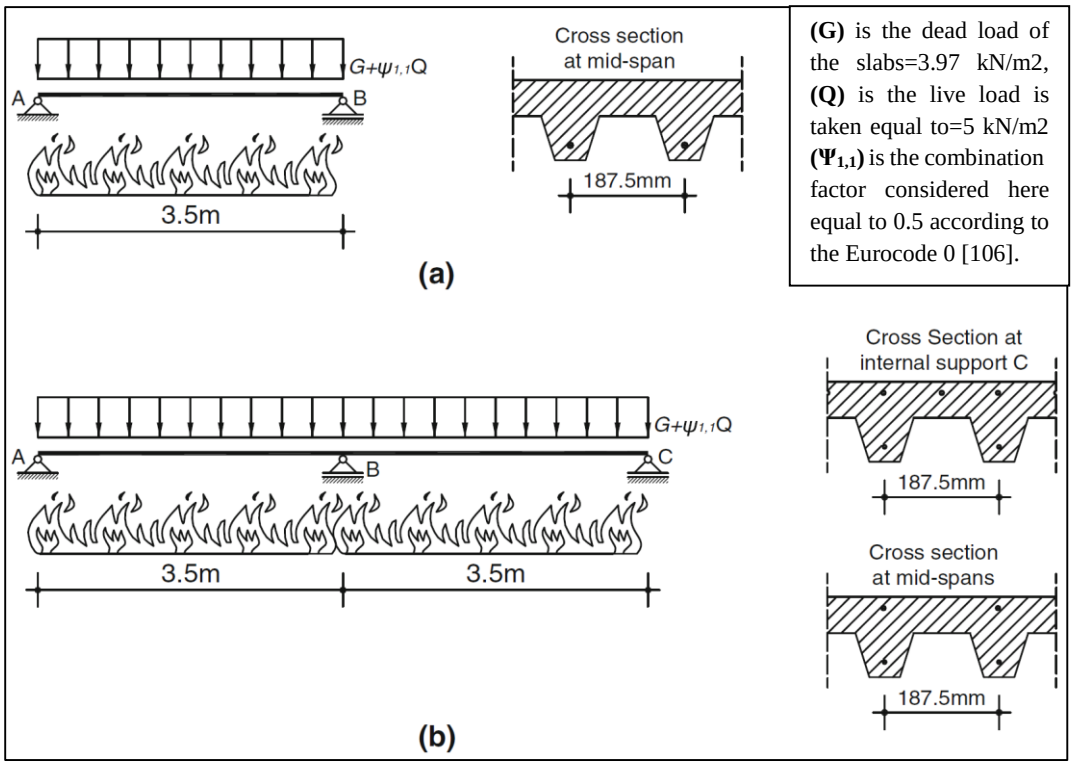


**Figure 2. 2: The two systems and the corresponding cross-sections proposed by Daphne and Euripidis: (a) simply supported system, (b) the continuous system** [43]**.**

**Abbas et al. (2015)** [10]**;** demonstrated that the inclusion of two sets of shear connectors in each line of the composite slab led to improvements in its ductility, load capacity, shear bond resistance, and slip behavior. A comparison with studies conducted by Ong [44] and Redzuan [45] (see Figure 2.3), which examined composite slabs without shear connections, emphasized the effectiveness of the shear connectors in enhancing the interaction between the steel plate and concrete.

Figure 2.4 demonstrates the enhanced interaction between the corrugated steel plate and concrete, resulting in increased shear bond resistance and reduced slip, by utilizing two lines of studs with a stud capacity of 91kN. Furthermore, the presence of end shear studs served as a warning mechanism by causing excessive deflection and promoting crack formation, thereby enhancing the overall performance and safety of the composite slab.

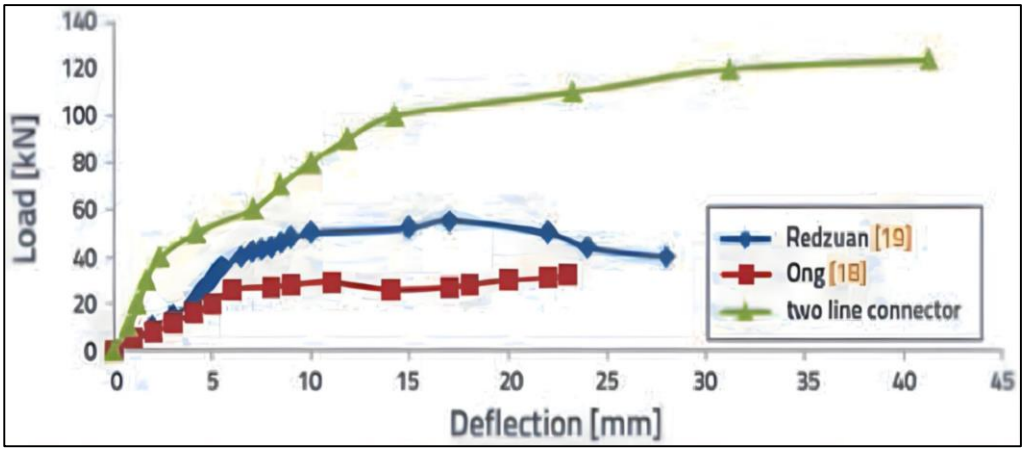


**Figure 2. 3: Load - deflection at mid span** [10]**.**

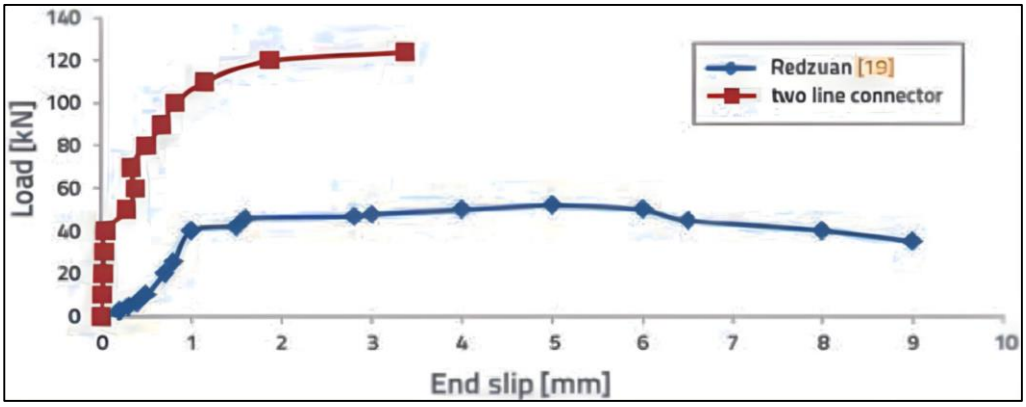


**Figure 2. 4: Load - end slip** [10].

**Siddh et al., (2017)** [46]**;** conducted an experimental study on mid span deflection and end slip in composite slabs consisting of trapezoidal profiled sheeting and concrete. The research involved testing four specimens to observe their actual behavior. Two specimens had a profile sheet thickness of 0.8 mm, with and without a V-notch, while the other two specimens had a thickness of 1.2 mm, also with and without a V-notch. Shear studs were incorporated at both ends of the sheet. Figure 2.5 illustrates the sheet configuration.

The results demonstrate that the load carrying capacity of the slab is improved when utilizing a V-notch in the profiled sheet. Shear bond failure primarily depends on the strength of the slab, whereas the sheet thickness significantly affects the behavior of the composite slab. Figures 2.6 and 2.7

present the load versus deflection behavior and load-slip behavior, respectively, for the tested specimens.

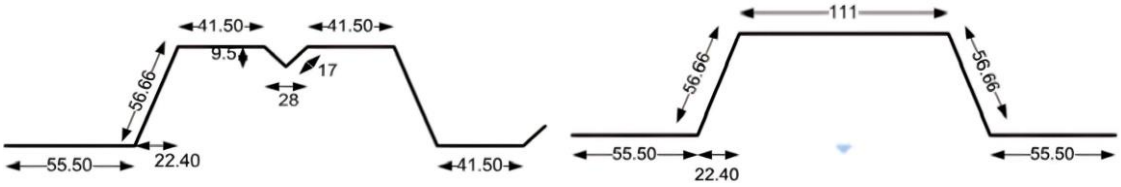


(a) (b)

**Figure 2. 5 : Profiled steel sheet details: (a) with V-Notch ,(b) without Notch** [46]**.**

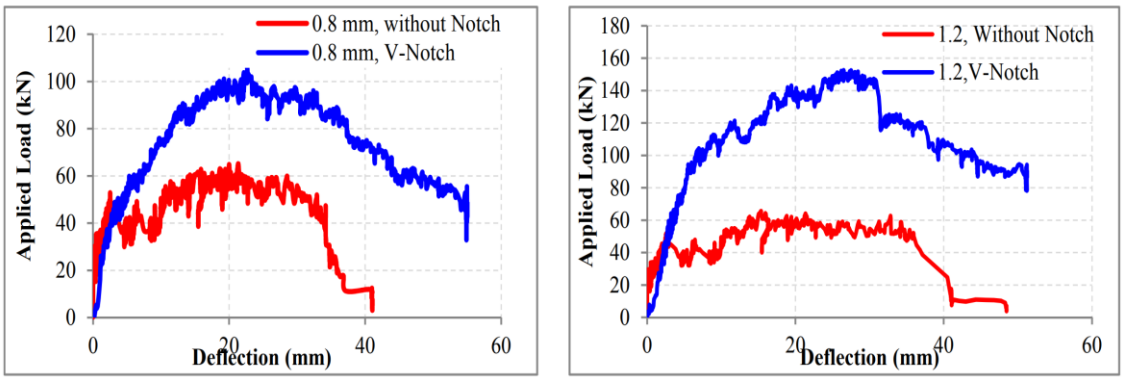


(a) (b)

**Figure 2. 6: Load–Deflection curve for specimen with thickness of profiled sheet (a) 0.8mm, (b) 1.2mm** [46]**.**

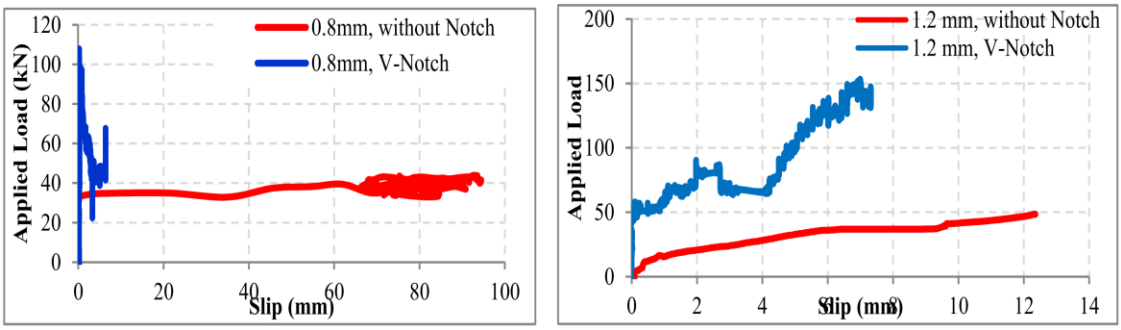


(a) (b)

**Figure 2. 7: Load–slip curve for specimen with thickness of profiled sheet (a) 0.8mm, (b) 1.2mm** [46]**.**

**Jiang et al. (2018)** [31]**;** presented a finite-element modeling investigation to analyze the thermal performance of composite floor slabs with corrugated steel decking exposed to fire. The study revealed that the fire resistance of the slabs is primarily determined by the maximum

temperature at the unexposed surface, rather than the average temperature. Additionally, the researchers found that the emissivity of the steel decking plays a significant role in the temperature distribution, and they proposed a temperature-dependent emissivity model to enhance temperature predictions.

Furthermore, the moisture content in the concrete was found to have a notable impact on the fire resistance. A 1% increase in moisture content resulted in approximately 5 minutes of improved fire resistance. The study also identified key geometric factors that influence heat transfer within the slabs. The height of the upper continuous portion of the slab was particularly influential in the thinner section, while the height of the rib and the width at the top of the rib significantly affected heat transfer in the thicker section. Figure 2.8 presents the temperature histories of composite slabs with different convective heat transfer coefficients on the fire-exposed surface.

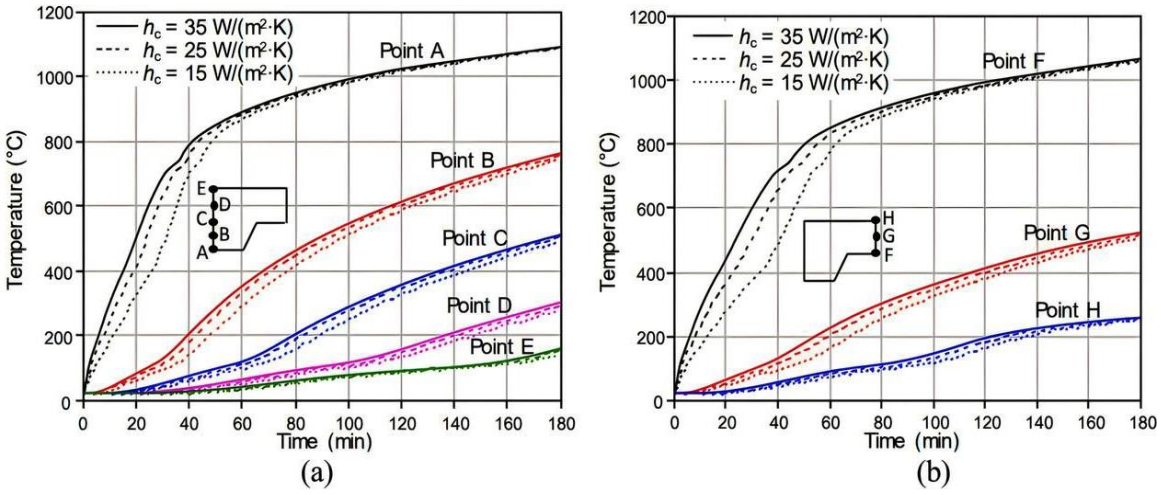


**Figure 2. 8: The temperature histories of composite slabs with different convective heat transfer coefficients ($h_c$) on the fire-exposed surface: (a) the thicker section of a slab, (b) the thicker section of a slab** [31].

**Katwal et al., 2020** [47]**;** employed a three-dimensional finite element model to investigate the load sharing mechanism between shear studs and profiled sheeting in push tests. They discovered that when the sheeting thickness is within the range of 0.9 mm to 1.5 mm, the sheeting alone is

capable of bearing 20-65% of the push load. Consequently, the actual load supported by the shear studs is lower than the prediction provided by Eurocode 4 [48], which does not consider the strength contribution of the sheeting.

The researchers conducted a parametric analysis to assess the influence of various parameters on load sharing, including sheeting orientation, stud position and layout, stud diameter and height, concrete grade, rib height, sheeting thickness, yield stress of sheeting, and level of transverse loading in composite slabs with trapezoidal steel sheeting. By comparing the results of the analysis with Eurocode 4 predictions, they highlighted the potential to enhance the accuracy of Eurocode 4 in estimating the ultimate push load and emphasized the necessity for new models to estimate the shear strength of studs.

**Ibrahim et al. (2021)** [49]**;** conducted an experimental study to examine the impact of incorporating shear connectors into composite deck slabs with different corrugated steel sheeting geometries, namely trapezoidal, triangular, and T-shapes as shown in Figure 2.9. They aimed to assess the behavior and longitudinal shear resistance of these composite slabs.

The findings revealed that the addition of shear connectors to composite slabs with trapezoidal and triangular shapes led to an increase in the ultimate load capacity by 22.2% and 17.8%, respectively, compared to slabs without shear connectors. However, the effect of adding shear connectors to the T-shaped composite slab was minimal and could be disregarded. Furthermore, the incorporation of shear connectors in composite slabs with trapezoidal and triangular shapes resulted in reduced deflection under the same load, thereby improving the overall performance of the slabs.

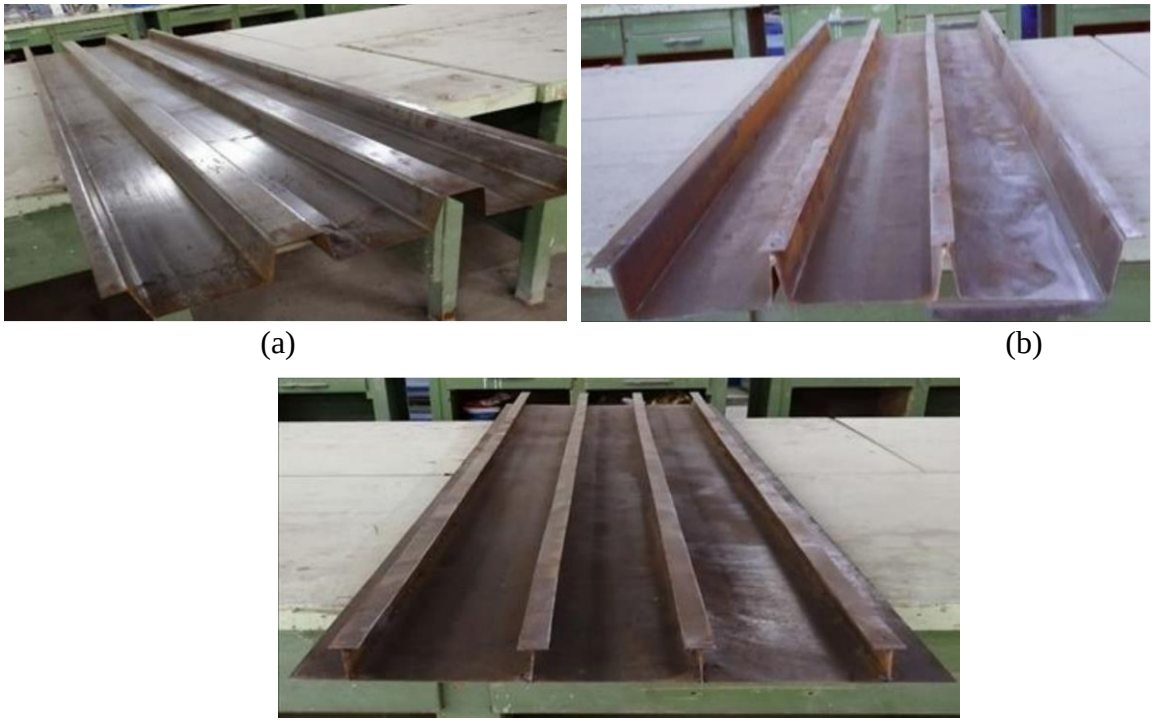

(a) (b)

(c)

**Figure 2. 9: Corrugation sheet types: (a) trapezoidal steel deck, (b) triangle steel deck, (c) T-shapes steel deck** [49]**.**

**Bolina et al. (2021)** [50]**;** investigated the performance of continuous steel decking concrete slabs when exposed to fire. Eight full-scale slabs measuring 2.56 × 4.60 m were subjected to the ISO 834 standard fire curve for 180 minutes. To assess the slab's structural continuity and induced hogging moment, a thermally-protected intermediate beam was introduced at mid-span. Several parameters were measured during the tests, including temperature distribution, surface temperatures of the unexposed slab, mid-span deflections, concrete cracking, rebar elongation, and relative slip between the steel decking and concrete.

The findings revealed that the composite behavior of the slab was lost within approximately 5 minutes of fire exposure, while structural continuity was compromised at around 10 minutes. The membrane effect, which contributes to the load-bearing capacity, was lost between 30 and 50 minutes, depending on the specific characteristics of the slab. The presence of negative rebars did not effectively maintain structural continuity. The

steel decking did not significantly contribute to the load-bearing capacity because it lost strength and detached (Figure 2.10) from the concrete within the first few minutes of the fire. However, embossments in the web of the steel decking improved shear strength and enhanced the composite action of the slab in case of fire.

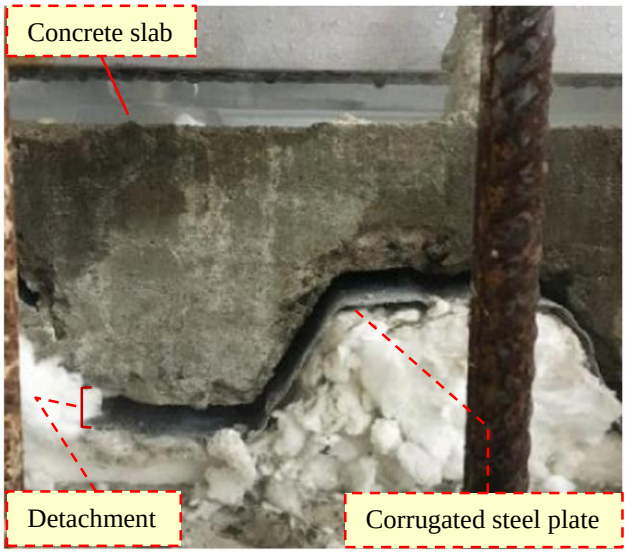


**Figure 2. 10: Detachment of the corrugated steel deck from the concrete** [50].

### 2.2.2 Composite Beam with Solid Slab

A composite beam with solid slab is formed by connecting a steel beam and a solid concrete slab to act as a single unit in resisting loads. The steel beam, typically an I-section or a wide flange section, provides the primary load-carrying capacity and stiffness, while the solid concrete slab acts as a composite deck, contributing to the overall strength and stiffness of the system. The beam and slab are connected through shear connectors, such as headed studs or through-deck welding, to ensure composite action between the steel and concrete components [23].

Additionally, the concrete slab acts as a fire-resistant cover to the steel beam, providing enhanced fire protection and allowing for longer fire resistance ratings. Moreover, the composite system exhibits improved stiffness and reduced deflection, resulting in enhanced serviceability performance and reduced vibration under dynamic loads [51].

**João et al., 2011** [52]**;** discussed the findings of an experimental investigation focused on studying the shear strength of Perfobond connectors under high temperature conditions. The authors presented an innovative examination of the behavior of Perfobond shear connectors during fire scenarios by conducted a series of modified push-out tests consisting of four sets, each comprising eight tests, at various temperature levels. The primary objective was to evaluate the strength and ductility of the shear connectors. The variables parameters were the number of holes in the Perfobond connectors, the presence of transversal reinforcement passing through these holes and a configuration involving two identical connectors placed side by side.

At room temperature, it was concluded that an increase in these variables led to an improvement in the load-carrying capacity of the connector. The resistance of the connections was more influenced by the number of connectors, while the number of connector holes had a relatively lesser effect. However, the results obtained from the tests conducted at high temperatures indicated a detrimental impact on the load-carrying capacity of the connector. It was observed that the connections made with two connectors exhibited the poorest behavior under fire conditions. Conversely, the connectors with a single hole and without any steel reinforcement passing through it demonstrated the best overall performance.

Finally, the authors concluded that the advantages observed at room temperature, resulting from the presence of reinforcing bars passing through the connector holes and the use of two connectors side by side, diminish as the temperature increases.

**Muteb and Rasoul (2016)** [53]**;** conducted a comprehensive investigation into the structural behavior of composite ultra-high

performance concrete steel beams under static loads. The study utilized a combination of experimental and theoretical approaches to gain a thorough understanding of the beams' performance. During the experimental phase, a series of tests were performed on seven composite beams. These beams were categorized into two groups based on different parameters. The first group comprised four beams, including a control beam designed to represent partial interaction. The remaining beams in this group incorporated varying numbers of shear connectors. The second group consisted of three beams, focusing on different distributions of shear connectors limited to the shear zone.

The numerical models aimed to simulate and investigate the structural behavior of the composite beams. The main findings of the research highlighted several significant conclusions. It was observed that the ultimate load capacity of the composite beams increased as the number of shear connectors increased. Furthermore, the measured end slip value exhibited a consistent decrease as the degree of partial shear connection increased from 41.6% to 58.3%, 83.3%, and up to 100%. These results indicate that a higher degree of partial shear connection leads to improved structural performance.

This study provided valuable insights into the role of shear connectors and the degree of partial shear connection in enhancing the load capacity and reducing end slip.

**XU et al. (2018)** [54]**;** aimed to investigate the role of perforated steel ribs in the load-carrying capacities of steel and concrete composite slabs. Six specimens with different shear connectors and steel bar areas were tested under negative bending. The tests recorded applied load, deformation, crack locations and trajectories, strains, and failure modes of each specimen. Shear cracks were observed in two specimens, while the

other specimens exhibited only bending cracks. The presence of perforated L-shaped ribs was found to reduce the risk of shear cracks in composite bridge deck slabs. Additionally, the perforated ribs contributed significantly to the load-carrying capacities of the composite slabs compared to plain ribs.

Based on the experimental findings, calculation methods were proposed to assess the flexural and shear strength of composite slabs. These methods quantitatively demonstrated the positive impact of perforated steel ribs on the load-carrying capacities of the slabs. Furthermore, the failure modes of the slabs could be accurately predicted.

In a study conducted by **Nina (2019)** [26]**;** the behavior of X-HVB 110 shear connectors was examined through experimental testing of two components: shear connectors and cartridge fired pins. The study investigated various parameters, including the spacing between shear connectors, the orientation of shear connectors in relation to the shear force direction (forward and backward orientation), and the influence of pins installation power levels.

The experimental testing consisted of two sets: one with forward orientation (HSF) and the other with backward orientation (HSB). The HSF set further varied the spacing between shear connectors in the HSFg and HSFg-2 test series, as shown in Figure 2.11 and Table 2.1 The study concluded that shear connectors in the forward orientation exhibited more favorable shear resistance and failure mechanisms compared to those in the backward orientation. The HSF test series demonstrated up to 12% higher ultimate shear force and 11% higher characteristic value of slip capacity compared to the HSB test series.

The reduction in spacing between shear connectors and their group arrangement in prefabricated concrete slabs did not have a negative impact on shear resistance or compromise ductility. The shear resistance, ductility, and failure mechanisms of X-HVB shear connectors were primarily influenced by the behavior, deformation capacity, and failure mechanisms of the cartridge fired pins. The pull-out resistance of the cartridge fired pins was affected by the anchorage mechanisms developed during the dynamic installation procedure and the properties of the steel base material.

The findings emphasize the advantages of forward orientation and highlight the importance of cartridge fired pins in determining shear resistance, ductility, and failure mechanisms. These results contribute to the understanding and optimization of XHVB 110 shear connectors in prefabricated concrete slabs but Unfortunately, these composite beams were tested at ambient temperature and effect of high temperatures were not considered in this study.

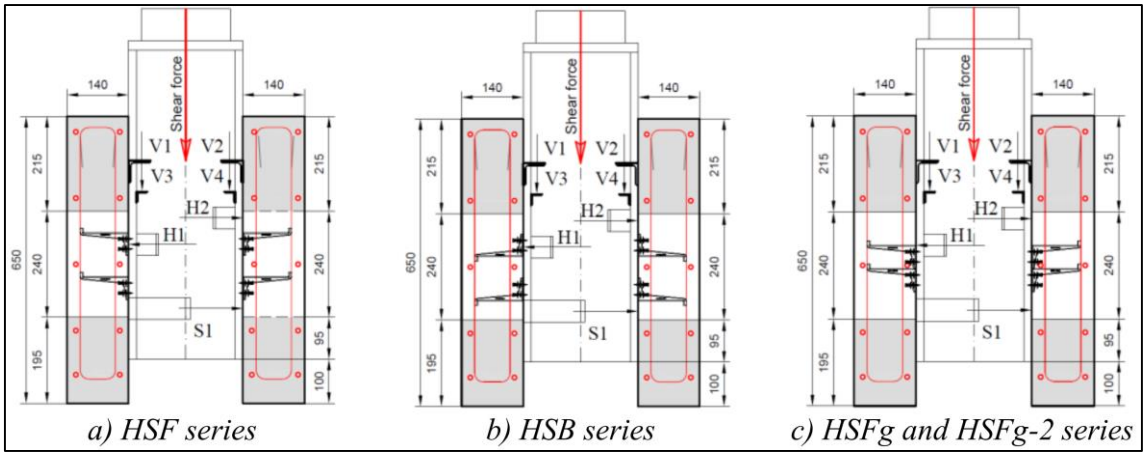


**Figure 2. 11**: **layout for push-out specimens** [26]**.**

**Table 2. 1: Geometrical properties of push-out specimens [26].**

| Series | Specimes number | Connectors number | Connectors spacing | | Concrete slabs | | Power level |
|---|---|---|---|---|---|---|---|
| | | | longit. | transv. | depth | dimensions | |
| | $N_{spc}$ | $N_{con}$ | (mm) | (mm) | (mm) | (mm) | |
| HSF | 4 | 8 | 100 | 50 | 140 | 600x650 | 3.5 |
| HSB | 4 | 8 | 100 | 50 | 140 | 600x650 | 3.5 |
| HSFg | 4 | 8 | 0 | 0 | 140 | 600x650 | 2.0 |
| HSFg-2 | 5 | 8 | 0 | 0 | 140 | 600x650 | 3.5 |

### 2.2.3 Composite Beam with Composite Slab

A composite beam with a composite slab comprises a steel section, such as an I-beam, a corrugated steel plate serving as formwork, and a concrete slab working together as a composite member. This construction provides a high strength-to-weight ratio, allowing for longer spans and reduced material usage. The composite action also improves the beam's stiffness, reducing deflection and enhancing occupant comfort. Additionally, the concrete deck provides fire resistance and protects the steel beam from heat exposure. Building upon the previous research efforts, several studies have examined different aspects of the behavior of composite beams with composite corrugated slab.

In 2007, **Nie et al.** [55]**;** conducted a series of experiments involving 13 steel-concrete composite beams. These beams were composed of corrugated steel plate, as depicted in Figure 2.12.

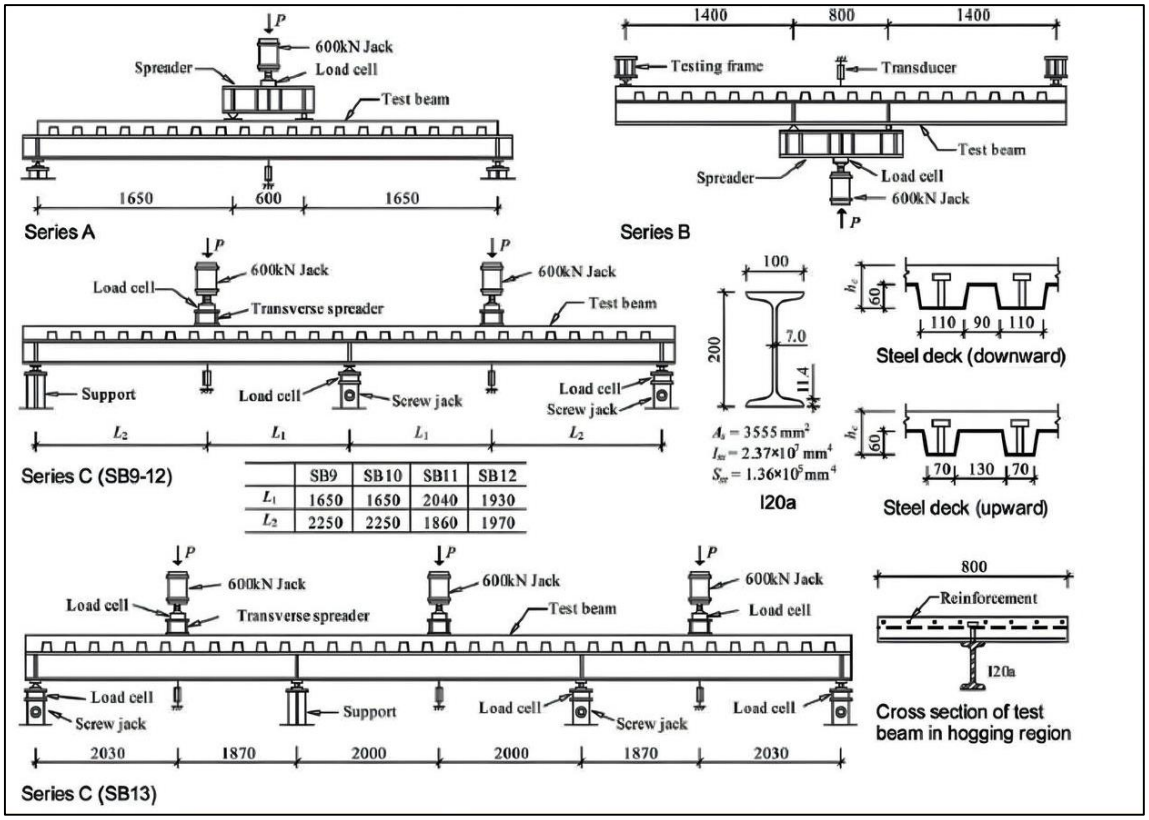


**Figure 2. 12: Test Samples of Nie et. al. Research Work** [55]**.**

The experiments focused on various factors, such as the arrangement of shear studs and profiled sheeting, the number of longitudinal reinforcement, and the loading conditions. Most of the specimens were constructed with partial shear connection, where the degree of shear connection ranged from 0.25 to 1.85 in relation to the required number of shear connectors.

To evaluate the experimental results, a comparison was made with the specifications outlined in EuroCode 4 (1994), AISC (1999), and theoretical predictions. The authors concluded that the test results aligned with the design codes and theoretical predictions. Furthermore, they determined that partial connection could be successfully employed in both positive and negative bending regions of continuous composite beams.

**Qureshi et al., (2011)** [56]**;** developed and validated a finite element model using ABAQUS program to analyze composite beams with

corrugated steel plate oriented perpendicular to the beam axis. The model incorporated material and geometric nonlinearities and employed elastic-plastic material models for steel components, along with the concrete damaged plasticity model for the concrete slab. Through a parametric study, the researchers investigated the impact of transverse spacing on push tests involving double studs positioned in favorable and staggered arrangements, while considering various concrete strengths as depicted in Figures 2.13 and 2.14.

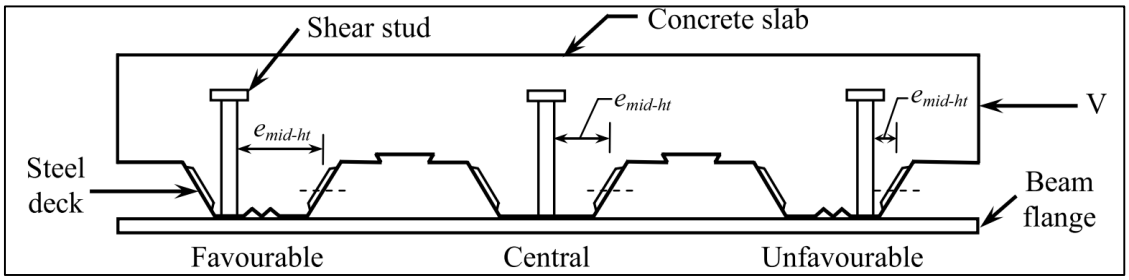


**Figure 2. 13: Different locations of the shear stud within a sheeting rib** [56]**.**

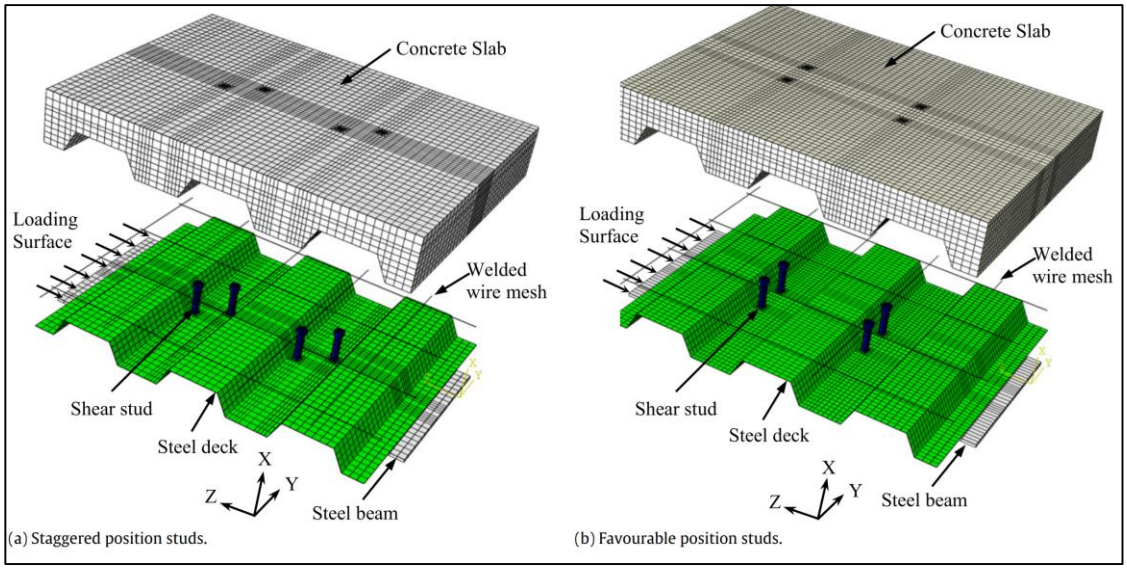


**Figure 2. 14: Finite element model adopted for parametric study showing parts of push test** [56]**.**

The findings revealed that pairs of shear connectors placed in the favorable position exhibited an average shear connector resistance of 94% compared to that of a single shear stud when the transverse spacing between the studs was 200 mm or more. In contrast, for the same spacing,

staggered pairs of studs exhibited a resistance of only 86% compared to a single stud. Notably, the strength of double shear studs in the favorable position surpassed that of staggered pairs of shear connectors.

In a study conducted by **Qureshi and Lam in 2020** [57], the researchers performed experiments using 24 full-scale push test specimens to investigate the behavior of composite beams with trapezoidal corrugated steel sheet placed perpendicular to the beam axis. The tests were conducted using a single-sided horizontal push test setup and were divided into two series, as illustrated in Figure 2.15. The first series focused on shear loading only, while the second series included both shear and normal loads. The researchers analyzed four parameters: the position and number of layers of wire mesh, the inclusion of a reinforcing bar at the bottom flange of the deck, the application of normal load and its position, and the layout of shear studs.

The results of the experiments showed that the position of the mesh on top of the deck flange or 30 mm below the top of the concrete slab did not have any significant effect on the strength and ductility of the studs. Therefore, both the industry practice of placing the mesh at a nominal cover from the top of the concrete slab and the Eurocode 4 requirement of locating the mesh 30 mm below the stud's head are deemed acceptable. When a double layer of mesh was used, the strength of the studs increased by 17% in push tests with a single stud per rib. The inclusion of a T16 reinforcing bar at the bottom of the deck rib (as shown in Figure 2.16 did not impact the behavior of the shear studs.

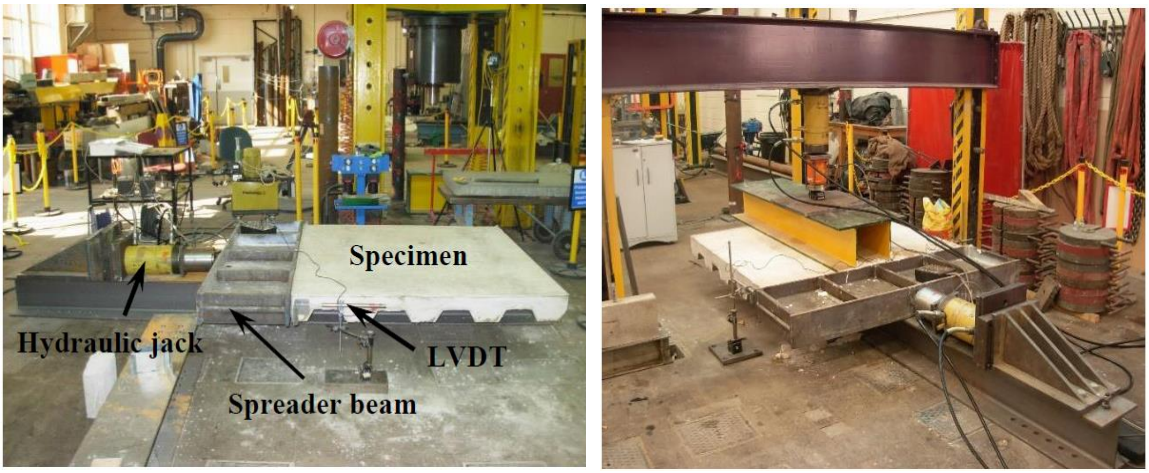


(a) First series (b) Second series with normal load

**Figure 2. 15: General test arrangement for push test** [57].

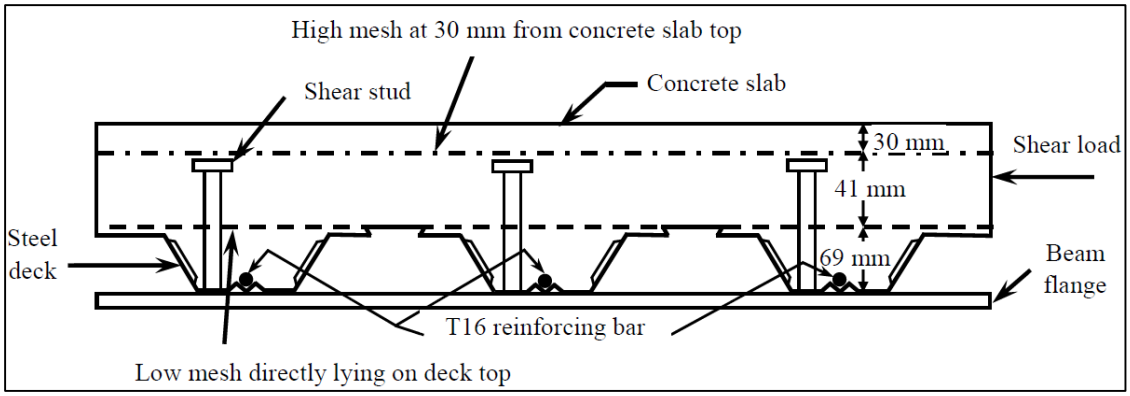


**Figure 2. 16: Details of mesh position and T16 reinforcing bar** [57].

The application of a normal load resulted in a 40% and 23% increase in stud strength for single and double studs per rib, respectively. Moreover, using studs only in the middle three ribs out of five led to a 23% increase in strength compared to the layout with studs in the first four ribs.

### 2.2.4 Composite Beam Under Fire Effect

When a steel–concrete beam under fire exposure, the structural steel beam and the concrete slab are both directly exposed to the fire while shear connectors are heated indirectly by heat transfer from the structural steel, as depicted in Figure 2.17. With relation to the temperatures achieved, these elements will lose their mechanical strength as a result of fire. The mechanical behavior of composite beams subjected to fire, on the other

hand, is much more complicated due to the various components present [58].

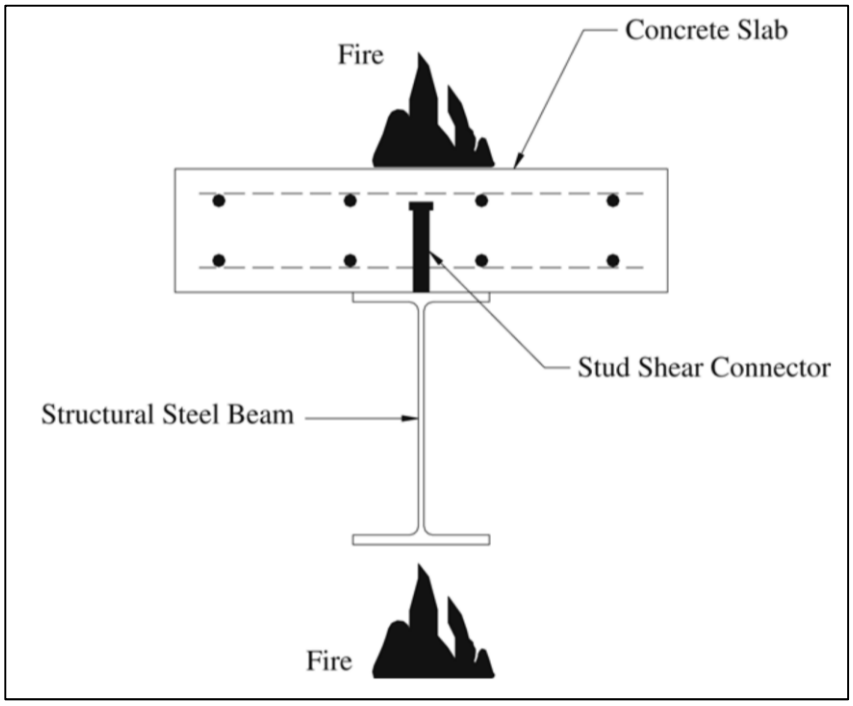


**Figure 2. 17: Schematic figure of the composite steel-concrete beam under fire** [58]**.**

**Newman and Lawson (1991)** [59]**;** conducted tests on four partially composite beams featuring a trapezoidal-shaped deck. These beams had a fire resistance rating of 1 hour, achieved by providing fire protection on the steel beam. The orientation of the deck was perpendicular to the beam span. The researchers investigated the impact of different fire protection materials and the presence of filled or unfilled voids between the top flange of the beam and the deck ribs.

Each beam was equipped with 19-mm diameter shear studs, positioned at one per rib along the beam's length with a spacing of 300 mm. The applied loading represented 66% of the nominal moment capacity of the partially composite beam under normal ambient conditions.

The test results indicated a slight difference in top flange temperatures between the cases with filled and unfilled voids. The temperature difference ranged from 20 to 60°C, with higher temperatures observed in

the unfilled void scenario. Despite this difference, the researchers concluded that, for fire resistance levels up to 90 minutes, it was not necessary to fill the voids, as this did not significantly affect the overall performance of the composite beams.

**Burnet and Oehlers (2001)** [60]**;** determined the parameters that influence both the mechanical bond and the chemical bond strength of trapezoidal and dovetailed rib shear connectors by conducting 33 push-test. The variable parameters were the effects of cross-section geometry, sheet thickness, embossments, and surface treatment, on the bond strength. It was found that the inclusion of embossments changed the shape of the load slip characteristics and the specimens with embossments required further slip after chemical bond failure to achieve their maximum shear capacity after which there was a gradual reduction in the shear capacity so the slip at the maximum shear capacity being a function of the geometry of the embossment.

Embossments were found to have a relatively minor effect on specimens with small values of the ratio width of rib opening ($b_r$) to width of flange ($b_f$) such as occurs in dovetailed sections but to have substantial effects on specimens with large values of br/bf as occurs in trapezoidal specimens. The chemical bond strength was found to be a function of the rib geometry and is therefore not predominantly an adhesive property as is usually assumed but predominantly a mechanical property to do with the peeling action.

The variation of bond strength with the shape parameter was found to be linear and the results converged to geometric focal points which can be determined directly from the shape of the rib cross-section and that of the embossments. These linear variations and focal points were independent of the surface treatment, embossment conditions and plate thicknesses and

applied to all types of bond that is the chemical bond, the residual bond immediately after chemical bond failure, the maximum bond strength and the bond strength at 5 mm slip.

**Kassem et al. (2009)** [61]**;** investigated the flexural behavior of steel-concrete composite girders under fire conditions using a three-dimensional nonlinear thermal structural finite element model. They examined various parameters and their effects on the girders, including end conditions, load ratio, material properties, and geometric configuration.

The findings revealed that the presence of longitudinal restraints significantly influenced the girders' behavior in fire conditions. Girders restrained near the neutral axis performed better than those restrained at the steel soffit. Lower load ratios and higher concrete stiffness relative to steel resulted in increased fire endurance, even after reaching a subjective failure criterion. The steel grade did not have a significant impact on the girders' structural behavior in fire conditions, while the fire endurance showed a linear relationship with the girder section factor.

The study also determined that using a small interface flange did not affect the composite girders' behavior in fire passively. Additionally, the configuration of the concrete slab was found to be an insignificant parameter for the girders' behavior under fire conditions. Furthermore, the study observed that Bernoulli beams with low stiffness exhibited a ductile behavior pattern in fire, while deep beams displayed a brittle behavior pattern.

**Mirza and Uy (2009)** [3]**;** conducted a numerical study using a three-dimensional nonlinear finite element program (ABAQUS) to investigate the behavior of headed studs as shear connectors in composite steel-concrete beams subjected to elevated temperatures. The study considered both solid and profiled slabs and developed a three-dimensional push test

model with a two-dimensional temperature distribution field to analyze the load-slip relationship and ultimate load behavior. See Figure 2.18.

The results demonstrated that the strength of shear connectors was highly sensitive to fire exposure. Profiled steel sheeting slabs exhibited greater fire resistance compared to solid slabs, based on their ambient temperature strength. The failure modes differed between the two types of slabs, with shear connection fracture dominating in solid slabs and concrete crushing and cracking dominating in profiled slabs. Stresses in the shear connector and concrete were lower in profiled slabs due to the addition of steel profiled sheeting.

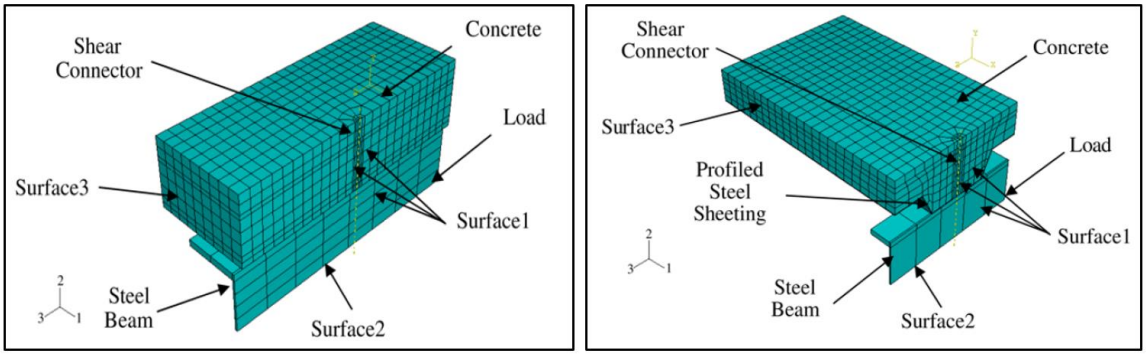


(a) (b)

**Figure 2. 18:** Finite element mesh and boundary condition of the [3]: (a) solid slab model, (b) profiled steel sheeting slab model.

Additionally, the profiled steel sheeting acted as a protective layer for the concrete slab. The profiled steel sheet slabs were able to withstand 60% of their ultimate load at elevated temperatures compared to ambient temperature, whereas solid slabs could only sustain 40% of their ultimate load As depicted in Figure 2.19.

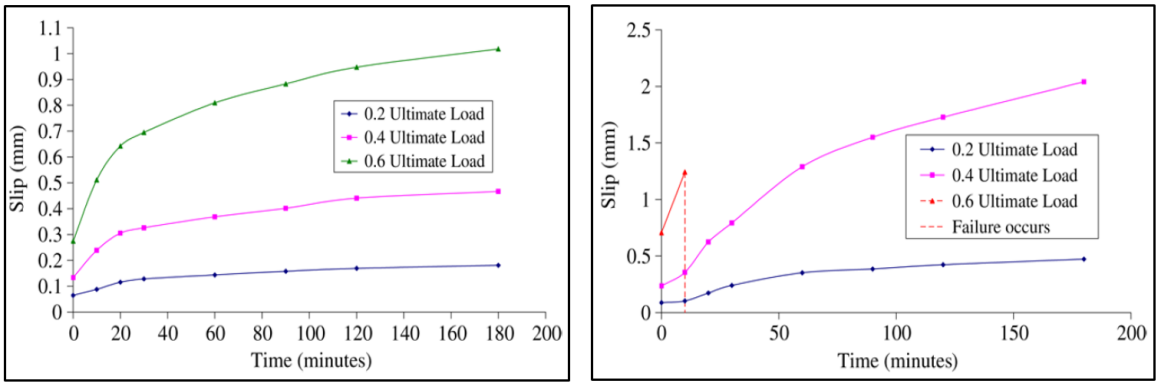


(a) (b)

**Figure 2. 19: Slip at different load levels according to time for [3]: (a) solid slab, (b) profiled steel sheeting slab model.**

**Mirza et al. (2011)** [62]**;** presented experimental studies that examined the effects of elevated temperatures on headed stud shear connectors in composite steel-concrete beams with solid and profiled steel sheeting slabs with details shown in Figure 2.20. Sixteen push tests were conducted to investigate the behavior of these connectors when subjected to elevated temperatures, considering the changes in material properties. The tests were progressively loaded up to the ultimate load to assess the structure's ability to withstand fire-induced loads.

The primary failure mode for the solid slabs was identified as headed stud shear connection failure, while the profiled slabs experienced concrete crushing and cracking failure. Notably, the solid slabs generally exhibited higher ultimate loads compared to the profiled slabs due to the failure of the headed studs. The profiled slabs, on the other hand, demonstrated greater ductility, attributed to the use of profiled steel sheeting. Despite the concrete failure, the profiled sheeting contributed to the enhanced ductility of the profiled slabs. Overall, the ambient temperature slabs exhibited the highest stiffness, ductility, and ultimate shear load compared to those exposed to temperatures of 200°C, 400°C, and 600°C. According to Eurocode 4, the solid slab and profiled slab experienced a reduction of 41%

and 64%, respectively, at 4 mm slip when exposed to elevated temperatures.

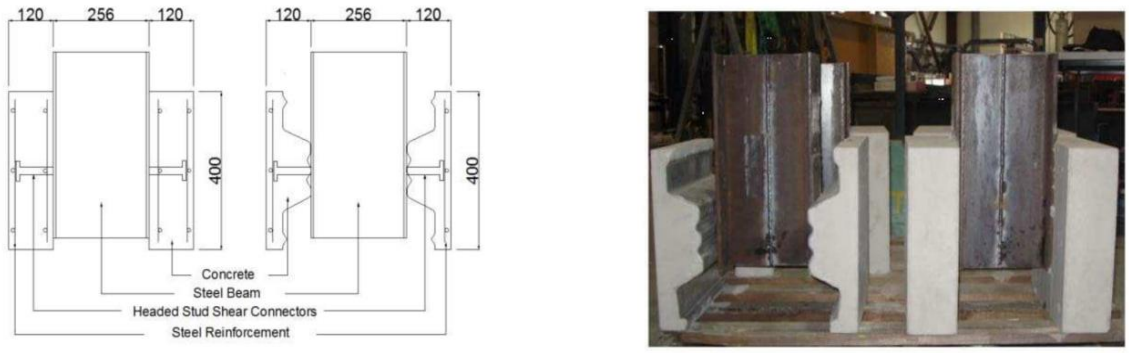


**Figure 2. 20: Details and Dimensions of push test specimens proposed by MIRZA et al.** [62]**.**

In a study presented by **Rodrigues and Laím (2014)** [63], the structural behavior of T, T-block, and T-Perfobond shear connectors under fire conditions was examined. The main objective was to evaluate the shear resistance, ductility, and collapse modes of these connectors when subjected to elevated temperatures. Several variable parameters were considered, including the number of holes in the connector, the presence of transversal reinforcement bars passing through the holes, the connector arrangement, and the connector height, among others.

The performance of the connectors was compared at different levels of elevated temperature, and a comparison was also made between their behavior at ambient and elevated temperatures. Experimental results were compared with predictions from existing analytical models that take into account changes in the shear strength of the T, T-block, and T-Perfobond connectors at elevated temperatures.

The research findings revealed that the shear resistance capacity of these connectors at elevated temperatures is significantly influenced by their shape relative to the steel beam. This indicates the importance of considering the shape of the connectors when designing for fire conditions.

**Chen et al. (2015)** [64]; conducted both numerical and experimental investigations to examine the behavior of shear connectors in composite slabs with steel profiled sheeting placed perpendicularly to the steel beam under various fire conditions. Six push-out tests were conducted at four different temperature levels, and the preparation and results of these tests were presented. Throughout the heating process, a non-uniform temperature profile was observed across the composite cross-section.

The results showed that the ultimate loads and initial stiffness generally decreased as the temperature of the shear connectors increased. At ambient temperature, concrete pull-out failure was observed, while shear stud failure occurred at high stud temperatures of approximately 600 °C. To further analyze the behavior of shear connectors under different temperature levels, a new three-dimensional model was developed using ABAQUS software, which allowed for both heat transfer and mechanical analyses. The numerical model was validated using the experimental measurements from this study.

By comparing the design predictions for shear connector capacity at elevated temperatures based on EC4 standards with those calculated from the finite element model and obtained from experimental tests, it was demonstrated that the EC4 design approach provided conservative estimates. Finally, the study proposed a new design equation to determine the decrease in capacity exhibited by shear connectors when exposed to elevated temperatures.

**Ellobody and Young (2015)** [65]**;** focused on the nonlinear analysis and design of unprotected composite castellated and non-castellated steel beams with profiled steel sheeting at elevated temperatures. The study incorporated the nonlinear material properties of steel, concrete, profiled steel sheeting, reinforcement bars, and shear connection behavior into finite

element models. Parametric studies were conducted to investigate the variables influencing the fire resistance and behavior of composite beams, including load ratios, fire curves, presence of web openings, and steel grades.

The findings demonstrated that simply supported unprotected composite castellated and non-castellated steel beams could have fire resistances below 30 minutes when exposed to the standard fire curve. The strength of the steel beam emerged as a significant factor influencing the behavior and failure modes of composite beams, potentially leading to changes in the failure mode during a fire. Comparisons between fire resistances obtained from finite element analyses and design values from Eurocode 4 for composite beams at elevated temperatures indicated that Eurocode 4 generally exhibited conservatism for most unprotected composite castellated and non-castellated steel beams, except for specific cases involving the standard fire curve under load ratios of 0.4 and 0.5. Figures 2.21 (a) and 2.22 (a) plotted the temperature contours using the thermal analysis for both composite castellated and noncastellated steel beam respectively. While Figures 2.21 (b) and 2.22 (b) plotted the principal stress distribution.

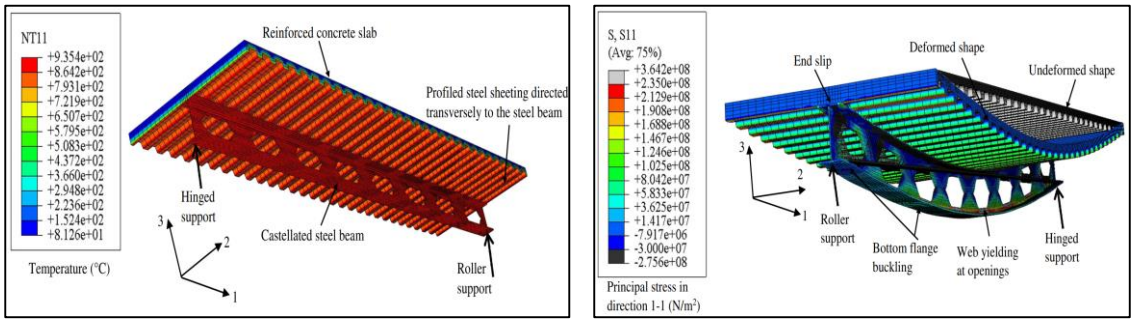


(a) Temperature contours at the end of the standard fire exposure

(b) Deformed shape and stress contours at failure

**Figure 2. 21: Composite castellated beam predicted by Ellobody** [65]**.**

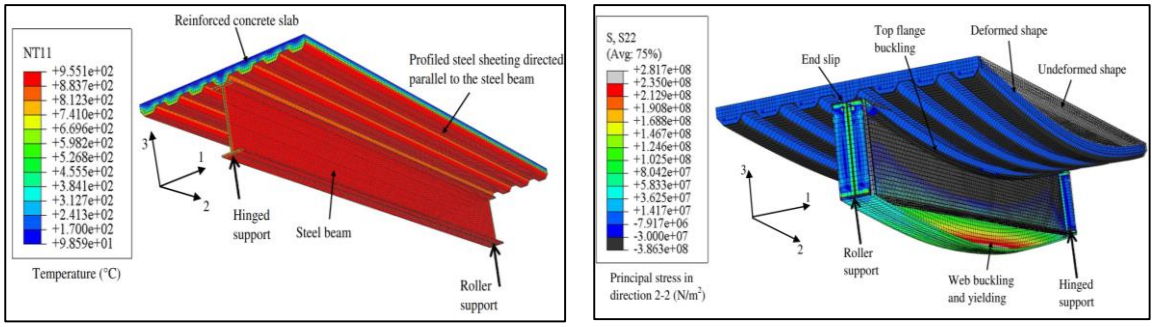


(a) Temperature contours at the end of the standard fire exposure

(b) Deformed shape and stress contours at failure

**Figure 2. 22: Composite noncastellated beam predicted by Ellobody** [65]**.**

While **Wang et al. (2016)** [66]**;** conducted an experimental investigation to examine the response of two composite beam specimens subjected to fire exposure. The specimens were similar in design, except for their shear connection ratios. One specimen was fully composite, while the other was partially composite with a 50% shear connection ratio. The details of the specimens and the truss reinforcement type used show in Figure 2.23.

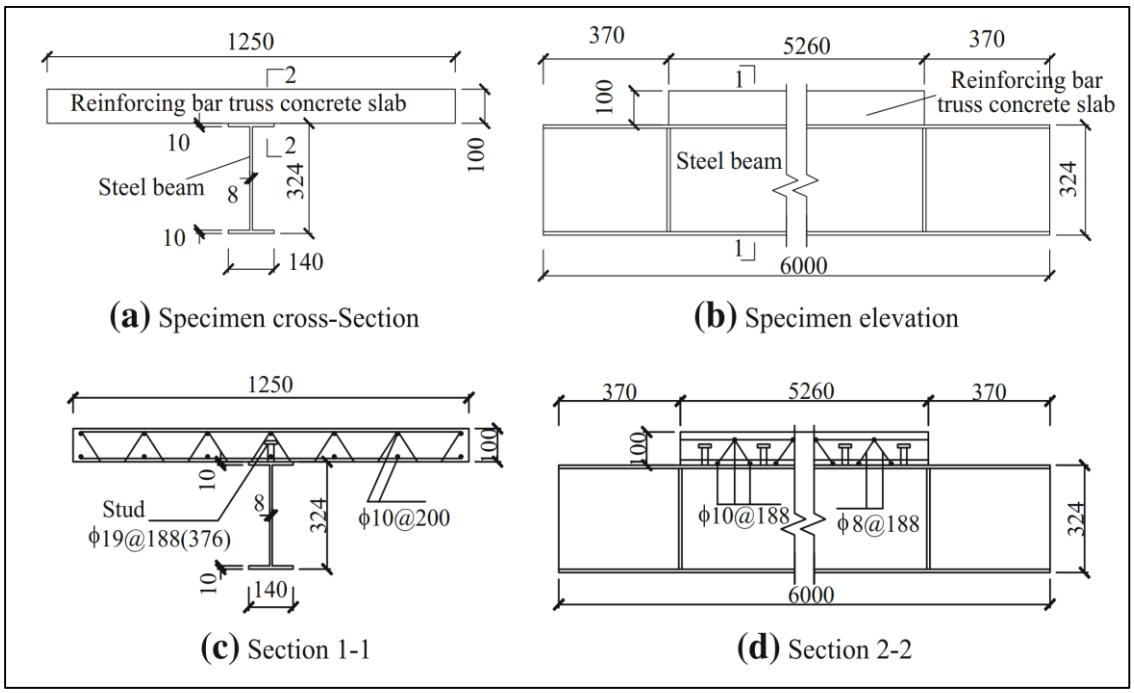


**Figure 2. 23: Details of specimens (unit: mm)** [66]**.**

The concrete slab for each specimen was constructed using a flat steel deck, and reinforcement was provided by a reinforcing bar truss. A

constant vertical load was applied at four locations along the span of both specimens. The specimens were then tested in a furnace using the ISO-834 standard fire curve. Both specimens exhibited significant deflections, indicating flexural yielding of the composite beams. Interestingly, the measured flexural capacities of the specimens were larger than those predicted by Eurocode 4. The researchers also observed that the shear connection ratio had a notable influence on the slip and uplift behavior of the concrete slabs at the interface.

The failure criterion for the specimens was defined as the maximum deflection reaching span/30. The time required to reach this failure criterion was nearly the same for both specimens, with the fully composite beam failing at 51 minutes of fire exposure and the partially composite beam failing at 49 minutes. A companion paper associated with this study explores the degradation of material properties at elevated temperatures, as well as the slip behavior of shear connectors. Additionally, it presents an analytical approach to predict the fire response of steel-concrete partially composite beams.

In light of previous studies by others, **Shahabi et al., (2016)** [67]**;** presented a numerical analysis approach to study the behavior of channel connectors under fire conditions and compare it with the analysis performed on headed stud and Perfobond shear connectors. The paper begins by reviewing the mechanism of different types of shear connectors and then proposes a non-linear thermomechanical finite element (FE) model of channel shear connectors embedded in high-strength concrete (HSC) subjected to fire.

Initially, an accurate FE model of the channel connectors tested at ambient temperature is developed to assess their strength when embedded in an HSC slab. The model's predictions are validated by comparing them with the experimental study conducted by Shariati et al. (2012) on the

testing of channel connectors at ambient temperature. Subsequently, the FE model is extended to investigate the behavior of channel connectors under fire conditions. A comparative study is conducted to assess the performance of channel connectors in comparison to headed stud and Perfobond shear connectors. The findings indicate that channel connectors offer a more cost-effective and easily applicable alternative to conventional shear connectors.

This paper contributes to the understanding of the behavior of channel connectors under fire, providing valuable insights for the design and implementation of composite structures. The numerical analysis approach allows for a comprehensive evaluation of the performance of different shear connectors, aiding in the selection of the most suitable option for specific applications.

**Erica and Amit (2017)** [68]**;** conducted a study using 3D finite element analysis to assess the structural behavior of composite beams with simple connections under combined gravity loads and design fire scenarios. The variable parameters, including connection type, deck type, continuity of the composite slab, slab reinforcement type, fire resistance rating, and design fire scenario.

It was concluded that when composite beams and simple connections were protected with a 1-hour fire resistance rating (FRR) and subjected to a 1-hour fire with subsequent cooling, there were no instances of premature fracture failure in the connections that would lead to the collapse of the composite beams. Furthermore, it was found that typical composite beams and simple connections, designed with a specific fire resistance rating (n-hour) and exposed to a design fire scenario involving the same (n-hour) heating followed by cooling, exhibited satisfactory performance without connection failure resulting in beam collapse.

**Choi (2019)** [69]**;** investigated the behavior of headed shear studs embedded in both a transverse trapezoidal deck and a solid slab under ambient and fire conditions. The researchers conducted twelve push-out tests following the ISO 834 standard fire using a customized electric furnace.

In the tests, a stud shearing failure was observed in the solid slab specimen, indicating that the failure was primarily governed by the concrete. However, in the transverse deck specimen, the failure mode transitioned from a concrete-dominated failure to stud shearing as the temperature increased. The experimental observations were compared with design requirements, and it was found that the Eurocode design guidance for the transverse deck slab provided a highly conservative estimate for shear resistance. To address this issue, the researchers proposed a new design formula that can determine the capacity of the shear connection regardless of the slab type when stud shearing occurs at high temperatures.

The study highlights the importance of understanding the behavior of headed shear studs in different types of slabs under fire conditions. The findings indicate that the failure mode can change with increasing temperature, which has implications for the design and assessment of composite structures.

**Lyu et al. (2020**) [70]**;** investigated the fire resistance of composite beams with restrained superposed slabs, Figure 2.24 shows the details of the experimental program. Three specimens were tested under uniformly distributed loads in a furnace. The variable parameters were the effects of the thickness of the postcast top layer in superposed slabs and the spacing of shear studs on the structural behaviour of composite beams under fire. It was found that the temperature of the concrete superposed slabs decreased long their heights from the bottom.

The most drastic change of the temperature along the slab cross section was found in the region with a distance of 40mm to the slab bottom. The concrete superposed slabs could impose restraints to the steel beams due to their incompatible deformations. Cracks were developed on the top surfaces of the specimens and the superposing interfaces between the precast slabs and postcast top layers were not broken. Also, the spacing of shear studs could have a significant effect on the fire resistance of composite beams, especially for their deformation recovery capacities. In contrast, the effect of the thickness of the postcast top layers was negligible.

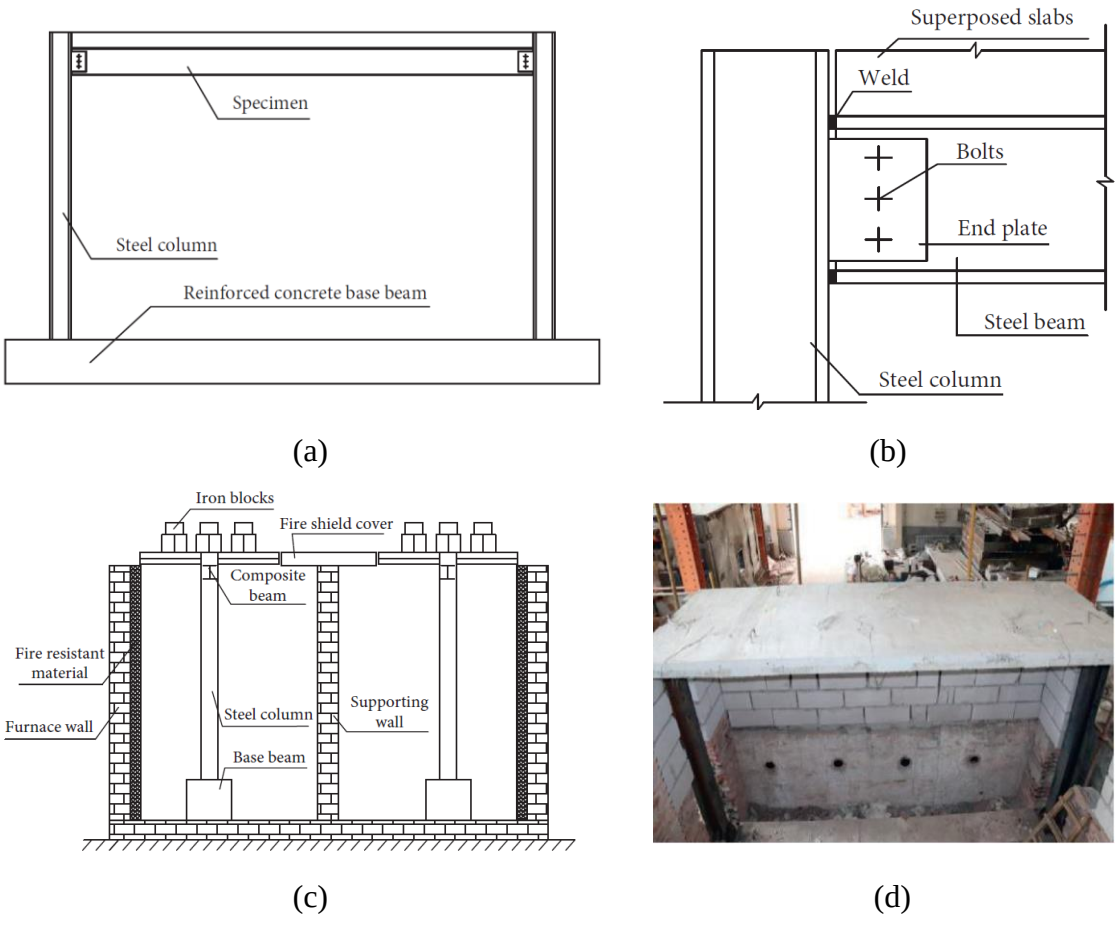


**Figure 2. 24: Experimental program: (a) specimen restraining scheme, (b) details of restraints, (c) test setup, and (d) composite beam specimen** [70]**.**

**Cirpici et al. (2020)** [71]**;** conducted a numerical investigation on the thermal performance of a composite beam with a composite slab system when exposed to different fire scenarios, including fast fire and ISO standard fire, specifically focusing on the concrete slab part. The researchers applied fire protection material to cover the steel beam and trapezoidal steel deck, except for the areas where the steel beam sits on the steel deck due to the presence of paint coating applied during the connection of the steel beam and slab. Two methods were used to apply the coating: one layer with a thickness of 1mm and four layers with a thickness of 0.25mm, applied individually.

The authors observed that a higher temperature gradient occurred in the open location between the steel deck and steel beam, reaching approximately 50°C. In contrast, the temperature was lower on the bottom side of the steel deck and on the lower flange and web of the steel beam, around 25°C as shown in Figure 2.25. This temperature distribution was attributed to the intumescent coating that delayed heat transfer to the inside and the fire resistance properties of the concrete, which contains cement and various aggregates known for their fire resistance.

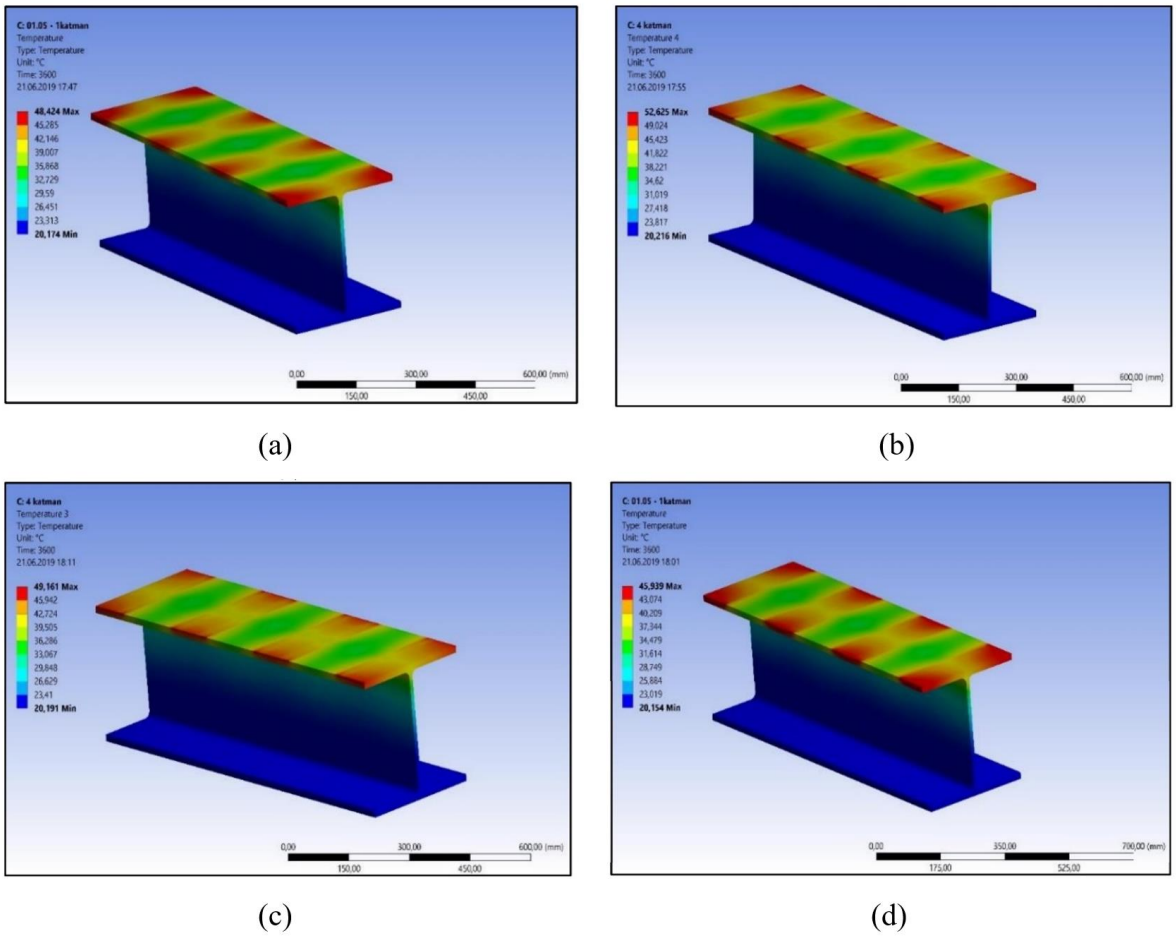


**Figure 2. 25: The temperature profile of steel beam due to protected by (a)one-layer intumescent coating, (b) four layers intumescent coating under (ISO 834) Standard fire, (c) one-layer intumescent coating under Fast fire and (d) four layers intumescent coating under Fast fire** [71].

The study concluded that there was little difference between the one-layer and four-layer coatings under both fast fire and ISO standard fire conditions. Additionally, the researchers noted that the use of fire insulation material on the steel profile deck and steel beam had a minor effect, reducing temperatures by approximately 6°C compared to the unprotected model as shown in Figure 2.26. This slight temperature reduction was attributed to the significant amount of heat absorbed by the concrete, which facilitated heat transfer from top to bottom.

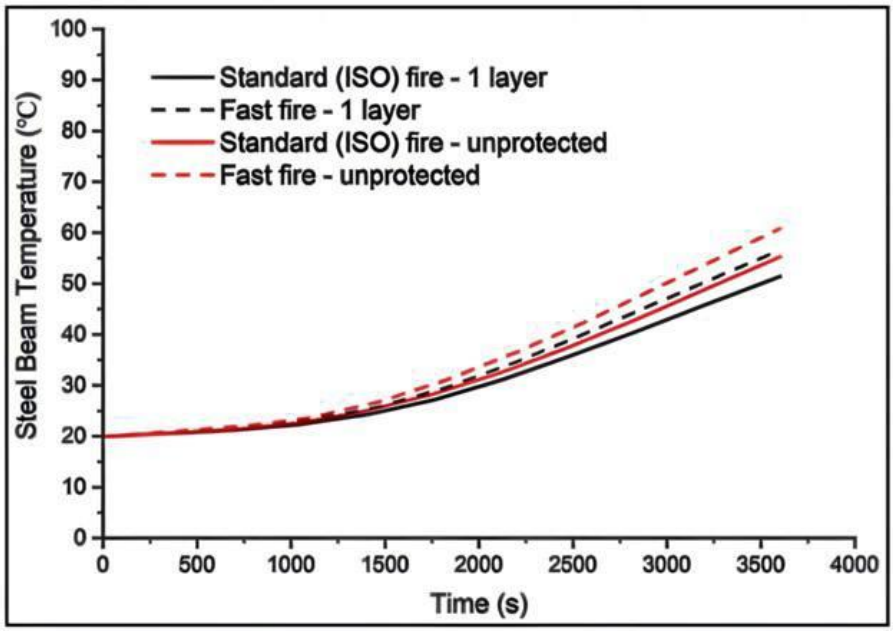


**Figure 2. 26: Comparison of protected and unprotected steel beam temperature results under standard (ISO) and fast fires** [71]**.**

**Nguyen and Park (2021)** [72]**;** studied the effect of the thickness of fire insulation on the strength degradation and temperature distribution of the composite beam. It was noticed that due to temperature degradation in the steel beam, the fire resistance of the beam improves as the fire insulation thickness increases. Whereas **Martinez and Jeffers (2021)** [58]**;** claimed that prescriptive fire insulations could not provide enough protection against traveling fires. Improved performance under traveling fires was obtained by good fire protection allocation selection using a performance-based design method. Insulation was removed from internal floor beams and applied to outside floor beams and girders.

**Wang et al. 2023** [73]; investigated the fire behavior of steel-concrete composite beams (SCB) and partially encased steel-concrete composite beams (PEB) using numerical analysis. They established numerical models using the ABAQUS software and validated them with experimental data. Parametric studies were conducted to analyze the impact of various factors, such as load ratio, concrete and steel strength, width of concrete slab, size

of steel beam, fire protection layer, and degree of shear connection, on the fire behavior of SCB and PEB.

The results of the analysis indicated that both SCB and PEB exhibited four deformation stages during a fire: elastic, elastic-plastic, plastic small deformation, and plastic large deformation. Under fire conditions, the web of SCB experienced a tension-compression-tension process, while the bottom flange of PEB could transition from tension to compression at lower load ratios. The failure mode of PEB, specifically the occurrence of concrete crushing, depended on the load ratio. In the case of SCB failure, only the bottom flange of the steel beam yielded, while the concrete was crushed.

The fire resistance of SCB was found to be approximately 22 minutes under various parameters, whereas PEB demonstrated a fire resistance ranging from 82 to 93 minutes under a load ratio of 0.4. Increasing the load ratio from 0.2 to 0.6 resulted in an 8-minute decrease in the fire resistance of SCB, whereas PEB experienced a significant reduction of 110 minutes.

## 2.3 CONCLUDING REMARK

The following conclusions can be summarized from the review of the literature:

- Thicker steel decks enhance fire performance, while concrete strength and mesh size have a minor impact.
- Corrugated steel sheeting thickness and V-notches affect load-carrying capacity and shear bond failure.
- The presence of shear connectors and the interaction between shear studs and corrugated sheeting influence the load sharing mechanism in composite slabs.

- Perforated steel ribs enhance load-carrying capacity and reduce shear cracks in composite slabs.
- Position and number of wire mesh layers have minimal effect on shear stud strength.
- Corrugated steel sheeting slabs have higher fire resistance than solid slabs. The failure modes vary between the two types: shear connection fracture is dominant in solid slabs, while corrugated slabs experience concrete crushing and cracking.
- The shear connection ratio had a notable influence on the slip and uplift behavior of the concrete slabs at the interface.
- the failure mode can change with increasing temperature.
- The spacing of shear studs had a significant effect on the fire resistance of the beams, while the thickness of the postcast top layers had a negligible effect.
- The ultimate load capacity and reduced end slip were influenced by the number of shear connectors and the degree of partial shear connection in composite beams.
- Composite castellated and non-castellated steel beams could have fire resistances below 30 minutes when exposed to the standard fire curve, and the strength of the steel beam influenced the behavior and failure modes of composite beams.
- Based on my current knowledge, there appears to be a lack of studies examining the behavior of the new type of shear connector (XHVB) under the influence of fire.

So, the present study implemented an analytical and an experimental investigation on the behavior of composite steel corrugated plate-concrete deck that mechanically connected with (XHVB) type of shear connecter

with steel beam and exposed to fire. Different parameters have been implemented such as:

1. Change in temperature levels.
2. The effect of side that exposed to fire (from to top or bottom).
3. The effect of direction of corrugated plate (parallel or transverse) with respect to the beam length.
4. Using single or double of the shear connecter in each line.
5. The orientation of shear connector relative to the direction of the shear force.

# CHAPTER THREE
# EXPERIMENTAL WORK

## 3.1 INTRODUCTION

This chapter provides a detailed account of the experimental program, including the research methodology adopted to achieve the objectives outlined in chapter one. It covers the preparation and curing of composite beam specimens, the burning process for these specimens, and the testing program.

Previous experimental work on the structural behavior of composite beam specimens with X-HVB shear connector types when exposed to fire has been limited. Therefore, this study aimed to investigate the effect of fire exposure from different sides (top of concrete slab or bottom of steel beam) at various temperature levels (350, 450, and 550°C).

The experimental investigation program was carried out at the Structure laboratory of the University of Babylon and included ten composite beam samples and twelve push-out test samples.

## 3.2 METHODOLOGY

To perform this study, many sequential steps were followed. These steps were started with preparing the required materials such as (steel section, X-HVB shear connecter, corrugated steel plate, end plates and in situ concrete).

The second step was to connect steel beam and corrugated steel plate with X-HVB shear connecter. The third step was a placement step using end plate as molds for concreting composite beam specimens, which were made to fit the dimensions of the model, while a wooden mold was used for concreting pushout specimens. These specimens were cured using water for 28 days and thereafter burned finally in different temperature levels. All the

models were left to cooled for one day. The final step was to test all the models and record their results and behaviors. Figure 3.1 shows a flow chart to summary these most important steps followed in this study.

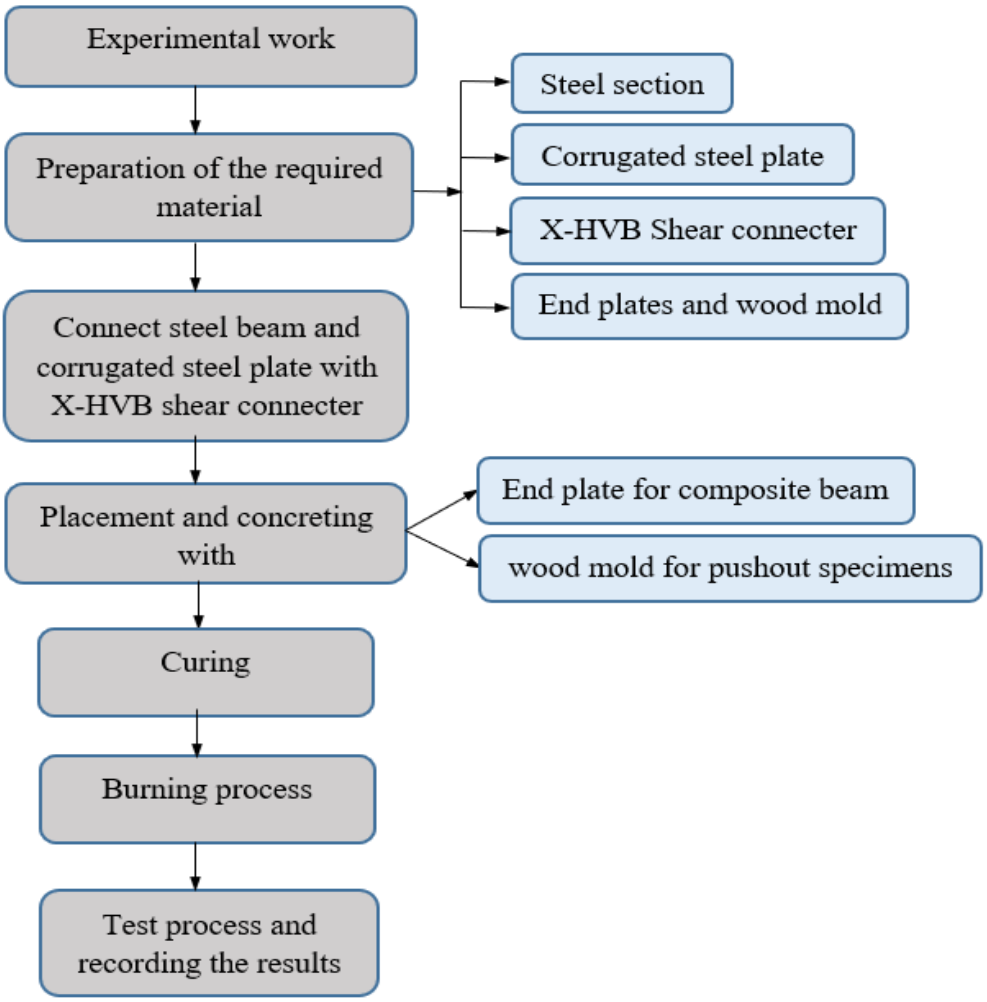


**Figure 3. 1: Details of the experimental program.**

## 3.3 DETAILS OF TEST SPECIMENS

All ten composite beam specimens have the same geometry, except for the orientation of the corrugated steel plate. In five specimens, the ribbed of the corrugated steel plate runs parallel to the steel beam, while in the other five, it runs perpendicular to the beam. Each specimen is 2000 mm long and consists of a composite concrete slab with a width of 660 mm and a thickness of 140 mm. The composite slab sits on top of the composite

section and is connected to the bottom part, which comprises corrugated steel plate and European I-steel beams (IPE 160).

The two components of the composite section (concrete and steel) are joined by X-HVB shear connectors, which are fixed to the top flange of the I-steel beam using two X-ENP-21 HVB cartridge fastening pins for each connector. The dimensions and number of shear connectors used are the same for all the test samples. As a result, the overall depth of each typical test sample is 300 mm, and it weighs around (675 kg) for specimen with parallel corrugated steel plate and (345 kg) with that of transverse plate. Figures 3.2 and 3.3 depict a typical cross-section for the test sample.

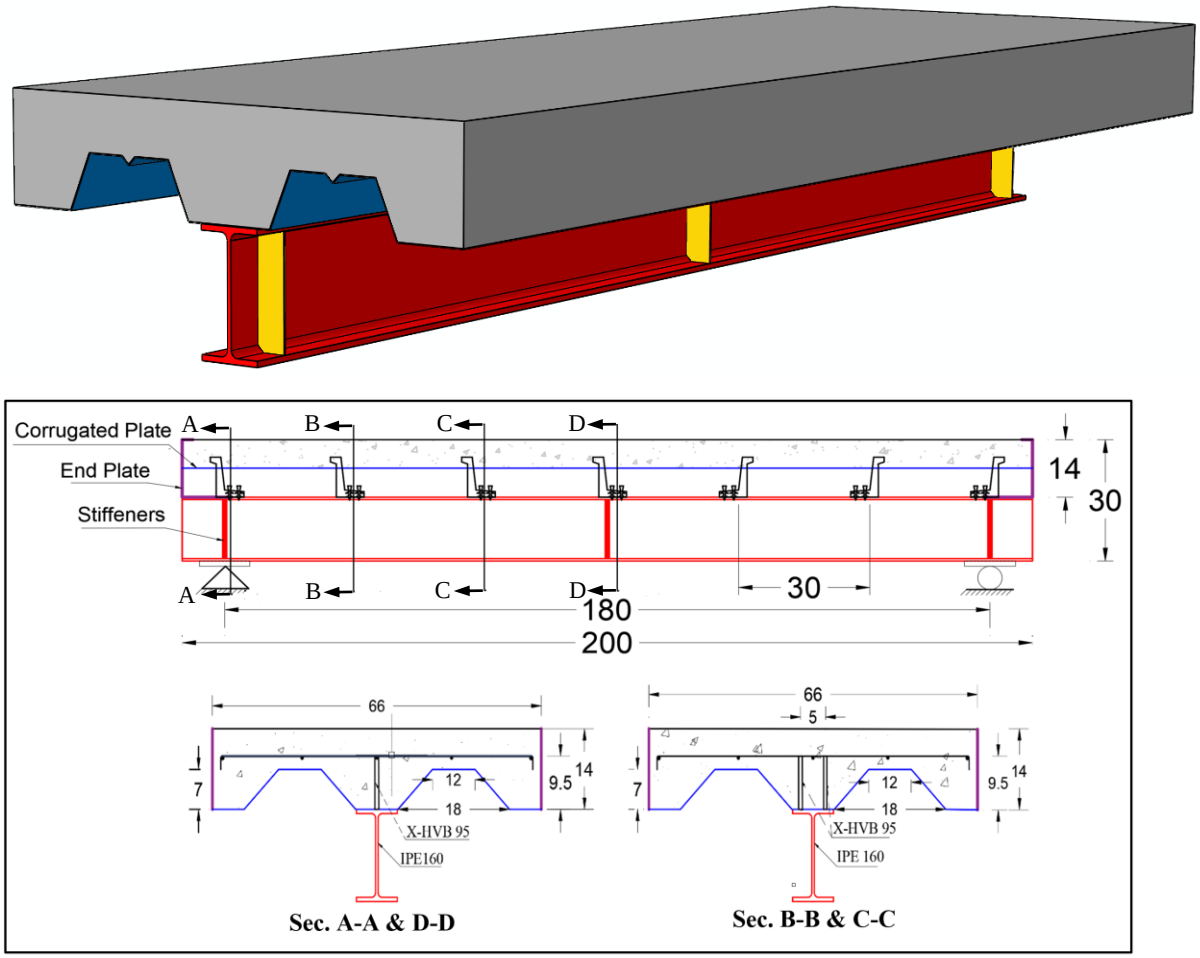


**Figure 3. 2: Composite beam specimens' details with parallel corrugated steel plate (all dimensions in cm).**

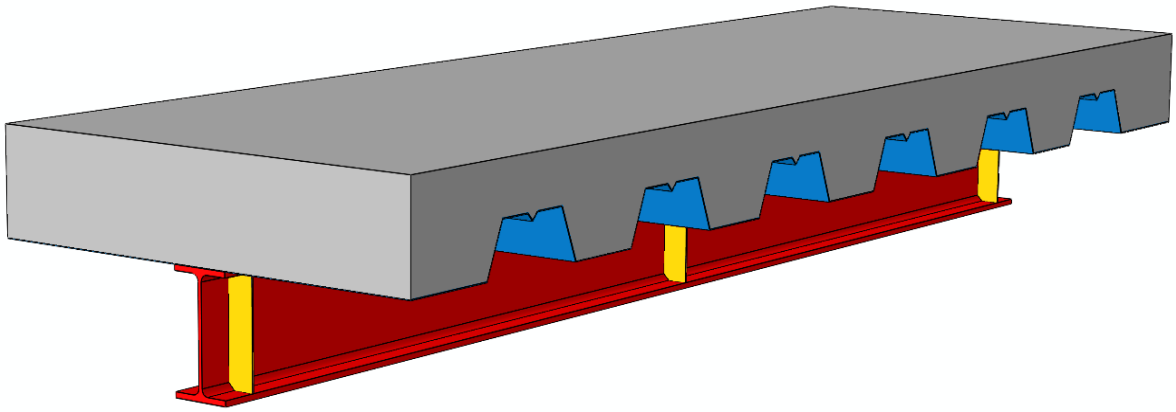

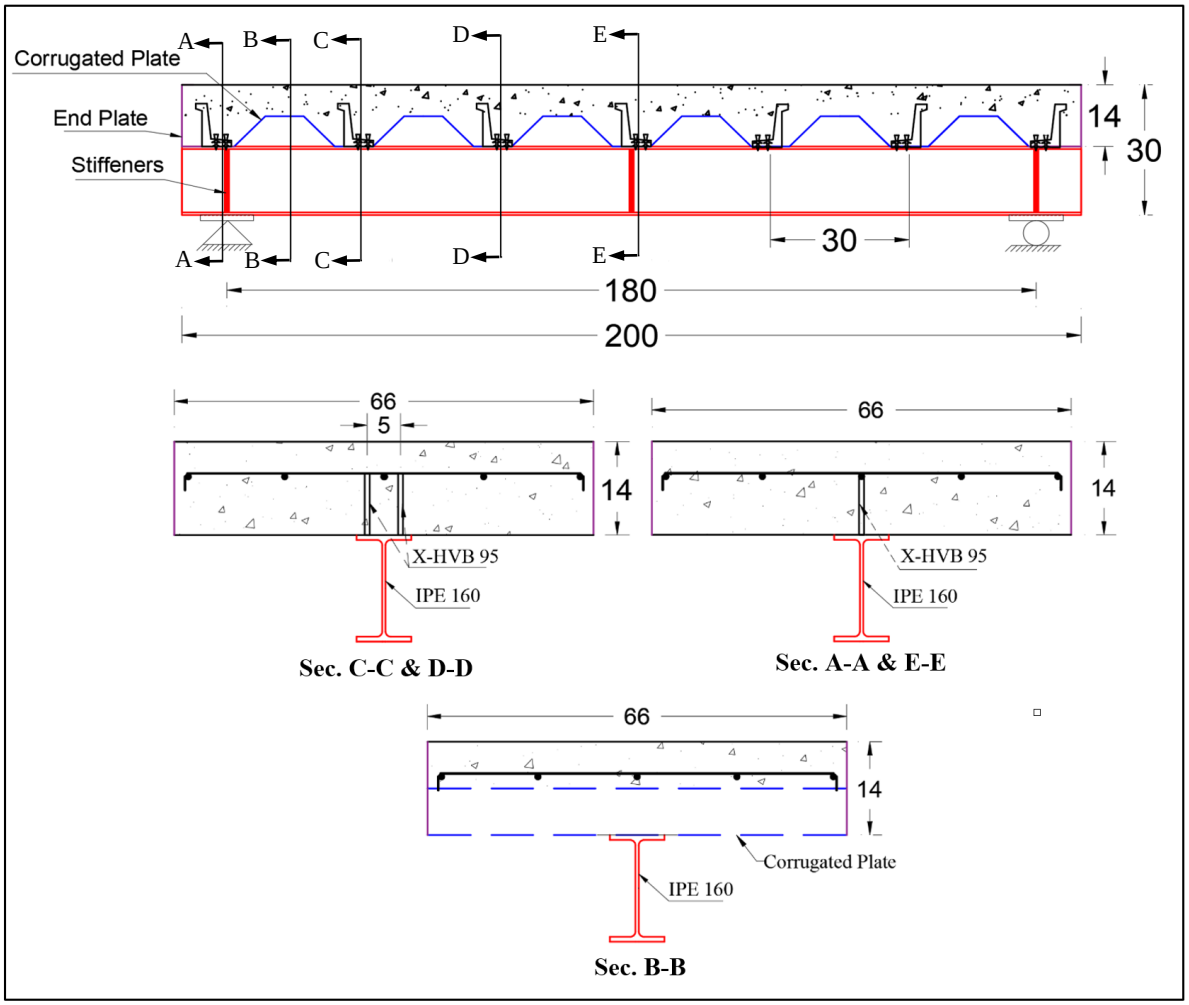


**Figure 3. 3: Composite beam specimens' details with transverse corrugated steel plate (all dimensions in cm).**

The variable parameters of the present investigation were classified into three main groups:

1. Exposure to fire at different temperatures (350℃, 450℃, and 550℃).

2. The orientation of the corrugated steel plate (parallel or transverse to the beam's length).

3. Subjected to fire from different directions (either slab surface or beneath the steel beam).

Two control samples were included in the study, one with a parallel corrugated steel plate and the other with a transverse corrugated steel plate, both tested at ambient temperature. The shear connectors were evenly spaced along the longitudinal axis of each I-steel beam with a center-to-center spacing of 300 mm for each X-HVB shear connector.

A naming system was used to identify each specimen, as shown in Figure 3.4. Each specimen was labeled with the letter 'C', followed by the direction of the corrugated plate relative to the steel beam ('D1' for parallel or 'D2' for transverse), and either 'B' or 'T' to indicate whether it was exposed to fire from the bottom of the beam or the slab surface, respectively. Finally, a temperature designation was used ('R1', 'R2', or 'R3') to indicate the temperature to which it was exposed (350, 450, or 550˚C).

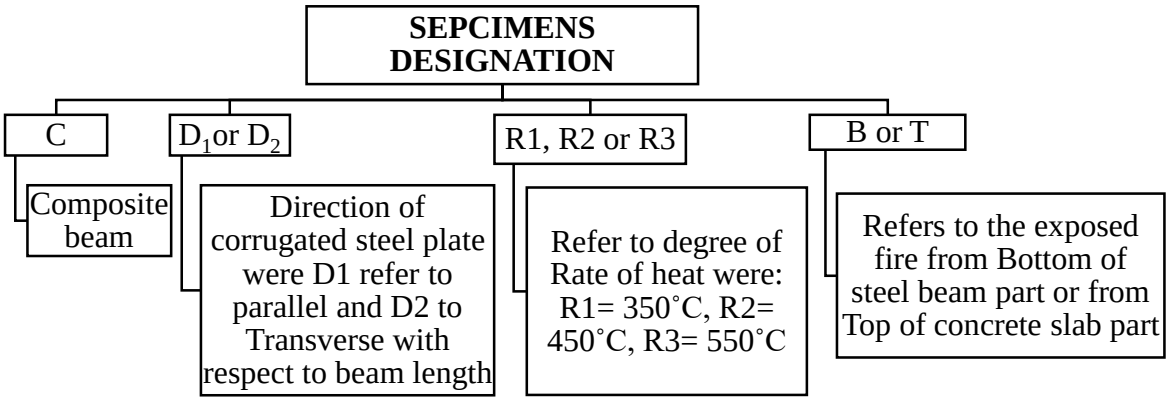


**Figure 3. 4: The specimen nomination system**

Table 3.1 provides information on each sample, including its name, the direction of corrugated steel plate to the length of the beam, direction of heat exposure and Temperature exposure (˚C).

**Table 3. 1: Composite beam specimens' details.**

| NO. | Sample designation | The direction of corrugated steel plate to the length of the beam | Direction of heat exposure from | Temperature (˚C) |
|---|---|---|---|---|
| 1 | CD1 | Parallel | N. A | 35 |
| 2 | CD1BR1 | Parallel | Bottom of steel beam | 350 |
| 3 | CD1BR2 | Parallel | Bottom of steel beam | 450 |
| 4 | CD1BR3 | Parallel | Bottom of steel beam | 550 |
| 5 | CD1TR2 | Parallel | Top of concrete slab | 450 |
| 6 | CD2 | Transverse | N. A | 35 |
| 7 | CD2BR1 | Transverse | Bottom of steel beam | 350 |
| 8 | CD2BR2 | Transverse | Bottom of steel beam | 450 |
| 9 | CD2BR3 | Transverse | Bottom of steel beam | 550 |
| 10 | CD2TR2 | Transverse | Top of concrete slab | 450 |

## 3.4 MATERIAL PROPERTIES

The following sections contain comprehensive explanations of the mechanical and chemical characteristics of the material utilized in concrete, as well as the properties of the shear connector, corrugated steel plate, and steel sections used in this study.

### 3.4.1 Steel Beam

The tested specimens were constructed using I-shaped steel beams, specifically European IPE 160 type as shown in Figure 3.5. Eight samples were taken from the web of steel beam according to ASTM (A370-05) [74] standard; two samples for each case of fire exposure (ambient temperature, 350,450 and 550 ˚C). The eight samples were cut by using a computerized laser cutting machine. Computerized tensile test machine was used to get mechanical properties of the specimens.

Figure 3.6 depicts the standard dimensions for samples according to ASTM. The results shown in Table 3.2 and the coupons were tested in the Material Laboratory of the Materials Engineering at Babylon University and the load deformation curve for steel coupons.

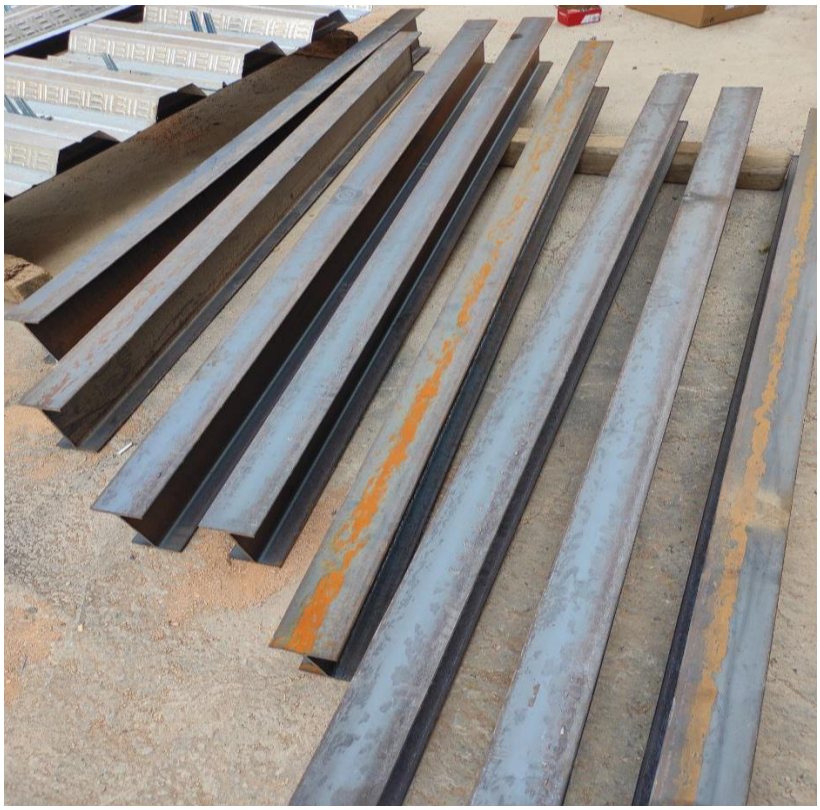

**Figure 3. 5: IPE 160 steel beam.**


**Figure 3. 6: Configuration of standard coupons specimens according to ASTM.**

**Table 3. 2: Results of tested steel coupons.**

| Specimen | Yield stress (MPa)* | Ultimate strength (MPa) * |
|---|---|---|
| Unburned | 235 | 320 |
| Burned at 350 ˚C | 207 | 294 |
| Burned at 450 ˚C | 195 | 280 |
| Burned at 550 ˚C | 187 | 271 |

* Each value represents the average of two tested samples.

### 3.4.2 X-HVB Shear Connecter

The role of the shear connector in composite action is very important. It prevents sliding between concrete slab and steel beam by resisting horizontal shear force, and prevents vertical splitting between them by resisting uplift force during loading. For those purposes X-HVB shear connectors of overall height (95 mm) were used in construction of test samples. The X-HVB shear connectors were fixed at the top flange of the steel beam with two X-ENP-21 HVB cartridge fired pins for each one shear connecter. Material properties of this type of shear connecter with X-ENP-21 HVB cartridge fired pins were provided by kindness of Hilti Company [75].

Push-out Test was applied in order to find out the strength and behavior of X-HVB shear connector. This test will be displayed and explained later. Figure 3.7 depicts the geometry of the X-HVB 95 studied in this research and illustrates the installation process of the X-HVB shear connector in detail.

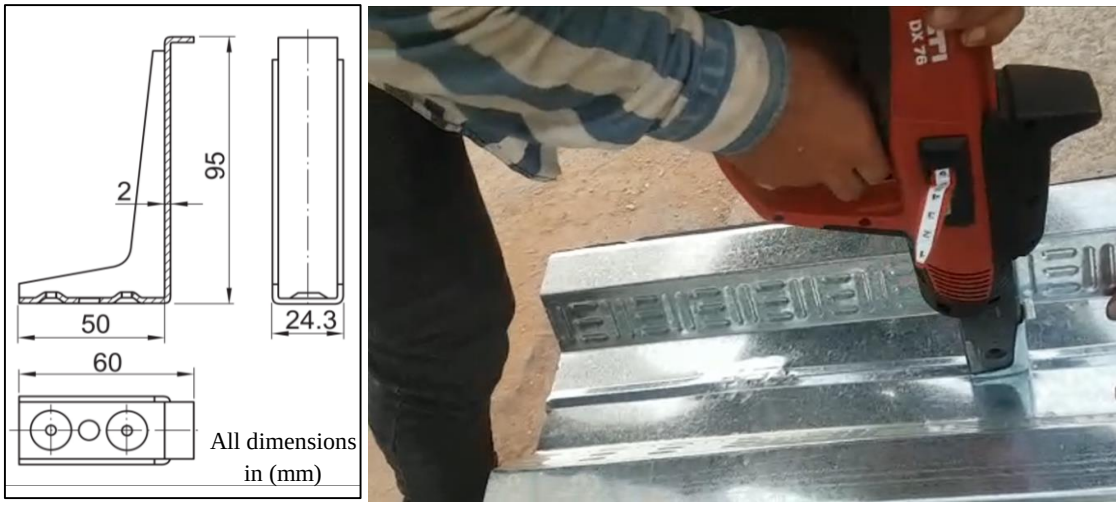


(a) (b)

**Figure 3. 7: X-HVB95 Shear Connector: (a) Detailed Geometry** [75]**; (b)Installation.**

### 3.4.3 Corrugated Steel Plate

The study utilized thin-walled cold-formed trapezoidal corrugated steel plates to construct composite slabs for all composite beam specimens. The steel plates were made of high-quality structural steel sheets that comply with ANSI/ASCE 3-91 standards [76], and were coated with a galvanized surface on each face for corrosion protection. Figure 3.8 depicts the corrugated steel plate's geometric shape, which has embossments facing opposite directions on adjacent webs. Corrugated steel plate had a depth of 70 mm, an average width of 150mm, a plate thickness of 1mm. The actual yield and ultimate strength were found by testing two coupons as shown in Figure 3.9 cutting of the effective area in the longitudinal direction of the thin steel sheet.

The dimensions of the "dog-bone" model for tensile test are according the ASTM A370 - 05 [74]. The most important command in determining the geometric properties is that there is adequate difference in the width between the middle and end parts of the test pieces. This makes sure that the stress at the middle section will be governing and failure will occur in this part. The tensile tests were performed using the testing machine

available at the Material Laboratory of the Material Engineering Department at Babylon University. Table 3.3 provides properties of the tested steel plate.

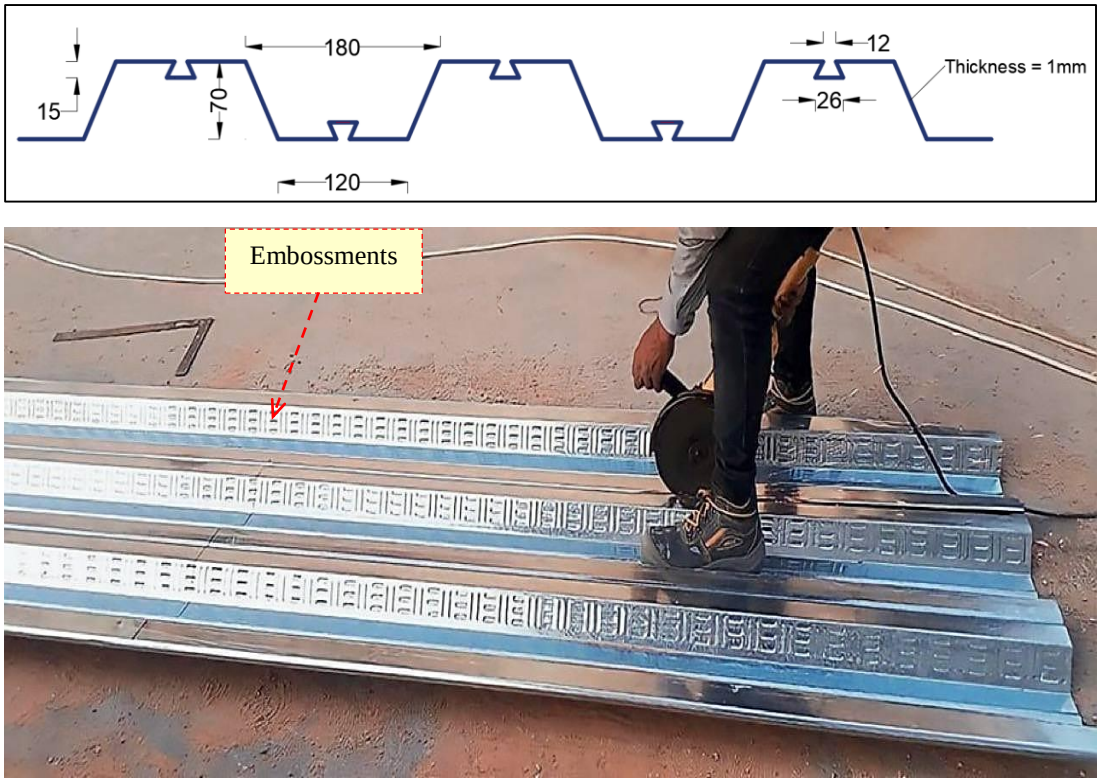


**Figure 3. 8: Trapezoidal corrugated steel plate.**

**Figure 3. 9: The tension test set-up to obtain the tensile strength of steel deck.**

**Table 3. 3: Properties of corrugated steel plate.**

| Specimen condition | Test pieces dimensions | | | Yield Stress (MPa) | Ultimate Stress (MPa) |
|---|---|---|---|---|---|
| | Thickness (mm) | Width (mm) | Gauge Length (mm) | | |
| Unburned | 1 | 14.8 | 90 | 275.81 | 365 |
| Burned at 350 ˚C | 0.97 | 14.77 | 91 | 240.21 | 320 |
| Burned at 450 ˚C | 0.98 | 14.78 | 90.5 | 231.11 | 294 |
| Burned at 550 ˚C | 0.89 | 14.5 | 90.8 | 215.21 | 270 |

### 3.4.4 Steel Reinforcement of Concrete

All of the composite slabs in the test sample were strengthened using the same amount and type of welded steel wire reinforcement, specifically BRC mesh steel wire reinforcement (MD 25) made up of deformed bars

with a diameter of 5.8 mm and spaced 150 mm c/c in both directions. This reinforcement provides an area of 176 $mm^2$/m.

Mesh reinforcement is used to resist strains due to shrinkage and temperature effects. Three test pieces were cut out of a mesh with a length of about 15mm. The tensile tests were performed using the testing machine available at the Material Laboratory of the Material Engineering College at University of Babylon as shown in Figure 3.10. The results of these tension test pieces are listed in Table 3.4.

**Figure 3. 10: The tension test set-up to obtain the material data from the reinforcement.**

**Table 3. 4: Tests results of steel reinforcement specimens.**

| Specimen | Yielding stress fy (MPa) | Tensile strength fu (MPa) |
|---|---|---|
| 1 | 395 | 442 |
| 2 | 483 | 520 |

| | | |
|---|---|---|
| 3 | 507 | 558 |
| Average | 462 | 507 |

Modulus of elasticity for steel (Es) is considered equal to 200 GPa

### 3.4.5 Cement

Cement (KAR) was used in casting all tested specimens. The chemical and mechanical properties of the cement used have been tested in Construction Material and Environmental Laboratories at the University of Babylon. The mechanical and chemical properties of the used cement are given in Tables 3.5 and 3.6, respectively. These properties have been checked according to the Iraqi specification limits (IQ. S No.5/2019) [77] for resistant cement.

**Table 3. 5: Mechanical properties of cement.**

| Mechanical Properties | Test results | IQ. S No. 5/2019 |
|---|---|---|
| Initial setting time (min) | 70 | ≥ 45 min |
| Final setting time (min) | 255 | ≤ 600 min |
| Fineness ($m^2/kg$) | 303 | ≥ 250 m2/kg |
| Compressive strength, MPa | | |
| 3 days | 17.39 | ≥ 15 MPa |
| 7 days | 27.06 | ≥ 23 MPa |

**Table 3. 6: Chemical analysis of cement.**

| Chemical composition | | % By weight. | Limits of IQ. S No.5/2019 |
|---|---|---|---|
| Lime | CaO | 61.25 | ------ |
| Silica | $SiO_2$ | 19.78 | ------ |
| Alumina | $Al_2O_3$ | 3.41 | ------ |
| Magnesia | MgO | 1.72 | ≤ 5% |

| | | | |
|---|---|---|---|
| Ratio | C3 A | 0.914 | ≤ 3.5% |
| Loss on ignition | L.O. I | 2.42 | ≤ 4% |
| Insoluble residue | I.R | 0.85 | ≤ 1.5 % |
| Lime saturation Factor | L.S. F | 0.953 | (0.66–1.02) % |

### 3.4.6 Coarse Aggregate

This work used coarse aggregate with a maximum aggregate size of 19 mm. The coarse aggregate was cleaned and washed with drinking water, then dried before use. The mechanical and chemical properties of coarse aggregate are given in Table 3.7. The sieve analysis of coarse aggregate lies within the lower and upper limits of the Iraqi specification (IQ. S No.45/2016) [78], as shown in Table 3.8.

**Table 3. 7: Mechanical and chemical properties of coarse aggregate.**

| Properties | Test results | IQ. S No. 45/2016 |
|---|---|---|
| Specific gravity | 2.66 | ------ |
| Sulfate content SO3 | 0.03% | ≤ 0.1 % |
| Absorption | 0.6% | ------ |
| Clay content | 0.2% | ≤ 3% |

**Table 3. 8: Grading of coarse aggregate.**

| Sieve Size (mm) | Passing % | |
|---|---|---|
| | Coarse aggregate | IQ. S No. 45/2016 |
| 37.5 | 100 | 100 |
| 20.0 | 100 | 100 - 95 |
| 9.5 | 43 | 60 - 30 |

| | | |
|---|---|---|
| 5.0 | 3 | 10 - 0 |

### 3.4.7 Fine Aggregate

In this work, natural sand was used as fine aggregate. The chemical and mechanical properties of sand are given in Table 3.9. The fine aggregate used has gradation that lies within the upper and lower limits of the ASTM C33/C33M specification [78] and Iraqi specification (IQ. S 45/206) zone (2) [79], as shown in Table 3.10. Fine aggregate has been tested at the University of Babylon in the Construction Material and Environmental Laboratories of the Civil Engineering Department.

**Table 3. 9: Chemical and mechanical properties of fine aggregate.**

| Properties | Test results | IQ. S No. 45/2016 zone (2) |
|---|---|---|
| Specific gravity | 2.6 | ------ |
| Fineness modulus | 3.8 | $\leq 5$ % |
| Sulfate content $SO_3$ | 0.22% | $\leq 0.5$ % |
| Absorption | 2% | ------ |

**Table 3. 10: Grading of fine aggregate.**

| Sieve no. | Sieve size (mm) | Passing % | | |
|---|---|---|---|---|
| | | Fine aggregate | IQ. S No. 45 Zone (2) | ASTM C 33/C 33M |
| 3/8 in | 9.5 | 100 | 100 | 100 |
| NO.4 | 4.75 | 91 | 90 - 100 | 90 - 100 |
| NO.8 | 2.36 | 83 | 75 - 100 | 80 - 100 |
| NO.16 | 1.18 | 74.8 | 55 - 90 | 50 - 85 |
| NO.30 | 0.60 | 57.2 | 35 - 59 | 25 - 60 |

| | | | | |
|---|---|---|---|---|
| NO.50 | 0.30 | 24.2 | 8 - 30 | 5 - 30 |
| NO.100 | 0.15 | 7.2 | 0 - 10 | 0 - 10 |

### 3.4.8 Water

Potable water is used for both mixing and curing of the specimens.

### 3.4.9 Crack Width Ruler

The Crack Width Ruler is a cost-effective alternative to a graduated microscope, which allows inspectors to determine the width of cracks in concrete or other building materials. It is a small and transparent gauge, similar in size to a credit card, with graded lines marked on it. Each line represents a specific width measurement.

By placing the gauge over the crack and identifying the line that matches its width, one can easily determine the crack's width measurement as shown in Figure 3.11. The ruler is made from Polyvinyl Chloride (PVC) plastic, and it comes in two ranges: Ruler A with a range of 0.004 - 0.100" (0.10 - 2.50mm) and Ruler B with a range of 0.1 - 7.0mm.

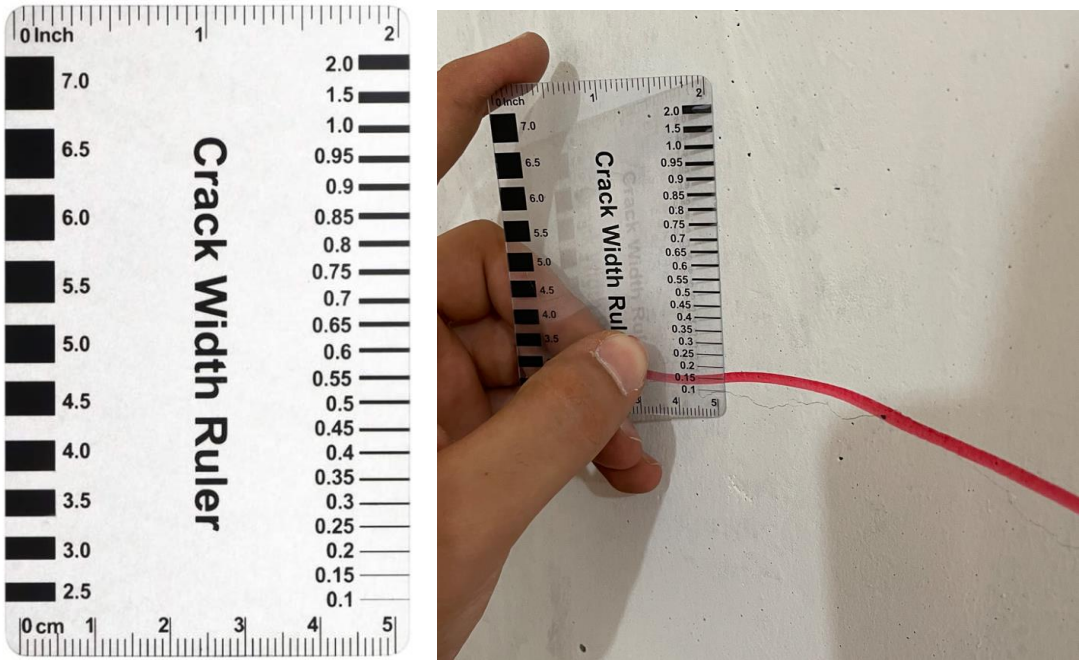


**Figure 3. 11: Crack width ruler.**

## 3.5 PUSHOUT TEST

The push out test has historically been the primary means used to evaluate the strength of shear connectors used in steel-concrete composite floors. To investigate the behavior of the X-HVB shear connector under direct shear, push-out tests were carried out on twelve samples. Among these samples, two were tested at ambient temperature to obtain the ultimate shear resistance of the connectors and establish their force-slip relationship under this condition. The remaining samples were tested after subjecting them to fire at different temperature levels (350, 450, and 550°C). Figure 3.17 depicts the nomination system for each specimen. The specimen is denoted by the letter 'P,' followed by ('D1' for parallel or 'D2' for transverse), which refers to the direction of the corrugated steel plate. 'S' refers to a single shear connector per line, 'd' refers to a double shear connector per line, and the change in the orientation of the shear connector is indicated by 'O1' or 'O2,' representing forward or backward to the shear force direction. Finally, a temperature designation ('R1,' 'R2,' or 'R3') is used to indicate the temperature to which it was exposed (350, 450, or 550˚C). Table 3.11 presents the scheduled details of all the specimens, while Figures 3.12 to 3.15 depict them visually.

The primary focus of the study was to examine the impact of varying levels of exposure to fire, as well as other factors such as the direction of corrugated steel plate (some of the specimens featured corrugated steel plates (1 mm thick) that were parallel to the length of the steel beam, while others had transverse plates), the degree of shear connection, and the orientation of the shear connector (backward or forward) in relation to the shear force direction.

The forward orientation of shear connectors adopted is characterized with the position of shear connector anchorage leg in front of fastening leg,

relative to the shear force direction, while fastening leg precede to the anchorage leg in the backward orientation of shear connectors, as presented in Figure 3.16. X-HVB 95 shear connectors fastened to the corrugated plate that rested on an IPE160 steel beam with X-ENP-21 HVB cartridge fastening pins are used. Mesh reinforcement is used for temperature and shrinkage effects.

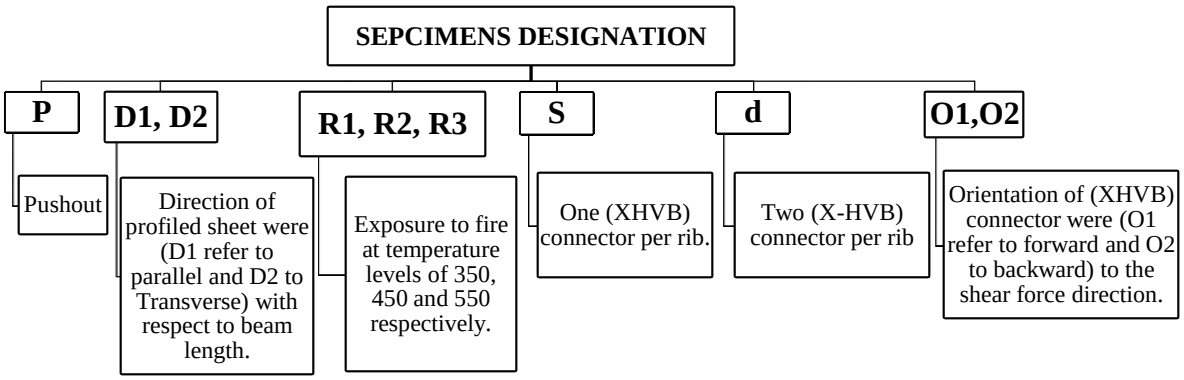


**Figure 3. 12: The specimen nomination system.**

**Table 3. 11: Pushout specimens' details.**

| NO. | Sample designation | Parameter | | | |
|---|---|---|---|---|---|
| | | **The direction of corrugated sheeting to the length of the beam** | **Number of (XHVB) connectors per bottom rib of corrugated sheeting** | **Orientation of (X-HVB) connector to the shear force direction** | **Temperature (℃)** |
| 1 | PD1SO1 | Parallel | Single | Forward | 35 |
| 2 | PD1SO1R1 | Parallel | Single | Forward | 350 |
| 3 | PD1SO1R2 | Parallel | Single | Forward | 450 |
| 4 | PD1SO1R3 | Parallel | Single | Forward | 550 |
| 5 | PD1dO1R2 | Parallel | double | Forward | 450 |
| 6 | PD1SO2R2 | Parallel | Single | Backward | 450 |
| 7 | PD2SO1 | Transverse | Single | Forward | 35 |

| | | | | | |
|---|---|---|---|---|---|
| 8 | PD1SO1R1 | Transverse | Single | Forward | 350 |
| 9 | PD2SO1R2 | Transverse | Single | Forward | 450 |
| 10 | PD1SO1R3 | Transverse | Single | Forward | 550 |
| 11 | PD2dO1R2 | Transverse | double | Forward | 450 |
| 12 | PD2SO2R2 | Transverse | Single | Backward | 450 |

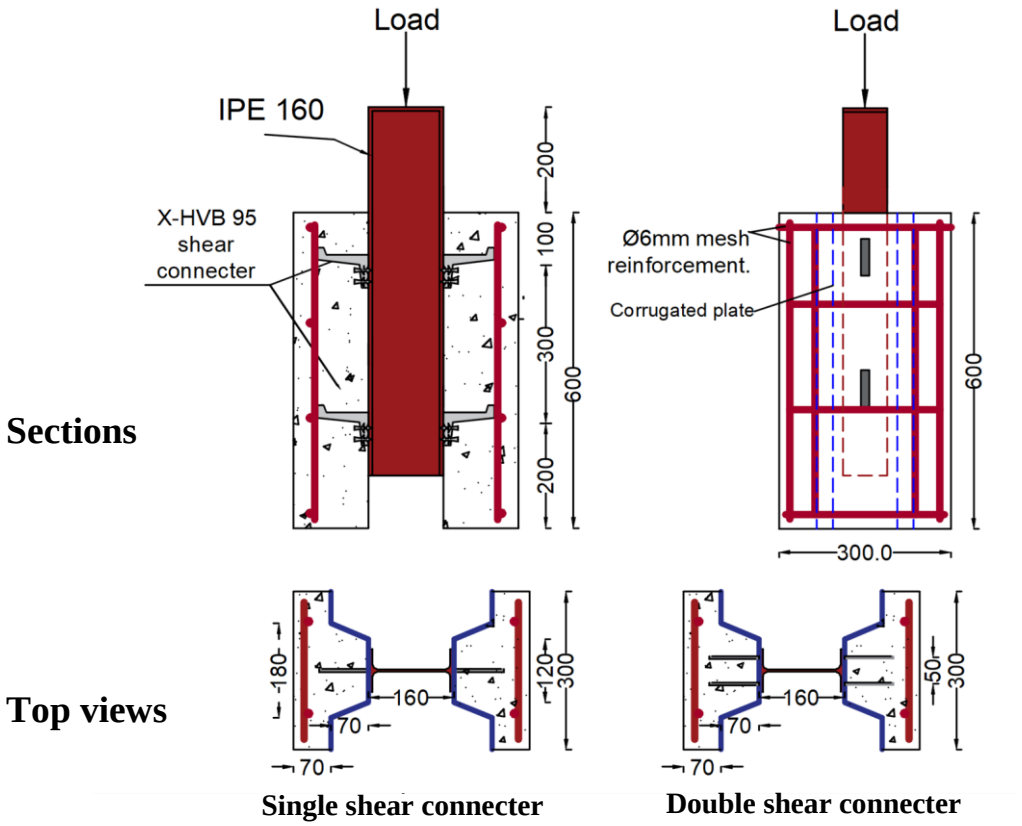


**Figure 3. 13: The dimensions and arrangement for pushout specimens for forward orientation of the shear connecter with parallel corrugated steel plate.**

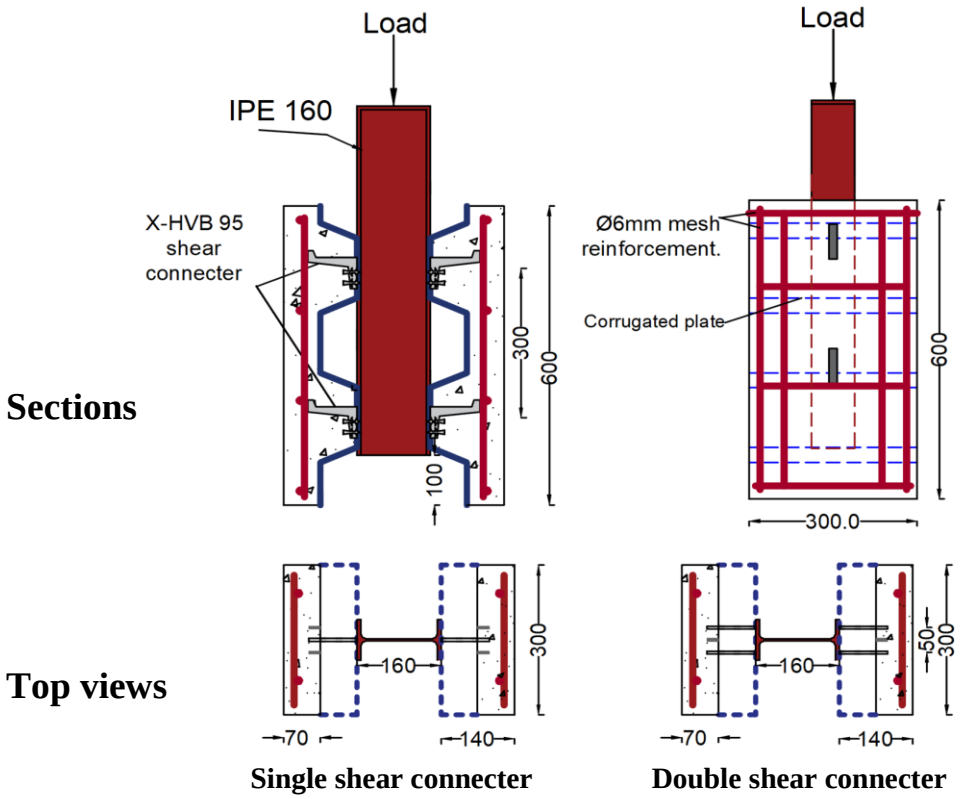


**Figure 3. 14: The dimensions and arrangement for pushout specimens for forward orientation of the shear connecter with transverse corrugated steel plate.**

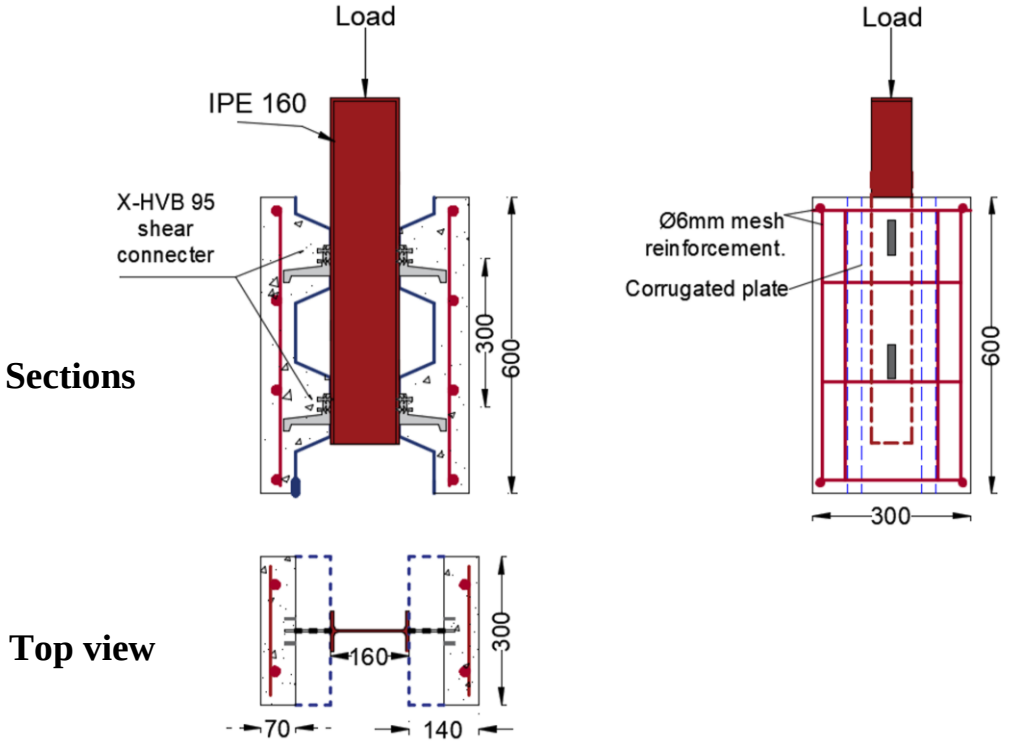


**Figure 3. 15: The dimensions and arrangement for pushout specimens for backward orientation of the shear connecter with parallel corrugated steel plate.**

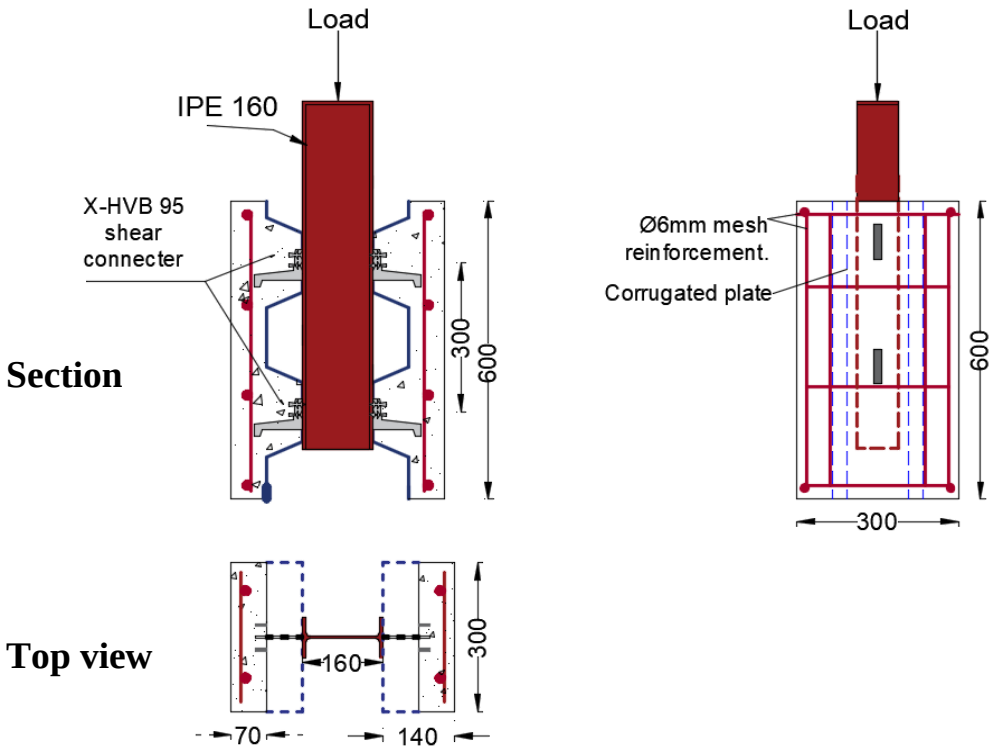


**Figure 3. 16: The dimensions and arrangement for pushout specimens for backward orientation of the shear connecter with transverse corrugated steel plate.**

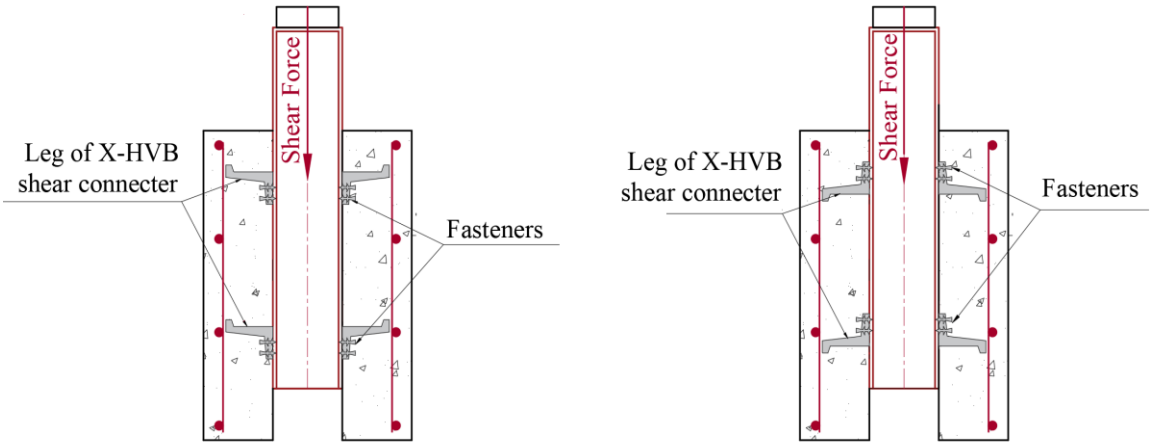


(a) (b)

**Figure 3. 17: X-HVB shear connecter' layout relative to shear force: (a) Forward, (b) Backward.**

## 3.6 CONCRETING AND CURING PROCEDURES OF THE SPECIMENS

Materials used in the concrete mix were previously explained. In this study, the concrete was provided by mixer trucks (ready mix concrete). The

compressive strength of concrete was established by conducting compression strength tests using a digital testing machine with a capacity of (1900 kN), the loading rate was applied at (0.3 MPa/sec) after 28 days. Figure 3.18 shows the compressive strength test machine. Twelve cubes measuring 150 x 150 x 150 mm, three of them tested at ambient temperature while others tested after exposed to fire flame at different temperature levels to determine the compressive strength.

Table 3.12 shows the results of the compressive strength test before and after burning. Each value in this Table represents the average value of (3) cubes in order to minimize the expected error in any measured result. Also, predicted compressive strength for cylinder ($f'c$) was illustrated in Table 3.12 according to (**BS 8110-1: 1997)** [86] equation as shown below:

$$f'_{c\,(NSC)} = 0.8\, f_{cu} \quad \textbf{(3-1)}$$

Where:

$f'c$: concrete compressive strength for cylinder (150mm×300mm), measured in N/mm² (MPa).

$f_{cu}$: concrete compressive strength for cube in N/mm$^2$ (MPa).

NSC: Normal Strength Concrete.

$$\text{Reduction in } f_{cu}\,(\%) = 100 - \frac{f_{cu}}{f_{cu\,(T=35^{o}C)}} \times 100 \quad \textbf{(3-2)}$$


**Figure 3. 18: Compressive strength testing machine.**

**Table 3. 12:** Test values of cube compressive strengths of samples before and after exposure to fire flame.

| **Burning temperature (°C)** | **Average compressive strength (MPa)** | | **Reduction in compressive strength (%)** |
|---|---|---|---|
| | ***fcu*** | ***fć* BS eq.** | |
| Without burning | 37.22 | 29.78 | … |
| 350 | 32.20 | 25.76 | 13.49 |
| 450 | 30.40 | 24.32 | 18.32 |
| 550 | 26.040 | 20.83 | 30.00 |

All beams' specimens used in this research were cast with the corrugated steel plate as the base and end plates from all sides while all pushout specimens cast by using wood mold. Before casting, corrugated steel plate and end plate were prepared by proper cleaning and the wood molds cleaning and lubricating the internal faces lightly by oil to prevent the adhesion with hardened concrete before casting and placed on a horizontal ground. See Figures 3.19 and 3.20.

The mesh reinforcement was positioned carefully on the top of the shear connecter inside the steel molds and sides cover being accurately maintained. After all the preparations was finished, the fresh concrete mixture poured into the molds by placing the concrete in three layers with each layer being vibrated using a vibrating table and full compaction was made sure by observing the air bubbles on the surface as presented in Figure 3.21. Thereafter, beam specimens were cured with saturated wet coverings by using burlap, while cube samples were cured in a water tank with a temperature of (25 ± 2 °C) as shown in Figure 3.22.

**Figure 3. 19: Composite beam specimens before concrete casting.**

**Figure 3. 20: Pushout specimens before concrete casting.**

**Figure 3. 21: Pouring concrete into the steel mold.**

**Figure 3. 22: Curing procedures for column specimens and samples.**

## 3.7 BURNING PROCESS

The fire exposure process was carried out in a furnace specially manufactured for burning structural members. The furnace is manufactured with outer dimensions of (2200 × 1000 × 1000 mm) (length× width× height respectively), and the wall thickness on all sides is 200 mm to fit the dimensions of the test specimens; the main structure is made from Thermostone brick and glue. The Thermostone brick is characterized by lightweight, thermal insulation properties, and fire resistance for up to 7 hours. Also, the furnace floor is made of Thermostone but with a thickness of 100mm to ensure full thermal insulation from the bottom and prevent heat leakage, in addition to a small opening drilled from two opposite sides of the furnace to provide sufficient air for the burners.

Figures 3.23 and 3.24 show the full details of the burning process and the furnace with the connections. The network of burners consists of six methane burners arranged in one line at one side of exposure and distributed along the inside length of the stove wall; all methane burners were connected in one pipeline to control the gas discharge. The primary purpose of the furnace compartment is to elevate the temperature levels of

the fire exposure to the target temperature and then hold the temperature constant for the required duration.

After preparing the furnace with all connections, two of the pushout specimens with the concrete cube and steel samples were held carefully by hand and placed inside the furnace and positioned fair-faced toward the methane burners with the same distance from the line of burners and the composite beam specimen positions on the top of the furnace. Then, the gas valve was opened and the burners was ignited by an ignition tool, the measured temperature was increased gradually.

When the target temperature reached, the electrical gas regulator started to work by regulating the gas flow so the target temperature stayed constant, the target temperature was measured by thermocouple placed in direct contact with fire flame, Figure 3.25 (a) show the details of the digital gage. The electric gas regulator and the thermocouples were connected to a digital gauge to control the gas discharge and keep the firing temperature constant at the target temperature, which was set in the digital gauge before the burning started.

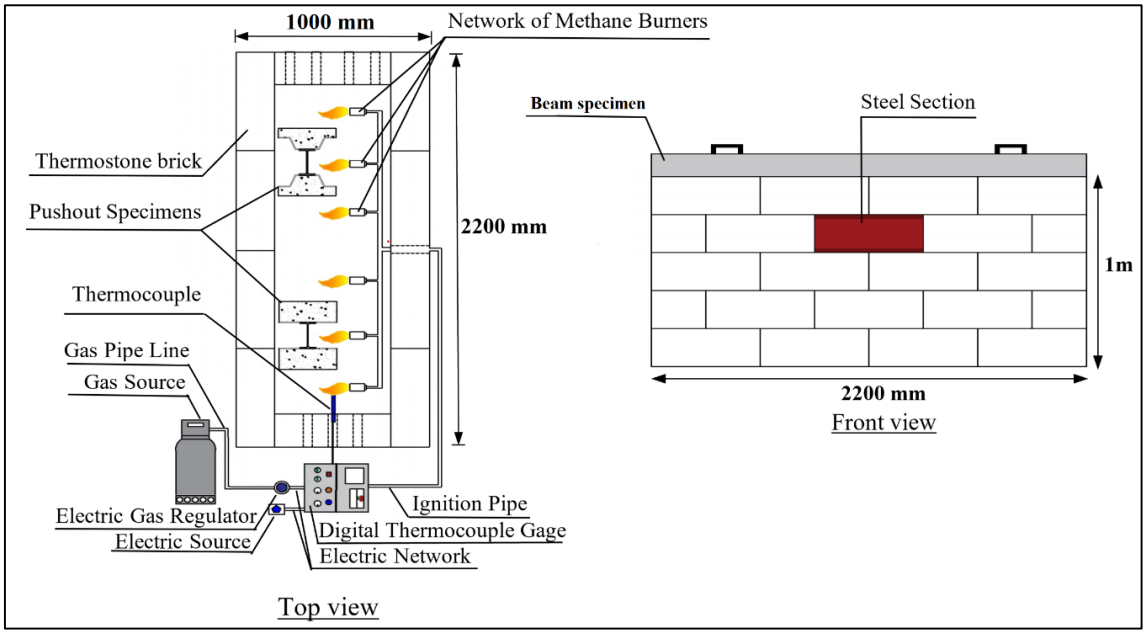


**Figure 3. 23: Top and Front view of the furnace and equipment.**

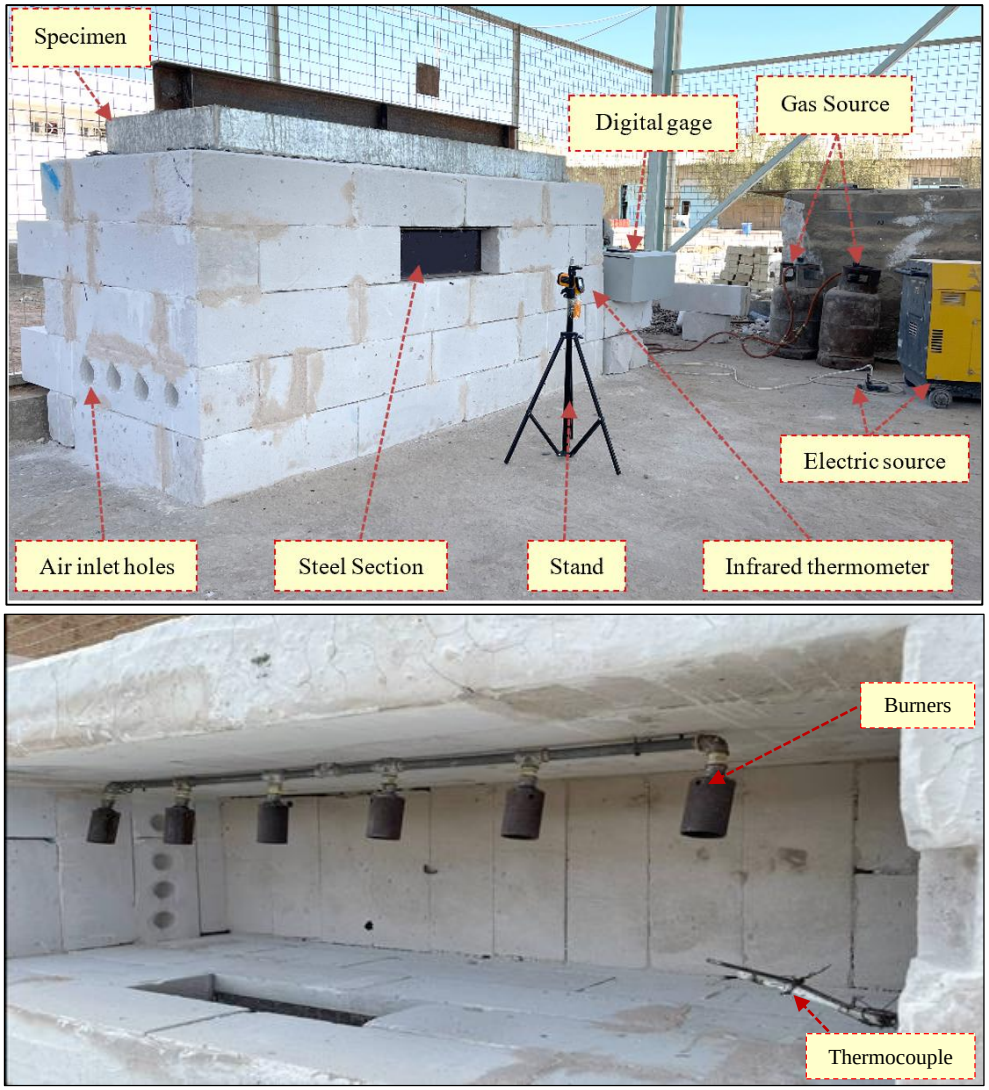


**Figure 3. 24: The full details of the burning process and stove with the connections.**

The temperature level is also ensured by using another method: an infrared thermometer. The infrared thermometer is fixed at a constant distance from the furnace that is used to measure the temperature of the steel section, which replaced the middle Thermstone brick on one side for the furnace to simulate the air temperature degree inside the furnace, see Figure 3.25 (b). The evolution phase of the fire following ISO 834 standard fire curve [42] fire exposure for 60 min and with the temperature levels 350 °C, 450 °C, and 550 °C for each case of fire exposure, as shown in Figure 3.26. The Figure also shows the convergence between the two methods (Digital thermocouple gage and infrared thermometer) for temperature measurement methods in the furnace. After the duration of burning was

finished (1 hour of fire exposure) the gas valve was closed and the specimens were cooled down to the ambient temperature before testing.


(a) (b)

**Figure 3. 25:** Methods used for temperature measure: (a) Digital thermocouple gage, (b) infrared thermometer.

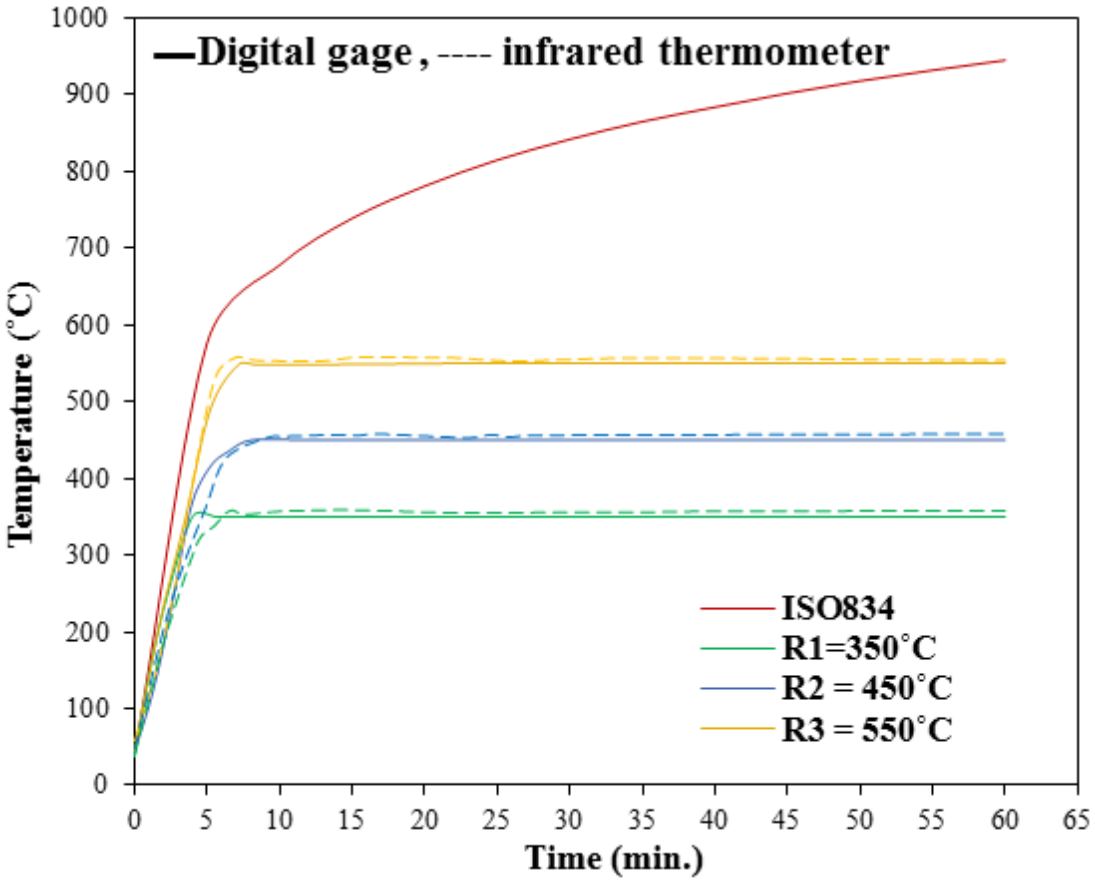


**Figure 3.26: Temperature evolution in specimens according to ISO 834 fire curve.**

## 3.8 INSTRUMENTATION AND TEST PROCEDURES

Figures 3.26 to 3.28 show the instrumentation and setup of the specimens. The composite specimen's setup is on a rigid steel girder supported with hinge and roller boundary conditions. Two LVDTs were used in the test, one placed in the middle of the span from bottom so that vertical displacement of the specimen could be measured while other one placed in the side of the composite slab to measure the slippage between steel beam and composite slab. A line load is involved in the mid span of composite beam. A hydraulic jack with a capacity of 500 kN was used to apply the load. A load cell with capacity of 300 kN was used to measure the load. The steel beam was used to transfer the load from the jack to the girder span. Bearing plates were used at supports and at loading line to avoid local yielding in steel and local crushing in concrete respectively. Then, the load is applied and recording the self-weight, the initial reading of the deflection.

While in pushout test, two linear variable displacement transducers (LVDT) were used. The LVDT1 and LVDT2 are placed vertically at the top of the concrete slab to measure the interface slip, as shown in Figure 3.32. The Figure shows the installation of all pushout specimens (heated and unheated) in the test frame. The specimens were loaded using a hydraulic jack and a load cell with a capacity of 300 kN. The load cell readings and LVDT perusals were registered on the data logger and saved on the computer for more analysis.

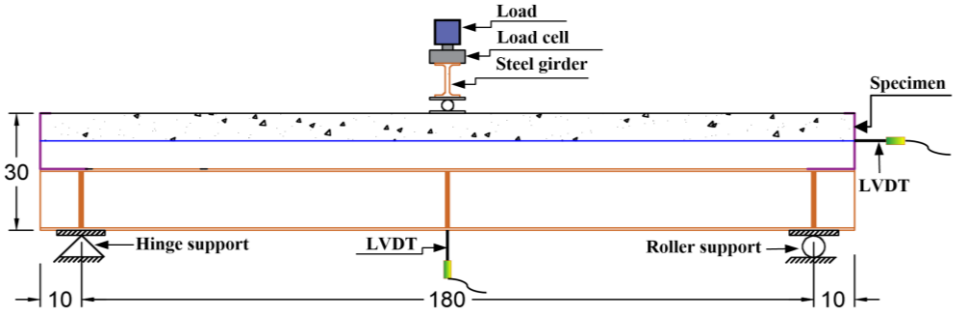

**Figure 3.26: The instrumentation and test setup of the specimens.**

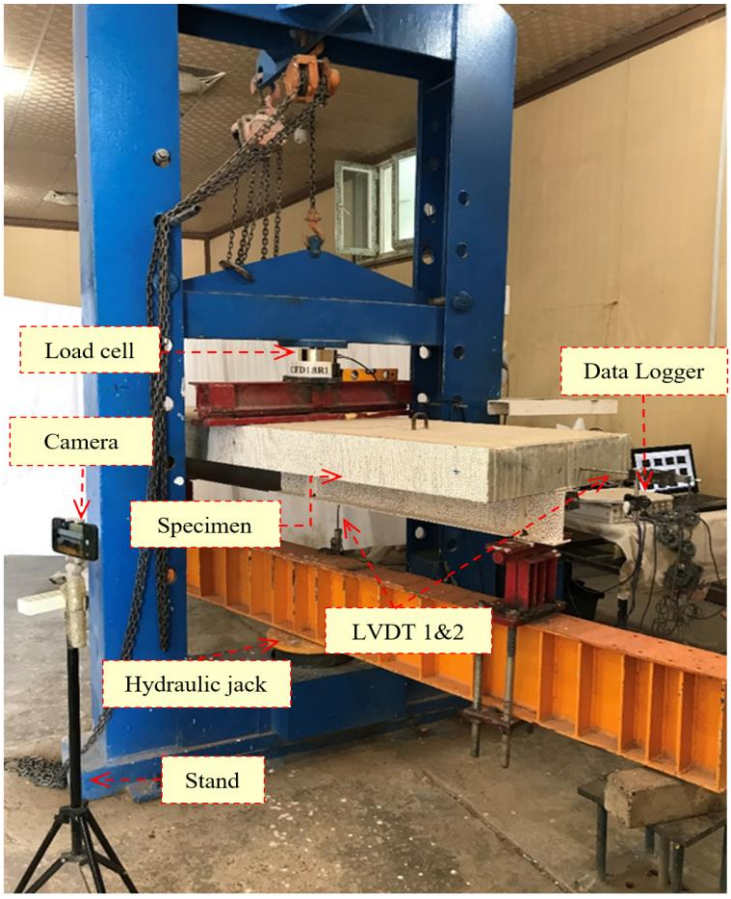


**Figure 3. 27: Details of the testing machine used in this study.**

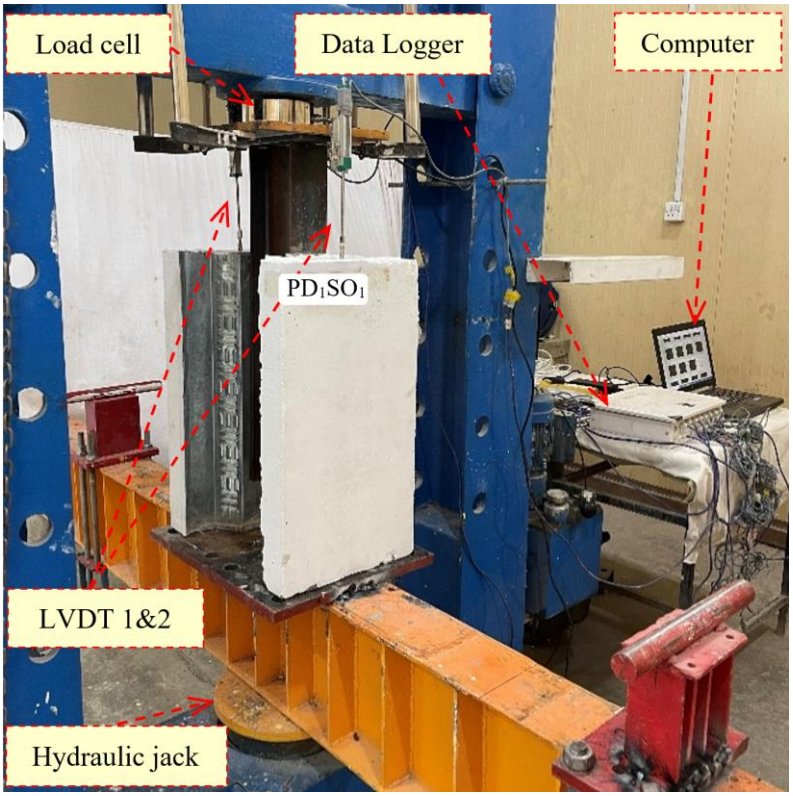


**Figure 3. 28: Details on the testing machine utilized in this study.**

# CHAPTER FOUR
# EXPERIMENTAL RESULTS AND DISCUSSION

## 4.1 INTRODUCTION

This study aims to conduct an experimental investigation into the behavior of composite steel corrugated plate-concrete deck mechanically connected to a steel beam with XHVB shear connector when subjected to concentrated load and exposed to fire. The chapter presents and discusses the results of the experimental program conducted in Chapter 3, which included composite beam specimens and pushout specimens. The objective of comparing the results of both specimen types was to determine the significance of the considered experimental variables.

The composite beam specimens comprised ten specimens according to the parametric study, the variable parameters were the effect of temperature change, the side exposed to fire (top or bottom), and the direction of the corrugated plate (parallel or transverse) with respect to the beam length. The pushout specimens consisted of twelve specimens that varied based on the rate of heat change, the direction of the corrugated plate, the use of a single or double shear connector in each line, and the orientation of the shear connector concerning the direction of the shear force.

The test results included load-carrying capacity, load versus mid-span deflection, load versus slip between concrete and steel, cracking load and crack patterns, stiffness and ductility ratio, and were compared between exposed and non-exposed composite beam and pushout specimens to fire.

## 4.2 TEST RESULTS FOR PUSH-OUT SPECIMENS

The objective of this study was to investigate the actual bond-slip behavior and ultimate shear flow resistance of the X-HVB 95 shear connections

adopted. The push-out tests were conducted on twelve specimens in compliance with BS specifications, with the details provided in the previous chapter.

The variable parameters included the exposure to fire at different temperature levels, the direction of the corrugated steel plate relative to the steel beam length (parallel or transverse), the degree of shear connection (single or double shear connector in each line), and the orientation of the shear connector (backward or forward) with respect to the shear force direction. The test results are presented in Table 4.1. Four key parameters are considered, comprising the ultimate force per shear connector ($P_u$), peak slip ($\delta_{peak}$), ultimate slip ($\delta_u$) and the shear connector stiffness ($K_{sc}$).

**Table 4. 1: Results of the tested push-out specimens.**

| No. | Specimen | Ultimate force $P_u$ (kN) | Peak slip $\delta_{peak}$ (mm) | Ultimate slip $\delta_u$ (mm) | Stiffness ($K_{sc}$) (kN/mm) |
|---|---|---|---|---|---|
| 1 | PD1SO1 | 138.24 | 4.79 | 6.89 | 75.60 |
| 2 | PD1SO1R1 | 116.64 | 4.84 | 4.80 | 44.37 |
| 3 | PD1SO1R2 | 101.89 | 4.21 | 4.53 | 36.58 |
| 4 | PD1SO1R3 | 92.15 | 3.75 | 4.00 | 26.65 |
| 5 | PD1dO1R2 | 184.76 | 4.06 | 5.03 | 86.22 |
| 6 | PD1SO2R2 | 92.17 | 3.83 | 5.6 | 28.42 |
| 7 | PD2SO1 | 151.52 | 3.54 | 6.51 | 265.16 |
| 8 | PD2SO1R1 | 118.91 | 5.76 | 6.21 | 89.50 |
| 9 | PD2SO1R2 | 105.52 | 4.09 | 6.05 | 50.94 |
| 10 | PD2SO1R3 | 95.00 | 4.26 | 6.03 | 45.86 |
| 11 | PD2dO1R2 | 229.94 | 3.50 | 3.98 | 98.15 |
| 12 | PD2SO2R2 | 95.54 | 5.01 | 5.80 | 42.33 |

As shown in Figure 4.1, *P*u represents the total ultimate force for shear connector and *δ*peak shows its corresponding slip. Moreover, according to EC4, *δ*u is taken as the slip corresponding to 0.9Pu in the descending part of the load–slip curve.

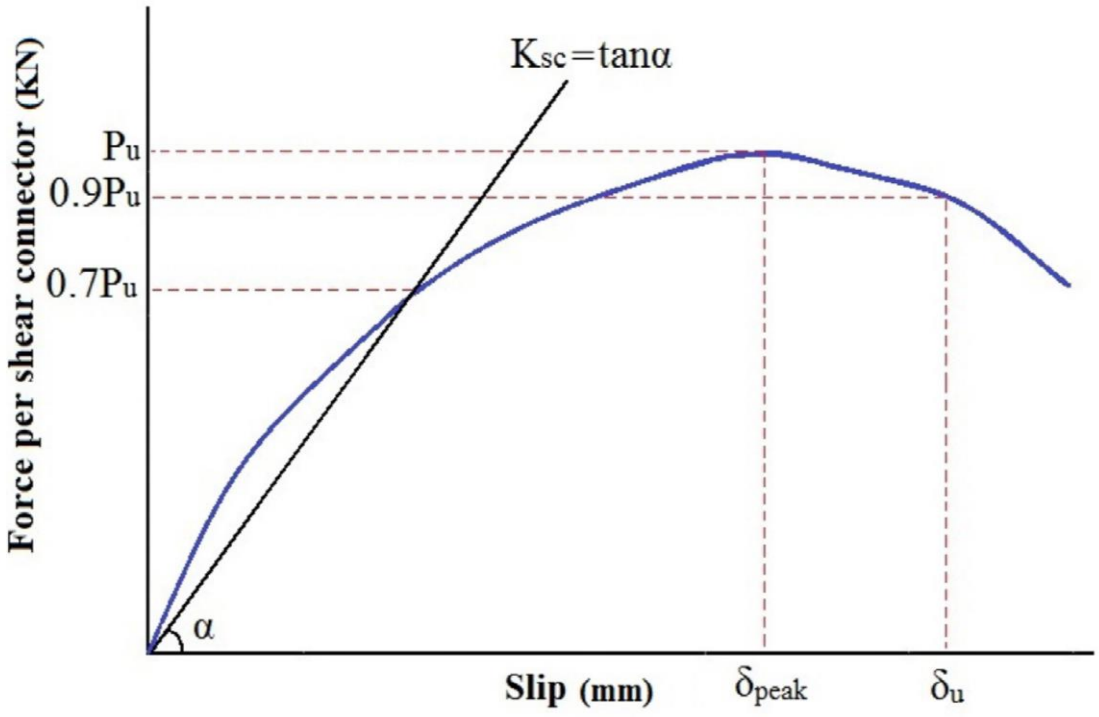


**Figure 4. 1: The key parameters of push-out tests, corresponding to EC4** [80]**.**

### 4.2.1 Effect of Temperature

The effect of temperature on the specimens was evident as their ultimate load decreased with increasing temperature. For specimens PD1SO1R1, PD1SO1R2, and PD1SO1R3, the drop in ultimate load was approximately 16%, 27%, and 34%, respectively. Similarly, specimens PD2SO1R1, PD2SO1R2, and PD2SO1R3 experienced decreases of around 22%, 31%, and 38%, respectively. Furthermore, an increase in temperature had a detrimental impact on the stiffness and ductility of all burned specimens, as clearly illustrated in Figures 4.2 and 4.3 and later will be discuss in section 4.2.5.

It has been observed that the rate of decrease in ultimate load in specimens with transverse corrugated steel plate is greater than that in specimens with parallel ones after exposure to fire could be due to several factors. Firstly, it is possible that the fire exposure resulted in a non-uniform temperature distribution along the specimens. The parallel sheeting configuration may have experienced a more favorable temperature distribution, leading to a lesser degree of structural weakening and better load resistance so the parallel sheeting arrangement may have provided better fire protection to the steel beam, slowing down the rate of temperature rise. Additionally, this difference can be attributed to the open location of the steel beam in transverse corrugated plate, which directly faces the fire and consequently leads to a reduction in the failure load.

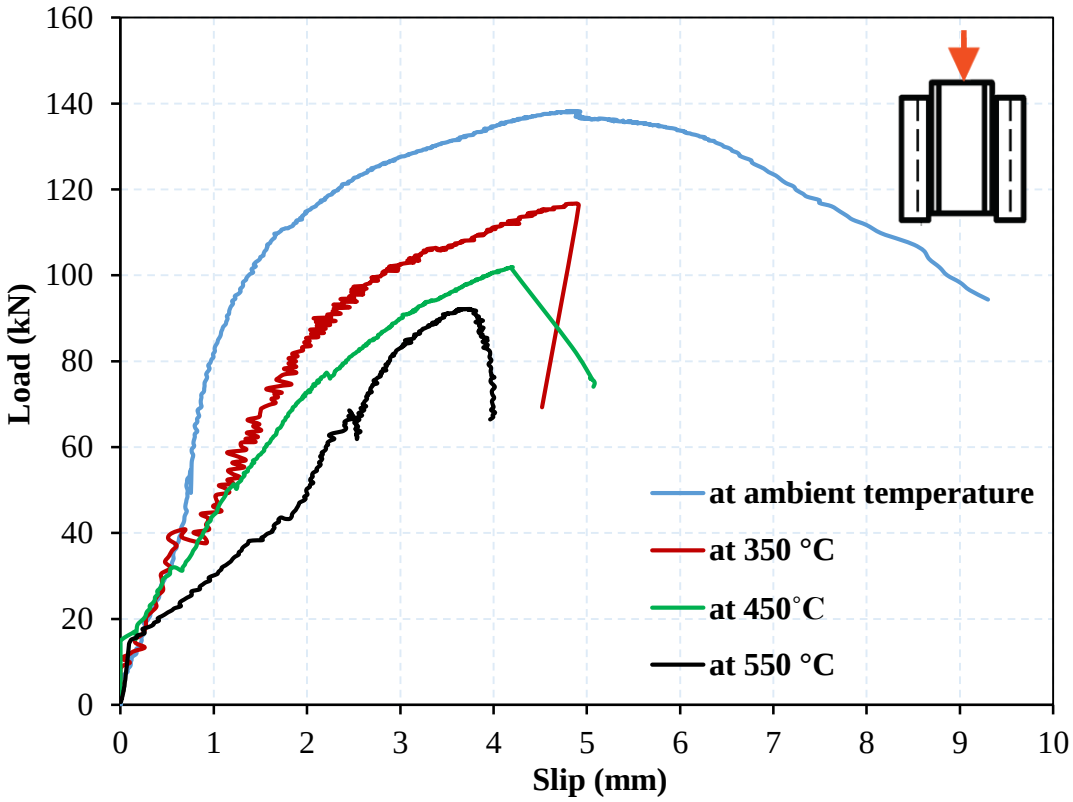


**Figure 4. 2: Effect of temperature levels on the shear resistance of X-HVB shear connectors with parallel corrugated steel plate to the steel beam.**

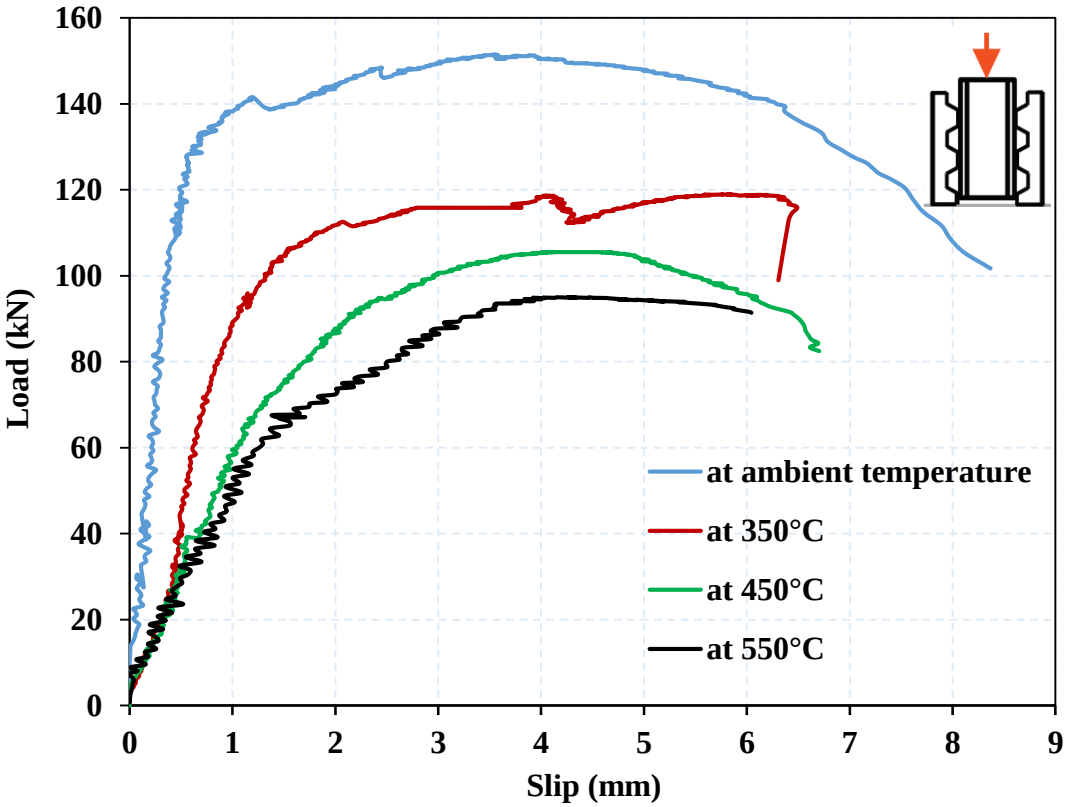


**Figure 4. 3: Effect of temperature levels on the shear resistance of X-HVB shear connectors with transverse corrugated steel plate to the steel beam.**

### 4.2.2 Effect of Degree of Shear Connection

Two scenarios have been employed to examine the impact of the degree of shear connection. In the first scenario, each steel beam flange length has two shear connectors placed at its center, with a longitudinal spacing of 300 mm. In contrast, in the second scenario, the degree of connection is increased, with four shear connectors positioned at each steel beam flange length, spaced longitudinally at 300 mm, with two shear connectors per line, placed 50 mm away from the center of the profiled steel sheet. Consequently, the first scenario has a total of four shear connectors per specimen, while the second scenario has a total of eight shear connectors per specimen.

It can be concluded that increasing the number of X-HVB shear connectors per rib from one to two per line in specimen with transverse sheeting leads to a 118% increase in the peak push load. In specimen with

parallel steel deck, the increase in peak push load is by about 81% as the number of X-HVB per line increases from one to two. See Figure 4.4. This is due to the transverse ribs of the sheeting act as additional shear keys, preventing the slab from sliding relative to the beam.

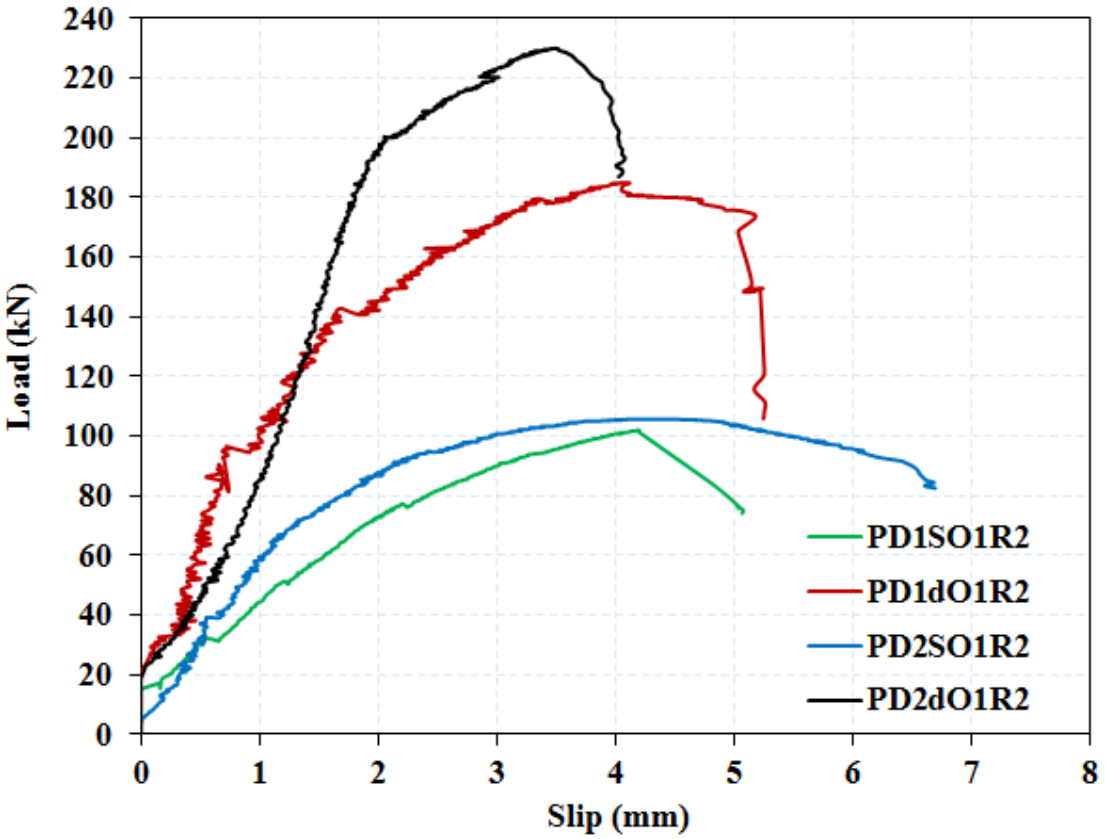


**Figure 4. 4: Influence of degree of shear connection on the shear resistance of X-HVB shear connectors.**

### 4.2.3 Effect of Orientation of X-HVB Shear Connecter

From Figure 4.5 and comparing the mean ultimate shear force and peak slip capacity, the forward orientation of shear connectors can be considered more favorable than the backward orientation. Approximately 11% higher average ultimate shear force capacity is obtained for the PD1SO1R2 and PD2SO1R2 test series compared to the PD1SO2R2 and PD2SO2R2 series. These distinguishing features may be related to the orientation of the shear connector fastening leg; that is, cartridge fastening pins are positioned behind the anchorage leg, relative to the shear force direction, and possible

confinement conditions in concrete developed behind the connector anchorage leg and beyond the fasteners.

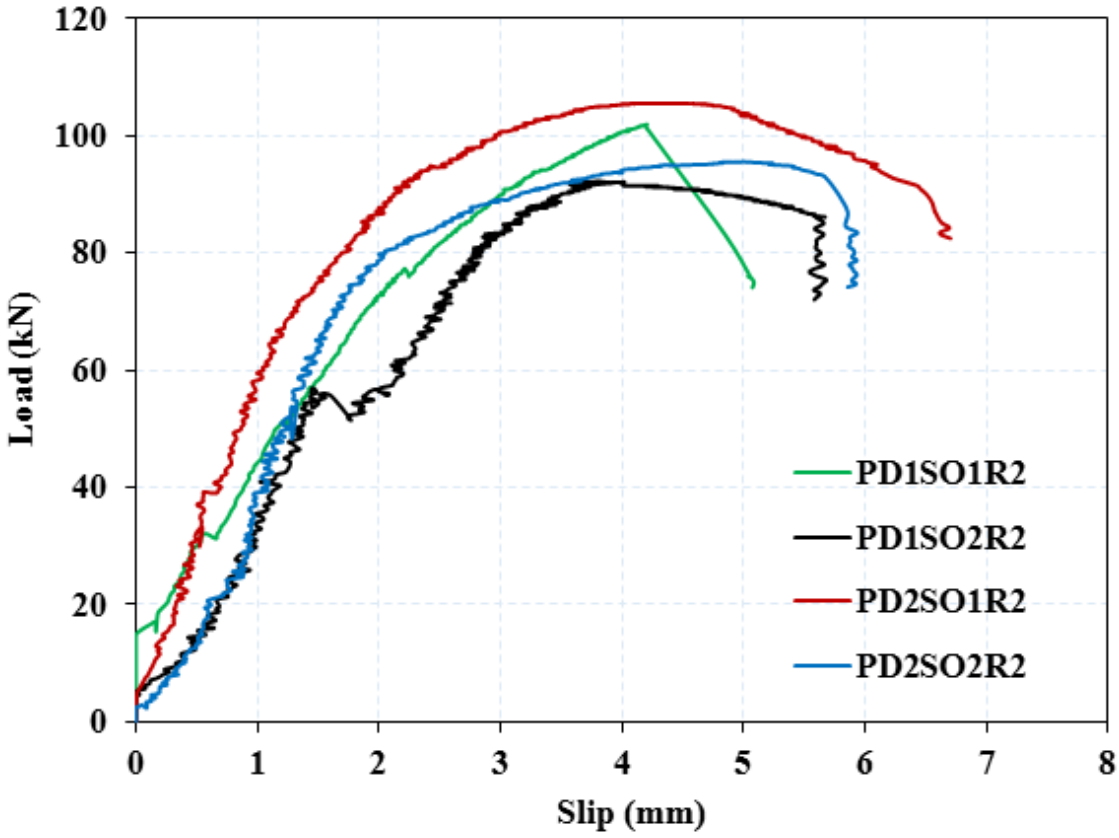


**Figure 4. 5: Influence of temperature levels on the shear resistance of X-HVB shear connectors with transverse corrugated steel plate to the steel beam.**

### 4.2.4 Effect of Direction of Corrugated Steel Plate

This section investigates the influence of the loading direction in relation to the direction of corrugated sheeting. Figure 4.6 presents the load versus slip relationships of X-HVB shear connectors for both the transverse and parallel directions of the corrugated sheeting at ambient temperature conditions while Figures 4.7 to 4.11 after exposure to fire.

For the specimen with a transverse profiled steel deck (PD2SO1), an increase of approximately 10% in the X-HVB shear capacity was observed compared to the specimen with a parallel profiled steel deck (PD1SO1).

The slip values gradually increased until failure, reaching interface slips of 4.79 mm for PD1SO1 and 3.54 mm for PD2SO1.

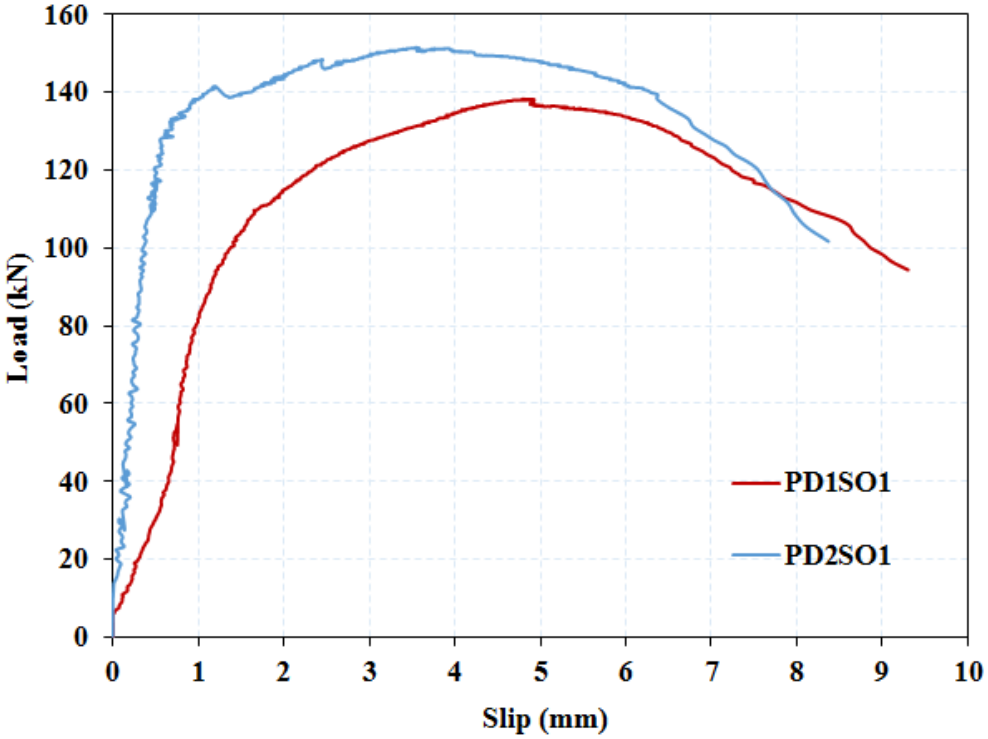


**Figure 4. 6: Influence of direction of corrugated steel plate on the shear resistance of X-HVB shear connectors at ambient temperature.**

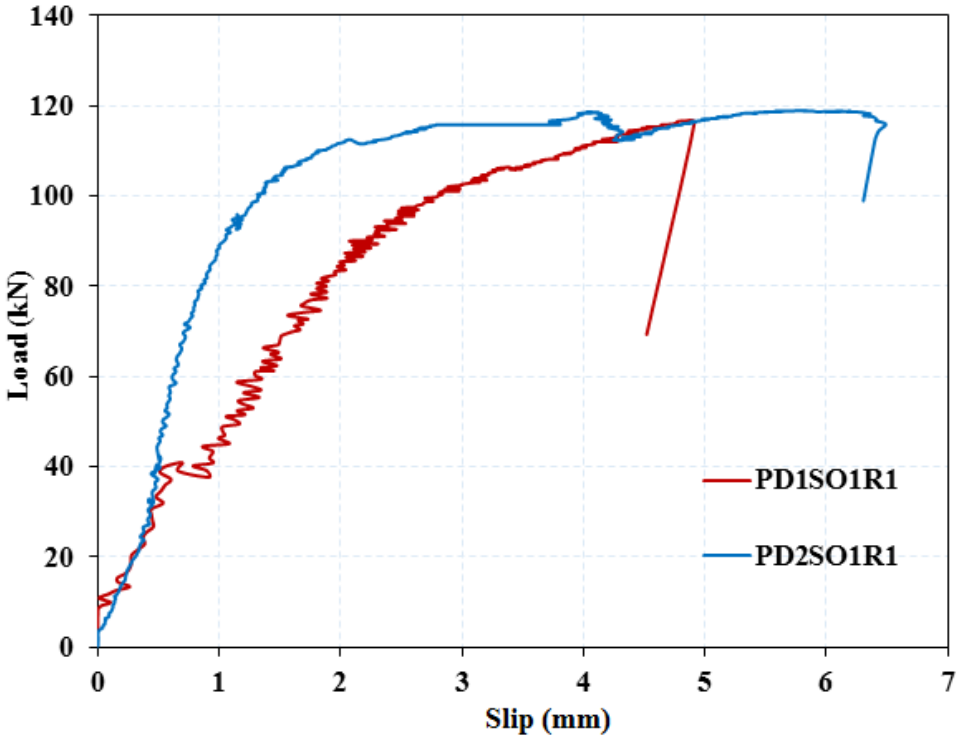


**Figure 4. 7: Influence of direction of corrugated steel plate on the shear resistance of X-HVB shear connectors at 350 ˚C.**

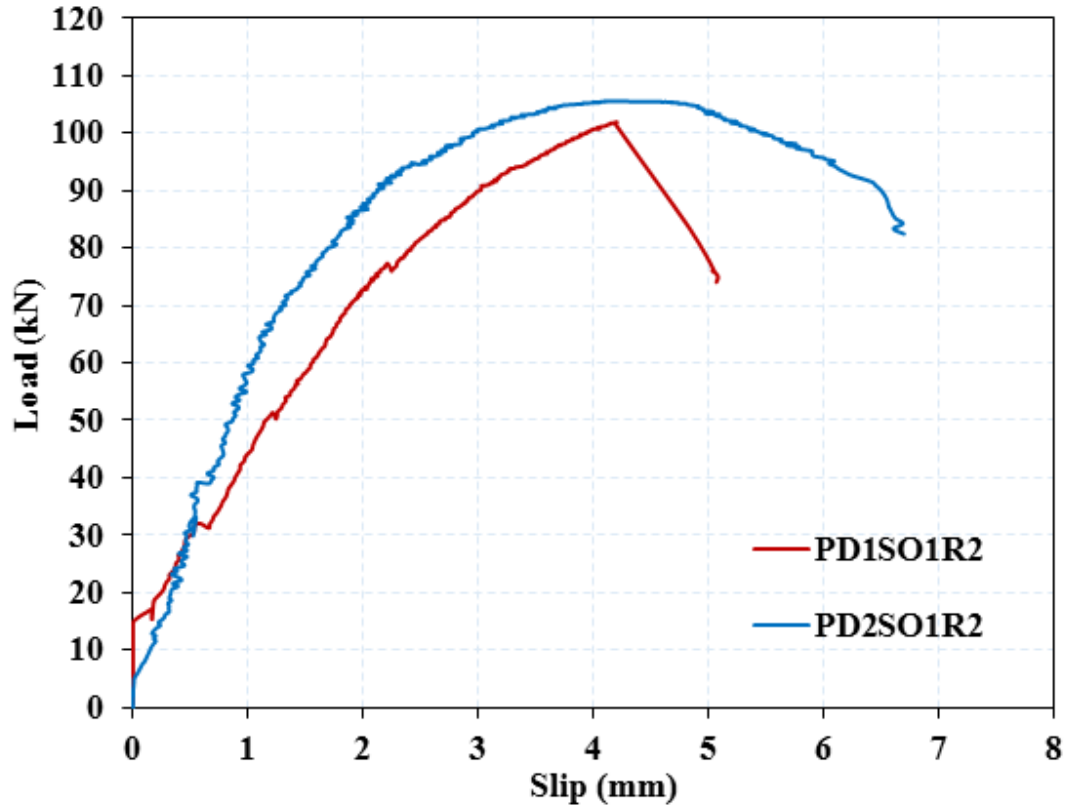


**Figure 4. 8: Influence of direction of corrugated steel plate on the shear resistance of X-HVB shear connectors at 450 ˚C.**

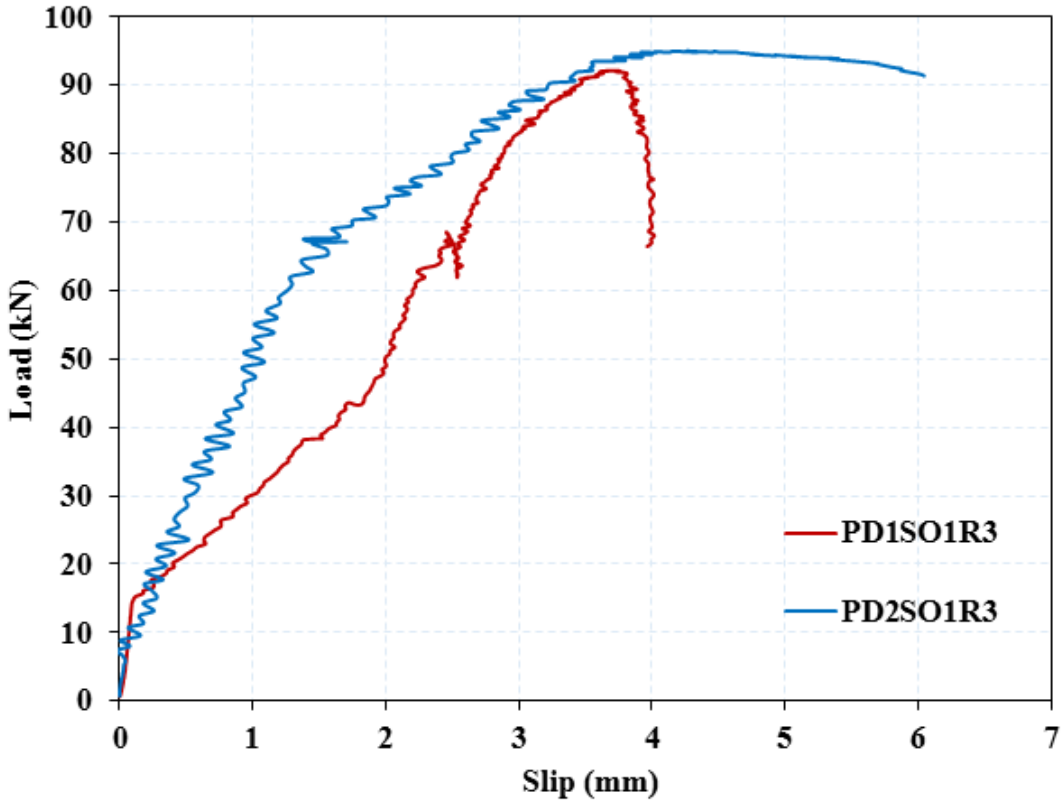


**Figure 4. 9: Influence of direction of corrugated steel plate on the shear resistance of X-HVB shear connectors at 550 ˚C.**

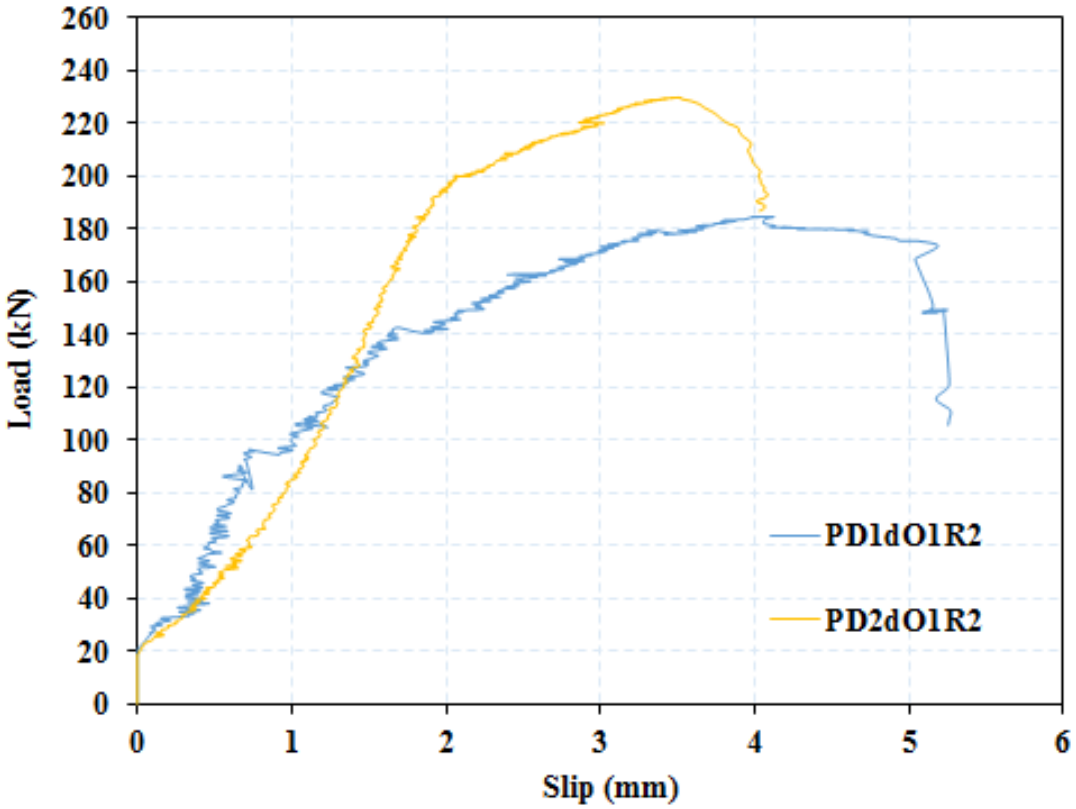


**Figure 4. 10: Influence of direction of corrugated steel plate on the shear resistance with double X-HVB shear connectors.**

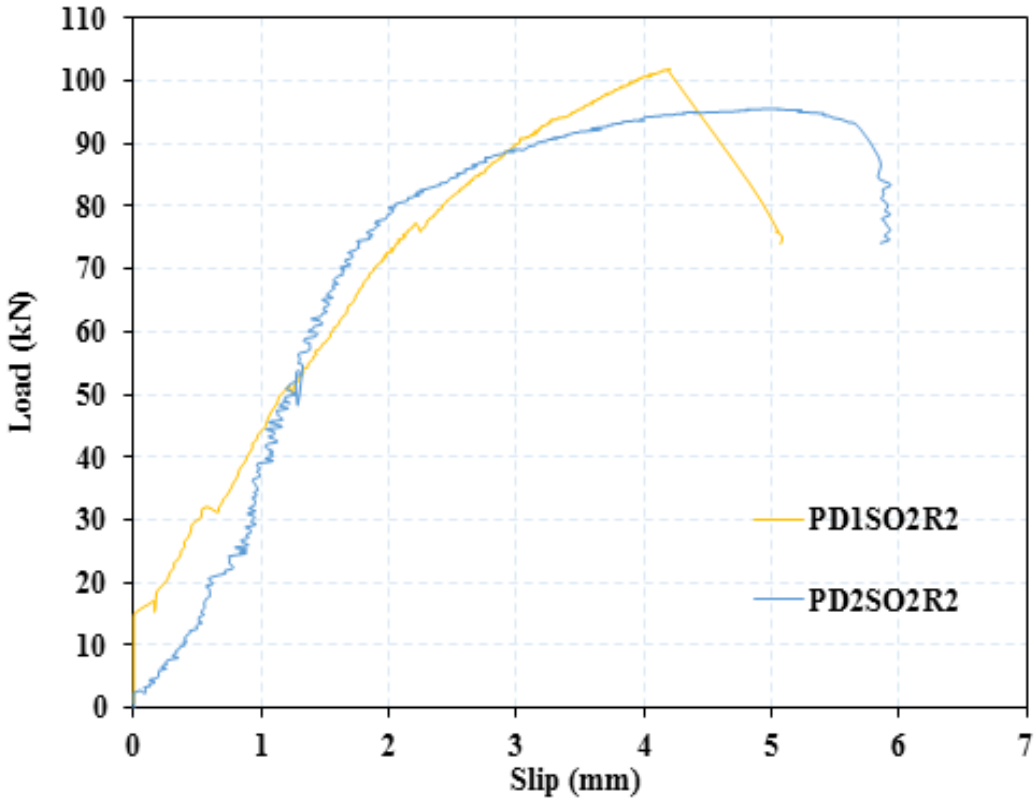


**Figure 4. 11: Influence of direction of corrugated steel plate on the shear resistance of X-HVB shear connectors with backward orientation.**

Additionally, it was observed from Figures 4.7 to 4.11 that the transverse corrugated steel plate specimen had a stiffer behavior compared to the parallel profiled steel deck. This can be attributed to the fact that transverse sheets transfer the load to the concrete slab through direct shear, friction, and the contribution of the bearing of concrete within ribs, whereas parallel sheets transfer the load to the bottom through direct shear of the connector and friction between sheeting and concrete.

While under the influence of fire exposure at all temperature levels and with a single, forward orientation of the shear connector, the difference between the two direction of corrugated steel plate either parallel and transverse to the steel beam was small. However, the specimens with transverse corrugated steel plate specimens showed a greater drop in performance after exposure to fire than the specimens with parallel corrugated steel plate, as explained in Section 4.2.1.

In contrast, when using a double shear connector and transverse corrugated plate, the ultimate load increased by approximately 25% compared to the specimens with parallel plates. In another hand, in specimens with a backward orientation of the shear connector, the difference in the direction of the corrugated steel plate did not appear to significantly affect the results.

### 4.2.5 Failure Mode

In terms of failure mechanisms, visual observations were conducted during and at the end of the loading stage to document the condition of both the unburned and burned pushout specimens. The aim was to study the development of failure mechanisms and assess the behavior of all specimens exposed to fire.

At ambient temperature, specimens PD1SO1 and PD2SO1 showed a failure mode characterized by a noticeable separation of the corrugated steel sheet from the concrete slab before all cartridge fastening pins pulled out from the steel section due to significant plastic deformation, leading to enlarged nail holes. The detachment (see Figure 4.12) occurred at approximately 116 kN for PD1SO1 and 140 kN for PD2SO1. Additionally, the corrugated steel plate around the fastener holes bulged, resulting in deformation of the holes. Moreover, a transverse crack appeared at the middle of the concrete slab. However, in the specimen with a transverse corrugated steel deck, the crack was wider, showing a transverse crack at the failure load with a width of 0.1 mm for PD1SO1 and 0.4 mm for PD2SO1 at 144 kN, as shown in Figure 4.13. This type of failure demonstrates ductile behavior, as clearly depicted in Figure 4.6.

While the specimens that exposed to fire, transverse (thermal) cracks became visible on the face of the concrete slab as a result of burning process, these thermal cracks were marked with a red marking pen, as depicted in Figure 4.14. It was observed that all specimens with parallel corrugated steel plates experienced shearing off of the top fastening pins between the corrugated steel sheet and the steel beam. Additionally, the bottom set of fastening pins experienced pullout, as depicted in Figure 4.15. The shearing of the fasteners indicates that the applied shear forces exceeded the capacity of the shear connectors, resulting in the fracture or shearing off of the pins. This failure occurred suddenly at lower loads and provided significantly less ductility, as shown in Figure 4.2. The only exception was specimen PFD1SO2, which failed through the pullout of all fastening pins from the steel beam, as shown in Figure 4.16. Furthermore, Figure 4.5 illustrates that the load reduction from 56 kN to 51 kN was due to the complete separation of the corrugated sheeting from the concrete.

While the failure mechanisms observed in specimens with transverse corrugated steel plate by the concrete failed and exhibited notable separation of the corrugated steel plate from the concrete, as depicted in Figure 4.17. except in the case of specimen PFD2dO1, failure occurred due to the expansion of transverse cracks generated from fire in the middle of each side of the concrete slab, resulting in a larger crack width. At the failure load, some of the fastening pins also pulled out from the steel beam as depicted in Figure 4.18.

**Figure 4. 12**: **Detachment of the corrugated steel sheet.**

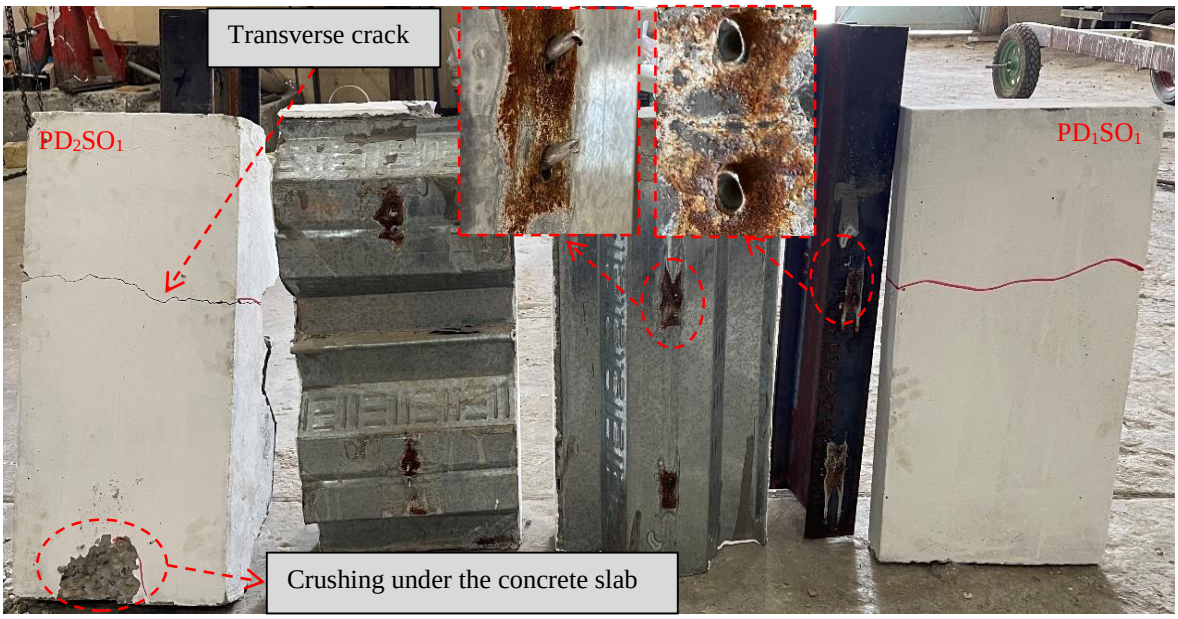


**Figure 4. 13: The failure mode of specimens PD1 and PD2.**

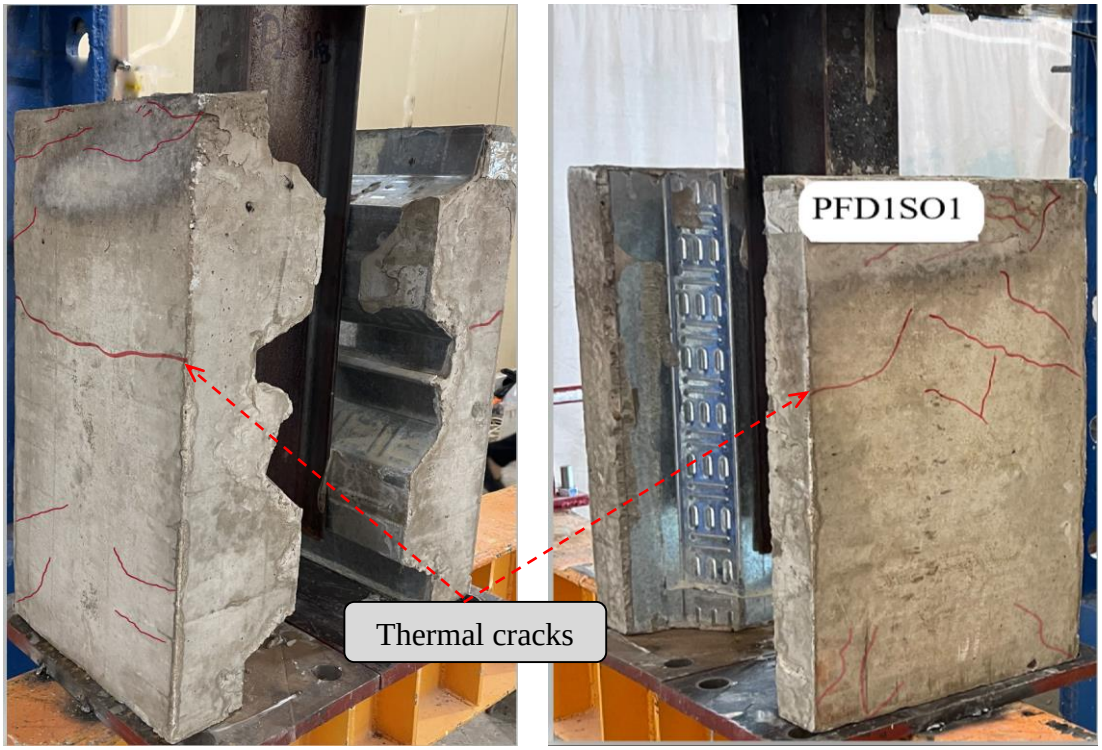


(a) Transverse sheeting (b) Parallel sheeting

**Figure 4. 14: The failure mode of specimens after exposed to fire before testing.**

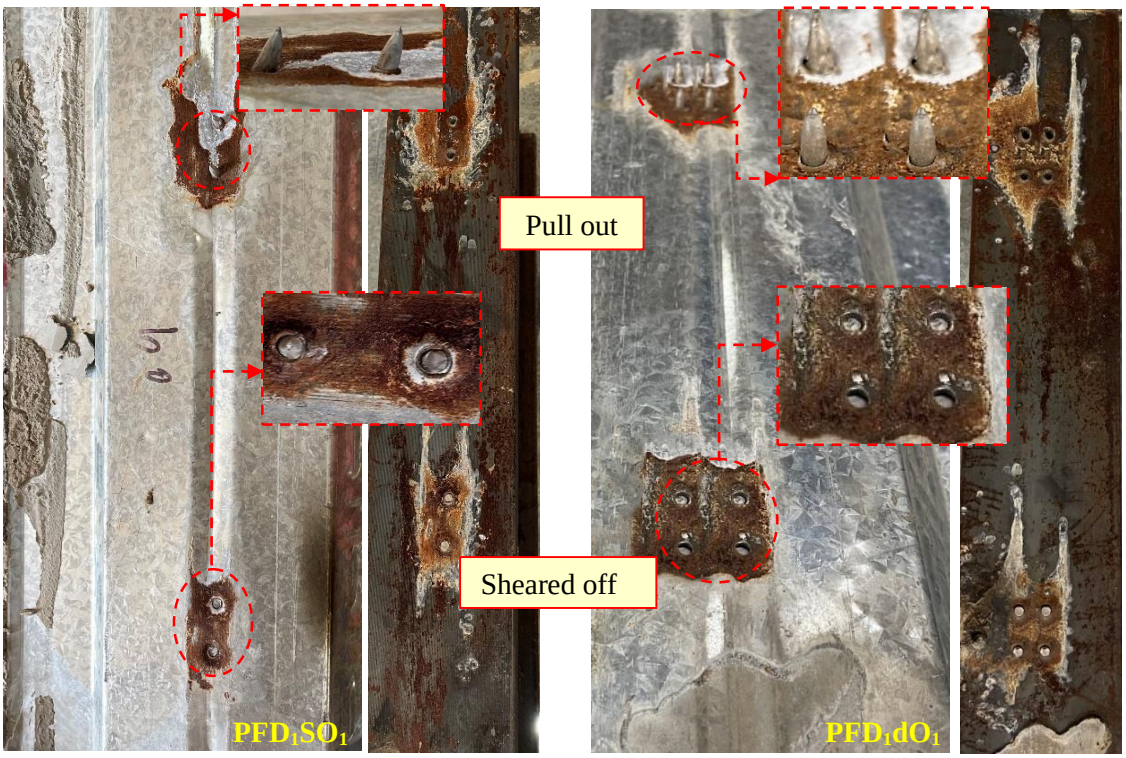


**Figure 4. 15: Failure mechanism for specimens $PFD_1SO_1$ and $PFD_1dO_1$.**

**Figure 4. 16: Failure mechanism for specimens PFD1SO2.**

**Figure 4. 17: The failure mode of specimens PFD2SO1 and PFD2SO2.**


**Figure 4. 18: Failure mechanism for specimen PD2dO1R2.**

### 4.2.6 Stiffness and Ductility

Many fundamental criteria, including ductility and stiffness, are used to analyses pushout results. EC4 uses the ultimate slip ($\delta u$) as a key parameter to classify the shear connectors with respect to the ductility. This code recommends if the characteristic slip capacity of each shear connector ($\delta uk=0.9\delta u$) is at least 6 mm, the shear connector is considered as a ductile connector. This is worth mentioning that a ductile shear connector has sufficient deformation capacity prior to failure in order to validate the perfect plastic behavior of the shear connection.

Besides, $K$sc represents the shear connector stiffness at serviceability load which is taken as the secant modulus corresponding to 0.7Pu [81]. It should be mentioned that for plotting the load–slip curves, the slip value was considered as the averaged values of two LVDTs which applied for recording the vertical slip between steel sections and concrete slabs. The

results of the stiffness and ductility tests for X-HVB shear connectors are listed in Table3.

The stiffness of the X-HVB shear connector for PD1SO1 and PD2SO1 specimens at ambient temperature is 76 kN/mm and 265 kN/mm, respectively. The high stiffness of PD2SO1, which is 3.5 times higher than that of PD1SO1 can be attributed to the rib of the corrugated steel plate being transverse to the beam length giving more resistance to slip than the parallel rib. In terms of temperature variations (350℃, 450℃, and 550℃), the stiffness of all the specimens and in both the parallel and the transverse direction of corrugated steel plate decreases. Nevertheless, upon exposure to the same temperature, the stiffness of specimens with transverse ribs to the steel beam remains higher than that with parallel ones.

While, upon exposure to the same temperature and using double shear connecter instead of one in each raw, the stiffness of samples with parallel ribs to the steel beam is increased by about 136% compared to the specimen with a single shear connecter. While in a specimen with transverse ribs to the steel beam, the stiffness increased by about 93% for a specimen with double shear connecter than the specimen with a single shear connecter under the same level of fire exposure. But when the orientation of the shear connecter changes to backward from forward relative to the shear force direction, the stiffness decreases by about 22% and 17% for specimens PFD1SO2 and PFD2SO2, respectively.

Regarding ductility, the behaviors of X-HVB shear connectors in both parallel and transverse directions of corrugated steel plate are ductile at an ambient temperature according to EC4, as shown in Figure 4.19. After burning the specimens, the X-HVB exhibits non-ductile behavior in the parallel direction of corrugated steel plate, while it continues to behave in a ductile manner in the transverse direction.

The increase of the shear connection ratio in PFD2dO1 and PFD1dO1 while applying the same fire-exposed scenario leads to brittle behavior. But this is not the case for specimens with backward orientation of the X-HVB shear connecter of PD1SO2R2 and PD2SO2R2; still behaving in a ductile manner for both directions of profiled steel sheet.

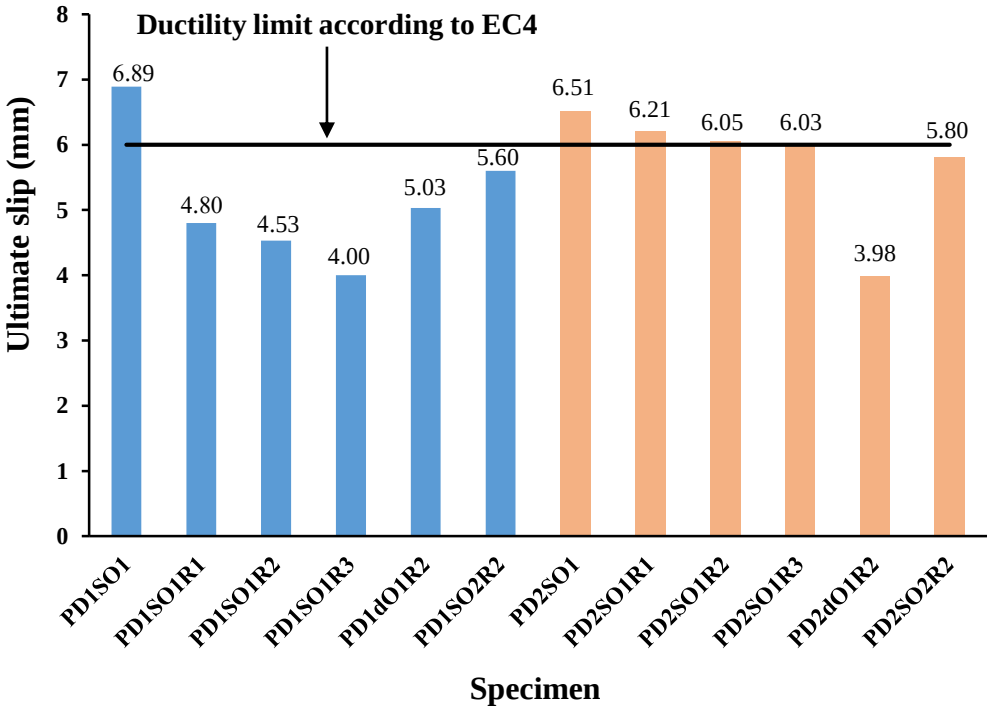


**Figure 4. 19: Ductility response for all the tested specimens.**

## 4.3 TEST RESULTS FOR COMPOSITE BEAM SPECIMENS

In order to cover a wide range of application of the fire behavior of composite beams, fire tests were conducted on full-scale specimens representing two types of structural systems. The first set consisted of five specimens with parallel corrugated steel plates, while the second set comprised specimens with transverse corrugated steel plates. Each set of specimen was subjected to fire exposure at different temperature levels (350, 450, and 550 ℃) and from different exposure directions (either from the bottom or the top), additionally, a control specimen was tested at ambient temperature. The composite specimens were designed to fail in flexure and were loaded with a line load at their mid-span point, while

being simply supported at their two ends. The loading was applied gradually in small increments until final failure at a constant rate of 0.5 kN/sec.

The test results included load-carrying capacity, load versus mid-span deflection, load versus slip between concrete and steel, crack patterns, stiffness, ductility ratio, and energy absorption. All girders were tested under the same type of loading. Table 4.2 presents the experimental results obtained from the tested composite girders.

**Table 4. 2: Summary of the results of composite girders.**

| Specimen | Ultimate load (kN) | Mid-span deflection (mm) | Peak slip (mm) | Ductility ratio | Stiffness (kN/mm) | Energy absorption (kN/mm) |
|---|---|---|---|---|---|---|
| CD1 | 219.86 | 34.39 | 6.18 | 3.46 | 16.59 | 5960.30 |
| CD1BR1 | 176.74 | 20.80 | 2.81 | 2.27 | 14.44 | 2587.75 |
| CD1BR2 | 155.56 | 12.98 | 2.13 | 1.56 | 14.06 | 1182.44 |
| CD1BR3 | 140.17 | 11.77 | 1.72 | 1.46 | 13.03 | 895.01 |
| CD1TR2 | 202.33 | 36.16 | 4.97 | 3.42 | 15.26 | 3589.98 |
| CD2 | 190.98 | 32.73 | 6.60 | 4.94 | 21.64 | 5255.17 |
| CD2BR1 | 147.56 | 12.56 | 2.52 | 1.69 | 14.90 | 693.52 |
| CD2BR2 | 127.24 | 11.22 | 1.81 | 1.50 | 13.10 | 491.56 |
| CD2BR3 | 114.00 | 10.15 | 1.57 | 1.41 | 12.44 | 616.08 |
| CD2TR2 | 171.95 | 26.94 | 8.33 | 4.21 | 20.15 | 3741.02 |

### 4.3.1 Load–deflection Response

Figure 4.20 illustrates the response of the tested specimens with parallel corrugated sheeting, whereas Figure 4.21 illustrates the response of the specimens with transverse corrugated sheeting. The progression of mid-

span vertical deflection is plotted against the applied load, comparing the effect of exposing the specimens to fire from the bottom of the steel beam at temperatures of 350°C, 450°C, and 550°C to the specimens tested at ambient temperature.

The experimental results indicated, as expected, that with the increase in fire temperature level, there was a reduction in the load-carrying capacity. At 350°C, the specimens with corrugated sheeting runs parallel to the steel beam experienced a loss of approximately 20%, while the specimens with corrugated sheeting runs transversely lost about 23% compared to the control (un exposure to fire) specimens after 1-hour fire exposure. At 450°C, the loss increased to about 29% for specimens with parallel corrugated sheeting and 33% for specimens with transversely sheeting. Furthermore, at 550°C, the loss further increased to about 36% for specimens with parallel corrugated sheeting and 40% for specimens with transverse corrugated sheeting compared to the control (un exposure to fire) specimens after 1-hour fire exposure.

The observed decrease in the ultimate load capacity of the specimens exposed to fire from bottom of the steel beam primarily stems from the lower fire resistance of steel structures. This is mainly due to the low specific heat and high thermal conductivity of steel. Moreover, the mechanical properties of steel, including strength and modulus, deteriorate more rapidly at elevated temperatures. Thus, the combined effect of these factors results in a reduction in the ultimate load capacity under fire exposure conditions.

Notably, when exposed to fire temperatures of 450°C and 550°C, all specimens exhibited sudden failure at smaller deflections, indicating shear connector failure. However, at ambient temperatures, failure occurred due to the yielding of the steel beam, resulting in failure at higher deflections.

Additionally, the ultimate deflection corresponding to the failure load decreased as the fire temperature increased. At 350°C, the ultimate deflection reduced by approximately 40% and 62% for specimens with parallel and transverse corrugated sheeting, respectively, compared to the corresponding control specimens. At 450°C, the ultimate deflection decreased by around 62% and 66% for specimens with parallel and transverse corrugated sheeting, respectively. Finally, at 550°C, the ultimate deflection decreased by approximately 65% and 69% for specimens with parallel and transverse corrugated sheeting, respectively, compared to the corresponding specimens.

Additionally, it is important to mention that specimens with parallel corrugated plate exhibited higher ultimate load compared to those with transverse corrugated plate, as shown in Figures 4.22 to 4.25. This is can be attributed to the parallel corrugated plates may enhance the load distribution and transfer of forces more effectively along the length of the beam. This arrangement could result in better load-sharing characteristics between the steel and concrete components of the composite beam. The parallel corrugations may provide a more direct and efficient load path, allowing for a more uniform stress distribution within the structure. On the other hand, transverse corrugated plates may introduce additional complexities in load transfer and distribution. The arrangement of corrugations perpendicular to the beam axis might lead to localized stress concentrations or uneven force transmission, potentially reducing the overall load-carrying capacity of the composite beam.

While specimens CD1TR2 and CD2TR2, which experienced heating from the top surface of the slab, exhibited behavior approximately similar to unheated specimens CD1 and CD2. However, this similarity did not hold true for specimens heated from the bottom surface. In contrast, specimens

CD1BR2 and CD2BR2, which were subjected to the same fire scenario, displayed a shift towards brittle behavior when heated from the bottom surface of the steel. This is due to concrete slab can act as a heat sink (due to low thermal conductivity and high specific heat of concrete. Differences in behavior were also observed after reaching the ultimate load in CD1TR2 and CD2TR2 due to the fire exposure from the concrete slab, as illustrated in Figures 4.26 and 4.27.

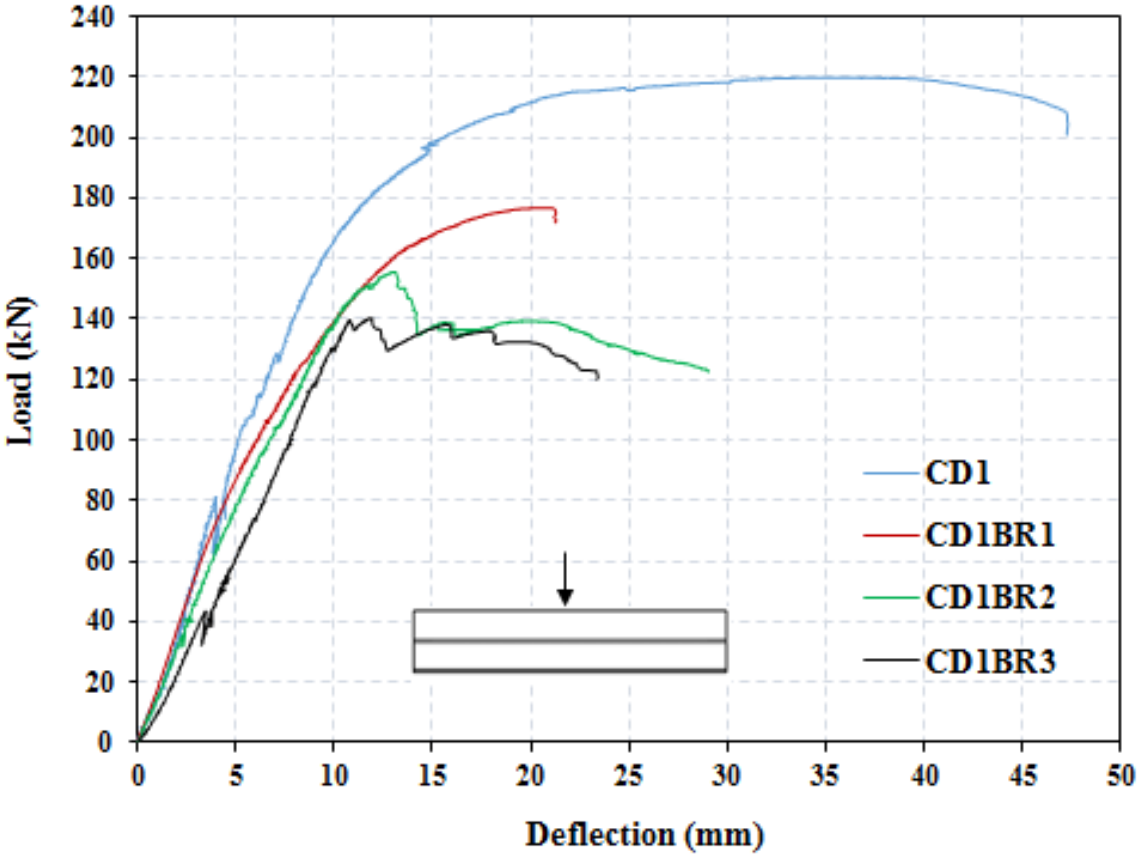


**Figure 4. 20: Load versus deflection curve at mid-span of composite beam with parallel corrugated plate.**

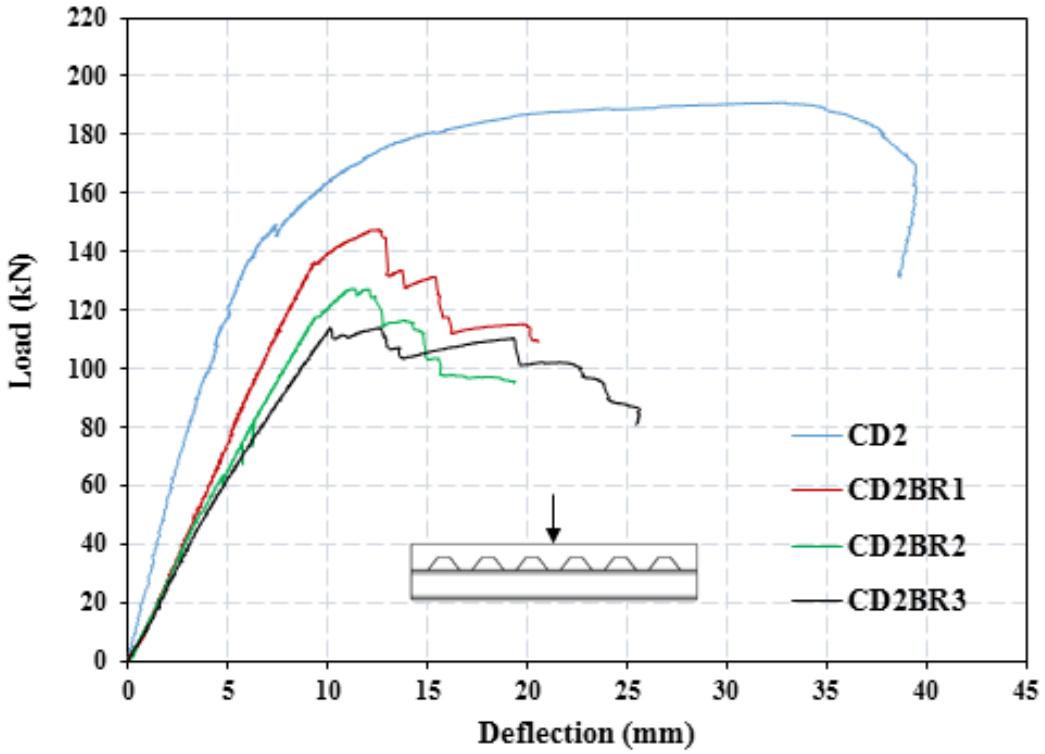


**Figure 4. 21: Load versus deflection curve at mid-span of composite beam with transverse corrugated plate.**

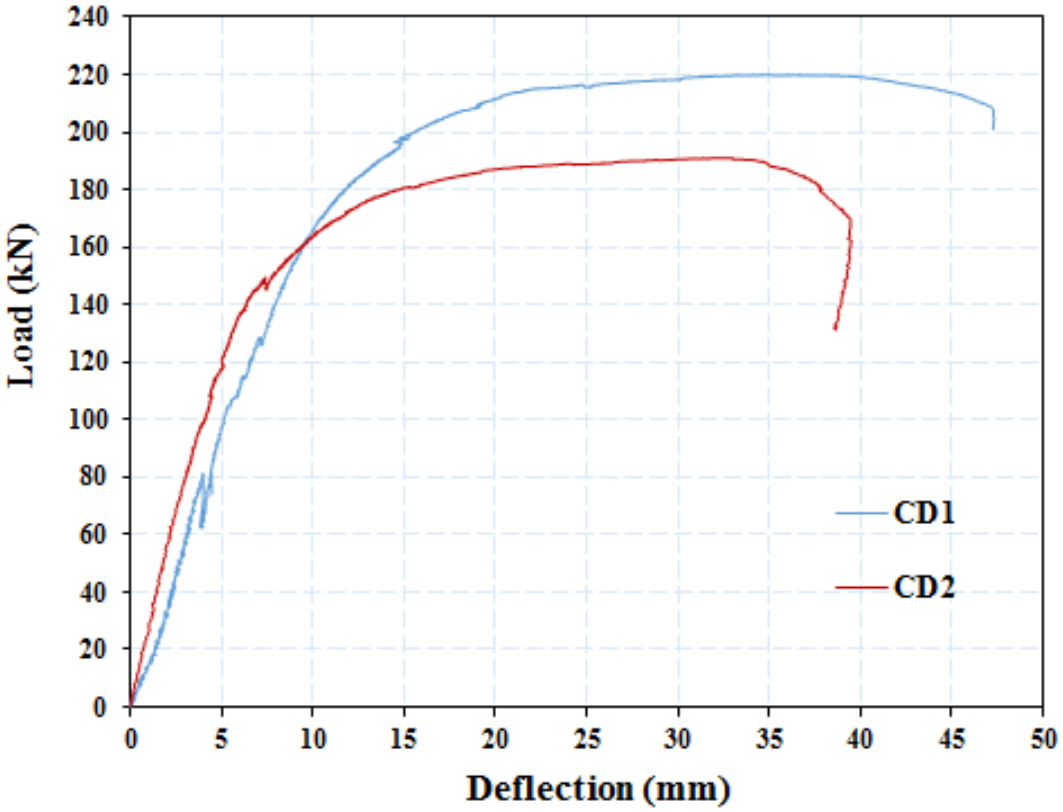


**Figure 4. 22: Load versus deflection curve at mid-span of composite beam at ambient temperature.**

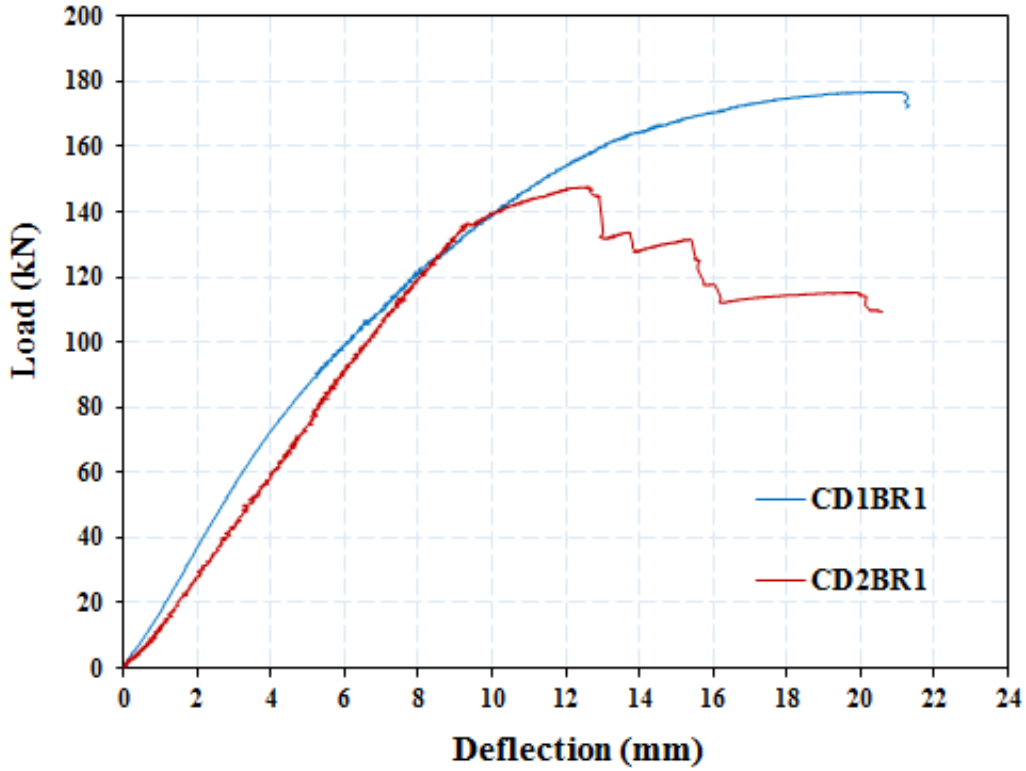


**Figure 4. 23: Load versus deflection curve at mid-span of composite beam at 350°C.**

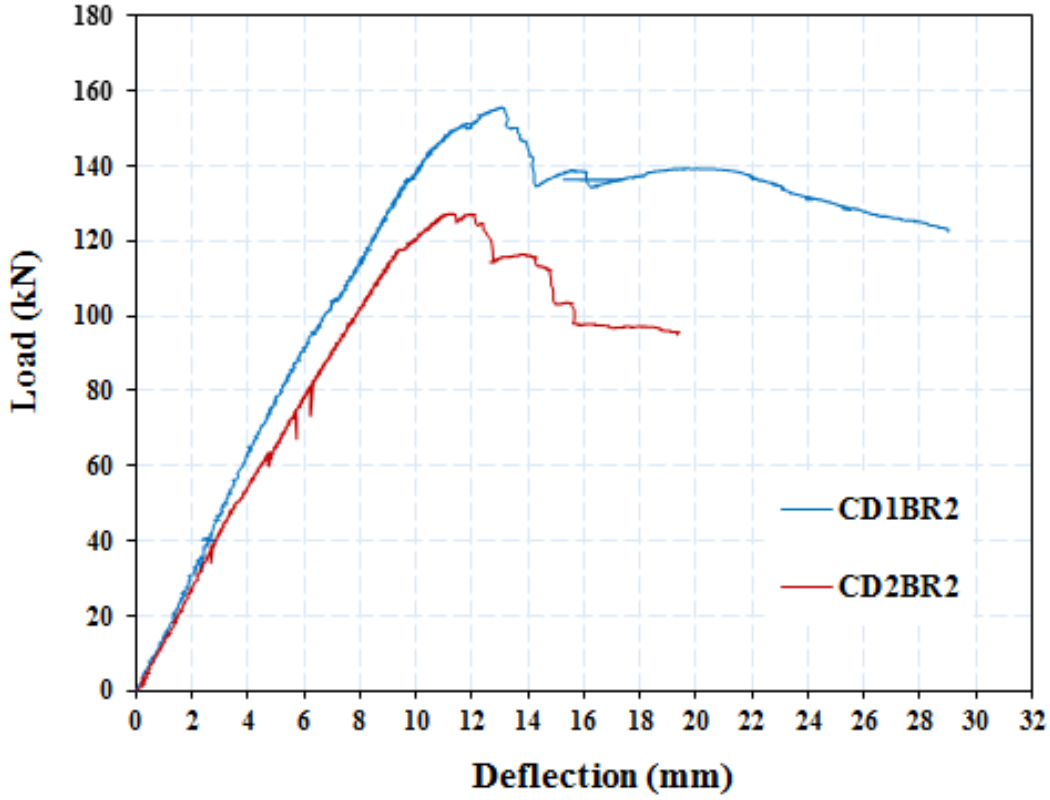


**Figure 4. 24: Load versus deflection curve at mid-span of composite beam at 450°C.**

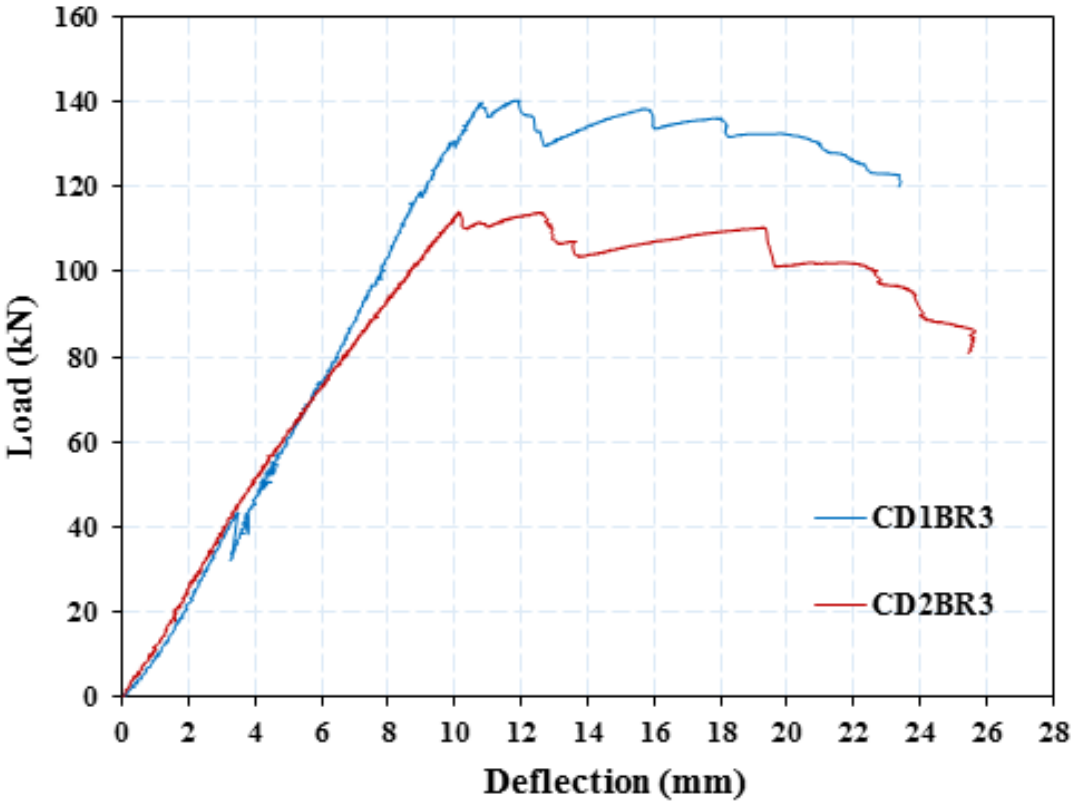


**Figure 4. 25: Load versus deflection curve at mid-span of composite beam at 550°C.**

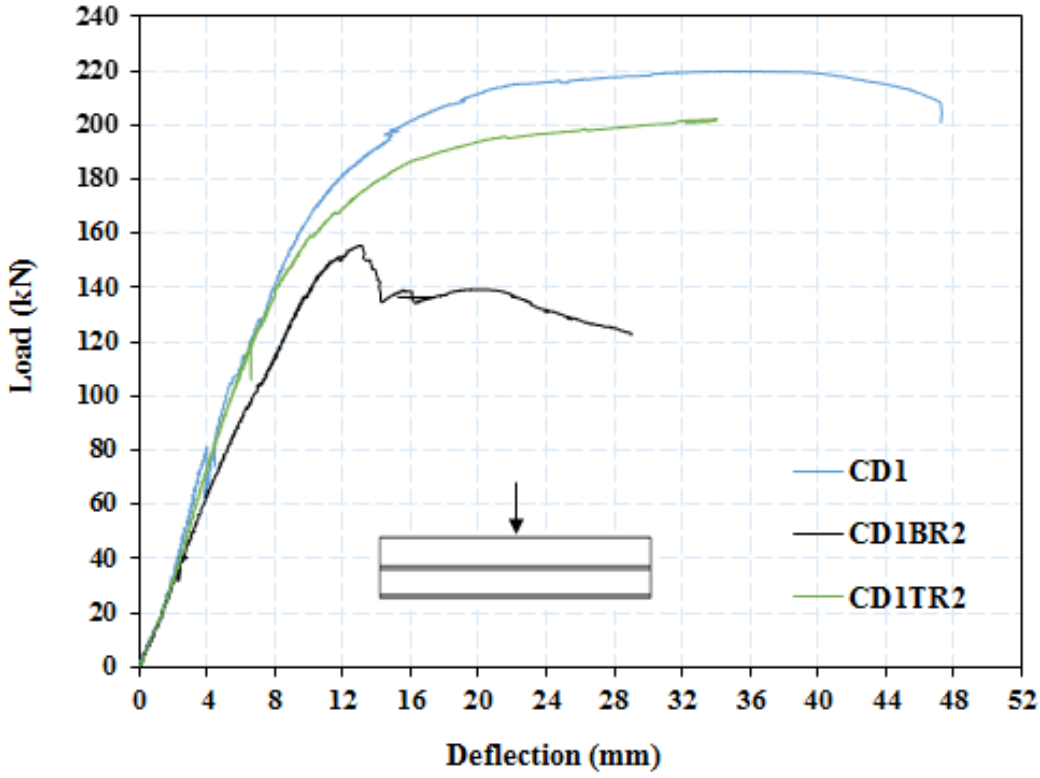


**Figure 4. 26: Effect of fire exposed direction on Load-Deflection Curve of composite beam with transverse corrugated plate.**

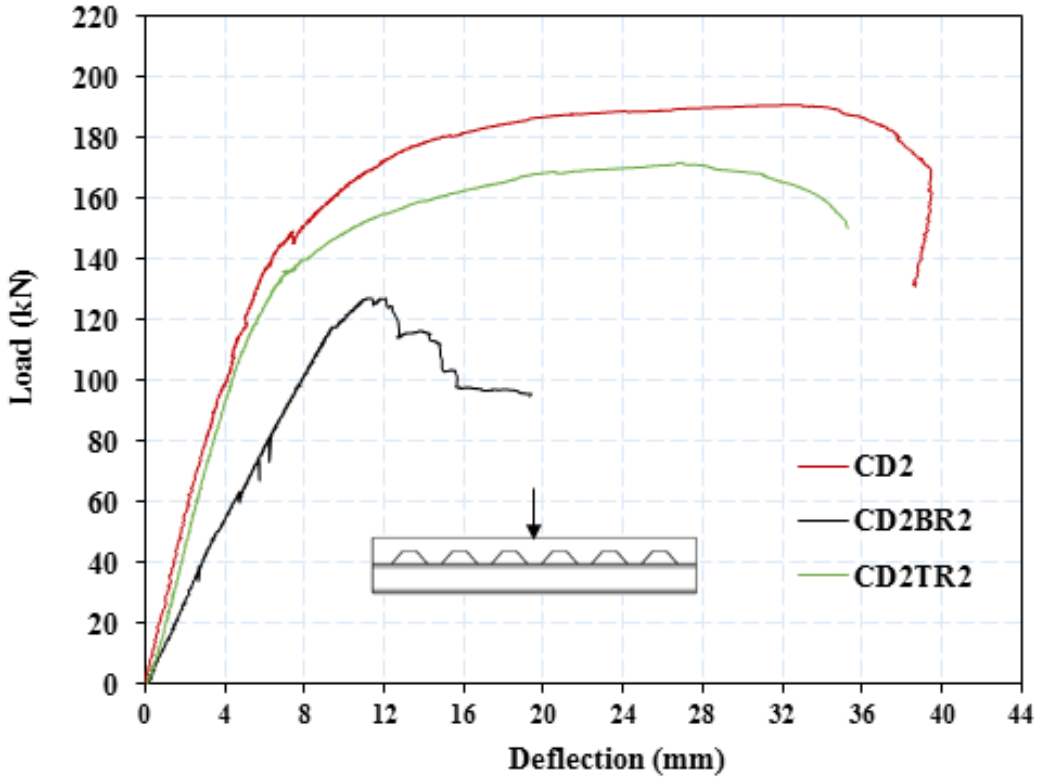


**Figure 4. 27: Load versus deflection curve at mid-span of composite beam with transverse corrugated plate.**

### 4.3.2 Load-slip Response

The shear deformation of the shear connectors caused the relative slips at the interface under the action of bending load. During the initial loading period, the relative slips of composite beam specimens were small due to the excellent interfacial bonding between the steel beam and the composite slab that supported by the shear connecter.

At ambient temperature, in specimens CD1 and CD2, significant increases in slip were observed once the applied load reached approximately 37% and 32% of the ultimate load for CD1 and CD2, respectively. These slips were a result of bond failure occurring at the interface between the steel and composite slab as depicted in Figure 4.28. Also, the ultimate slip in specimen CD2 is greater by about 8% more than specimen CD1. This is due to the effect of corrugated sheet orientation.

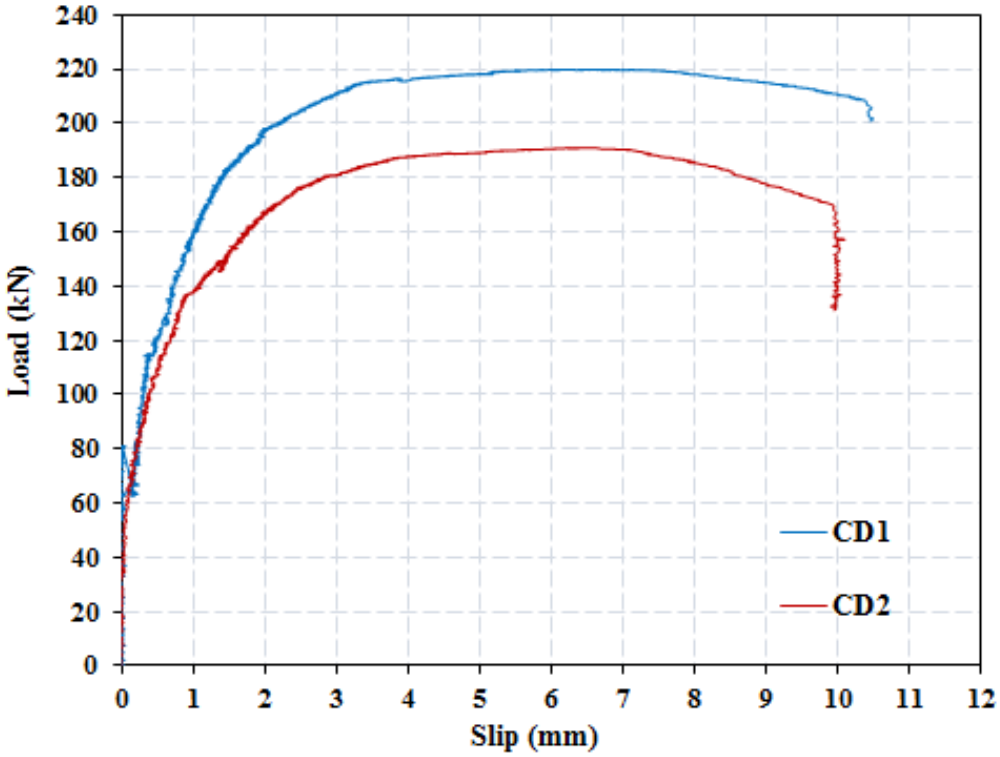


**Figure 4. 28: Influence of direction of corrugated steel plate to the steel beam (parallel or transverse) on the shear resistance of X-HVB shear connectors at ambient temperature.**

Under fire exposure condition, it was observed that the load-slip response of composite beam specimens is affected by both the level of fire temperature and the orientation of the corrugated sheeting with respect to the steel beam. For specimens with parallel corrugated plate that exposed to temperature (350, 450 and 550 ˚C) from the bottom of steel beam, the composite beam-end slip at ultimate load decreased by 54%, 65% and 72% than that of the unheated composite beam, respectively. While the reduction in specimen with transverse corrugated plate by about 62%, 73% and 76% than that of the unheated composite beam as shown in Figure 4.29 and 4.30. It was concluded that as the temperature increases, the ultimate relative slip of the composite beam specimen decreases. This is primarily due to the decrease in the shear connector's performance in resisting shear force as the temperature rises, resulting in faster failure and reduced slip.

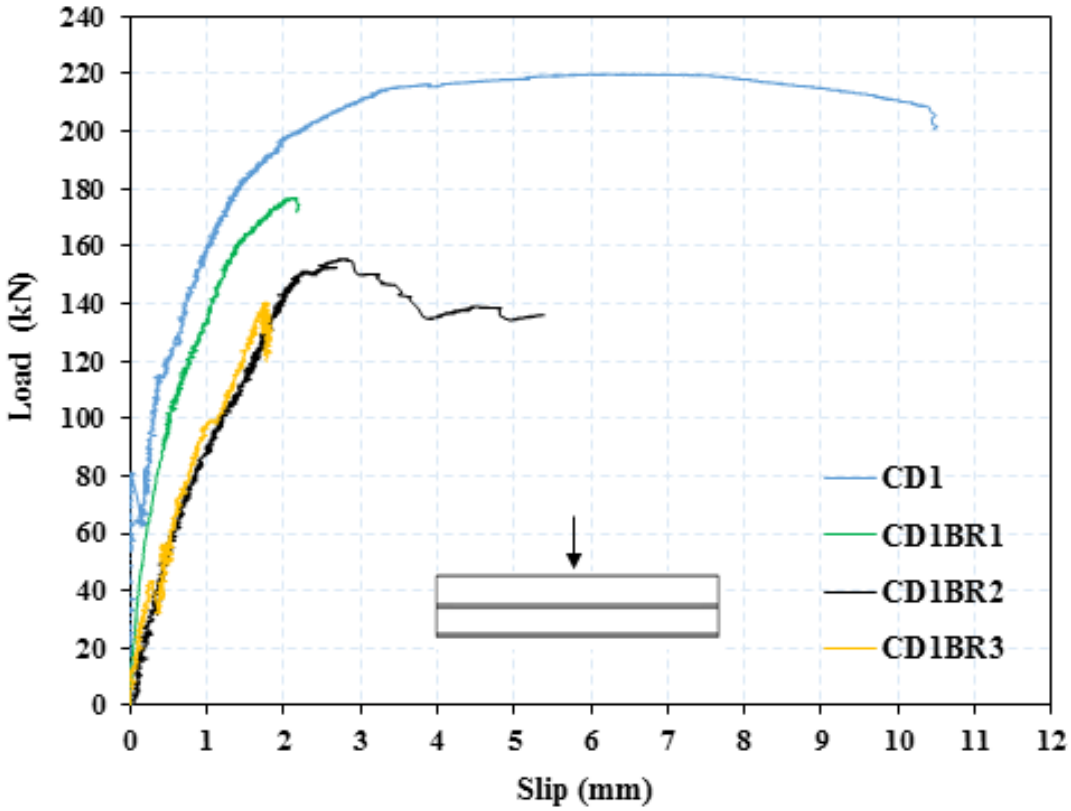


**Figure 4. 29: Influence of exposure to fire on the shear resistance of X-HVB shear connectors with parallel corrugated plate to the steel beam.**

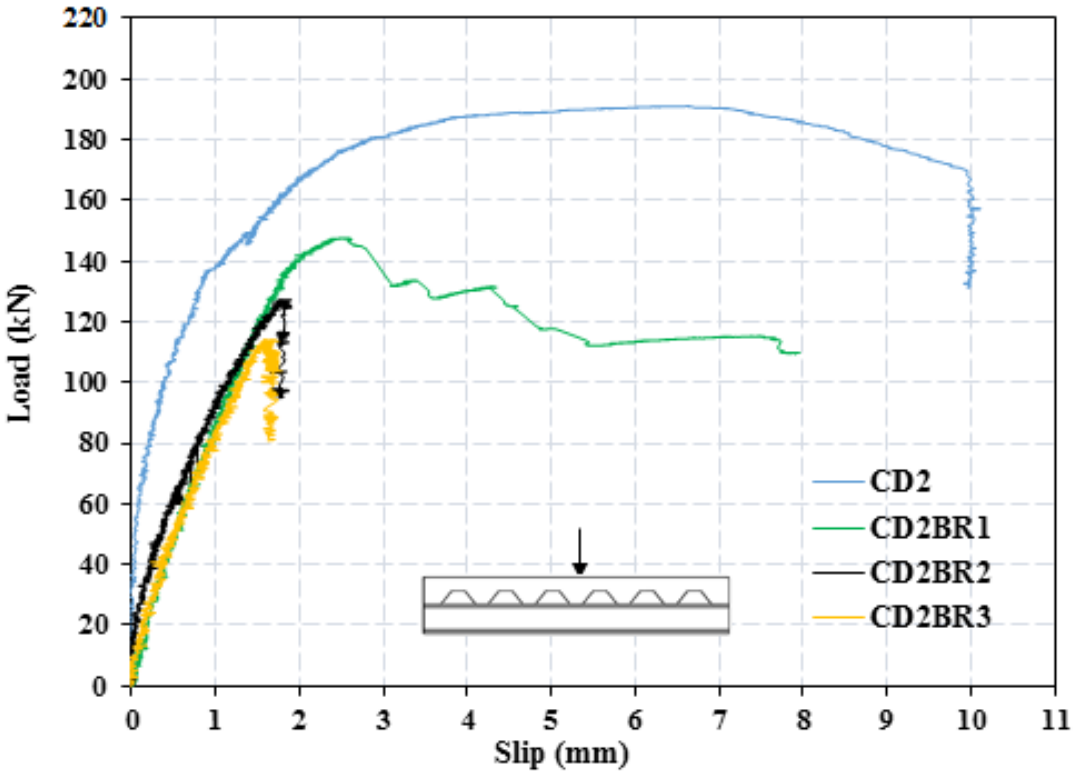


**Figure 4. 30: Influence of exposure to fire on the shear resistance of X-HVB shear connectors with transverse corrugated plate to the steel beam.**

It is also worth noting that the percentage decrease in ultimate slip is higher for specimens with transverse corrugated sheeting compared to those with parallel corrugated sheeting. This can be attributed to the difference in the orientation of the corrugated sheeting. The transverse corrugated sheeting provides less resistance to slip due to its configuration, resulting in a larger decrease in ultimate slip compared to the parallel corrugated sheeting. Additionally, the transverse orientation may affect the load transfer mechanism and contribute to a greater reduction in the ultimate slip of the composite beam specimen.

While for specimens exposed to fire from the concrete slab surface (CD1TR2 and CD2TR2), the slips began to increase at approximately 40% and 25% of the ultimate load for specimens with parallel and transverse corrugated plates, respectively. Furthermore, the ultimate slip in specimen CD1TR2 decreased by about 19% than specimen CD2 but in specimen CD2TR2 increased by about 26% than specimen CD2. See Figure 4.31 and 4.32.

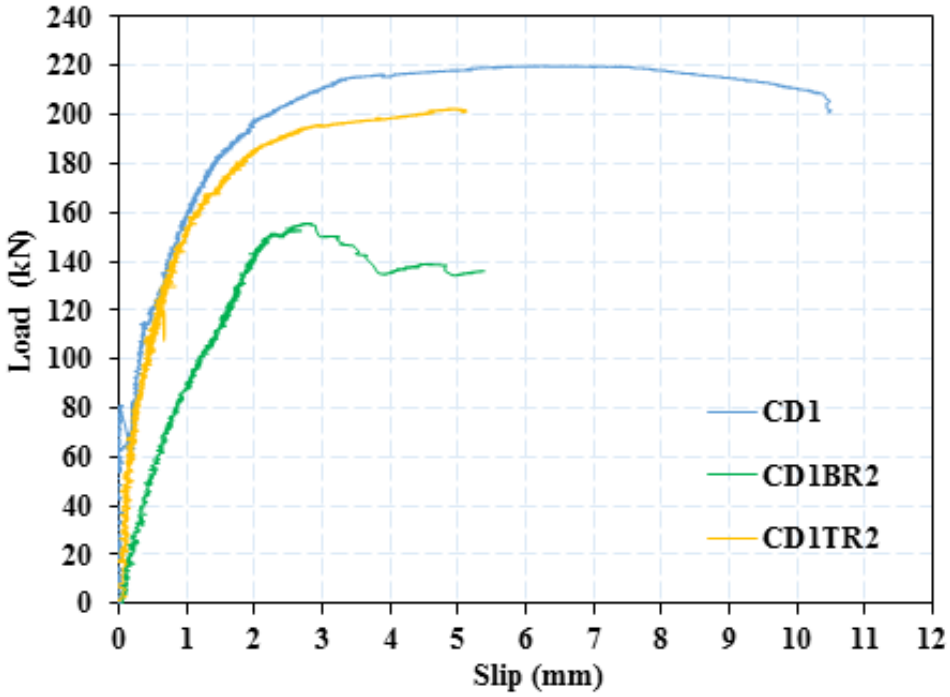


**Figure 4. 31: Effect of direction of fire exposure on load slip curve of composite beam under fire exposure for specimens with parallel corrugated plate.**

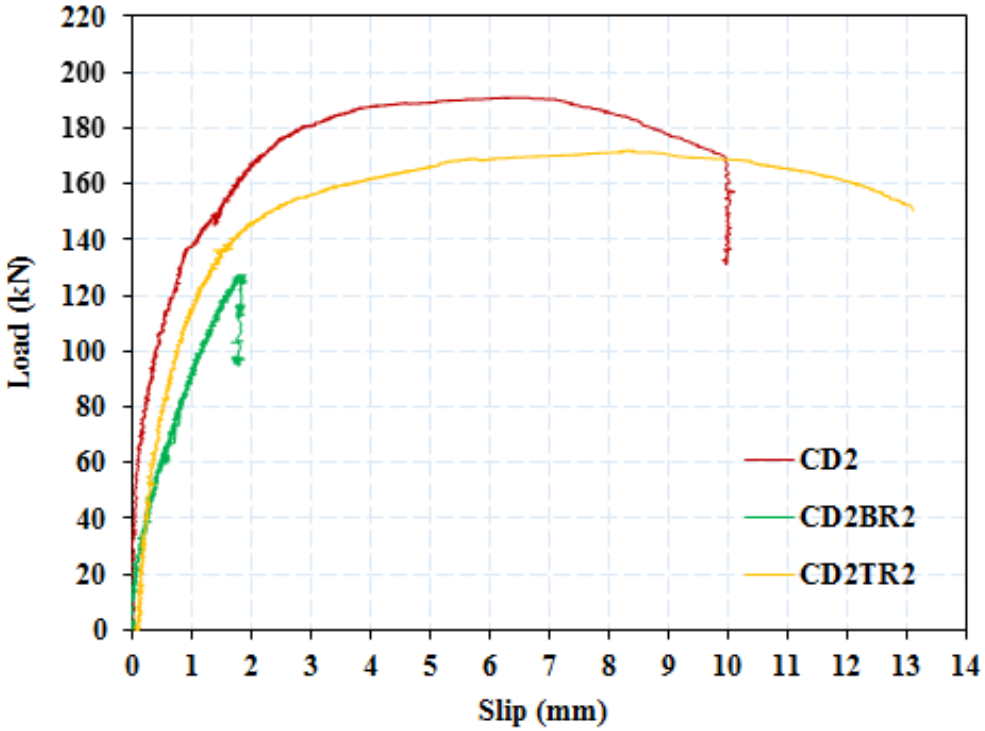


**Figure 4. 32: Effect of direction of fire exposure on load slip curve of composite beam under fire exposure for specimens with transverse corrugated plate.**

### 4.3.3 Failure Mode

During the loading stage, visual observations were conducted to assess the behavior of both unburned and burned composite beam specimens exposed to different levels of firing. These observations aimed to capture the state of the specimens and study the development of failure mechanisms. As the specimens were exposed to fire, transverse cracks appeared at the top of the slab due to the thermal effects generated. These cracks were a direct consequence of the elevated temperatures experienced during fire exposure. Notably, approximately 16 min. after the initiation of the burning process, the cracks became permeable, allowing water and steam to seep through. This occurrence can be observed in Figure 4.33, where the thermal cracks were clearly marked using a red marking pen.

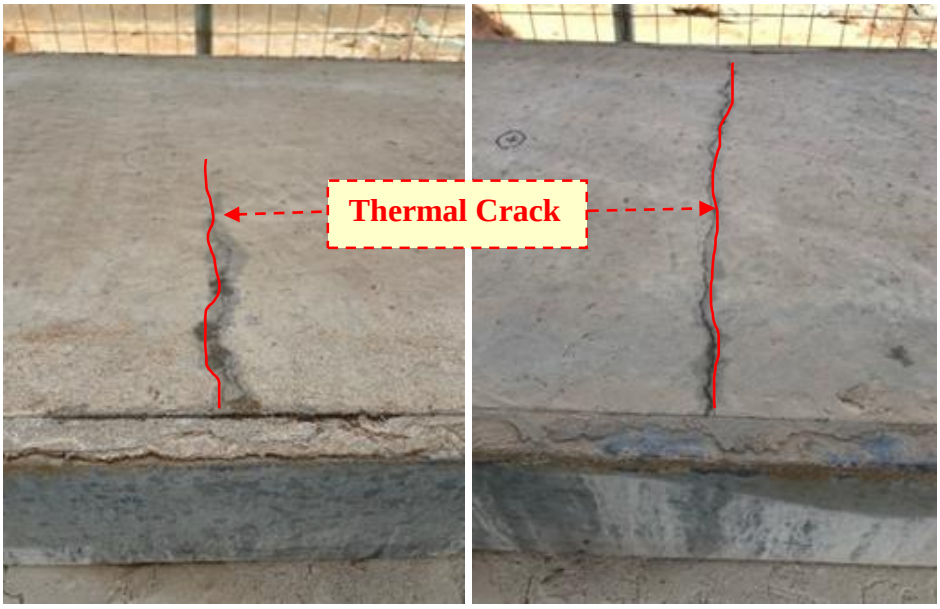


**Figure 4. 33: Formation of transverse cracks due to the effects of fire during the fire process.**

The observations from the tests conducted on the specimens (CD1 and CD2) showed that the dominant response and failure mode were related to flexural behavior. These specimens experienced significant degradation in flexural capacity, ultimately leading to failure through yielding of the steel beam. In specimen CD1, a longitudinal crack (see Figure 4.34) was observed extending from the mid-span of the top face of the concrete slab to the support. These cracks had a width of 0.45mm and appeared at a load of 82 kN. As a consequence, the ultimate load-bearing capacity reduced from 82 kN to 63 kN, as illustrated in the load-deflection curve presented in Figure 4.22 (a). These cracks progressively propagated and widened until reaching the failure load. A blue marking pen was used to mark this crack. When the applied load reached 126 kN, the shear connectors in the specimens became dislocated, resulting in a separation between the steel beam and the corrugated slab. Furthermore, at a load of 206 kN, the top rib of the corrugated steel plate exhibited buckling, occurring approximately 10 cm away from the load point as shown in Figure 4.22 (b).

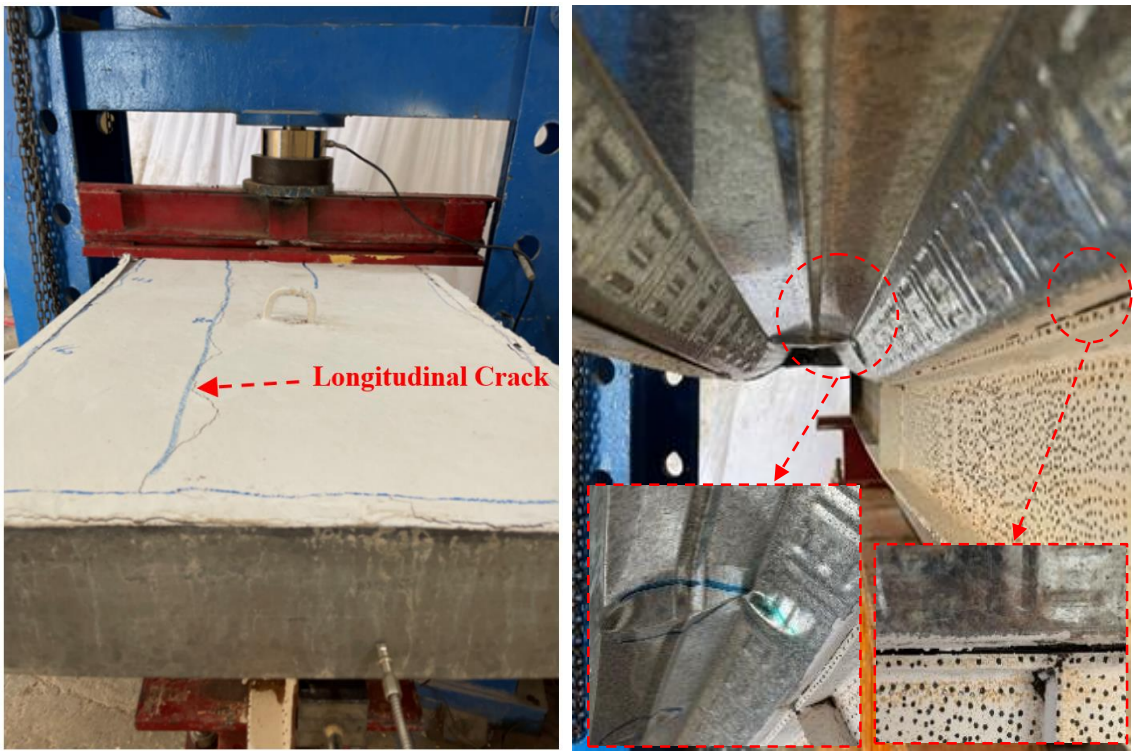


(a) (b)

**Figure 4. 34: Failure mode in specimen CD1.**

Similarly, CD2 exhibited behavior similar to CD1. However, the first longitudinal crack appeared at a higher load, approximately 92 kN, with a smaller width of about 0.1mm. The crack initiated from the mid-span near the loading zone and extended continuously towards the support region as the load reached approximately 137 kN, with a width of about 0.4mm. Additionally, at approximately 150 kN, crushing occurred under the loading zone, which resulted in a temporary reduction in load, followed by a subsequent rise in the load reading. This behavior is also illustrated in the load-deflection curve shown in Figure 4.28 and the failure mode depicted in Figure 4.35. When the load reached the failure load, most of the shear connector fasteners separated from the steel beam.

In contrast, the failure of the burning specimens CD1BR1 and CD1BR2 was attributed to shear connector failure, characterized by the separation of the shear connector from the steel beam with a brittle failure mode. Hair longitudinal cracks also appeared on the top face of the slab, as depicted in

Figure 4.36. Specimen CD1BR3 exhibited behavior similar to that of CD1BR1 and CD1BR2 but with the presence of more longitudinal cracks observed on the top of the composite slab, as shown in Figure 4.37.

In contrast, CD2BR1 exhibited different behavior, with a transverse crack appearing near the support region after the appearance of longitudinal crack, as shown in Figure 4.38, leading to failure by concrete and shear connector. Specimens CD2BR2 and CD2BR3 failed directly by shear connector failure, exhibiting a brittle failure mode. see Figure 4.39.

While specimens CD1TR2 and CD2TR2 exhibited good behavior by displaying more ductile behavior. These specimens followed the same behavior as CD1BR2 and CD2BR2 but with wider transverse cracks and higher ultimate load at failure. see Figures 4.40 and 4.41.

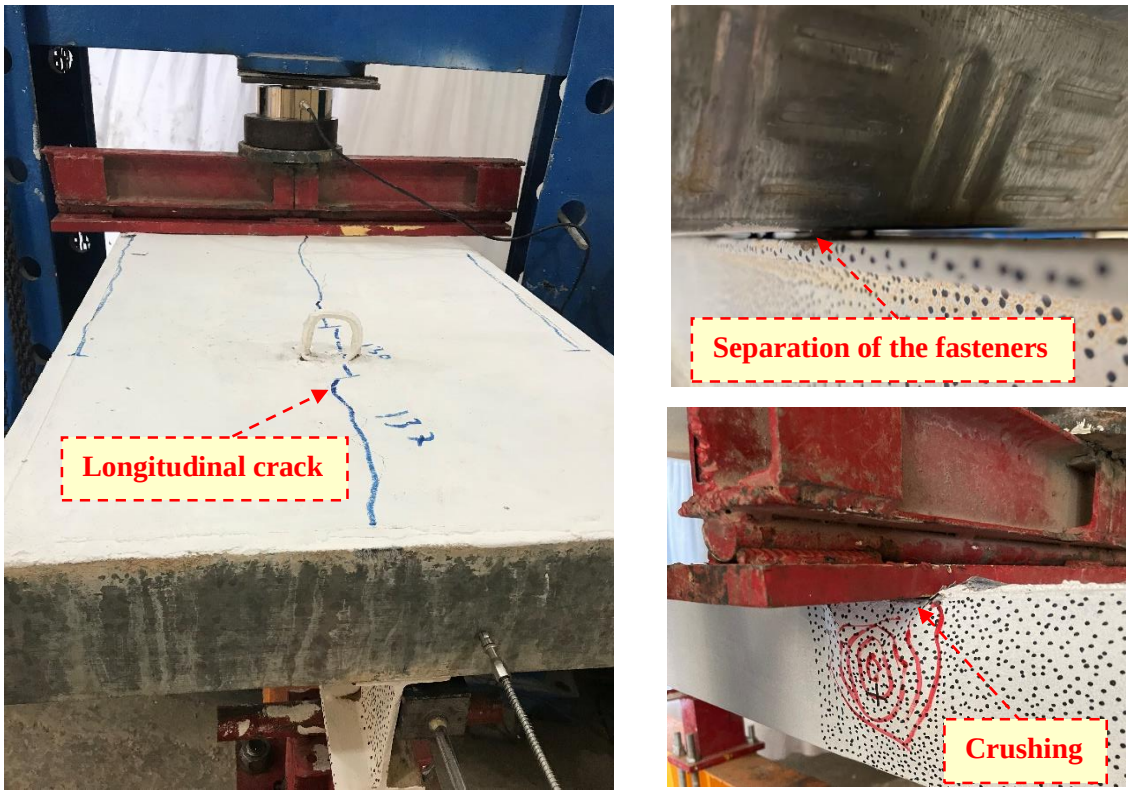


**Figure 4. 35: Failure mode in specimen CD2.**

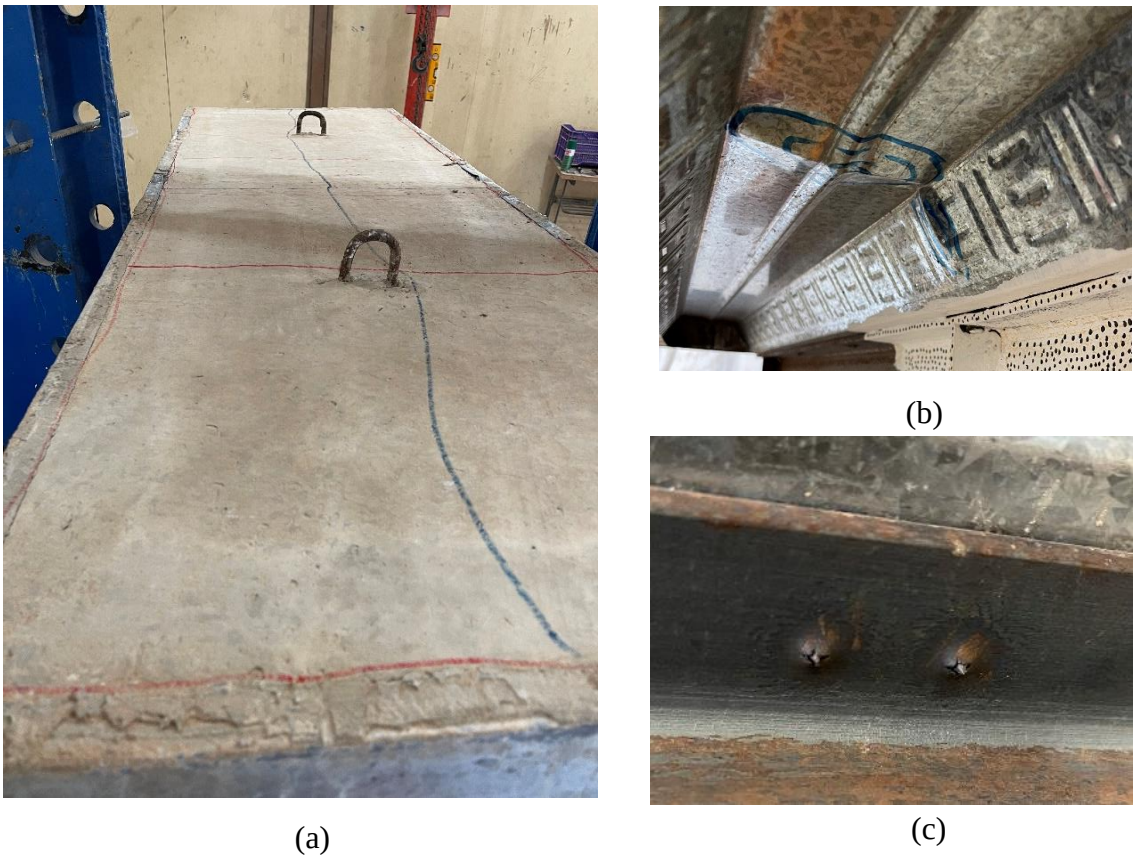

(a) (b) (c)

**Figure 4. 36**: Thermal and longitudinal cracking in specimen CD1BR1.


**Figure 4. 37: Thermal and longitudinal cracking of composite slab in composite beam CD1BR3.**

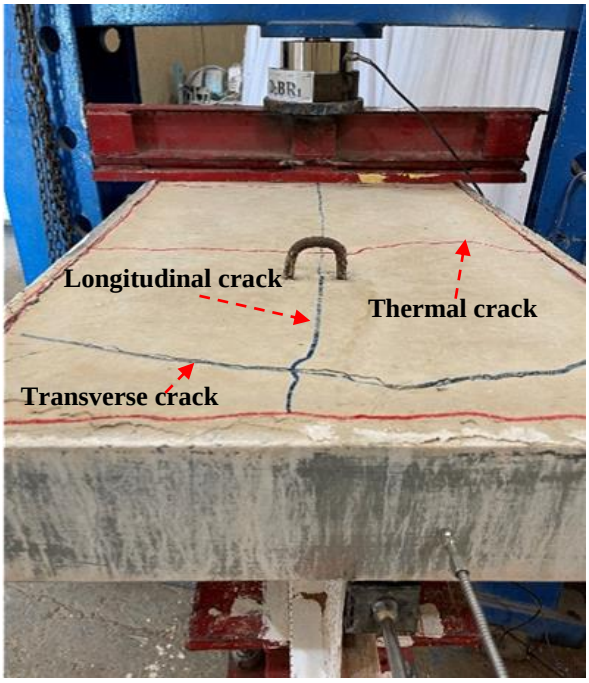


**Figure 4. 38: Thermal and longitudinal cracking of composite beam CD2BR1.**

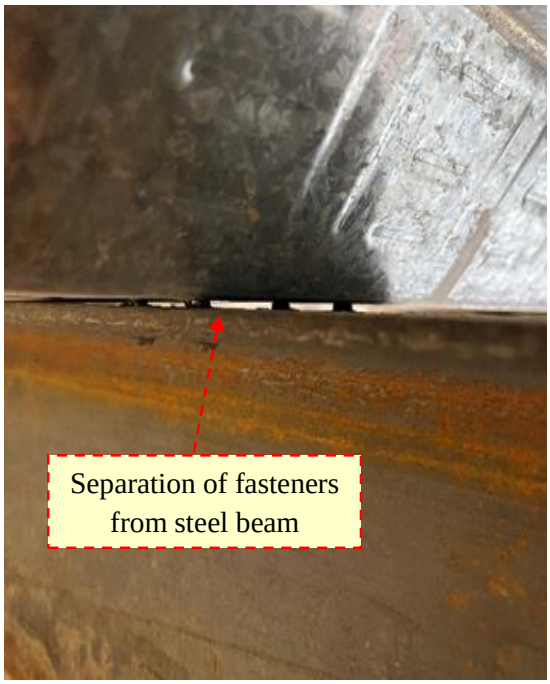


**Figure 4. 39: shear connecter failure.**


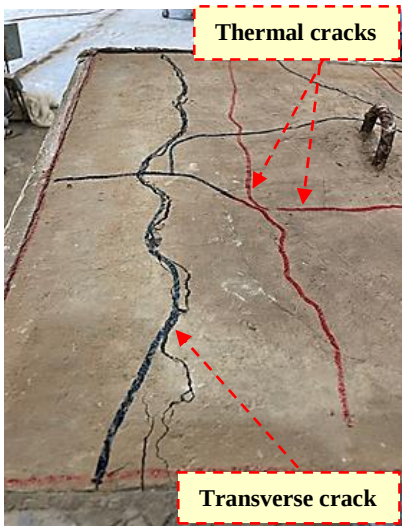


(a) (b)

**Figure 4. 40: Cracking and separation of composite slab in composite beam CD2TR2.**


**Figure 4. 41: Cracking and separation of composite slab in composite beam CD1TR2.**

### 4.6.4 Stiffness and Ductility

This study calculated the initial stiffness for the burned composite beam and compared it with the control specimen (unburned). The initial stiffness was estimated by using the secant of the force versus displacement passing through the point at which the applied force reaches 75 % of the ultimate load [88]. The overall results of the initial stiffness are shown in Figure 4.42. According to the Figure, all of the burned specimens demonstrated a decrease in initial stiffness compared to the control (unburned) specimens. For instance, CD1BR1, CD1BR2, and CD1BR3 showed reductions of 13%, 15%, and 21%, respectively, compared to the unburned specimen (CD1). On the other hand, CD2BR1, CD2BR2, and CD2BR3 showed much more significant reductions, with initial stiffness decreasing by 45%, 69%, and 81%, respectively, compared to the unburned specimen (CD2).

Interestingly, the reduction in initial stiffness for specimens that were heated from the top of the concrete slab (CD1TR2 and CD2TR2) was less severe. Specifically, CD1TR2 and CD2TR2 showed initial stiffness reductions of approximately 9% and 27%, respectively, compared to their respective unburned specimens (CD1 and CD2).

Regarding ductility, the ductility index was defined as the ratio of ultimate displacement to yielding displacement [89]. The ultimate displacement ($\Delta u$) corresponding to the ultimate load. On the other hand ($\Delta y$) was calculated based on Park [90]. Based on Figure 4.42, it is evident that an increase in temperature led to a greater reduction in ductility for the burned composite beam specimens in both corrugated plate directions. In particular, the ductility index of the burned specimens (CD1BR1, CD1BR2, and CD1BR3) was 35%, 55%, and 58% less than the control specimen (CD1), respectively. Moreover, the reduction in ductility for specimens CD2BR1, CD2BR2, and CD2BR3 was significantly higher, with a reduction of approximately 192%, 229%, and 250% compared to the control specimen (CD2), respectively. This decrease in ductility was attributed to the sudden failure of the burned specimens' overlays by shear connectors due to high stress concentrations before they could reach their full capacity.

On other hand, the reduction in ductility for burned specimens with transverse corrugated observe more than that with parallel corrugated steel plate, this due to transverse corrugate plate might have been more effect to fire damage due to their orientation. Transverse sheets might have allowed the fire to penetrate more easily into the internal structure of the composite slab, causing more extensive damage and reducing the ductility to a greater extent.

It is worth noting that the reduction in ductility for specimen CD1TR2 was not as significant, only about 1%. However, for specimen CD2TR2, the reduction in ductility was approximately 15%.

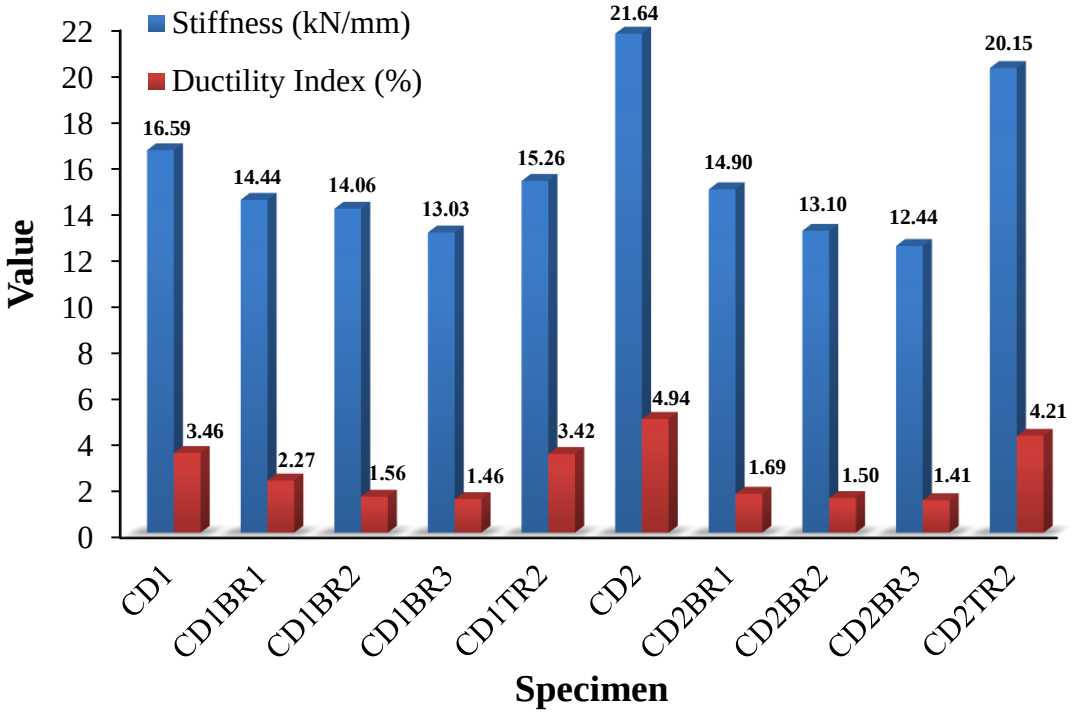


**Figure 4. 42: Stiffness and Ductility index response for all the tested specimens.**

### 4.6.5 Energy Absorption Capacity

In this study, the energy absorption capacity is determined by analyzing the load-deflection curve and calculating the integral of the curve [82]. The data presented in Figure 4.43 indicates that an increase in temperature leads to a decrease in the energy absorption capacity of the composite beam specimen. Furthermore, the direction of the temperature exposure appears to have a significant impact on this reduction in energy absorption capacity.

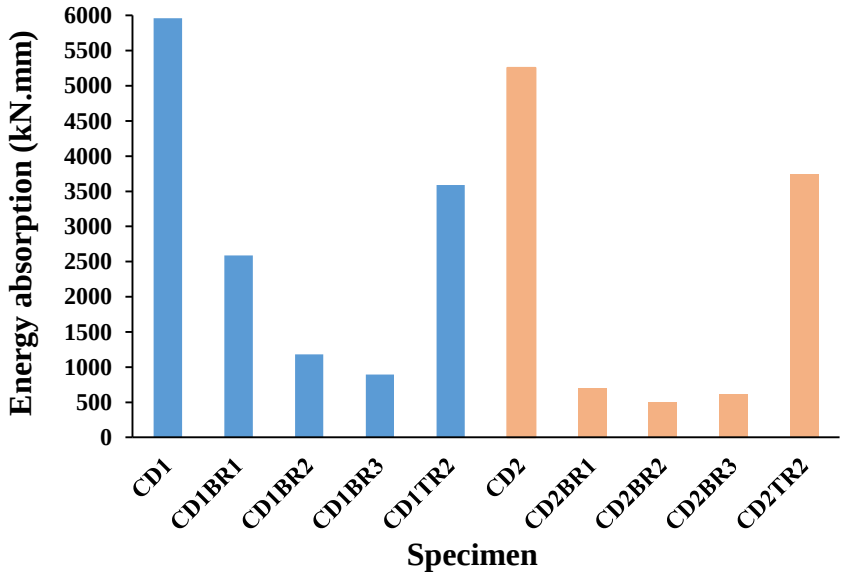


**Figure 4. 43: The results of energy absorption capacity for all tested specimens.**

Specifically, when the specimen is exposed to fire from the steel beam and with parallel corrugated steel plate (CD1BR1, CD1BR2, and CD1BR3), the reduction in energy absorption capacity is about 1.3, 4, and 5.6 times that of the specimen CD1. Similarly, for the specimens exposed to fire from the steel beam but with transverse corrugated steel plate (CD2BR1, CD2BR2, and CD2BR3), the reduction in energy absorption capacity is about 6.6, 9.6, and 7.5 times that of the specimen CD2. On the other hand, when the fire is exposed from the slab (CD1TR2 and CD2TR2), the reduction in energy absorption capacity is about 13% and 27% compared to CD1 and CD2, respectively. Therefore, the specimen CD2TR2 has about 15% more energy absorption capacity than CD1TR2.

At ambient temperature, the specimen with parallel corrugated steel plate (CD1) has an energy absorption capacity that is about 13% higher than that of the specimen with transverse corrugated steel plate (CD2). Additionally, under fire exposure conditions, all specimens with parallel corrugated steel plate exhibit greater energy absorption capacity than those with transverse corrugated steel plate.

## 4.4 DIGITAL IMAGE CORRELATION METHOD

Digital Image Correlation (DIC) presents a non-destructive optical tracking method that allows for 2D measurement of relative changes in sequential images. The advantage of using DIC method is threefold; relative cheapness compared to use of strain gauges and LVDTs; high precision of measurement; and potential to obtain entire field measurement distributions. Obtaining entire field measurements allows for a clear understanding of stress localizations in testing, thereby providing invaluable failure information. Consequently, any non-conformity in material or loading is high visible in this form of analysis.

For all specimens, DIC was utilized during the testing to measure the displacement and strain. In order to perform accurate DIC, a regular pattern of dots was painted onto each steel beam and on the end plate of the composite slab. Camera, which has a maximum resolution of 12 megapixels was used for imaging as shown in Figure 4.44. The DIC analysis required a series of photos to be taken from each video of the beam being tested, with a device used for taking the image from video every 10 kN from the applied load. Each photo was then loaded as a “Deformation Image” into the 2D image correlation program GOM Correlate [83], and the relative movement of each painted point to every other one was calculated.

By defining the target surface as the front face of the beam only, displacement and strain distributions in both the x and y axes were determined. By specific placement of “Extensometer” above and below the interface (at (top, middle, bottom) of slab and also at (top, middle, bottom) for the beam, these values were tracked with respect to the increase in load and exported for analysis of strain. As a means of validation of DIC analysis in this study, the results obtained were compared to results

obtained from experimental work. Figure 4.45 show good agreement between experimental and DIC method in load-deflection curves.

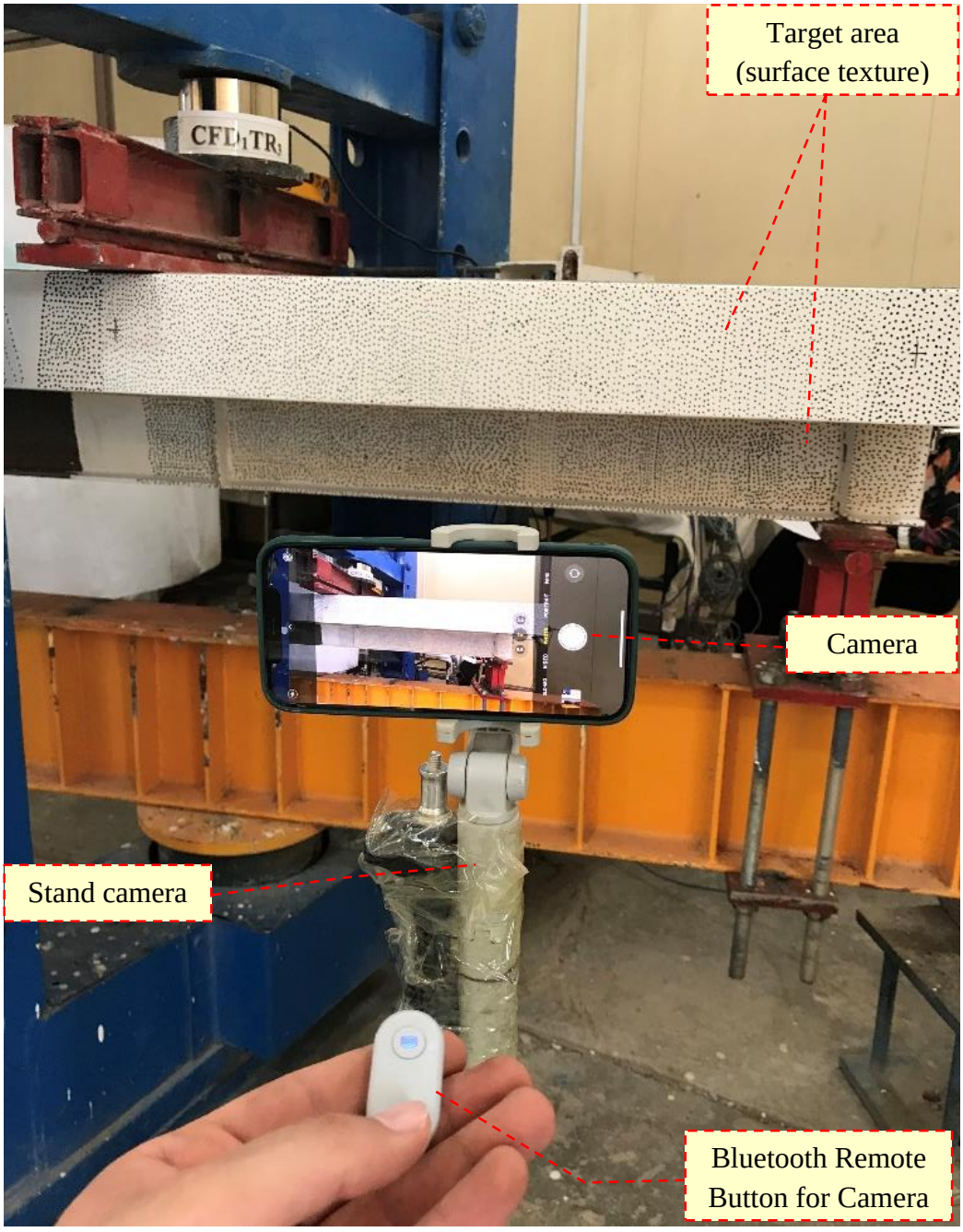


**Figure 4. 44: Digital Image Correlation method set-up.**

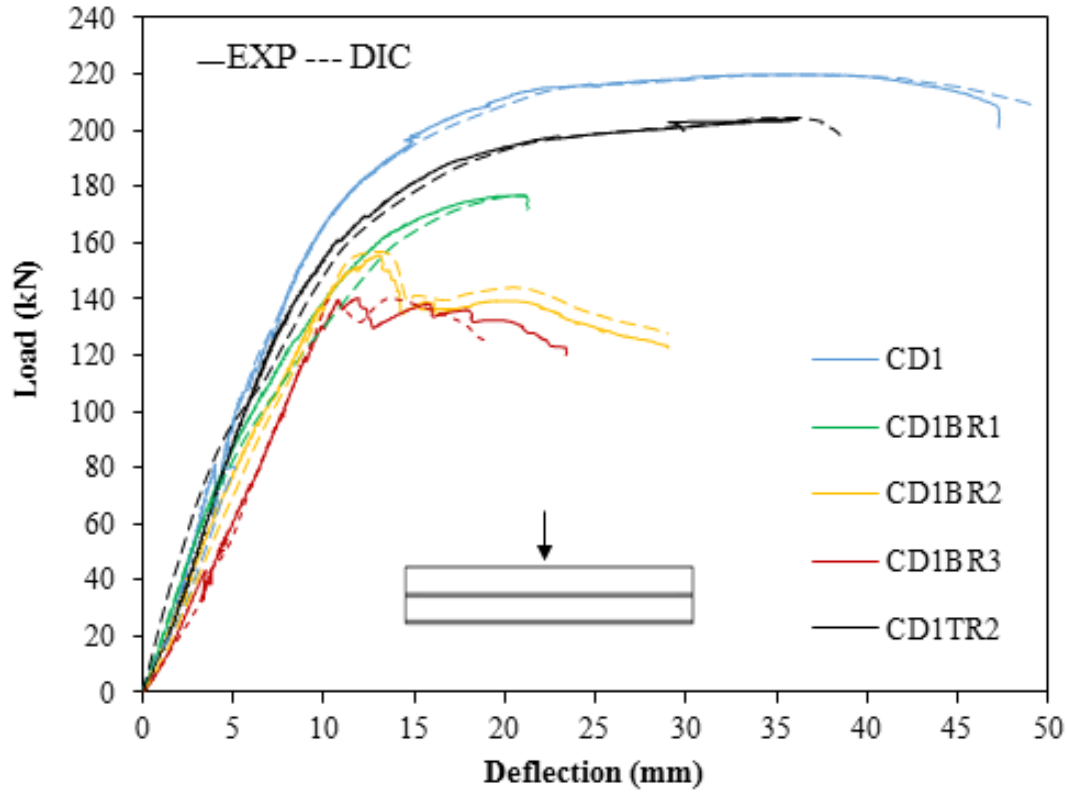


(a) Parallel corrugated plate

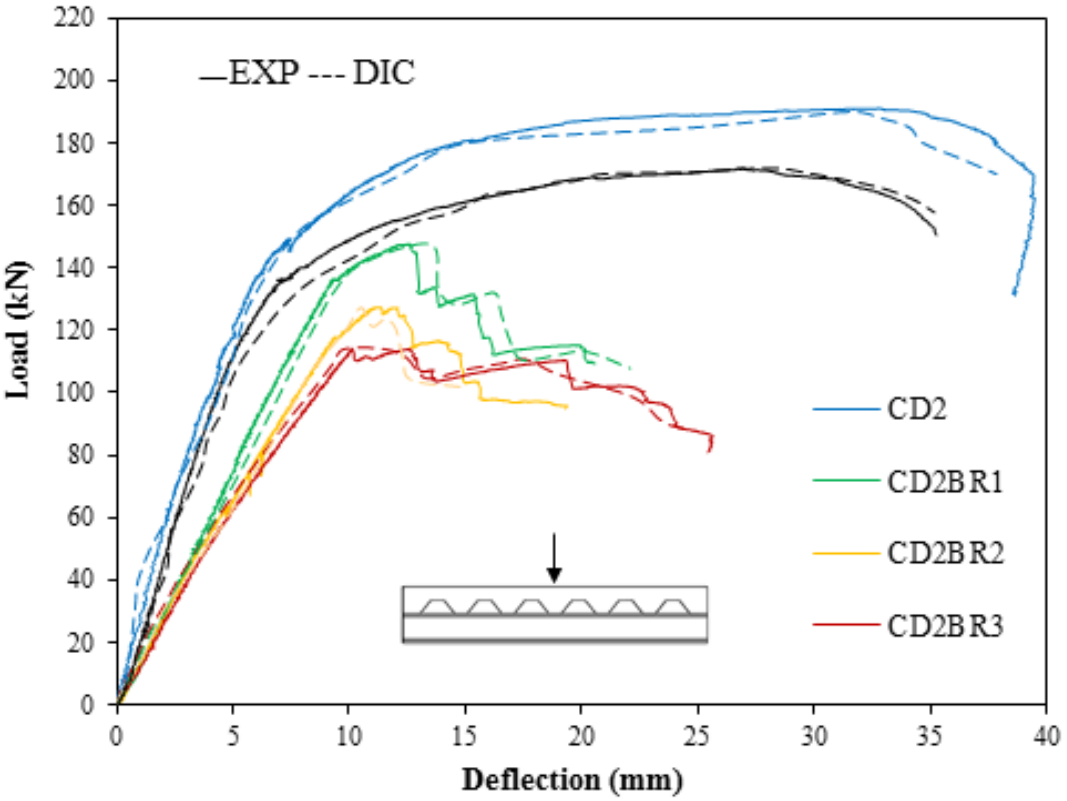


(b) Transverse corrugated plate

**Figure 4. 45**: **A Comparative Analysis of Load-Deflection Behavior: Experimental vs. DIC Methods.**

### 4.4.1 Distribution of Normal Strain

Normal strain obtained by using DIC analysis by extensometer of size (50 mm). The extensometers were placed at mid-span on both the concrete deck and steel beams. The measured results of normal strains along the height of the cross section with respect to load increments for each tested beam are presented in Figures 4.46 and 4.47.

The results of the normal strains are plotted against the position of the recorded strain in the vertical direction (depth) of the mid-span section. Each line in the graphs of strain represents a stage of loading as listed in the legend of the graphs.

Referring to the plotted results of the normal strain indicates that there is a jump in the values of the recorded normal strains at the depth of (140 mm) measured from the top face of the slab. This depth represents the position of contact surface between composite slab and steel beam. The reason of this jump is the horizontal slip occurred between slab and beam, in other word the partial interaction between the composite components. Thus, the amount of that jump in the values of normal strains depends on the amount of the horizontal slip. The amount of that jump increases with slip increasing and decreases with slip decreasing.

Based on the results in Figures (4-46) and (4-47), it appears that there are two sets of samples being compared: CD1BR1, CD1BR2, and CD1BR3 versus CD1, and CD2BR1, CD2BR2, and CD2BR3 versus CD2. The strains in the samples exposed to temperature are greater than those in the control samples for both sets.

The direction of corrugated steel plate does not have a significant effect on the values of strains at ambient temperature, but it does have an effect after the samples are exposed to fire. Specifically, the samples with transverse corrugated steel plate exhibit more strain than those with parallel

corrugated steel plate after being exposed to fire. This is likely due to the decrease in stiffness of the burned girders, which increases deflection and subsequently increases strains.

Finally, there appears to be a difference in strain values depending on the direction from which the samples are exposed to fire. Samples exposed to fire from the top of the concrete slab exhibit smaller differences in strain values compared to those exposed to fire from the bottom of the steel beam. The reason for this difference is unclear based on the given information.

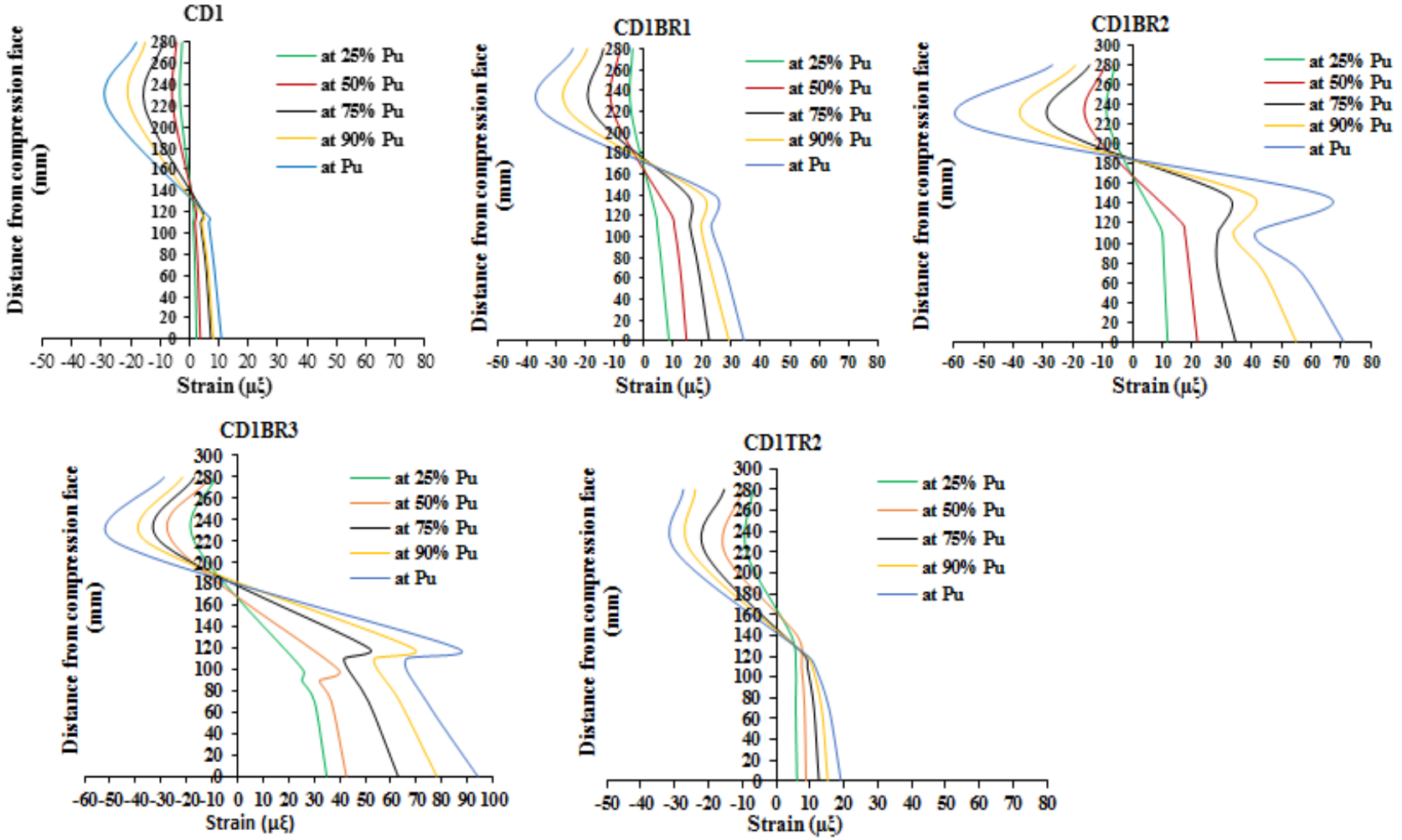


**Figure (4-46): Normal Strain at Mid-Span Section for composite beam with parallel corrugated steel plate.**

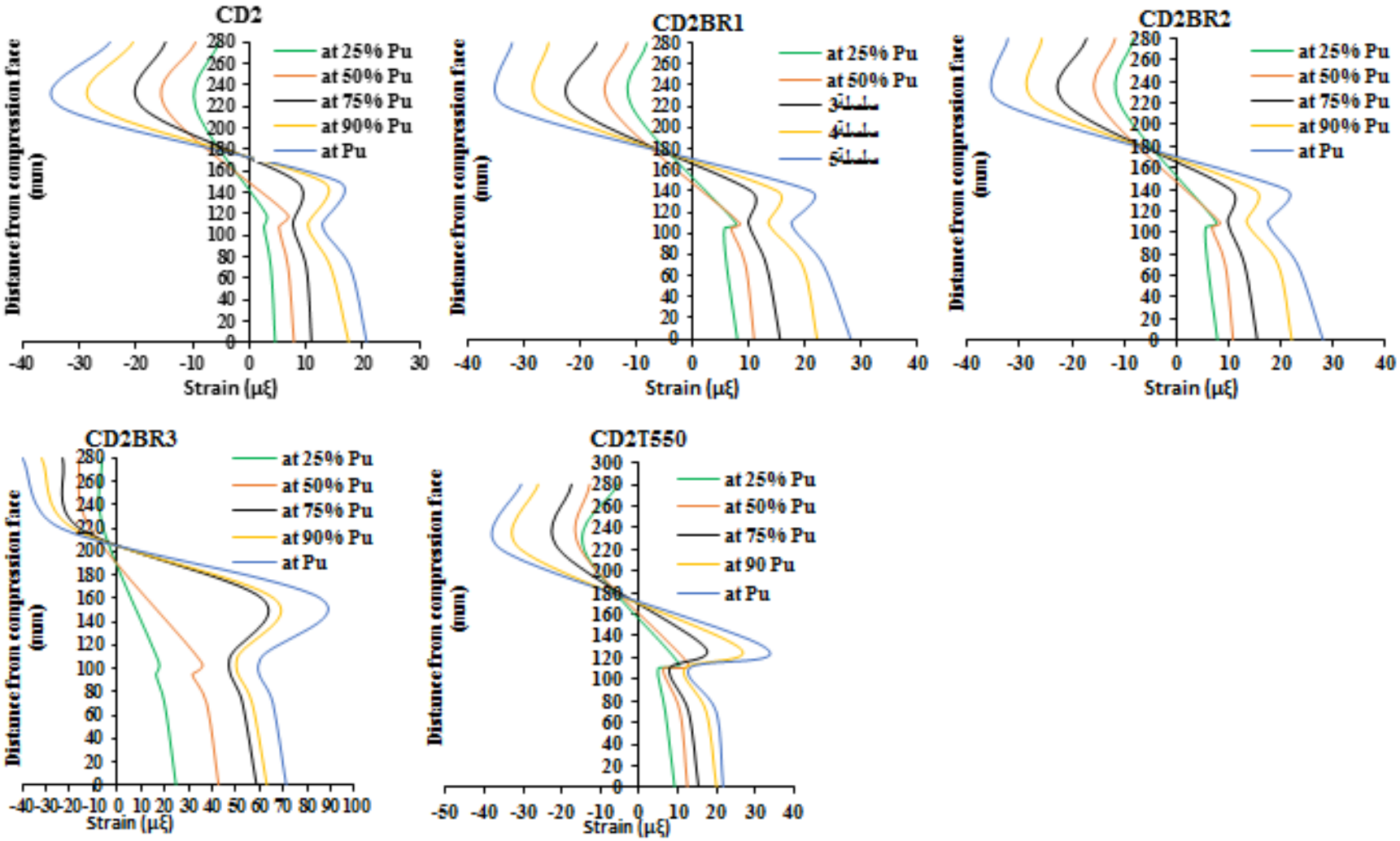


**Figure (4-47): Normal Strain at Mid-Span Section for composite beam with transverse corrugated steel plate.**

# CHAPTER FIVE
# NUMERICAL ANALYSIS BY FINITE ELEMENT

## 5.1 INTRODUCTION

The primary goal of this chapter is to validate the current nonlinear finite element model used to investigate the behavior and ultimate load capacity of composite beams connected by X-HVB shear connectors with and without exposure to fire flame, the orientation of the profiled steel plate (parallel or transverse to the beam's length), and fire exposure direction (either from the slab surface or from the bottom of the steel beam). Numerical analyses are performed using the ABAQUS Standard/Explicit 2017 finite element model to establish the validity and degree of accuracy of the adopted analytical finite element model and to compare the results with the experimental results shown in Chapter 4.

## 5.2 FINITE ELEMENT MODELING

All specimens were modeled to investigate the strength, deflection, and behavior of composite steel beams under both fire-exposed and non-exposed conditions. In the modeling process, the concrete slab, steel beam, corrugated steel plate, and X-HVB shear connectors, stiffeners, and plates were represented using an 8-node linear brick element with reduced integration and hourglass control (C3D8R) for specimens at ambient temperature, while using an 8-node thermally coupled brick, trilinear displacement and temperature, reduced integration, hourglass control (C3D8RT) for specimens exposed to fire. The reinforcement was modeled using a three-dimensional two-node truss element (T3D2).

Modeling the adopted composite steel-concrete beam specimens with different levels of exposure to fire temperature and location requires a high degree of accuracy. These specimens consist of various components with

diverse material properties, including concrete, steel beams, reinforcement, shear connectors, bearing plates, corrugated steel plates, and cartridges. To achieve a simulation that closely simulates the real response, careful consideration must be given to the method and type of interaction among these components.

## 5.3 MATERIAL PROPERTIES

In three-dimensional finite element analysis, the performance of any structure under load is determined by the behavior of the material used to construct the member (modulus of elasticity, Poisson's ratio, and material stress-strain relationship). Composite steel-concrete beams were constructed from various materials (concrete, steel beam, shear connector, corrugated steel plates, steel plate, and reinforcing steel) that joined together to form a composite system.

Appendix **B** shows the behavior and properties of the materials used in this study at ambient temperature, and Appendix **C** explains the mechanical properties of the materials at elevated temperatures.

## 5.4 MODELING OF SPECIMENS

This section discusses the composite steel-concrete beams parts and assembly, the interactions between the elements and the load and boundary conditions used in this study.

### 5.4.1 Parts and Assembly

The specimens consisted of many parts: a concrete deck, a steel beam, corrugated steel plates, an X-HVB shear connector, cartridges, a bearing plate at support and load, reinforcing bars, and stiffeners, as shown in Figures 5.1 and 5.2. Each component is drawn separately, assembled, and merged with the other elements to form the composite beam. The assembly of parts used in modeling specimens is shown in Figures 5.3 and 5.4.

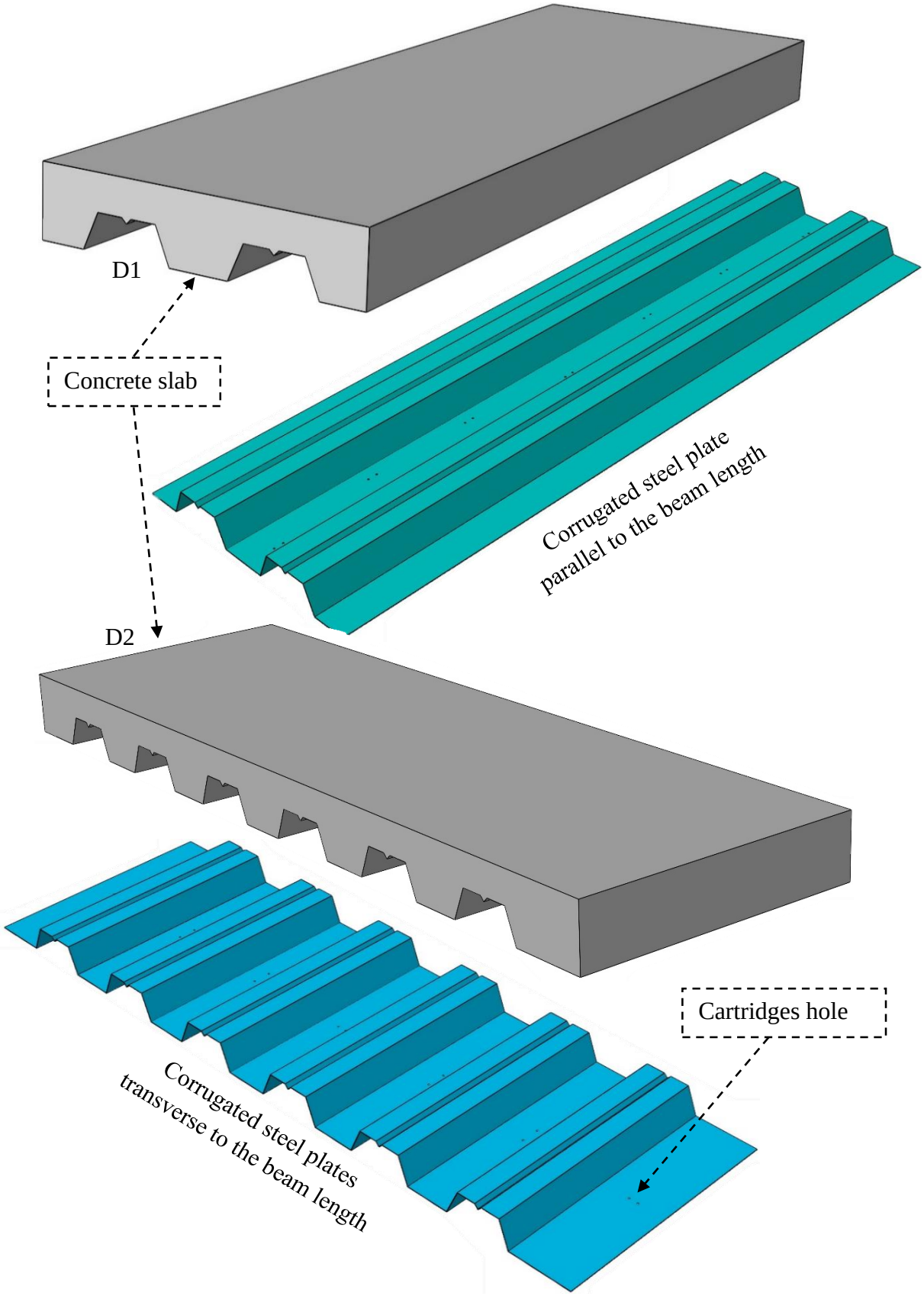


**Figure 5. 1: Concrete slab and corrugated steel plate for both direction.**

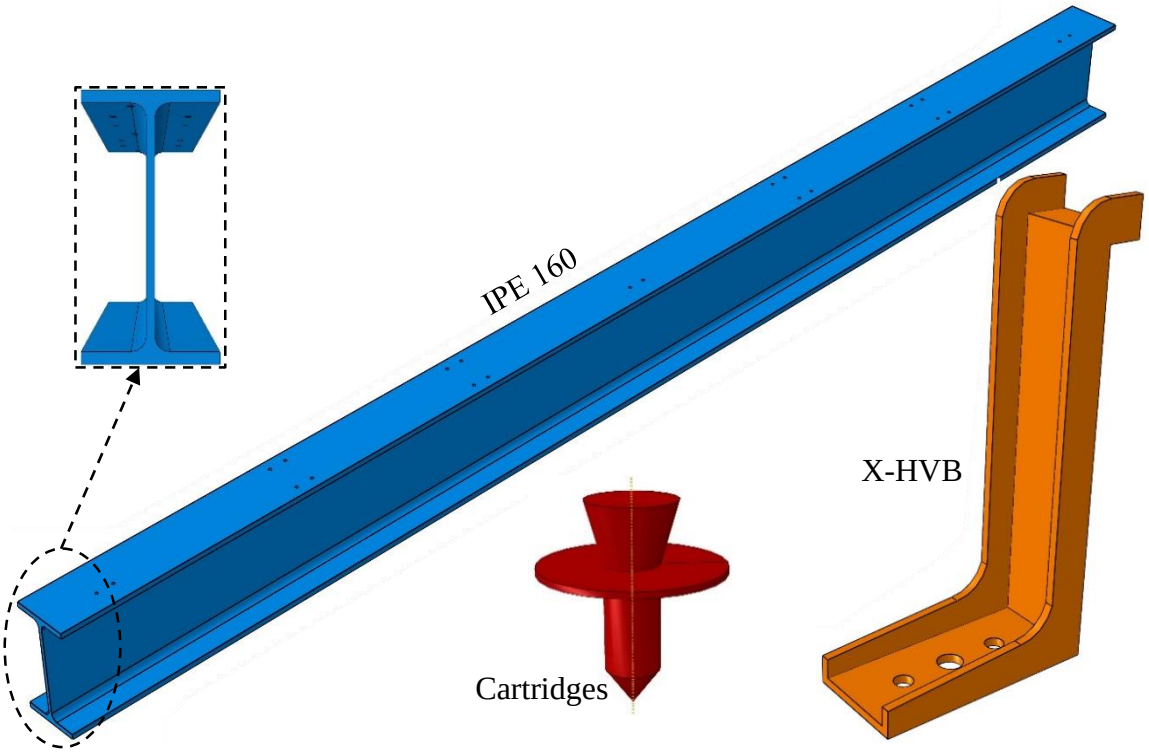


**Figure 5. 2: Parts used in the modeling of specimens.**

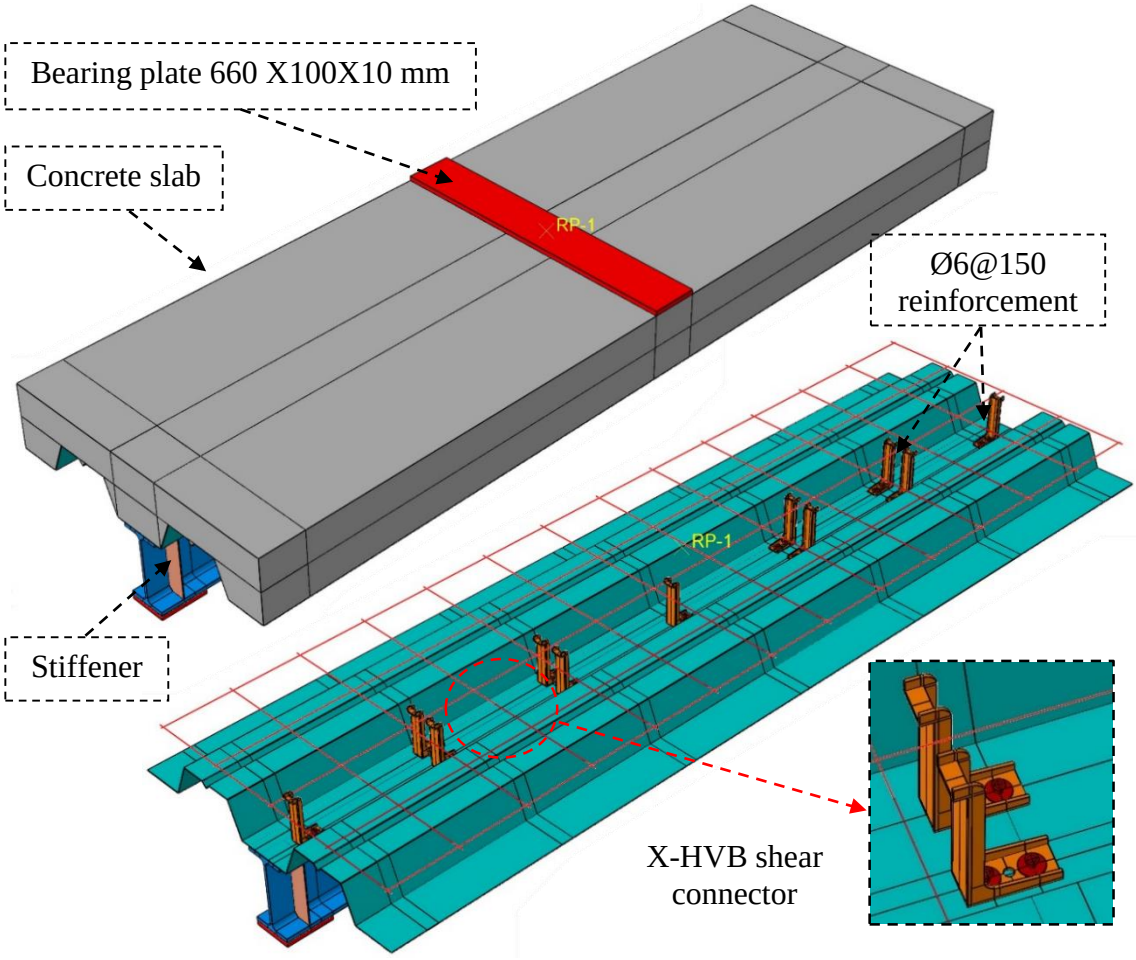


**Figure 5. 3: The Assembled Parts of Composite beam for direction 1.**

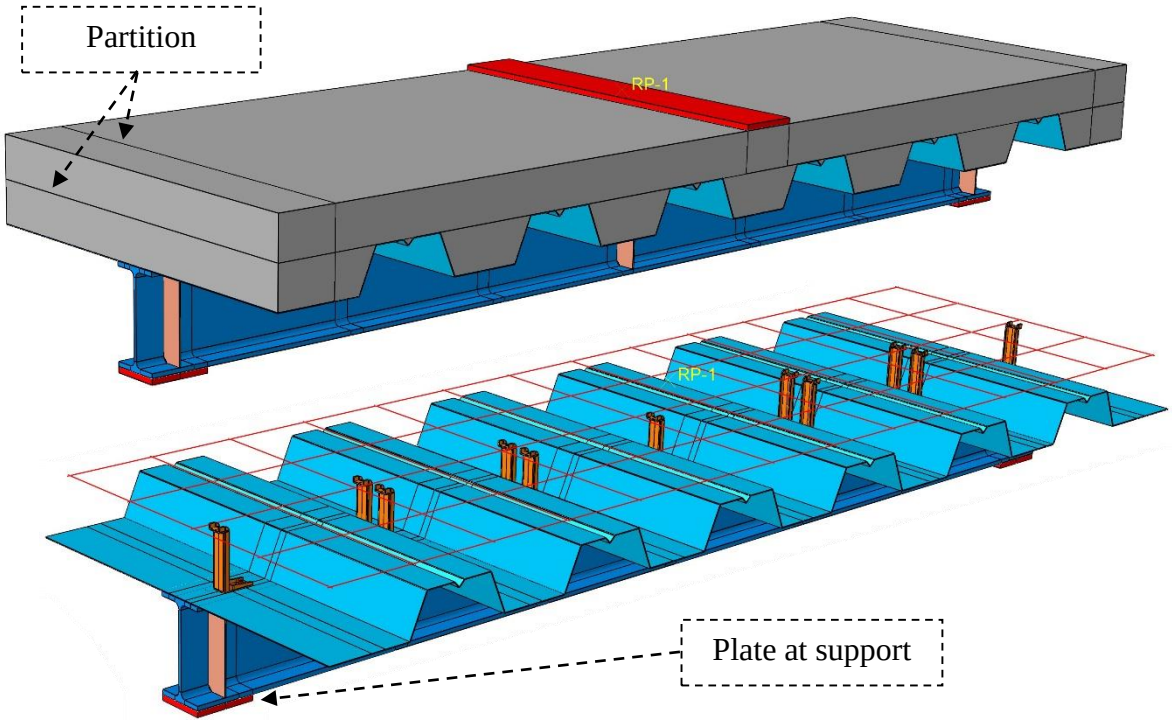


**Figure 5. 4: The Assembled parts of composite beam for direction 2.**

### 5.4.2 Finite Element Modeling Interaction

After assembling the parts, which must be connected together to operate a composite system, the surface-to-surface contact (Standard) provided by ABAQUS was used at all interfaces between the cartridge fired pin, X-HVB shear connector, the concrete slab, and the steel beam. The "hard contact" algorithm was used to depict the contacted behavior in the normal direction, allowing interaction forces to be transferred without interfering with the interaction.

To describe the tangential responses, the "penalty" algorithm was used, which could simulate the effect of friction by introducing a friction coefficient. Friction coefficient of 0.3 was set for contact surface between cartridge fired pin and steel beam flange and X-HVB shear connector. In addition, the embedded region constraint used for linked the reinforcing bars and the X-HVB shear connector with concrete slab, with the interface slip being neglected.

### 5.4.3 Loading and Boundary Conditions

The finite element model was loaded at the same locations in the experimental work for all composite beams, and the load was represented as a concentrated load applied on the mid of the bearing plate (at mid-span of composite beam). The supports were modeled similarly to the experimental work, in which a single line of nodes constrained the displacement in the directions x, y, and z for hinge support cases, and a single line of nodes constrained the displacement in the directions x and y-axis and free displacement was assumed in the direction z for case roller support. In addition, to avoid model coupling, the rotation in the direction of x-axis was constrained in both supports. Figure 5.5 shows the applied load and boundary conditions of the modeled composite beams.

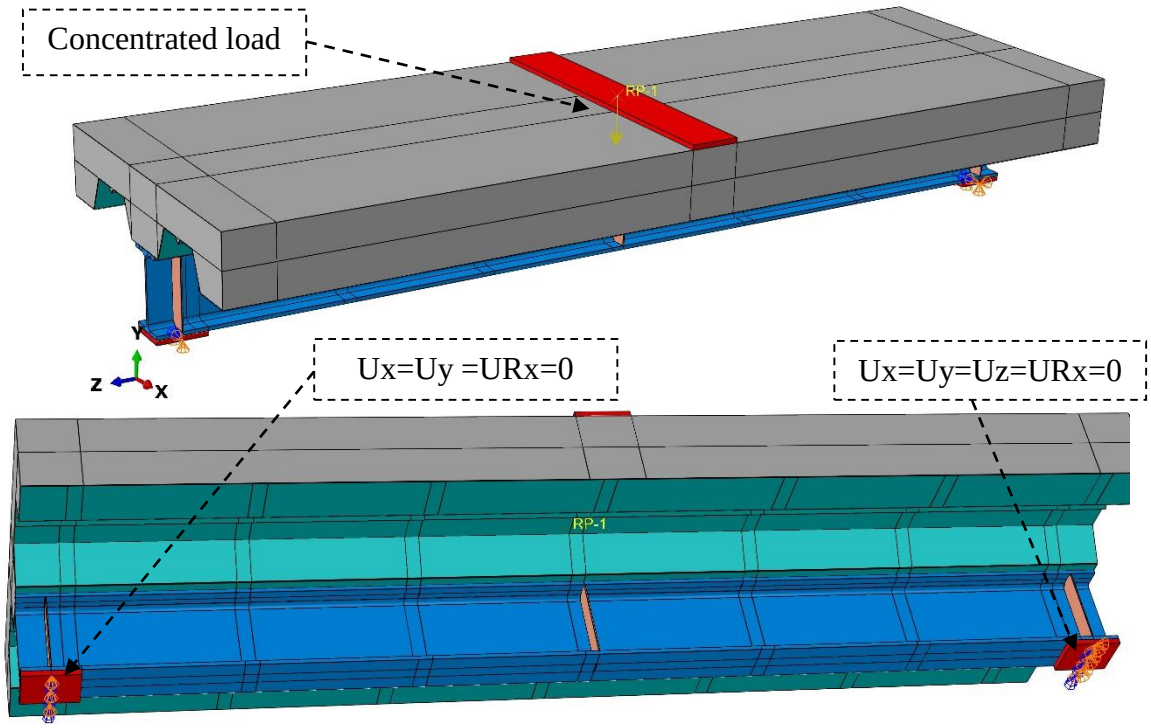


**Figure 5. 5: Boundary conditions of modeled composite beam.**

## 5.5 CONVERGENCE STUDY

The main aim of the convergence study is to select the proper mesh size of the model with a minimum number of elements and maximum convergence based on the results of the experimental test. This is practically achieved when the decrease in mesh size has a negligible effect on the results. The specimen CD1 with the same material properties were modeled with a decrease in the element sides of 40, 30, 25, 20, and 15 mm.

The deflection at the mid-span for specimen with different mesh sizes was observed at the same applied load level of 100 kN. A convergence study showed that the difference could be ignored when the mesh size decreased from 30 mm to 20 mm; therefore, the 30 mm model for beam, concrete slab, corrugated steel plates, reinforcing bar, and bearing plates was adopted for all tested specimens (see Figure 5.6). The mesh details of the composite beam model are shown in Figure 5.7. On the other hand, all of the X-HVB shear connectors and cartridges in this model have a mesh size of 5.0 mm.

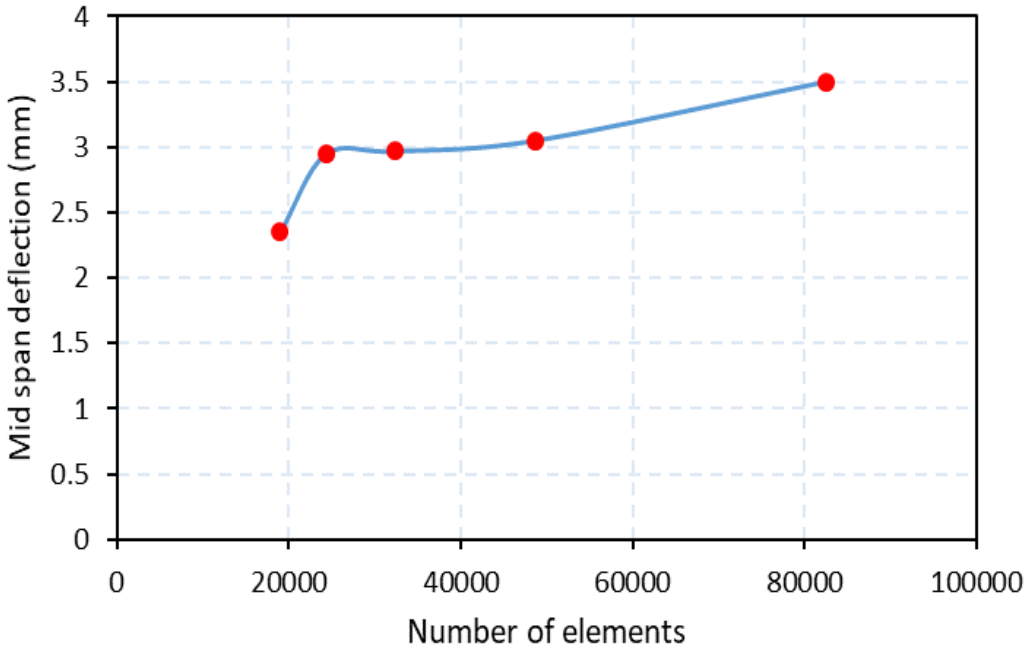


**Figure 5. 6: The convergence study results.**

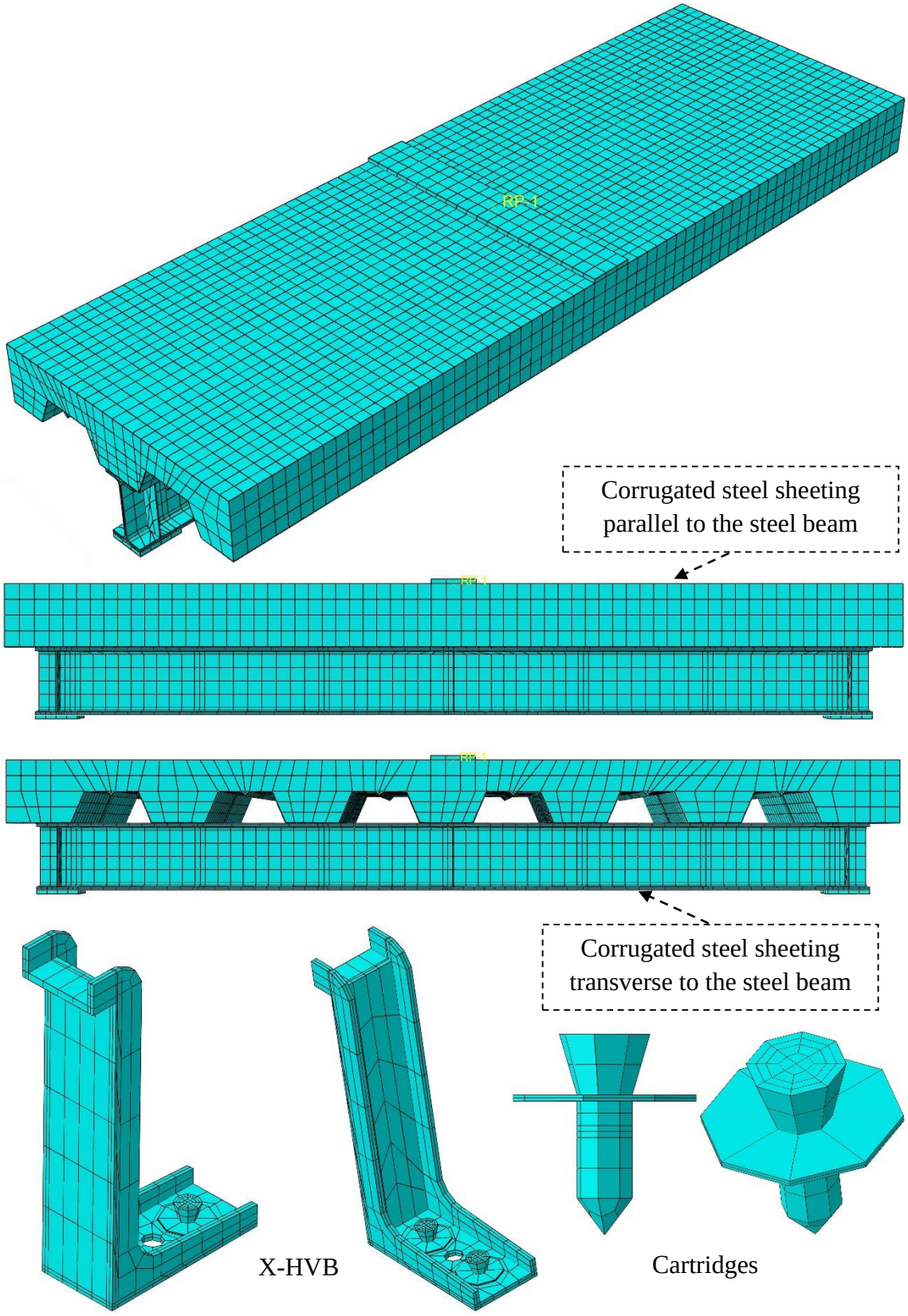


**Figure 5. 7: Finite Element Mesh of composite beam.**

## 5.6 RESULTS OF FINITE ELEMENT ANALYSIS

The experimental results for composite beam specimens with and without fire exposed are compared to the results of finite element analysis using the ABAQUS program, 2017. The ABAQUS results, including the ultimate load and deflection, were compared with the experimental results and showed good convergence. As a result, and after determining the validity of these models, expanding the experimental program by studying many parametric studies that affected the composite beam behavior.

The comparison between the ultimate load and ultimate deflection from the experimental tests and numerical models from finite element analysis of the analyzed composite joints is listed in Table 5.1. The difference in results ranged from a 2.21% to a 6.54% increase in ultimate load. While the increase in deflection for specimens ranged from 9.68% to 13.01% compared with the experimental results, except for the specimens CD1TR2 and CD2TR2 exposed to fire from the top, with a reduction in deflection of 10.77% and 8.61%, respectively.

**Table 5. 1:** Comparison of experimental and numerical results.

| **Specimens** | **Ultimate load (kN)** | | $\frac{P_{u)\ Num.} - P_{u)\ EXP.}}{P_{u)\ EXP.}}$ | **Ultimate deflection (mm)** | | $\frac{\Delta_{u)\ Num.} - \Delta_{u)\ EXP.}}{\Delta_{u)\ EXP.}}$ |
|---|---|---|---|---|---|---|
| | $P_{u)\ EXP.}$ | $P_{u)\ Num.}$ | % | $\Delta_{u)\ EXP.}$ | $\Delta_{u)\ Num.}$ | % |
| CD1 | 219.86 | 226.16 | 2.86 | 34.67 | 39.18 | 13.01 |
| CD1BR2 | 155.56 | 159.57 | 2.58 | 12.98 | 14.08 | 8.45 |
| CD1TR2 | 202.33 | 209.68 | 3.63 | 33.99 | 30.33 | -10.77 |
| CD2 | 190.98 | 195.20 | 2.21 | 32.73 | 35.90 | 9.68 |
| CD2BR2 | 127.24 | 135.56 | 6.54 | 11.22 | 12.62 | 12.48 |

| | | | | | | |
|---|---|---|---|---|---|---|
| CD2TR2 | 171.95 | 179.00 | 4.10 | 29.94 | 27.36 | -8.61 |

### 5.6.1 Specimens with Parallel Corrugated Steel Plate

In this part, the composite specimens with parallel-corrugated steel plates were tested at ambient temperature and after burned at 450 °C for a 60-minute period of exposure. The Figures 5.8, 5.10 and 5.12 compare the load-deflection curves obtained from the experimental and numerical results. In addition, the failure mode obtained by numerical analysis for all these specimens is approximately similar to the experimental failure mode.

Figures 5.9, 5.11 and 5.13 depict the von Mises equivalent stress distribution at ultimate load for the specimens CD1, CD1BR2, and CD1TR2. The colors represent stress distribution, ranging from blue for the lowest values to red for the highest allowable stress. The white color indicates regions where stresses have exceeded the permissible limits. These regions signify areas that have undergone yielding in the composite beam after failure, serving as a crucial indicator of how controlled variables impact the behavior of the specimens.

It is noted that the yield stress zone is large for specimen CD1 compared with the other two specimens exposed to fire due to the cartridges failing faster under the fire effect. Thus, the stresses imposed on the beam are less than those on the un burning specimen.

While Figure 5.14 depicts the temperature distribution in the composite specimens after 60 minutes of burning, while Figure 5.15 depicts the fire temperature distribution at different depths from the exposed faces of the composite beam at different times. These Figures show that as the time of exposure to fire increases, the temperature of the composite specimens increases towards the other face.

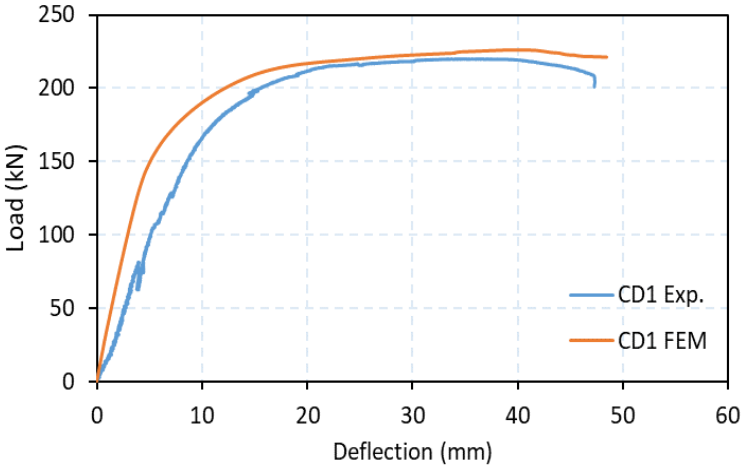


**Figure 5. 8: Load-deflection curve for specimen CD1.**

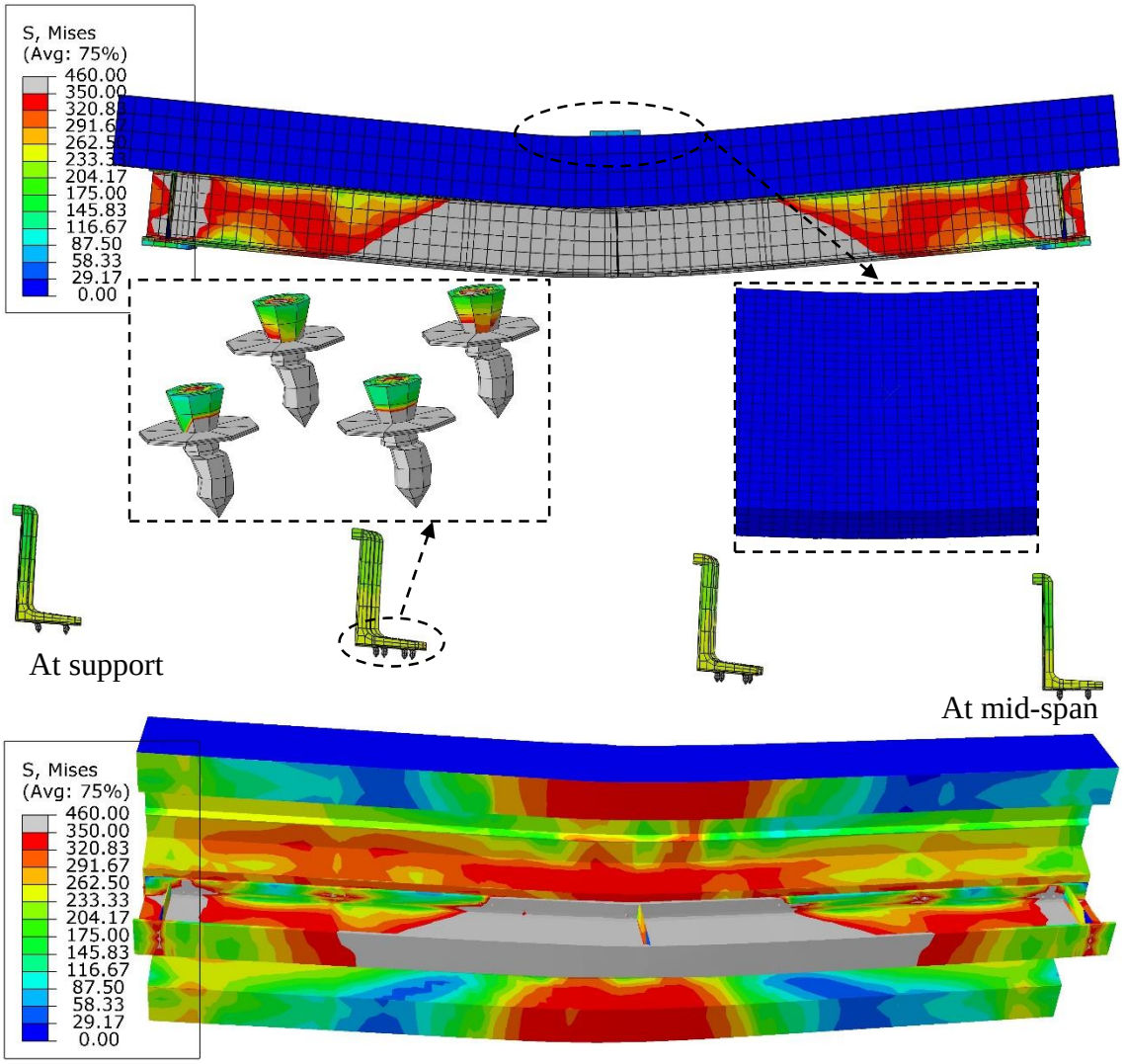


**Figure 5. 9: Von-Mises equivalent stress distribution of specimen CD1.**

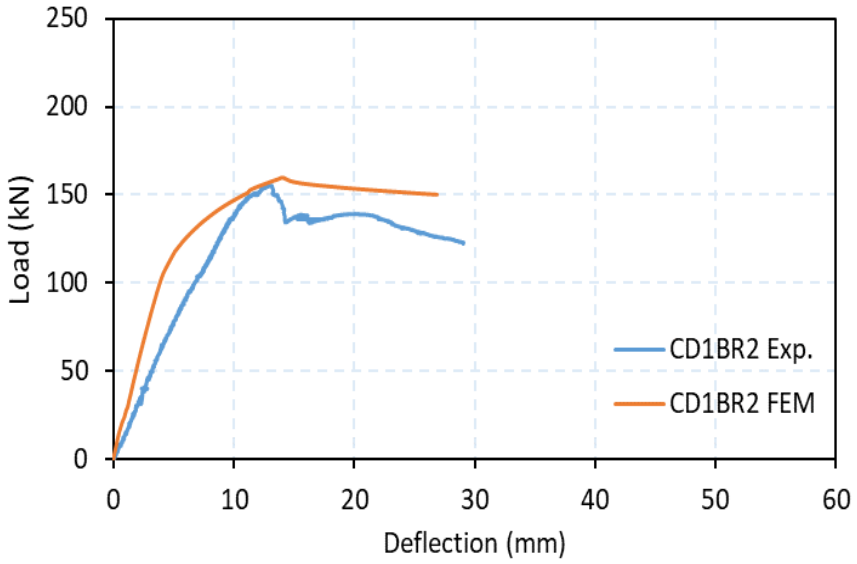


**Figure 5. 10: Load-deflection curve for specimen CD1BR1.**

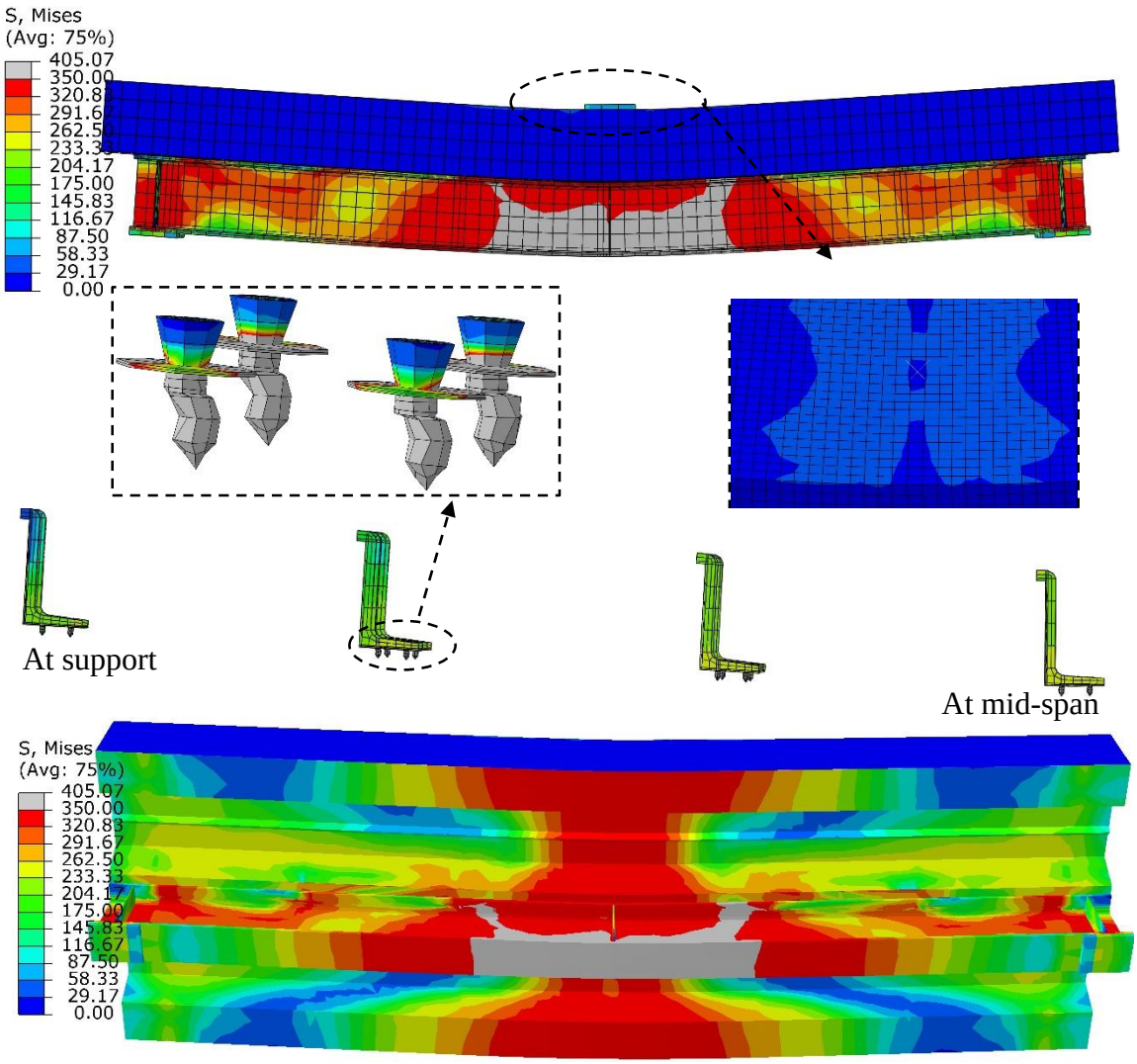


**Figure 5. 11: Von-Mises equivalent stress distribution of specimen CD1BR2.**

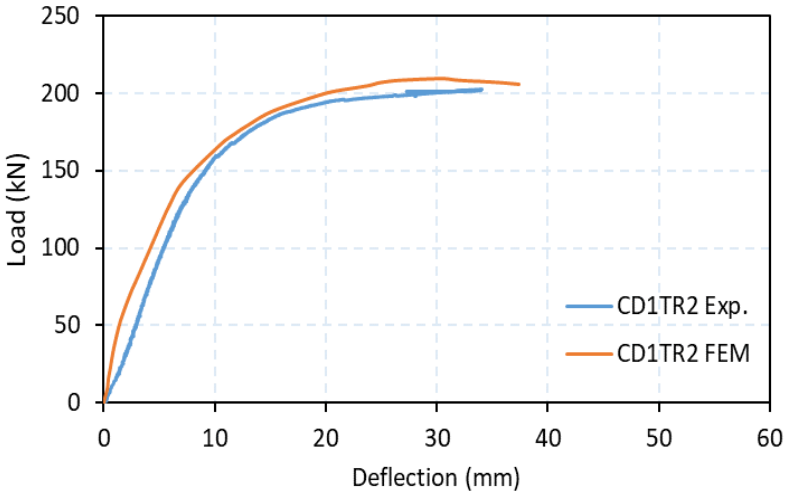


**Figure 5. 12: Load-deflection curve for specimen CD1TR1.**

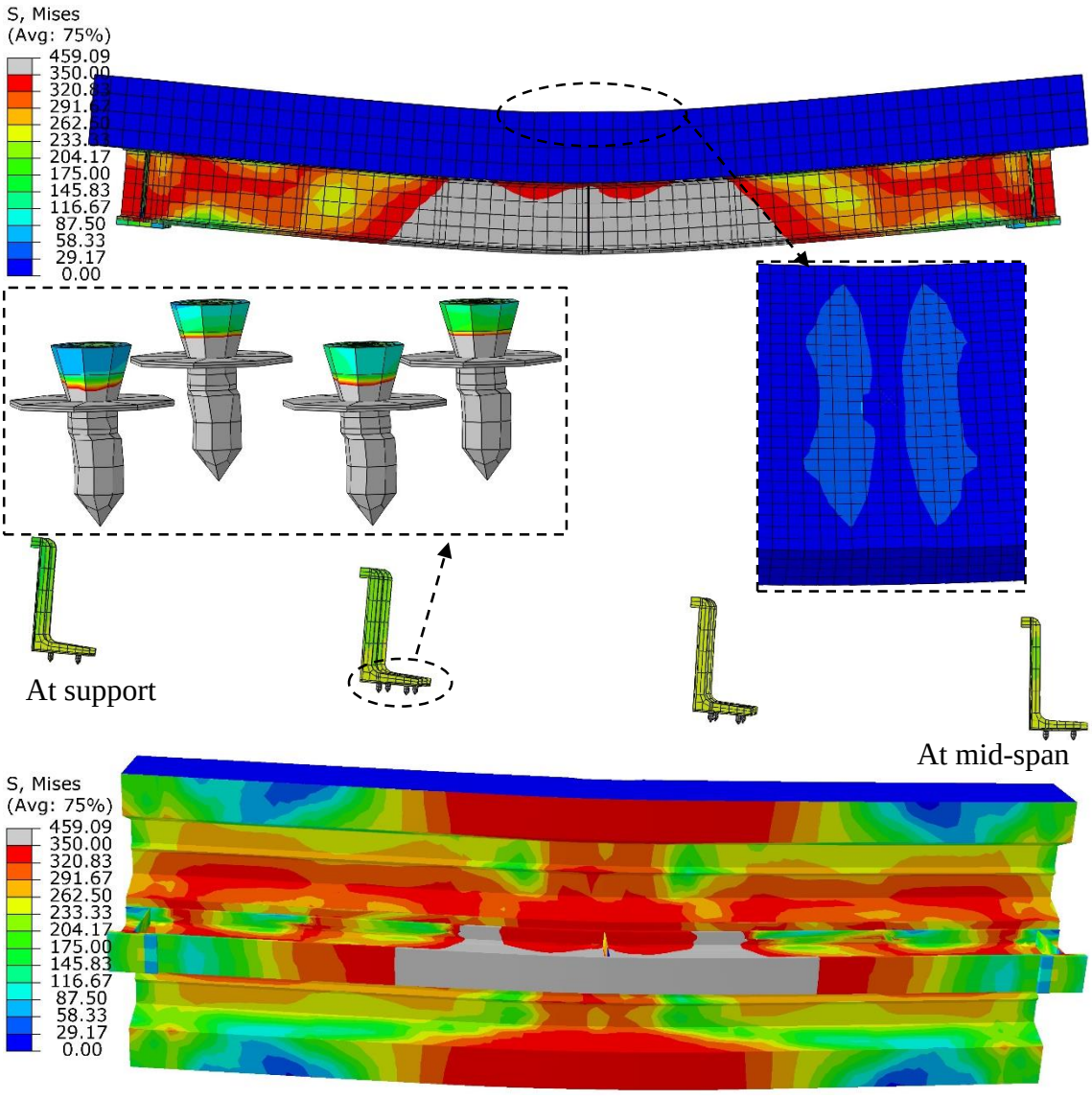


**Figure 5. 13: Von-Mises equivalent stress distribution of specimen CD1TR2.**

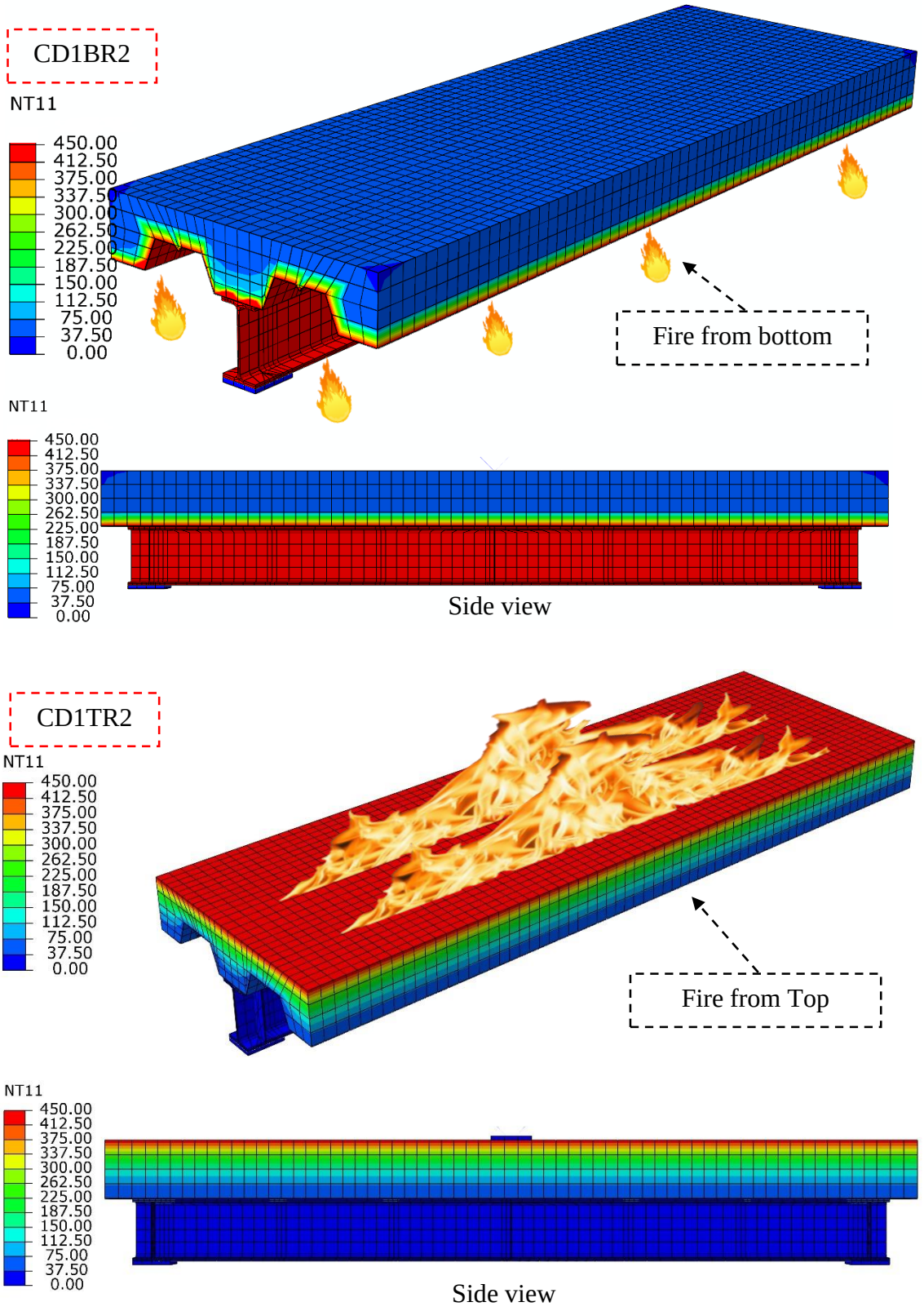


**Figure 5. 14: Temperature distribution in specimens CD1BR2 and CD1TR2 after 60-minutes of burning at 450°C.**

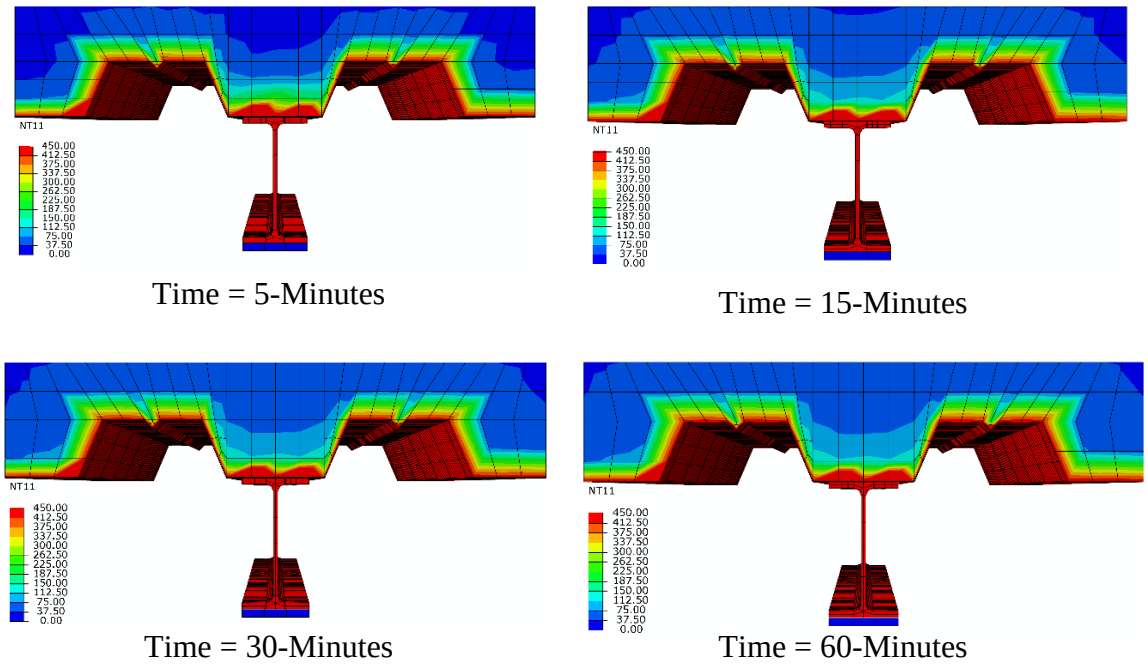


Time = 5-Minutes Time = 15-Minutes

Time = 30-Minutes Time = 60-Minutes

**(a) CD1BR2**

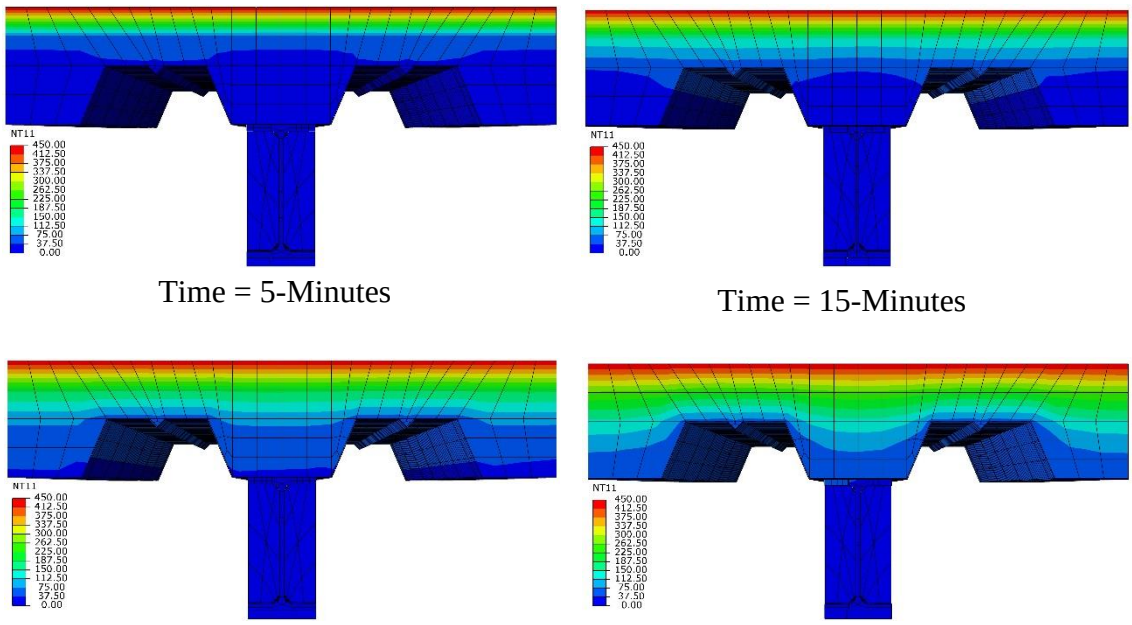


Time = 5-Minutes Time = 15-Minutes

Time = 30-Minutes Time = 60-Minutes

**(b) CD1TR2**

**Figure 5. 15: Heat transfer with time for specimens CD1BR2 and CD1TR2 burned at 450°C.**

### 5.6.2 Specimens with Transverse Corrugated Steel Plate

The composite specimens with transverse-corrugated steel plates were tested at ambient temperature and after burned at 450 °C for a 60-minute period of exposure. The Figures 5.16, 5.10 and 5.12 compare the load-deflection curves obtained from the experimental and numerical results.

The von Mises equivalent stress distribution at ultimate load for the specimens CD2, CD2BR2, and CD2TR2 are shown in Figures 5.17,5.19 and 5.21, in these Figures, the color gradient, as previously explained in 5.6.1.

The temperature distribution in the composite specimens after 60 minutes of burning is shown in Figure 5.22 and the Figure 5.23 depicts the fire temperature distribution at different depths from the exposed faces of the composite beam at different times. These figures show that as the time of exposure to fire increases, the temperature of the composite specimens increases towards the other face.

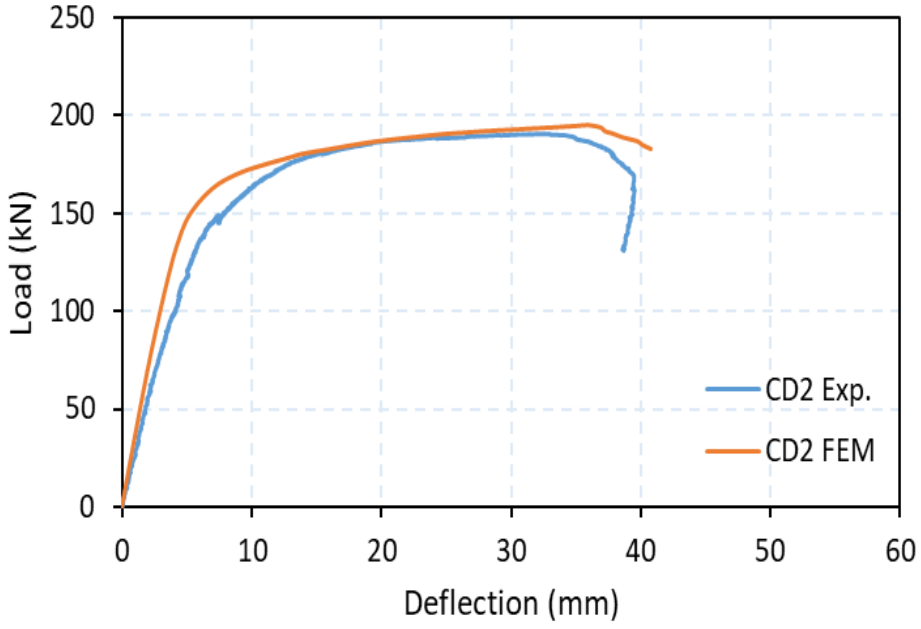


**Figure 5. 16: Load-deflection curve for specimen CD2.**

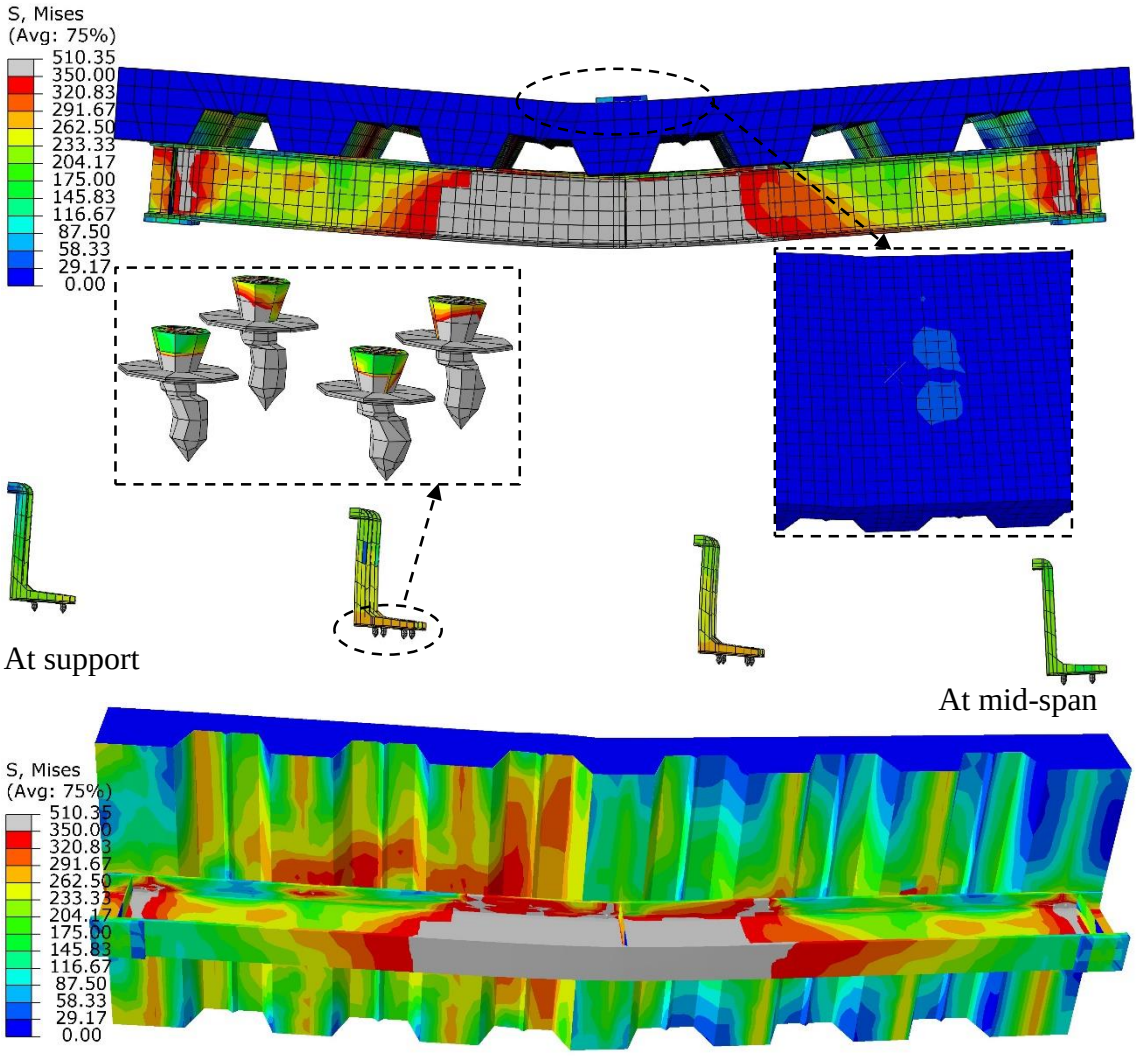


**Figure 5. 17: Von-Mises equivalent stress distribution of specimen CD2.**

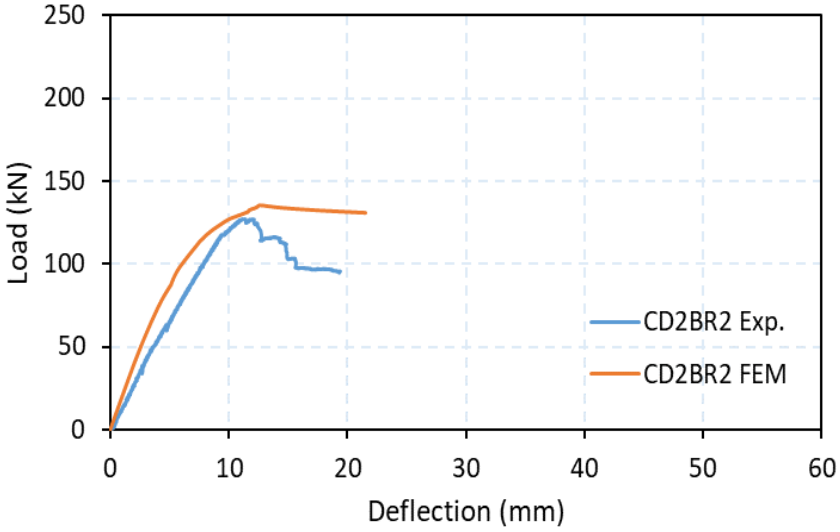


**Figure 5. 18 : Load-deflection curve for specimen CD2BR2.**

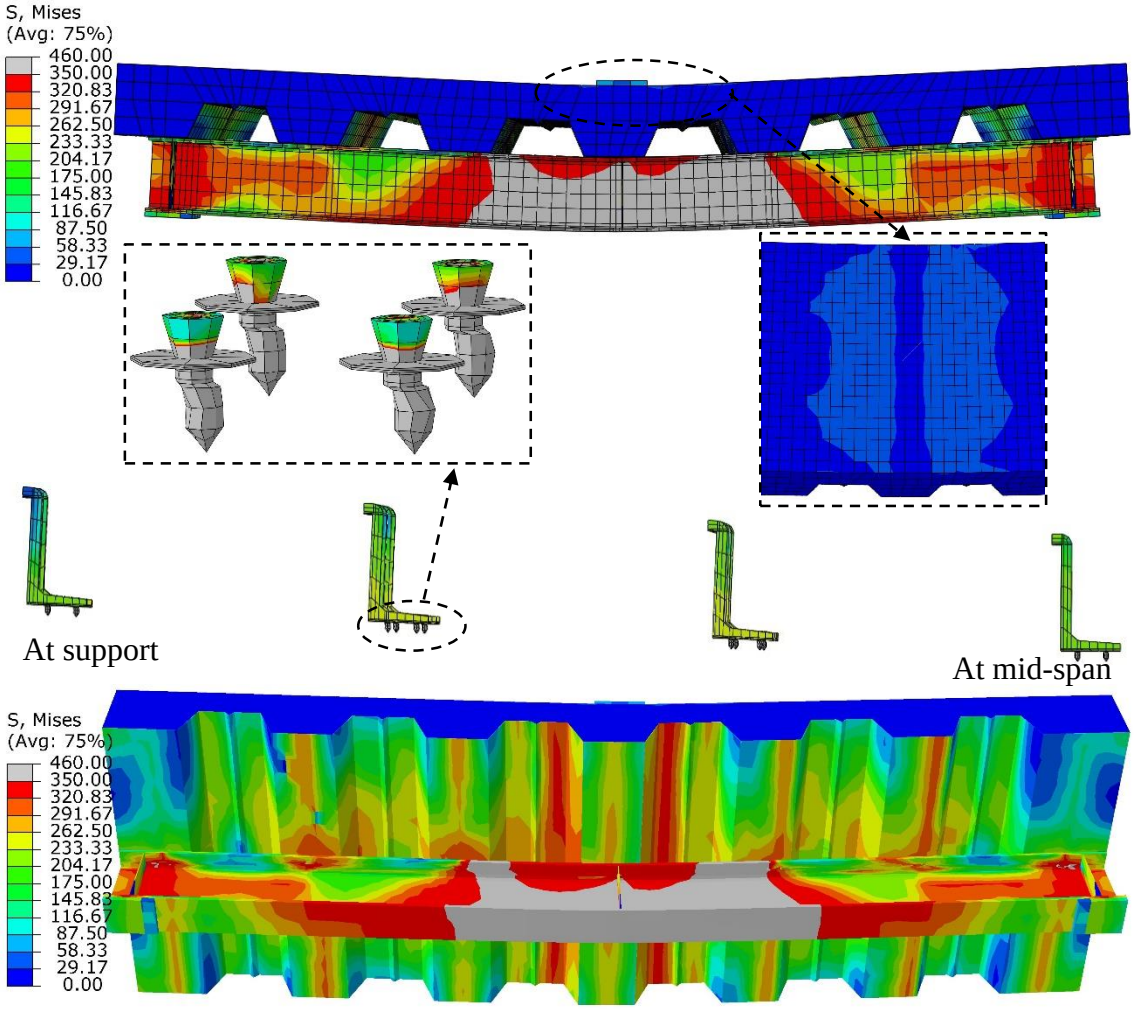


**Figure 5. 19: Von-Mises equivalent stress distribution of specimen CD2BR2.**

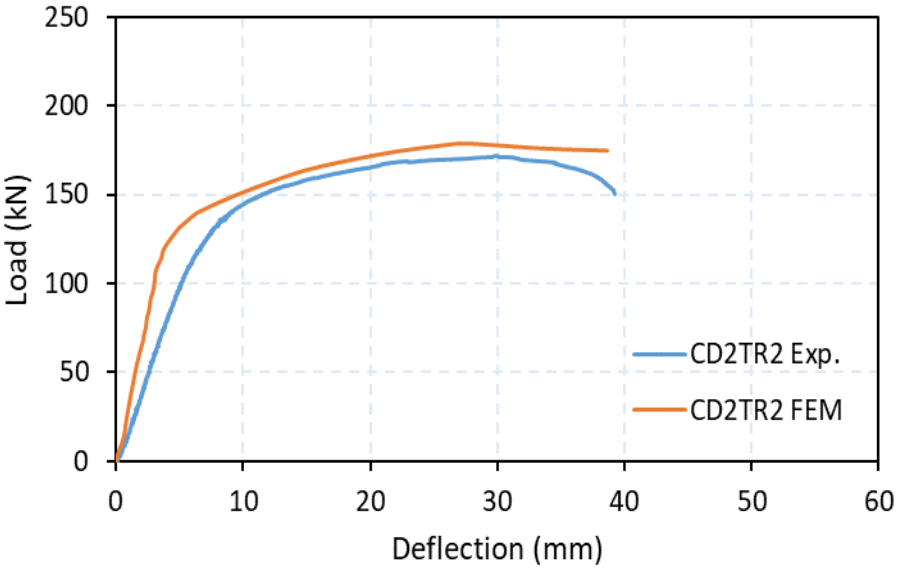


**Figure 5. 20: Load-deflection curve for specimen CD2TR2.**

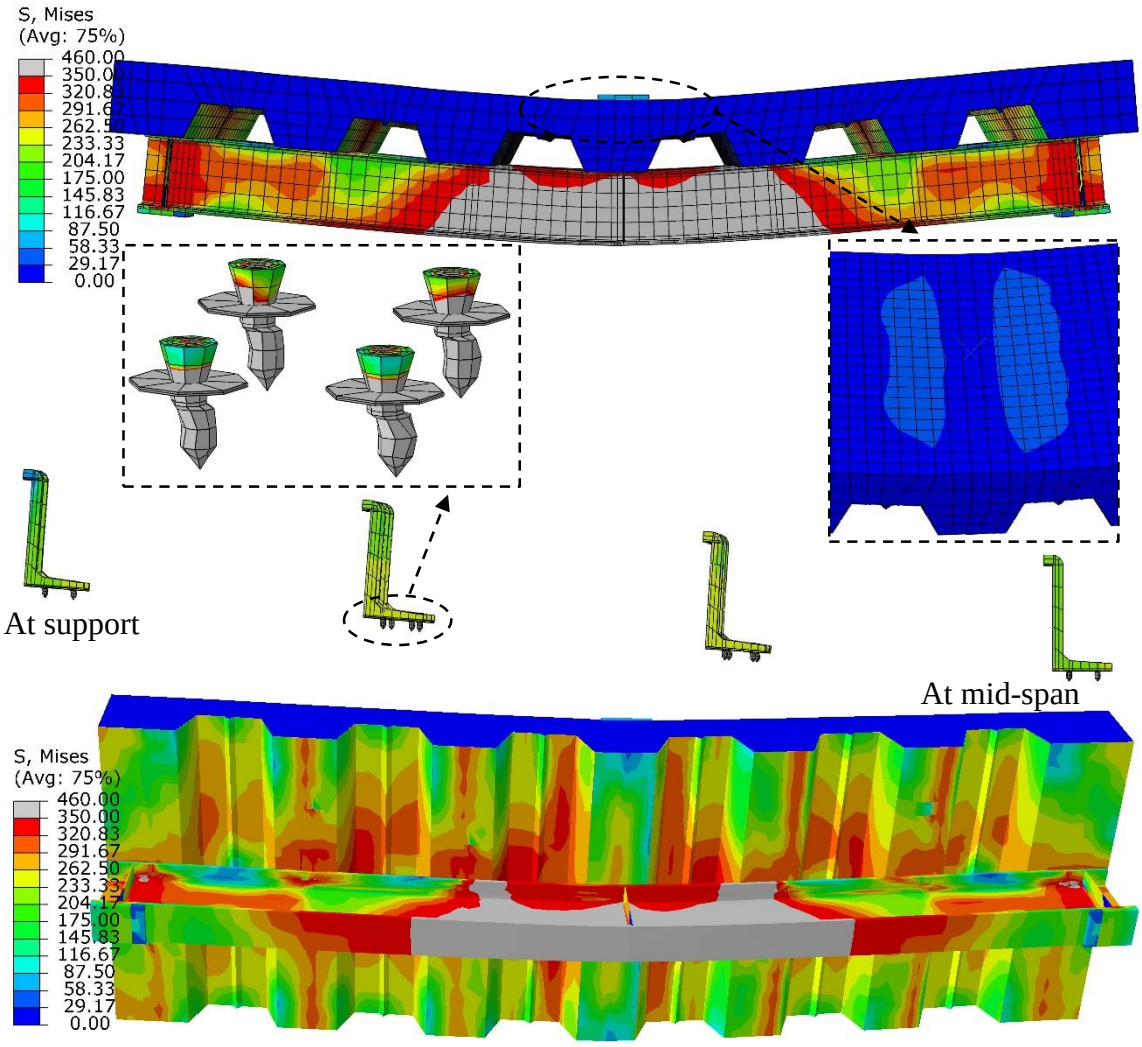


**Figure 5. 21: Von-Mises equivalent stress distribution of specimen CD2TR2.**

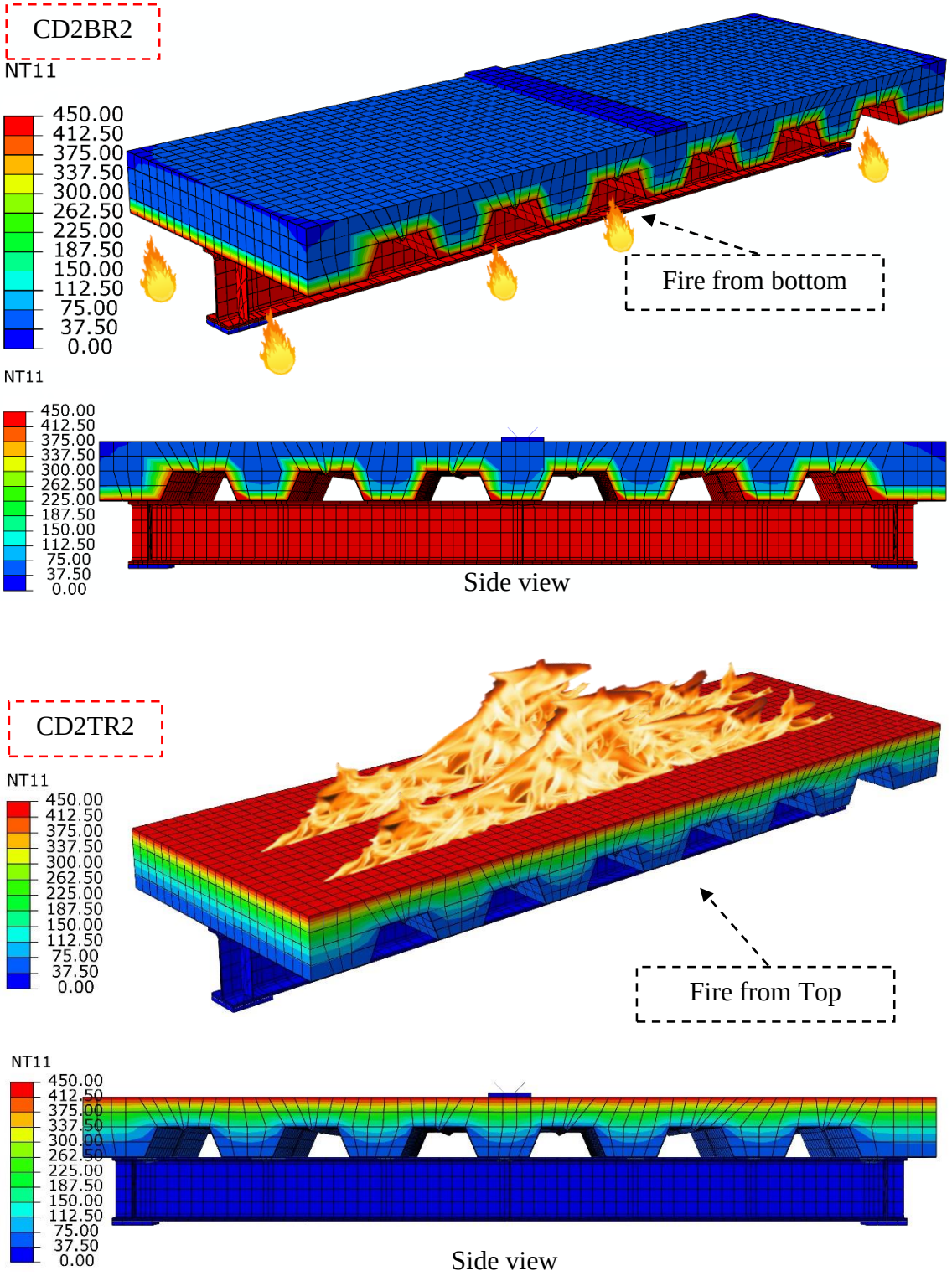


**Figure 5. 22: Temperature distribution in specimens CD1BR2 and CD1TR2 after 60-minutes of burning at 450°C.**

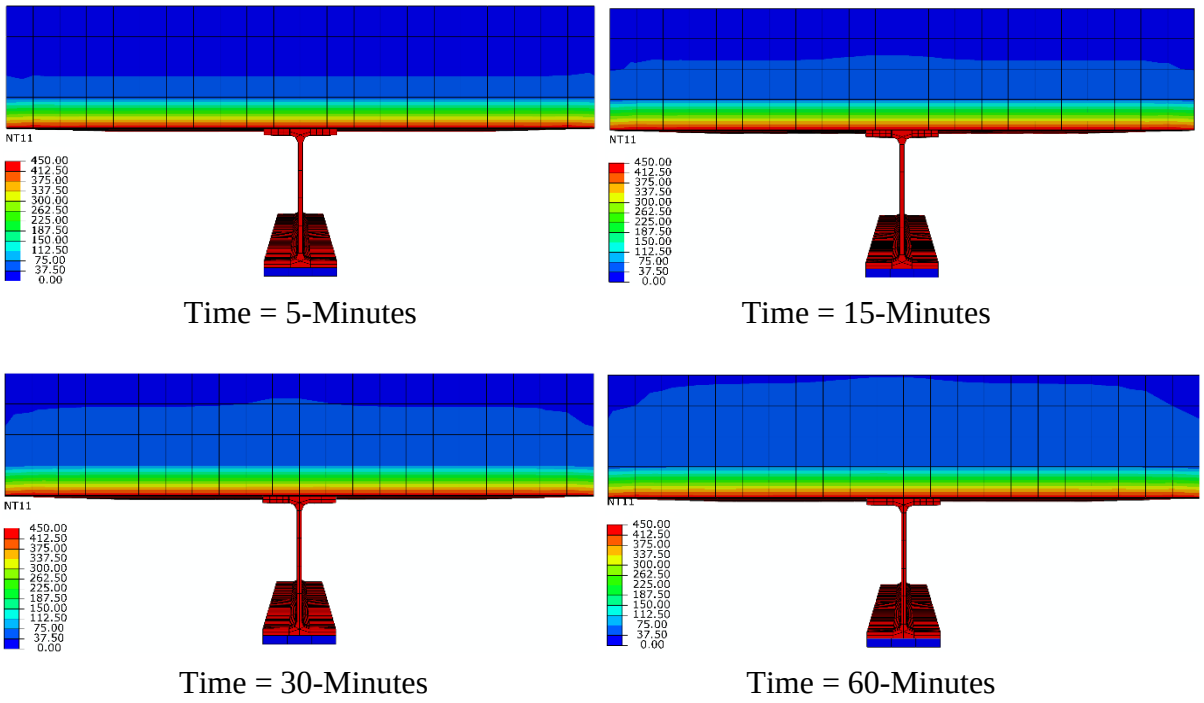


Time = 5-Minutes Time = 15-Minutes

Time = 30-Minutes Time = 60-Minutes

(a) CD2BR2

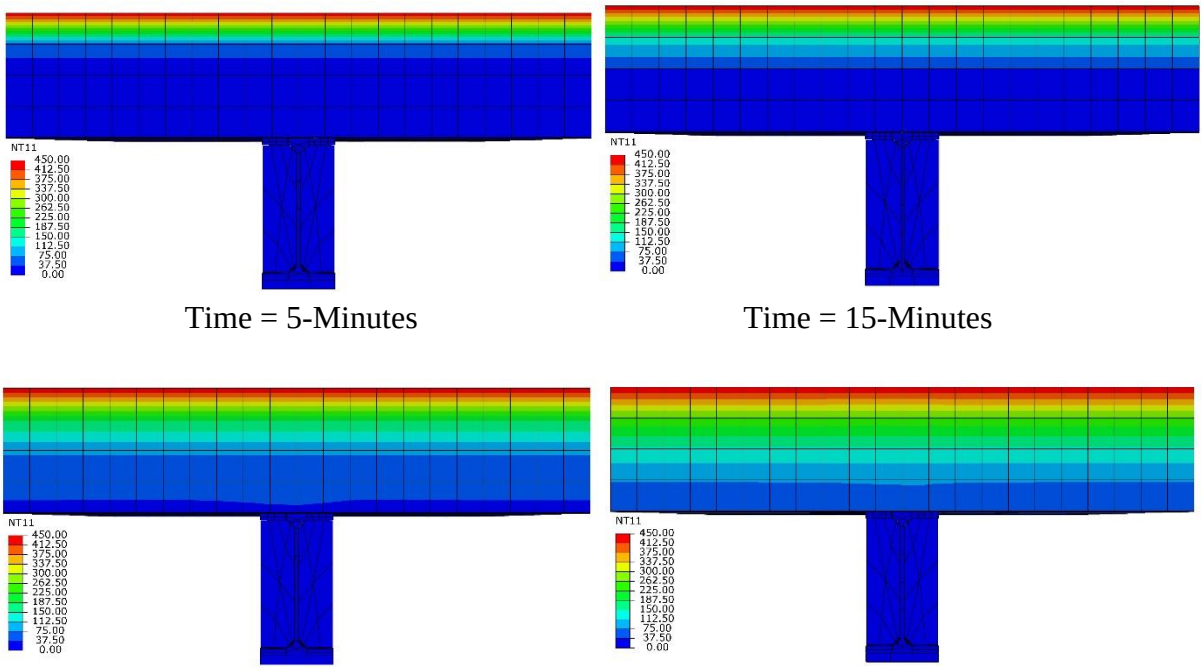


Time = 5-Minutes Time = 15-Minutes

Time = 30-Minutes Time = 60-Minutes

(b) CD2TR2

**Figure 5. 23: Heat transfer with time for specimens CD1BR2 and CD1TR2 burned at 450°C.**

## 5.7 PARAMETRIC STUDY

After studying the convergence of composite beam specimens with different directions of corrugated steel plates and obtaining reasonably well-agreed convergence between the experimental and numerical results, the experimental program was expanded to investigate a set of variables and their impact on the behavior of composite beams. The variables studied include: Direction of fire exposure (from both side top and bottom) and size of steel profile (IPE160 and IPE200).

The details and suggested names of the specimens studied in the parametric study are shown in Table 5.2. The suggested specimens are compared with the control specimens CD1BR2 and CD2BR2, which have the same details as the experimental specimens. In addition, the results of the ultimate load and deflection of all these specimens are listed in Table 5.3.

**Table 5. 2: The details of the studied variables.**

| Specimen name | Symbol of variable | Variable |
|---|---|---|
| CD1BR2 | Control | Fire from bottom side for specimen with parallel-corrugated steel plates (same experimental specimen) |
| CD2BR2 | Control | Fire from bottom side for specimen with transverse-corrugated steel plates (same experimental specimen) |
| CD1BTR2 | BT | Fire from bottom and top sides |
| CD2BTR2 | BT | |
| CD1$d_{200}$ | $d_{200}$ | Size of steel beam (use section IPE200) with and without exposed to fire |
| CD1BR2$d_{200}$ | $d_{200}$ | |
| CD2$d_{200}$ | $d_{200}$ | Size of steel beam (use section IPE200) with and |

| | | |
|---|---|---|
| CD2BR2$d_{200}$ | $d_{200}$ | without exposed to fire |

**Table 5. 3: Results of the parametric study.**

| Specimen name | Ultimate load (kN) | Variation in load % * | deflection (mm) | Variation in deflection %* |
|---|---|---|---|---|
| CD1BR2 | 159.57 | - | 14.08 | - |
| CD2BR2 | 135.56 | - | 12.62 | - |
| CD1BTR2 | 134.88 | -15.47 | 18.23 | 29.50 |
| CD2BTR2 | 113.53 | -16.25 | 15.78 | 25.00 |
| CD1$d_{200}$ | 271.00 | 69.83 | 20.24 | 43.78 |
| CD1BR2$d_{200}$ | 208.00 | 30.35 | 21.85 | 55.23 |
| CD2d200 | 223.23 | 64.67 | 19.23 | 52.34 |
| CD2BR2d200 | 156.40 | 15.37 | 16.14 | 27.90 |

* The specimens in the parametric study are compared with a control specimen in the same orientation. Specifically, the specimen with parallel-corrugated steel plates is compared with specimen CD1BR2, while the specimen with transversely corrugated steel plates is compared with CD2BR2.

### 5.7.1 Effect of Fire Exposure from Bottom and Top Sides

In multi-story buildings, there is more than one possibility in the event of a fire, as shown in Figure 5.24. To comprehensively investigate the impact of fire direction on the behavior of composite beams, a finite element analysis was conducted. Specifically, we focused on case c from Figure 5.24, where fire exposure occurred simultaneously from both the top and bottom surfaces of the specimen. This case was compared to the two other scenarios: one where fire was solely exposed from the top, and the other

where fire originated solely from the bottom. This comparative analysis seeks to provide valuable insights into how different fire exposure conditions influence the performance of composite beams in fire-prone environments.

It was observed that the reduction in ultimate load was 15.5% and 16.25% when compared to specimens exposed to fire from the bottom, and 35.7% and 36.5% when compared to specimens exposed to fire from the top, for parallel and transverse corrugated steel plates, respectively. The load-deflection curves for these specimens are shown in Figures 5.25 and 5.26. In addition, the von Mises equivalent stress distribution at ultimate load for the specimens CD1BTR2 and CD2BTR2 is shown in Figure 5.27. Figures 5.28, 5.29 and 5.30 depict the temperature distribution in the composite specimens CD1BTR2 and CD2BTR2 after 60 minutes of burning.

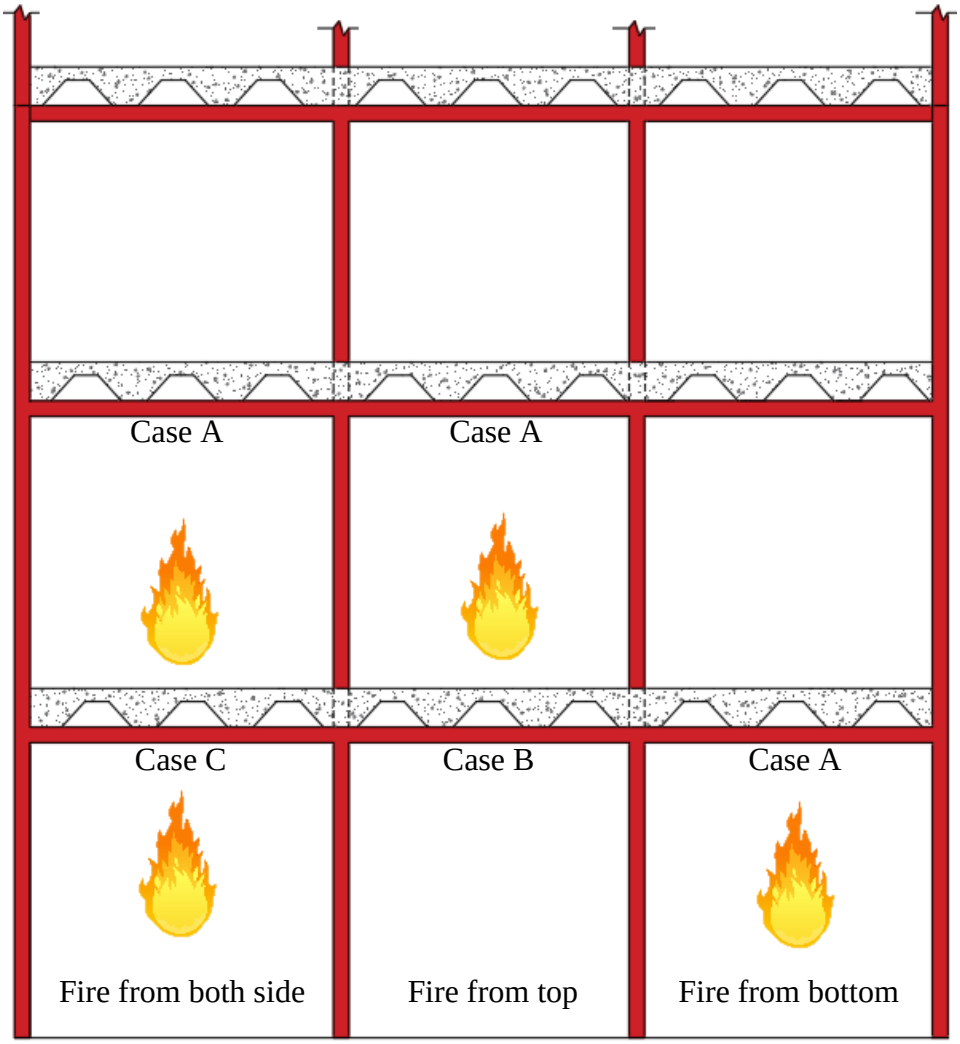


**Figure 5. 24: Cases of fire exposure in multi-story buildings.**

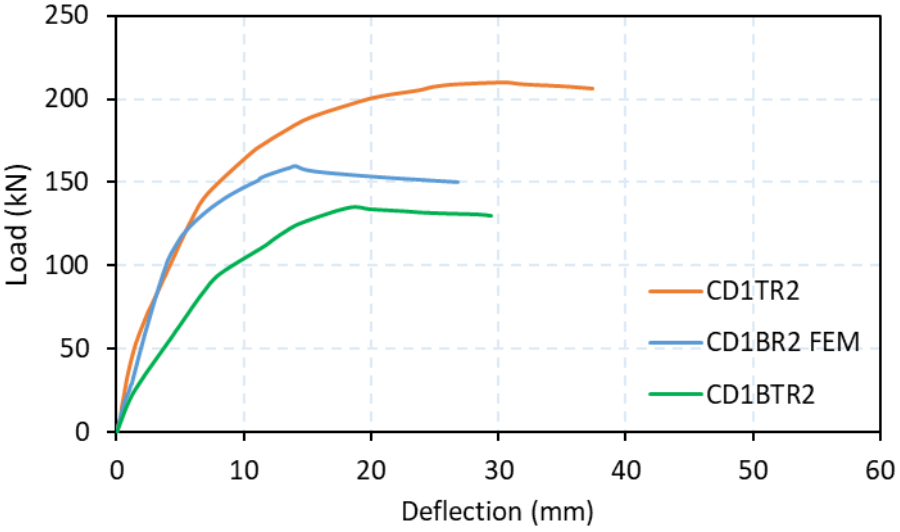


**Figure 5. 25: Load-deflection curve for specimen CD1BTR2.**

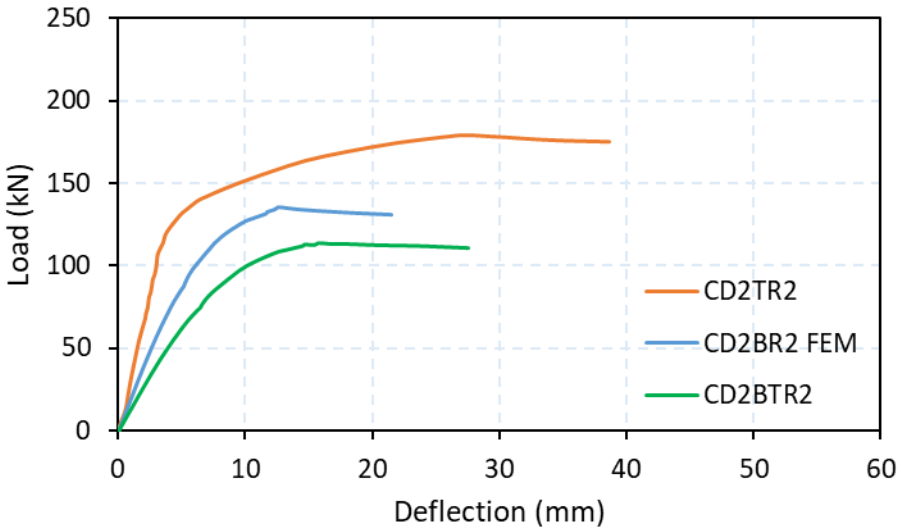


**Figure 5. 26: Load-deflection curve for specimen CD2BTR2.**

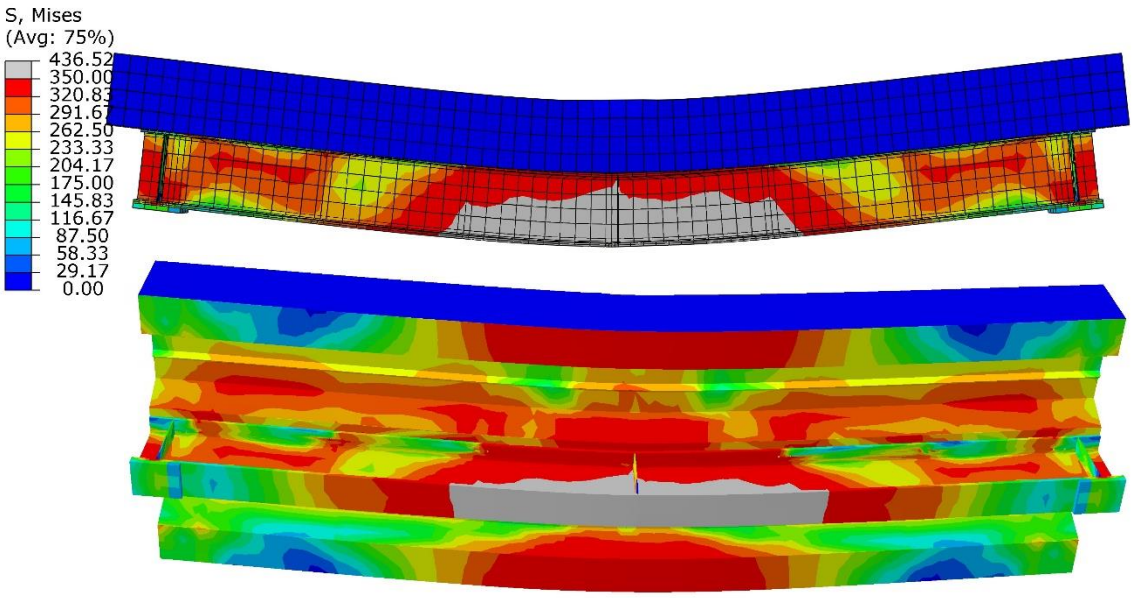

**(a)** CD1BTR2

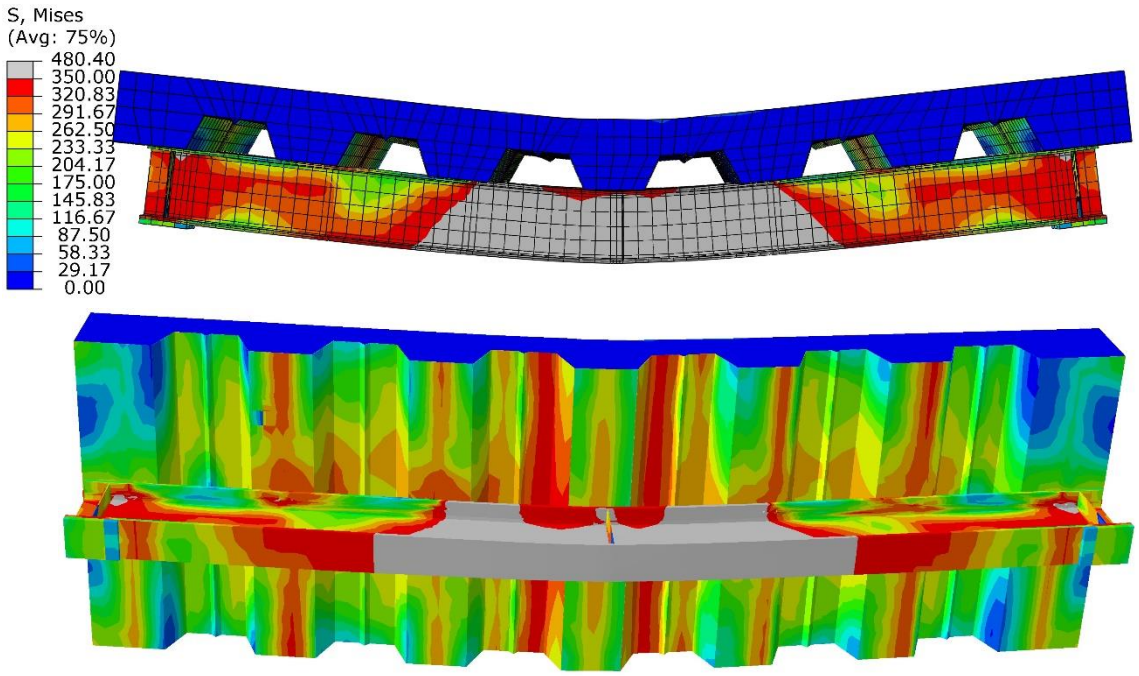


**(b)** CD2BTR2

**Figure 5. 27: Von-Mises equivalent stress distribution of specimens CD1BTR2 and CD2BTR2.**

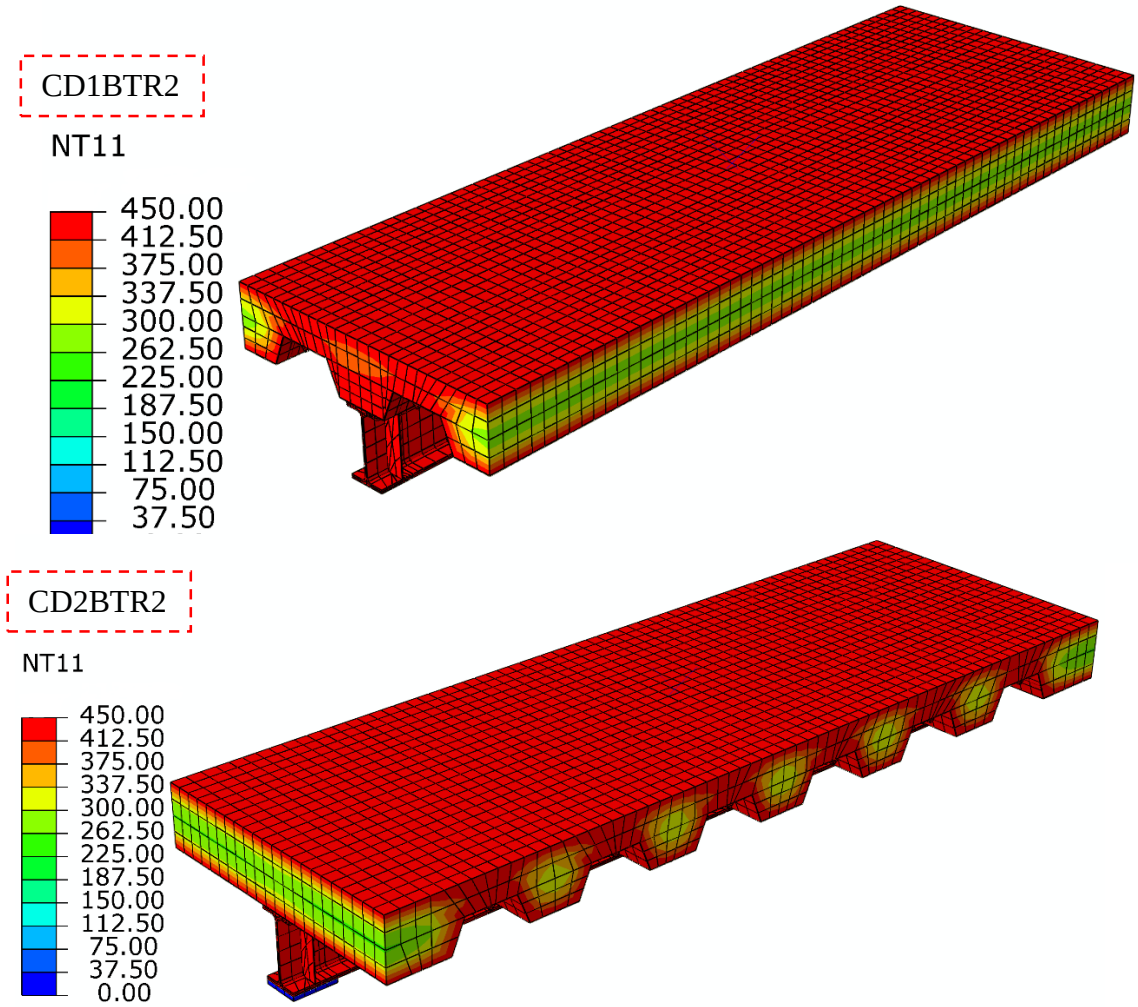


**Figure 5. 28: Temperature distribution in specimens CD1BTR2 and CD2BTR2 after 60-minutes of burning at 450°C.**

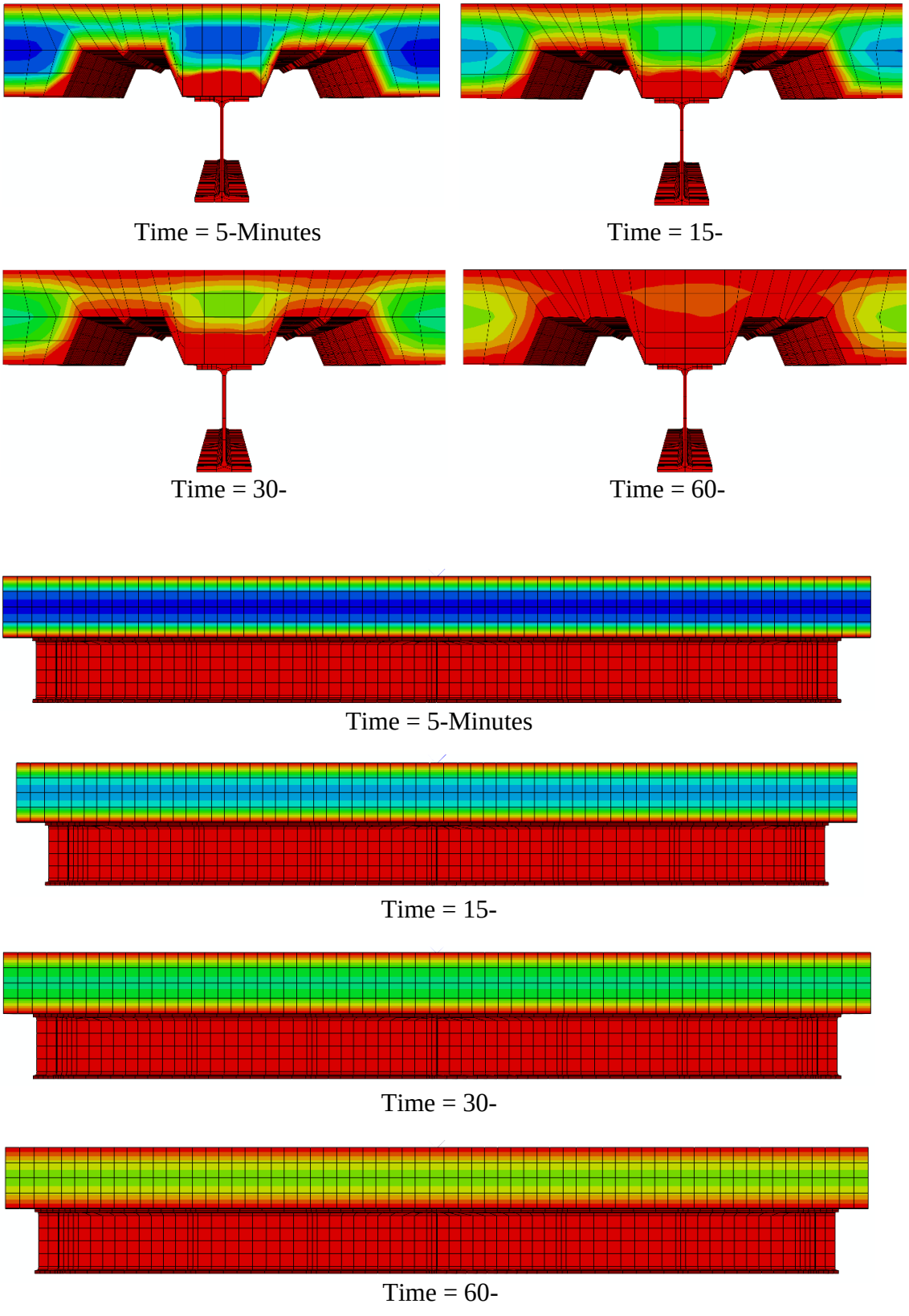


**Figure 5. 29**: **Heat transfer with time for specimen CD1BTR2 burned at 450°C.**

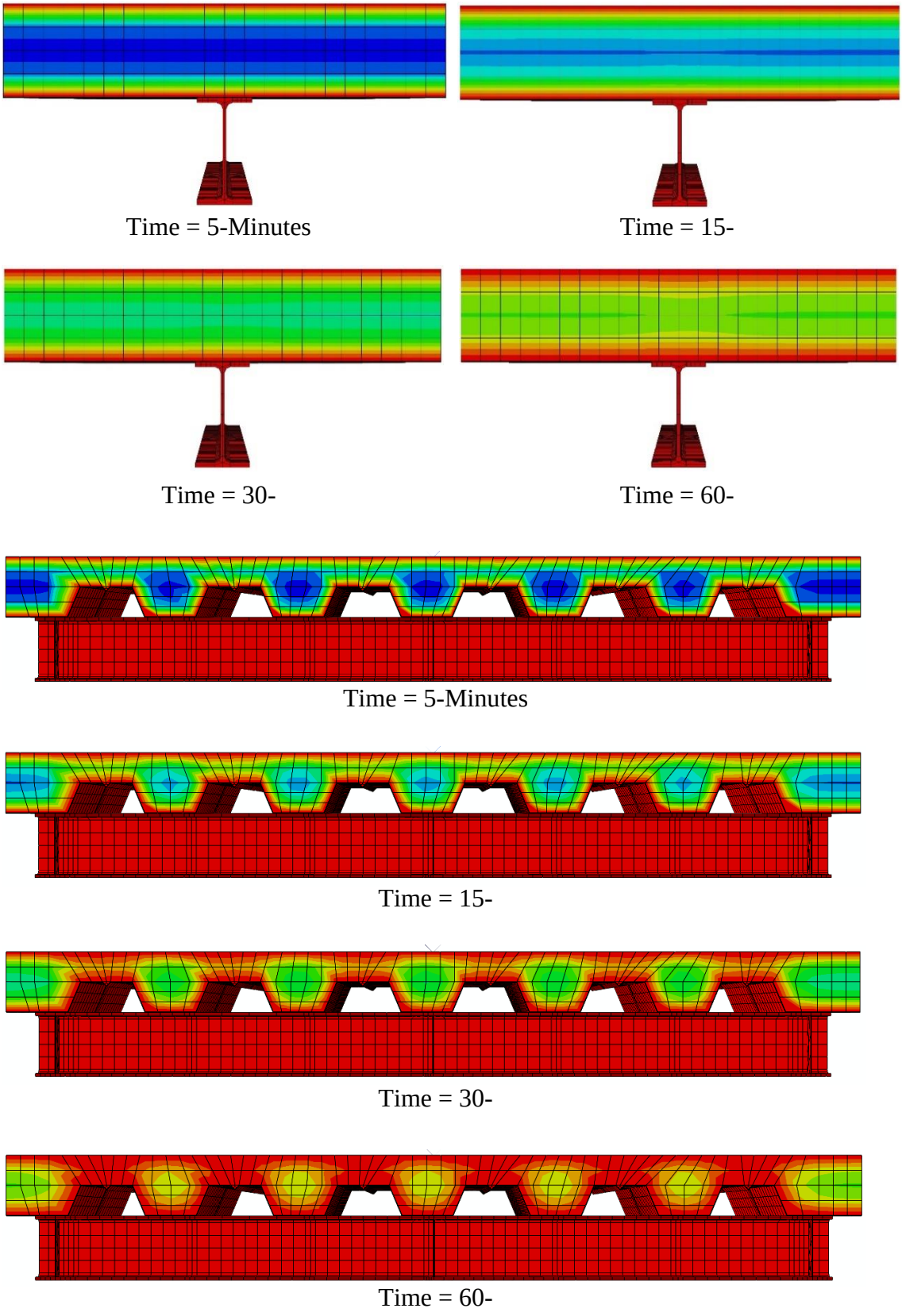


**Figure 5. 30: Heat transfer with time for specimen CD2BTR2 burned at 450°C.**

### 5.7.2 Effect of Size of Steel Beam Profile

The study of the size of the steel beam profile in composite steel-concrete beams is a fundamental parameter that intersects structural engineering, architecture, economics, and safety. Consequently, a thorough exploration of its effects on composite steel-concrete beams is crucial for informed decision-making in the construction industry. This study equips engineers, architects, and project stakeholders with the knowledge needed to design and build structurally sound, cost-effective, and aesthetically pleasing structures that meet both functional and safety objectives.

This section examines the impact of steel beam sections on the behavior of composite beams. Comparing specimens with IPE200 steel beams to those with IPE160 steel sections, the ultimate load increased by 19.82% and 30.35% for parallel-corrugated steel plates specimens at ambient temperature and under fire from the bottom, respectively (see Figure 5.31).

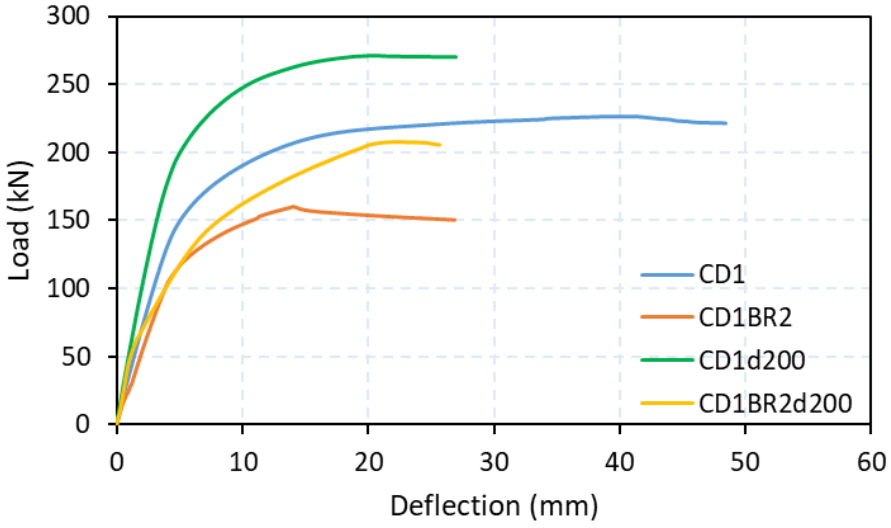


**Figure 5. 31**: **Load-deflection curve for specimens with steel beam section IPE200 and parallel-corrugated steel plate.**

Furthermore, when compared with the IPE160 steel beam, increasing the beam section resulted in a reduced appearance of the yield zone,

depicted in white color, as shown in Figure 5.32. The temperature distribution in the composite specimens CD1d200 and CD1BR2d200 after 60 minutes of burning is illustrated in Figure 5.33.

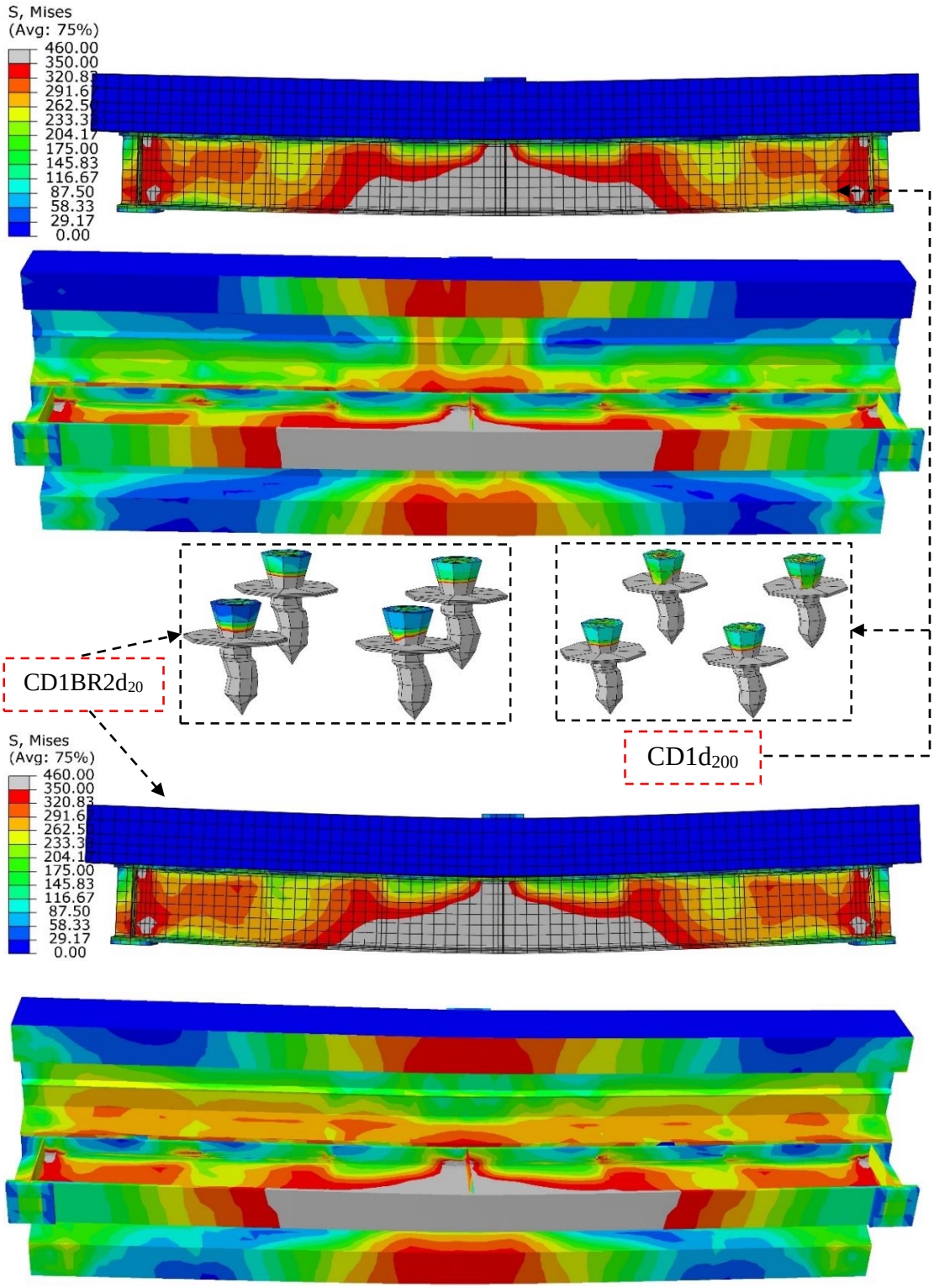


**Figure 5. 32: Von-Mises equivalent stress distribution of specimens CD1d$_{200}$ and CD1BTR2d$_{200}$.**

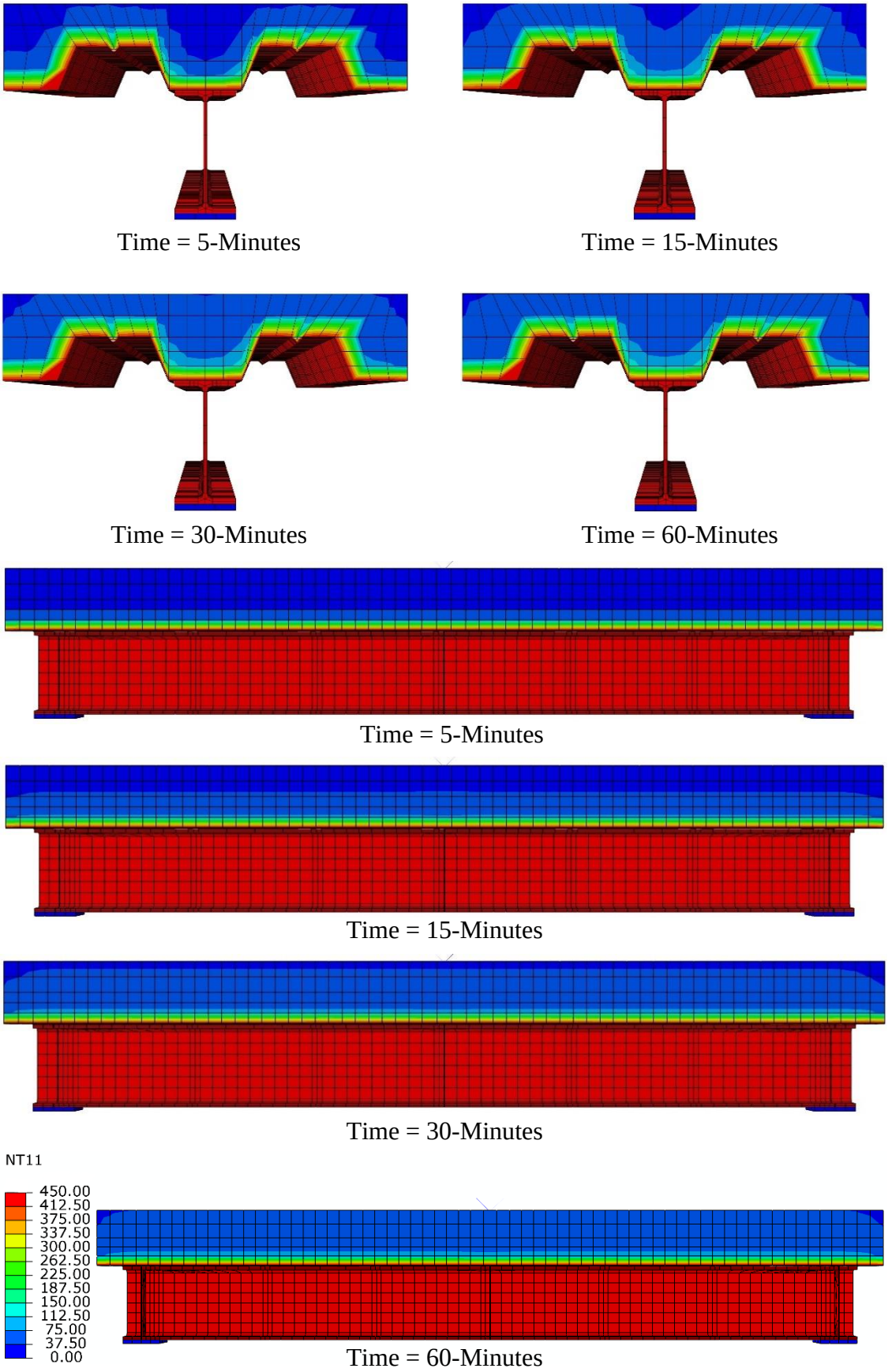


**Figure 5. 33: Heat transfer with time for specimen CD1BR2d$_{200}$ burned at 450°C.**

While comparing specimens with IPE 200 steel beams to those with IPE160 steel sections, for transversely corrugated steel plate specimens without fire and under fire from the bottom, the ultimate load increased by 14.35% and 15.37%, respectively, as shown in Figure 5.34. The von Mises equivalent stress distribution at ultimate load and the temperature distribution in the composite specimens CD2d200 and CD2BR2d200 after 60 minutes of burning are illustrated in Figures 5.35 and 5.36, respectively.

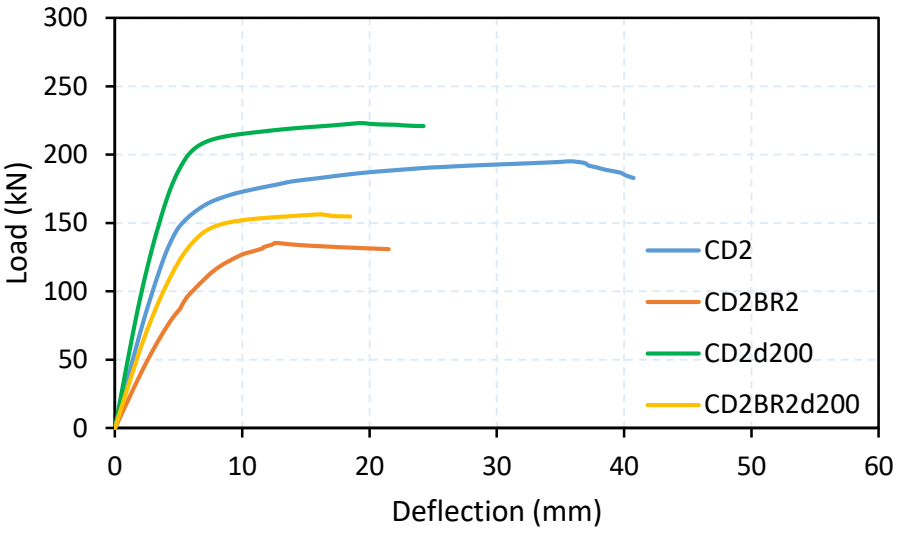


**Figure 5. 34: Load-deflection curve for specimens with steel beam section IPE200 and transversely -corrugated steel plate.**

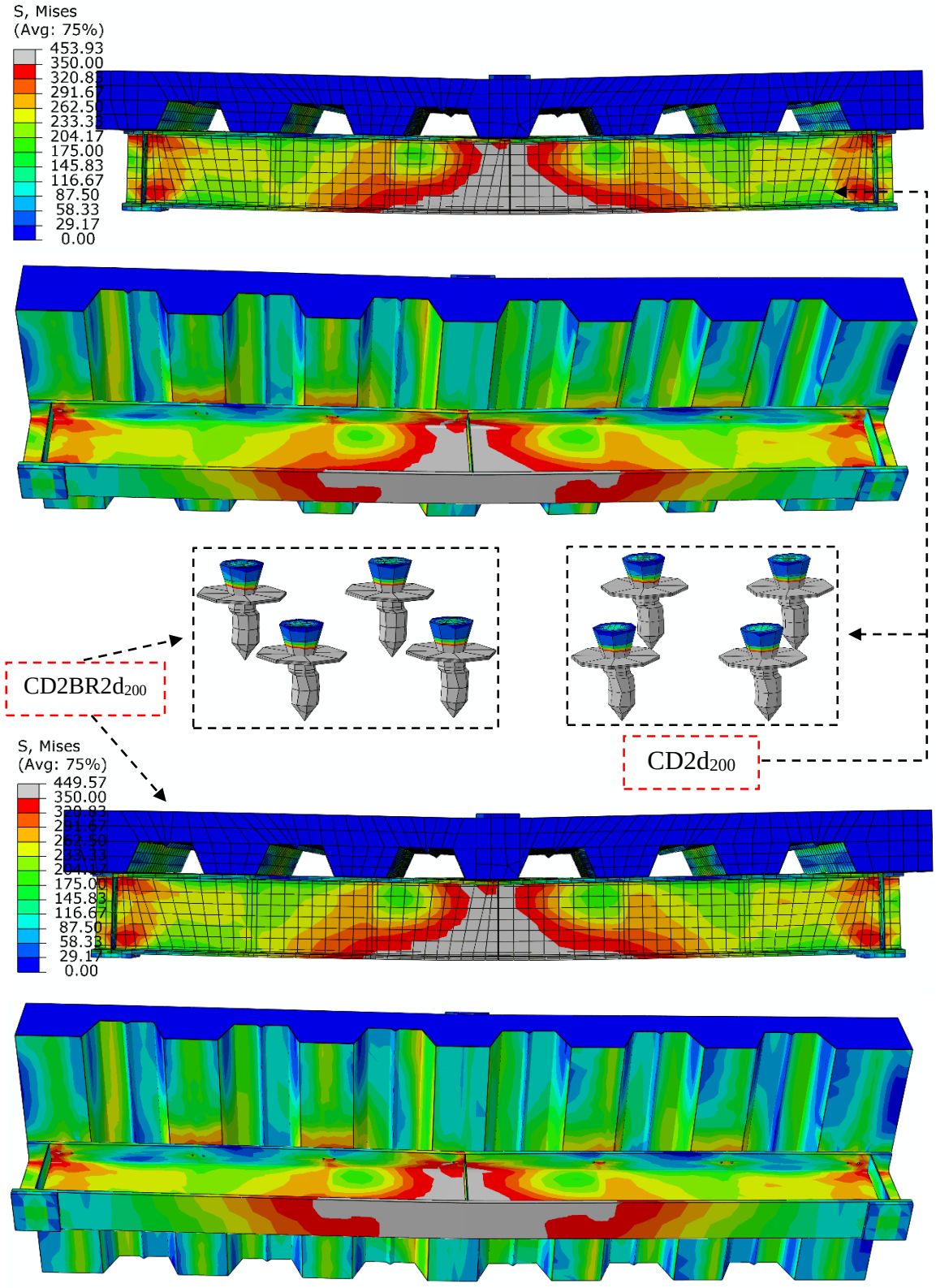


**Figure 5. 35: Von-Mises equivalent stress distribution of specimens CD2d$_{200}$ and CD2BTR2d$_{200}$.**

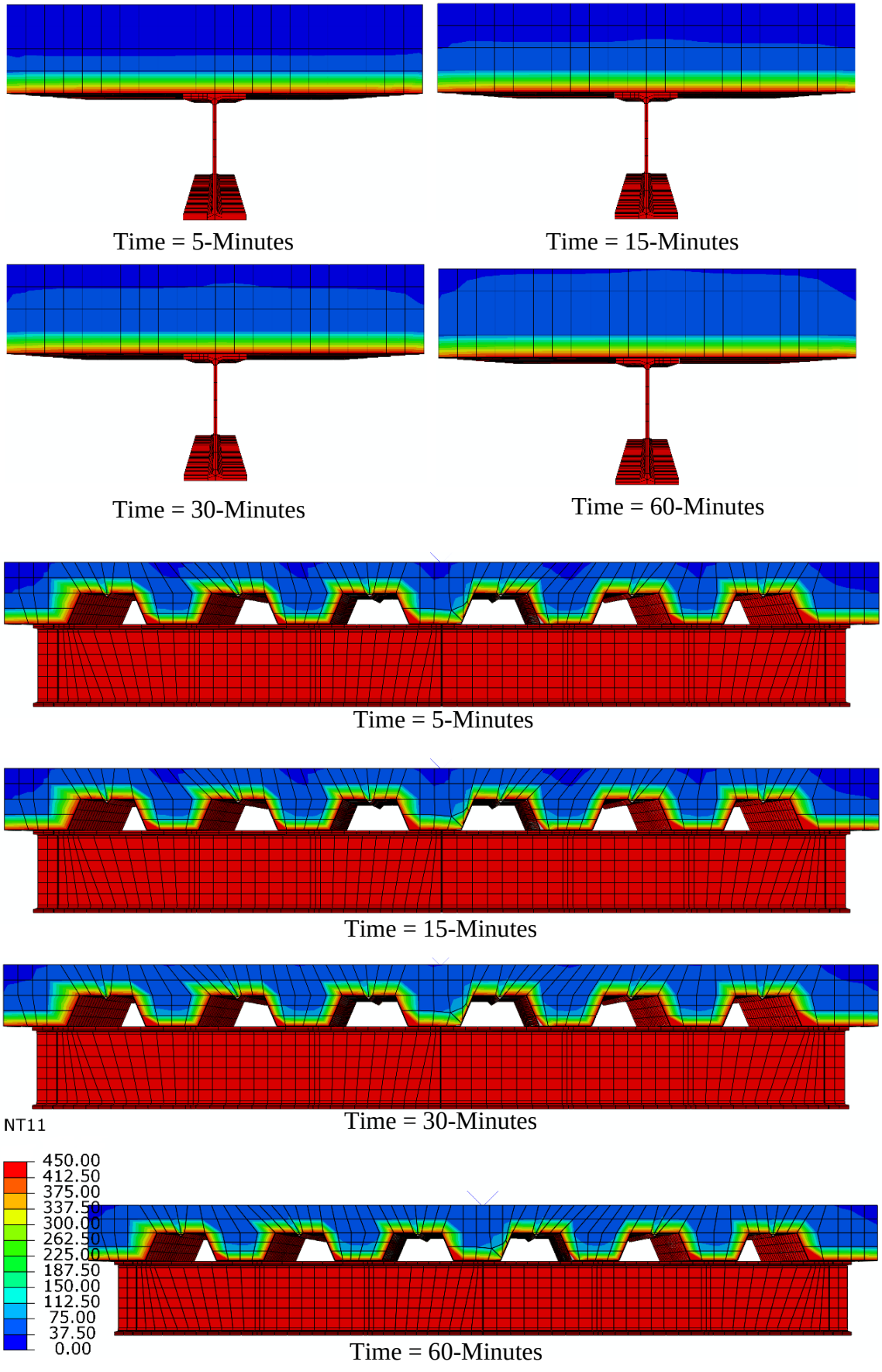


**Figure 5. 36: Heat transfer with time for specimen CD2BR2d$_{200}$ burned at 450°C.**

# CHAPTER SIX

# Conclusions AND Recommendations

## 6.1 INTRODUCTION

The primary goal of this thesis is to study the behavior of X-HVB shear connecter in composite beam under fire conditions. A secondary goal of the thesis is to develop a finite element model to help further investigations in the analysis of composite beam structures under fire exposures.

## 6.2 KEY FINDINGS

Based on the investigated variables in this research different conclusion points concerning the structural behavior of composite beam and pushout specimens under exposure to fire were drawn which can be outlined under different titles as follows:

### 6.2.1 Conclusions Based on Experimental Pushout Test

Mechanically fastened shear connectors (X-HVB) by HILTI company represent an innovation in achieving shear connection between steel beams and solid or composite concrete slabs. Despite the great benefits of this types of shear connector and this behavior on fire exposure, there is a lack of readily available study results in this area. An experimental study of X-HVB 95 shear connectors presented in this study should lead to better insight into the behavior of shear connection achieved with this type of shear connector. The main points that are concluded from this paper are as follows:

1) At ambient temperature, specimen with transverse corrugated plates demonstrated a 10% higher ultimate load and a 245% greater stiffness compared to that with parallel corrugated plates. However, the

specimens with parallel corrugated sheet exhibited approximately 6% higher ductility than that with transverse corrugated plate.

2) Under fire exposure, specimens with transverse corrugated steel plates sustained a higher ultimate load and maintained ductile behavior post-temperature exposure, contrasting with specimens with parallel corrugated steel decks that exhibited brittle behavior.
3) Increasing the temperature results in a reduction in stiffness, with the percentage of stiffness reduction proportionally increasing as the exposed fire temperature rises.
4) The forward orientation of shear connectors is more favorable for shear resistance, showing a 29% increase for specimens with parallel corrugated plates and a 21% increase for specimens with transverse corrugated plates compared to the backward orientation.
5) For parallel and transverse sheeting, the value of peak push load increases as the number of X-HVB shear connecter per raw increases from one to two by about 118% and 81%, respectively, but influence the ductility as it becomes brittle.
6) Shear resistance, ductility, and failure mechanisms of X-HVB shear connectors are mostly related to the direction of corrugated steel plates and the degree of shear connection.
7) It was found that the shear connector orientation relative to the direction of shear force strongly influences shear resistance, slip capacity, and failure mechanisms.

### 6.2.2 Conclusions Based on The Composite Beam Specimens

This section explores the behavior of a composite beam–slab structural system that is connected by a new type of shear connector, the Hilti X-HVB, under fire conditions. Initially, the load-carrying capacity of the composite beam is estimated under ambient temperature. Next, the beam is

tested after being exposed to varying levels of temperature, as well as the orientation of the corrugated steel plate with steel beam length. Based on the results, several conclusions regarding the load-carrying capacity of the composite beam under fire conditions:

1) The fire exposure temperature level has a significant effect on the behavior of composite steel-concrete beams. As the fire exposure temperature level increases, the ultimate load capacity and stiffness of the beams decrease.
2) The orientation of the corrugated steel deck also has a significant effect on the behavior of the beams. Beams with parallel corrugated steel decks have better fire performance than beams with transverse corrugated steel decks. This is because parallel corrugated steel decks provide more shear resistance between the steel beam and the concrete slab, which is critical for load transfer in fire-exposed conditions.
3) At ambient temperature, the composite beam with transverse corrugated plate demonstrates an enhanced stiffness and ductility of approximately 33% and 43% respectively in comparison to the beam with parallel corrugated plate. This variation in stiffness and ductilty between the two configurations indicates the influence of the steel profile orientation on the overall structural behavior.
4) At fire exposed conditions, specimens with parallel corrugated plates demonstrate a greater ductile behavior. This behavior highlights the interplay between the profile orientation and thermal effects on the composite beam's performance.
5) The ultimate relative slip of the composite beam specimens decreases significantly as the temperature of the burned specimens' increases. This is attributed to thermal expansion, material degradation, and a

reduction in interfacial shear resistance between the steel beam and concrete slab.

6) Both at ambient temperature and under fire-exposed conditions, specimens with parallel corrugated plates exhibit a higher energy absorption capacity than specimens with transverse corrugated plates. This is because the parallel profiled plates provide more shear resistance, which allows the composite beam to deform more before failure and absorb more energy.

7) The direction of fire attack (from top or bottom) of composite beam strongly effects on the strength reduction.

8) Exposure the specimen to fire from top (concrete slab) leads to reduction in ultimate load by about 8% and 11% for specimens compared to the unburned specimen.

9) The proposed DIC method is capable of tracing the load- deflection response of composite beams.

10) The numerical analyses by ABAQUS program show that the behavior of specimens and the ultimate loads are in good match with the experimental results for composite beam specimens with the novel type of shear connecter (X-HVB) at ambient and elevated temperature.

11) The reduction in ultimate load for specimens that exposed to fire from both top and bottom faces was 15.5% and 16.25% compared with specimens exposed to fire form bottom and 35.7% and 36.5% compared with specimens exposed to fire form top for parallel and transverse corrugated steel plates, respectively.

12) Substituting IPE200 for IPE160 steel beams improved performance with a 19.82% and 14% increase in ambient ultimate load, and a more significant 30.35% and 15.37% increase under fire conditions for parallel and transverse corrugated steel plate specimens, respectively.

## 6.3 RECOMMENDATIONS

1) Optimization study to select the perfect geometry of the corrugated steel plate for the designed composite girders with X-HVB shear connecter type.
2) Studying the effect of repeated loading on the behavior of composite girders with X-HVB shear connecter.
3) The effect of protected steel beam and the bottom of corrugated steel plate by intumescent coating.
4) Investigating the effect of high strength concrete on fire resistance of composite beam with X-HVB shear connecter type.
5) Investigating the effect of span to depth ratio on the behavior of composite beam with X-HVB shear connecter.
6) Investigating the effect of type of cooling.

## REFERENCES


[1] J. W. Rackham, G. H. Couchman, and S. J. Hicks, “Composite slabs and beams using steel decking: best practice for design and construction,” 2009.

[2] D. Collings, *Steel-concrete composite bridges*. Thomas Telford, 2005.

[3] O. Mirza and B. Uy, “Behaviour of headed stud shear connectors for composite steel–concrete beams at elevated temperatures,” *J. Constr. Steel Res.*, vol. 65, no. 3, pp. 662–674, 2009.

[4] S. Shahabi, N. Sulong, M. Shariati, and S. Shah, “Performance of shear connectors at elevated temperatures-A review,” *Steel Compos. Struct*, vol. 20, no. 1, pp. 185–203, 2016.

[5] D. Nethercot, *Composite construction*. CRC Press, 2003.

[6] J. Q. Qureshi, “Finite element modelling of steel-concrete composite structures,” University of Leeds, 2010.

[7] D. D. R. Panchal, “Advanced design of composite steel-concrete structural element,” *Pp ISSN-2248*, vol. 9622, 2014.

[8] I. Vayas and A. Iliopoulos, *Design of steel-concrete composite bridges to Eurocodes*. CRC press, 2013.

[9] A. Albarram, J. Qureshi, and A. Abbas, “Effect of Rib Geometry in Steel–Concrete Composite Beams with Deep Profiled Sheeting,” *Int. J. Steel Struct.*, vol. 20, no. 3, pp. 931–953, 2020.

[10] H. S. Abbas, S. A. Bakar, M. Ahmadi, and Z. Haron, “Experimental studies on corrugated steel-concrete composite slab,” *Gradevinar*, vol. 67, no. 3, pp. 225–233, 2015.

[11] K. W. Poh and M. M. Attard, “Calculating the load-deflection behaviour of simply-supported composite slabs with interface slip,” *Eng. Struct.*, vol. 15, no. 5, pp. 359–367, 1993.

[12] P. Vainiūnas, J. Valivonis, G. Marčiukaitis, and B. Jonaitis, “Analysis

of longitudinal shear behaviour for composite steel and concrete slabs," *J. Constr. Steel Res.*, vol. 62, no. 12, pp. 1264–1269, 2006.

[13] P. Mäkeläinen and Y. Sun, "The longitudinal shear behaviour of a new steel sheeting profile for composite floor slabs," *J. Constr. Steel Res.*, vol. 49, no. 2, pp. 117–128, 1999.

[14] N. Gluhović, Z. Marković, M. Spremić, and M. Pavlović, "Experimental investigation of X-HVB shear connectors in prefabricated composite decks," *Zb. Rad. građevinskih Konstr. Srb. Simp. 2016, 15-17. Sept. Zlatibor*, pp. 439–448, 2016.

[15] J. G. Ollgaard, R. G. Slutter, and J. W. Fisher, "Shear strength of stud connectors in lightweight and normal weight concrete, AISC Eng'g Jr., April 1971 (71-10)," *AISC Eng. J.*, pp. 34–55, 1971.

[16] P.-G. Lee, C.-S. Shim, and S.-P. Chang, "Static and fatigue behavior of large stud shear connectors for steel–concrete composite bridges," *J. Constr. steel Res.*, vol. 61, no. 9, pp. 1270–1285, 2005.

[17] W. Deng, Y. Xiong, D. Liu, and J. Zhang, "Static and fatigue behavior of shear connectors for a steel-concrete composite girder," *J. Constr. Steel Res.*, vol. 159, pp. 134–146, 2019.

[18] C. Wang, D. Cao, X. Liu, Y. Jing, W. Liu, and G. Yang, "Initial elastic stiffness of bolted shear connectors in steel-concrete composite structures," *Adv. Civ. Eng.*, vol. 2022, pp. 1–13, 2022.

[19] J. da C. Vianna, L. F. Costa-Neves, P. C. G. da S. Vellasco, and S. A. L. De Andrade, "Experimental assessment of Perfobond and T-Perfobond shear connectors' structural response," *J. Constr. Steel Res.*, vol. 65, no. 2, pp. 408–421, 2009.

[20] J. da C. Vianna, S. A. L. De Andrade, P. C. G. da S. Vellasco, and L. F. Costa-Neves, "Experimental study of Perfobond shear connectors in composite construction," *J. Constr. Steel Res.*, vol. 81, pp. 62–75, 2013.

[21] E. Baran and C. Topkaya, “An experimental study on channel type shear connectors,” *J. Constr. Steel Res.*, vol. 74, pp. 108–117, 2012.

[22] S. Maleki and S. Bagheri, “Behavior of channel shear connectors, Part I: Experimental study,” *J. Constr. Steel Res.*, vol. 64, no. 12, pp. 1333–1340, 2008.

[23] R. P. Johnson and D. Anderson, *Designers’ guide to EN 1994-1-1: eurocode 4: design of composite steel and concrete structures. General rules and rules for buildings*. Thomas Telford, 2004.

[24] ANSI/AISC-360-05 An American National Standard, *Specification for Structural Steel Buildings*. Chicago, Illinois, 2005.

[25] E. C. for Standardization, “EUROCODE 4, Design of composite steel and concrete structures-Part 1.1: General rules and rules for buildings,” *prEN 1994-1-1*. 2004.

[26] N. Gluhović, “Behaviour of shear connections realised by connectors fastened with cartridge fired pins: doctoral dissertation,” *Универзитет у Београду*, 2019.

[27] HILTI Direct Fastening Technology Manual 2014, *S.E. & O, Germany*. 2014.

[28] N. Gluhović, Z. Marković, M. Spremić, and M. Pavlović, “08.30: Experimental investigation and specific behaviour of X-HVB shear connectors in prefabricated composite decks,” *ce/papers*, vol. 1, no. 2–3, pp. 2080–2089, 2017.

[29] C. Wu, S. Yu, J. Liu, and G. Chen, “Development and testing of hybrid precast steel-reinforced concrete column-to-H shape steel beam connections under cyclic loading,” *Eng. Struct.*, vol. 211, p. 110460, 2020.

[30] Y. C. Wang, “Performance of steel–concrete composite structures in fire,” *Prog. Struct. Eng. Mater.*, vol. 7, no. 2, pp. 86–102, 2005.

[31] J. Jiang, J. A. Main, J. M. Weigand, and F. H. Sadek, “Thermal

performance of composite slabs with profiled steel decking exposed to fire effects," *Fire Saf. J.*, vol. 95, pp. 25–41, 2018.

[32] L. A. Sabri, "THE RESPONSE OF COMPOSITE CONCRETE-I-BEAMS UNDER THE EFFECT OF BOTH FIRE AND EXTERNAL LOADINGS," *Iraqi J. Mech. Mater. Eng.*, no. first conf./eng. coll., 2009.

[33] D. Zhang, X. Lin, H. Wang, Y. Dong, J. Zhang, and H. Hu, "Experimental Investigation on Fire Behavior and Quantitative Restraint Forces of Steel–Concrete Composite Floor Systems," *J. Struct. Eng.*, vol. 148, no. 10, p. 04022156, 2022.

[34] L. Choe *et al.*, "Fire resilience of a steel-concrete composite floor system: full-scale experimental evaluation for US Prescriptive approach with a 2-hour fire-resistance rating (test# 1)," *Tech. Note (NIST TN). Gaithersburg, MD Natl. Inst. Stand. Technol.*, 2021.

[35] C. Time, P. Girders, and C. H. M. Inn, "American Institute of Steel Construction".

[36] A. W. Beeby and R. S. Narayanan, *Designers' Guide to EN 1992-1-1 and EN 1992-1-2. Eurocode 2: Design of Concrete Structures: General Rules and Rules for Buildings and Structural Fire Design*, vol. 17. Thomas Telford, 2005.

[37] B. Ansi, "AISC 360-16, specification for structural steel buildings," *Chicago AISC*, 2016.

[38] J.-P. Jaspart and K. Weynand, "Design of joints in steel and composite structures," 2016.

[39] S. A. L. de Andrade, P. C. G. da S. Vellasco, J. G. S. da Silva, and T. H. Takey, "Standardized composite slab systems for building constructions," *J. Constr. Steel Res.*, vol. 60, no. 3–5, pp. 493–524, 2004.

[40] W. S. Easterling, D. R. Gibbings, and T. M. Murray, "Strength of

shear studs in steel deck on composite beams and joists," *Eng. J.*, vol. 30, no. 2, pp. 44–55, 1993.

[41] R. Fike and V. Kodur, "Enhancing the fire resistance of composite floor assemblies through the use of steel fiber reinforced concrete," *Eng. Struct.*, vol. 33, no. 10, pp. 2870–2878, 2011.

[42] S. Guo, "Experimental and numerical study on restrained composite slab during heating and cooling," *J. Constr. Steel Res.*, vol. 69, no. 1, pp. 95–105, 2012.

[43] D. Pantousa and E. Mistakidis, "Advanced modeling of composite slabs with thin-walled steel sheeting submitted to fire," *Fire Technol.*, vol. 49, no. 2, pp. 293–327, 2013.

[44] K. C. G. Ong and M. A. Mansurt, "Shear-bond capacity of composite slabs made with profiled sheeting," *Int. J. Cem. Compos. Light. Concr.*, vol. 8, no. 4, pp. 231–237, 1986.

[45] R. Abdullah and W. S. Easterling, "New evaluation and modeling procedure for horizontal shear bond in composite slabs," *J. Constr. steel Res.*, vol. 65, no. 4, pp. 891–899, 2009.

[46] S. P. Siddh, Y. D. Patil, and H. S. Patil, "Experimental studies on behaviour of composite slab with profiled steel sheeting," *Mater. Today Proc.*, vol. 4, no. 9, pp. 9792–9796, 2017.

[47] U. Katwal, Z. Tao, M. K. Hassan, B. Uy, and D. Lam, "Load sharing mechanism between shear studs and profiled steel sheeting in push tests," *J. Constr. Steel Res.*, vol. 174, p. 106279, 2020.

[48] E. C. for Standardization, "Design of composite steel and concrete structures. Part 1-1: General rules and rules for buildings," in *Eurocode*, 2004.

[49] I. Abbas, A. M. Ibrahim, and T. A. Jassim, "The Effect of Adding Shear Connectors to the Composite Slabs with Different Geometry of Profile Steel Sheet," *Diyala J. Eng. Sci.*, vol. 14, no. 2, pp. 1–17,

2021.

[50] F. L. Bolina, B. Tutikian, and J. P. C. Rodrigues, “Experimental analysis on the structural continuity effect in steel decking concrete slabs subjected to fire,” *Eng. Struct.*, vol. 240, p. 112299, 2021.

[51] F. P. V. Ferreira, C. H. Martins, and S. De Nardin, “Advances in composite beams with web openings and composite cellular beams,” *J. Constr. Steel Res.*, vol. 172, p. 106182, 2020.

[52] J. P. C. Rodrigues and L. Laím, “Behaviour of perfobond shear connectors at high temperatures,” *Eng. Struct.*, vol. 33, no. 10, pp. 2744–2753, 2011.

[53] H. H. Muteb and Z. M. R. A. Rasoul, “Behavior of composite ultra high performance concrete-steel beams (experimental and finite element analysis studies),” *J. kerbala Univ.*, vol. 14, no. 2, 2016.

[54] X. Xu, Y. Liu, and Y. Zuo, “Contribution of perforated steel ribs to load-carrying capacities of steel and concrete composite slabs under negative bending,” *Adv. Struct. Eng.*, vol. 21, no. 12, pp. 1879–1894, 2018.

[55] J. Nie, J. Fan, and C. S. Cai, “Experimental study of partially shear-connected composite beams with profiled sheeting,” *Eng. Struct.*, vol. 30, no. 1, pp. 1–12, 2008.

[56] J. Qureshi, D. Lam, and J. Ye, “Effect of shear connector spacing and layout on the shear connector capacity in composite beams,” *J. Constr. steel Res.*, vol. 67, no. 4, pp. 706–719, 2011.

[57] J. Qureshi and D. Lam, “Experimental investigation of shear connector behaviour in composite beams with metal decking,” *Steel Compos. Struct.*, vol. 35, no. 4, pp. 475–494, 2020.

[58] J. Martinez and A. E. Jeffers, “Structural response of steel-concrete composite floor systems under traveling fires,” *J. Constr. Steel Res.*, vol. 186, p. 106926, 2021.

[59] G. M. Newman and R. M. Lawson, *Fire resistance of composite beams*. Steel Construction Institute, 1991.

[60] M. J. Burnet and D. J. Oehlers, "Rib shear connectors in composite profiled slabs," *J. Constr. Steel Res.*, vol. 57, no. 12, pp. 1267–1287, 2001.

[61] A. T. Kassem, A. F. Hassan, and M. M. Seddeek, "Behavior of composite steel-concrete girders in fire condition," in *International Conference on Aerospace Sciences and Aviation Technology*, The Military Technical College, 2009, pp. 1–12.

[62] O. Mirza, B. Uy, and S. Krezo, "Experimental studies on the behaviour of headed stud shear connectors for composite steel concrete beams under elevated temperatures," *Adv. Steel Alum. Struct.*, pp. 467–473, 2011.

[63] J. P. C. Rodrigues and L. Laím, "Experimental investigation on the structural response of T, T-block and T-Perfobond shear connectors at elevated temperatures," *Eng. Struct.*, vol. 75, pp. 299–314, 2014.

[64] L.-Z. Chen, G. Ranzi, S.-C. Jiang, F. Tahmasebinia, and G.-Q. Li, "Behaviour and design of shear connectors in composite slabs at elevated temperatures," *J. Constr. Steel Res.*, vol. 115, pp. 387–397, 2015.

[65] E. Ellobody and B. Young, "Nonlinear analysis of composite castellated beams with profiled steel sheeting exposed to different fire conditions," *J. Constr. Steel Res.*, vol. 113, pp. 247–260, 2015.

[66] W. Wang, M. D. Engelhardt, G. Li, and G. Huang, "Behavior of steel–concrete partially composite beams subjected to fire—part 1: experimental study," *Fire Technol.*, vol. 53, no. 3, pp. 1039–1058, 2017.

[67] S. Shahabi, N. Sulong, M. Shariati, M. Mohammadhassani, and S. N. R. Shah, "Numerical analysis of channel connectors under fire and a

comparison of performance with different types of shear connectors subjected to fire," *Steel Compos. Struct*, vol. 20, no. 3, pp. 651–669, 2016.

[68] E. C. Fischer and A. H. Varma, "Fire resilience of composite beams with simple connections: Parametric studies and design," *J. Constr. Steel Res.*, vol. 128, pp. 119–135, 2017.

[69] S. Choi, "Experimental studies on the behaviour of headed shear studs for composite beams in fire," *Steel Compos. Struct.*, vol. 32, no. 6, pp. 743–752, 2019.

[70] J. Lyu, Q. Chen, H. Xue, Y. Cai, J. Lyu, and S. Zhou, "Fire Resistance of Composite Beams with Restrained Superposed Slabs," *Adv. Mater. Sci. Eng.*, vol. 2020, 2020.

[71] B. K. Cirpici, S. N. Orhan, and T. Kotan, "Finite element study on composite slab-beam systems under various fire exposures," *Steel Compos. Struct.*, vol. 37, no. 5, pp. 589–603, 2020.

[72] X. T. Nguyen and J. S. Park, "Inelastic Strength for Fire Resistance of Composite I-Beam Covered by Insulation Material Subjected to Basic Loading Condition," *Metals (Basel).*, vol. 11, no. 5, p. 739, 2021.

[73] W. Wang, B. Jiang, F. Ding, and L. Wang, "Numerical analysis on mechanical behavior of steel-concrete composite beams under fire," *Struct. Des. Tall Spec. Build.*, p. e2012.

[74] A. Standard, "A370-05,'Standard Test Methods and Definitions for Mechanical Testing of Steel Products,' ASTM International, West Conshohocken, PA."

[75] Hilti X-HVB System, "Solutions for shear connection," Germany: S.E. & O, 2016.

[76] A. 3-91, "Standard for the structural design of composite slabs," American society of civil engineers, 1992.

[77] N. . I.Q.S, " Iraqi Standard Specification, Portland cement," *2019*.

[78] A. Standard, “ASTM C33/C33M–18 Standard Specification for Concrete Aggregates,” *West Conshohocken, PA*, 2018.

[79] Central Organization for Standardization and Quality Control, *Iraqi Standard Specification for the Portland Cement*, IQS (5). Baghdad, Iraq, 1984.

[80] M. Hosseinpour, M. Zeynalian, A. Ataei, and M. Daei, “Push-out tests on bolted shear connectors in composite cold-formed steel beams,” *Thin-Walled Struct.*, vol. 164, p. 107831, 2021.

[81] M. Pavlović, Z. Marković, M. Veljković, and D. Buđevac, “Bolted shear connectors vs. headed studs behaviour in push-out tests,” *J. Constr. Steel Res.*, vol. 88, pp. 134–149, 2013.

[82] M. Gholikord, E. Etemadi, M. Imani, M. Hosseinabadi, and H. Hu, “Design and analysis of novel negative stiffness structures with significant energy absorption,” *Thin-Walled Struct.*, vol. 181, p. 110137, 2022.

[83] “GOM correlation.” Technical Documentation as of V8 SR1, Braunschweig, Germany; 2016.

[84] A. C. I. Committee, “American Concrete Institute and International Organization for Standardization (2008),” *Build. code Requir. Struct. Concr. (ACI 318-08) Comment.*.

[85] K. E. Barth, “Steel bridge design handbook design example 2a: Two-span continuous straight composite steel I-girder bridge,” United States. Federal Highway Administration. Office of Bridges and Structures, 2015.

[86] W.-F. Chen, *Plasticity in reinforced concrete*. J. Ross Publishing, 2007.

[87] A. M. Neville and J. J. Brooks, *Concrete technology*, vol. 438. Longman Scientific & Technical England, 1987.

[88] A. C. I. (ACI), “Building Code Requirements for Structural Concrete

and Commentary, ACI 318M-14." American Concrete Institute (ACI) Farmington Hills, MI, 2014.

[89] M. A. Tantawy, "Effect of high temperatures on the microstructure of cement paste," *J. Mater. Sci. Chem. Eng.*, vol. 5, no. 11, p. 33, 2017.

[90] M. Y. H. Bangash, "Concrete and concrete structures: Numerical modelling and applications," 1989.

[91] H. Kupfer, H. K. Hilsdorf, and H. Rusch, "Behavior of concrete under biaxial stresses," in *Journal proceedings*, 1969, pp. 656–666.

[92] D. Eriksson and T. Gasch, "FEM-modeling of reinforced concrete and verification of the concrete material models available in ABAQUS," *R. Inst. Technol. Stock. SWEDEN*, 2010.

[93] S. M. Chassib, S. K. Zemam, and M. J. Madhi, "New approach of concrete tensile strength test," *Case Stud. Constr. Mater.*, vol. 12, p. e00347, 2020.

[94] M. Smith, "ABAQUS/Standard User's Manual, Version 6.9," 2009.

[95] S. V Chaudhari and M. A. Chakrabarti, "Modeling of concrete for nonlinear analysis Using Finite Element Code ABAQUS," *Int. J. Comput. Appl.*, vol. 44, no. 7, pp. 14–18, 2012.

[96] R. Malm, "Shear cracks in concrete structures subjected to in-plane stresses." KTH, 2006.

[97] J. Lee and G. L. Fenves, "Plastic-damage model for cyclic loading of concrete structures," *J. Eng. Mech.*, vol. 124, no. 8, pp. 892–900, 1998.

[98] S. H. Tan, L. K. Seah, and S. C. Fok, "Connections in cold-formed thin-walled structures," *Comput. Struct.*, vol. 60, no. 1, pp. 169–172, 1996.

[99] E. Thorenfeldt, "Mechanical properties of high-strength concrete and applications in design," in *Symposium Proceedings, Utilization of High-Strength Concrete, Norway, 1987*, 1987.

[100] R. Park and T. Paulay, *Reinforced concrete structures*. John Wiley & Sons, 1991.

[101] K. & S. Hibbitt Inc., "ABAQUS/Standard User's Manual Volume IIII and ABAQUS CAE Manual." Version 6.14 Hibbitt, Karlsson & Sorensen, Inc Pawtucket, RI, USA, 2014.

[102] E. Ellobody and B. Young, "Performance of shear connection in composite beams with profiled steel sheeting," *J. Constr. Steel Res.*, vol. 62, no. 7, pp. 682–694, 2006.

[103] P. Code, "Eurocode 2: design of concrete structures-part 1-2: general rules-structural fire design," 2005.

[104] Z. P. Bažant, M. F. Kaplan, and Z. P. Bazant, "Concrete at high temperatures: material properties and mathematical models," 1996.

[105] G. Khoury, Y. Anderberg, K. Both, J. Fellinger, N. P. Hoj, and C. Maiorana, "Fire design of concrete structures-materials, structures and modelling," 2007.

[106] H. Gulvanessian, J.-A. Calgaro, and M. Holický, *Designer's guide to EN 1990: eurocode: basis of structural design*. Thomas Telford, 2002.

# APPENDIX A

# DESIGN OF THE TESTED COMPOSITE BEAM SPECIMENS

## 1) Decking ribs parallel to the beam axis

The cross-section of the selected composite girder explained in **Figure (A-1)**.

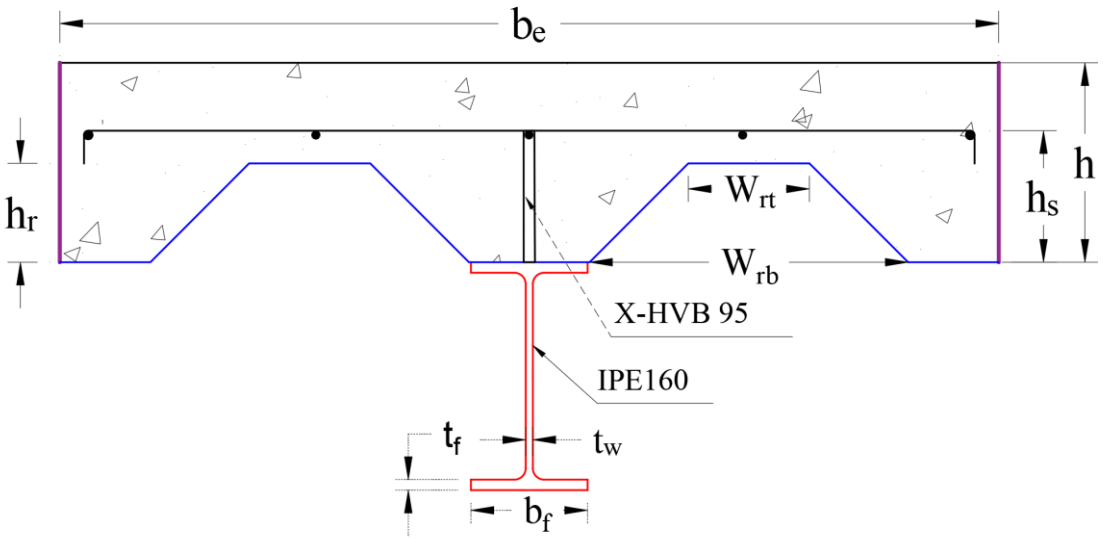


**Figure (A-1): Typical cross-section (all dimensions in mm).**

## DESIGN STEPS

1. Calculating effective slab width ($b_e$):

   In composite section, the width of slab is controlled by the limitations of effective flange width as follows:

- AISC (I3.1a) (16-83**)** [84], "the effective width of the concrete slab is the sum of the effective widths for each side of the beam centerline, each of which shall not exceed:"

(1) 1/8 of the beam span, c. to c. of supports;

(2) 1/2 the distance to the centerline of the adjacent beam; or

(3) The distance to the edge of the slab.

- AASHTO [85], " The total width of slab effective as a T-girder flange shall not exceed:"

(1) 1/4 span length of the girder.

(2) 6 times slab thickness.

(3) Clear distance between webs.

Thus, the slab width $b_c = b_e = \frac{L}{4}$ = 1800 / 4 = 450mm.

The slab width (be= 660 mm) will be used as a multiple of the standard width of corrugated plate.

2. Using standard, I-steel section (IPE160) with the following properties:

| | | |
|---|---|---|
| Root depth (mm) | d | 160 |
| Flange thickness (mm) | $t_f$ | 7.4 |
| Flange width (mm) | $b_f$ | 82 |
| Web thickness (mm) | $t_w$ | 5 |
| Yielding stress (MPa) | $F_y$ | 235 |
| Ultimate strength (MPa) | $F_u$ | 320 |
| Modulus of elasticity (MPa) | $E_s$ | 200000 |

This section is selected to be equivalent to the concrete action.

3. Slab thickness equal to 140 mm and the design strength of the concrete used in the deck slab was 30 MPa.
4. Design strength of the specimen:

a- Elastic stage:

The modulus of elasticity and modular ratio are:

$Ec = 4700 \times \sqrt{f'c} = 25743\ MPa$ (ACI-Code [41])

$$n = \frac{E_s}{E_c} = \frac{200000}{25743} \cong 8$$

- Depth to the elastic neutral axis (y):

$$y = \frac{\sum A \times y}{\sum A}$$

Take the datum at the top of the steel beam section

$$y = \frac{\frac{1}{8}\left[(140\times660\times70)-\left(4\times\frac{1}{2}\times30\times70\times\frac{70}{3}\right)-(2\times120\times70\times35)\right]+(2010\times-80)}{\frac{1}{8}\left[(140\times660)-\left(4\times\frac{1}{2}\times30\times70\right)-(2\times120\times70)\right]+2010} = 51.4\ mm$$

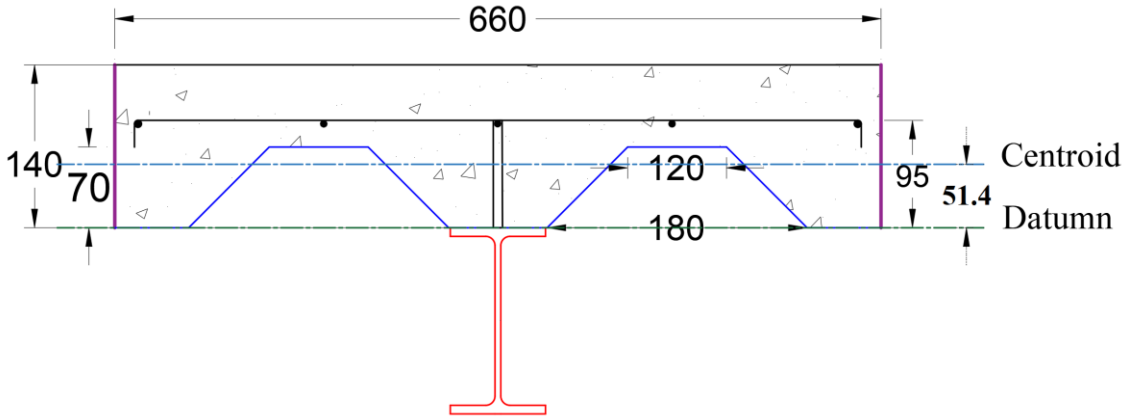


$$I_{tr} = [8.69 \times 10^6 + 2010 \times 131.4^2] + \left[\frac{660\times140^3}{12\times8} + \frac{660\times140}{8} \times 15.5^2\right] - 2 \times \left[\frac{120\times51.4^3}{12\times8} + \frac{120\times51.5\times(27.25)^2}{8}\right] - 4 \times \left[\frac{30\times51.4^3}{36\times8} + \frac{30\times51.4\times0.5}{8} \times 36.33^2\right] = 62.8 \times 10^6 mm$$

- Section modulus for the concrete and steel:

$$S_{xc} = n \times \frac{I_{tr}}{y} = 5670 \times 10^3 \text{mm}^3$$

$$S_{xs} = \frac{I_{tr}}{Ys} = 297 \times 10^3 \text{mm}^3$$

- Calculating maximum elastic moment:

$$M = f'_c \times S_{xc} = 170\ \text{kN.m}$$

$$M = F_y \times S_{xs} = 69.80\ \text{kN.m}\ \ (\text{control})$$

The total applied load ($P_n$) for the beam loaded by one concentrated loads ($P_n$) applied at the third points of span;

$$p_n = \frac{4M}{L} = 155\ \text{kN}$$

**b- Plastic stage:**

- Tensile Yielding of the Steel Section

$$F_{s\,max.} = A_g F_y = 472\ \text{kN}$$

- Concrete Crushing

$$F_{c\,max.} = (0.85 \times f'_c \times b_e \times h)$$
$$= 2356\ \text{kN}$$

$F_{c\,max.} > F_{s\,max.}$ The slab is adequate, then

Calculating maximum plastic moment:

$$Mp = F_{s\,max.} \times (h + 2h_r + d)/2 = = 87\text{kN.m}$$

$$p_n = \frac{4M}{L} = 193\text{kN (control)}$$

5. Ultimate vertical shear:

The contribution of the concrete slab to the resistance to vertical shear is small and difficult to determine and is, therefore, neglected. Therefore, only the web of the steel section and adjacent parts of the steel flange are taken into account. The vertical shear resistance, is given by:

$$V_s = 0.6F_y \times h \times t_w = 113\ \text{kN}$$

$$V_n = 2V_s = 226\ kN$$

6. X-HVB shear connectors distribution:

In this study used X-HVB 95 type and its number is determining by the design longitudinal shear force of the beam divided by the design shear resistance of single shear connector

Shear resistance ($Q_n$) of this type is (28 KN) for composite beam with solid slab while for slab with corrugated sheet multiplied by reduction factor which dependent on decking orientation and and profile geometry [75]:

- $k_1$ = 1, since $\frac{bo}{hp}$ = 2.14 >1.8

Longitudinal shear force; $V' = \min (F_{s\,max}, F_{c\,max}) = 472\ kN$

$\therefore No.\ of$ X-HVB shear connector $= \frac{472}{28} \cong 17$

Calculating Degree of Composite Action:

D.C.A=(Provided connectors)/(No. of connectors for full composite action)

D.C.A=11/18=65%≥25%

2)Decking ribs transverse to the beam axis

The cross-section of the selected composite girder explained in **Figure (A-2)**.

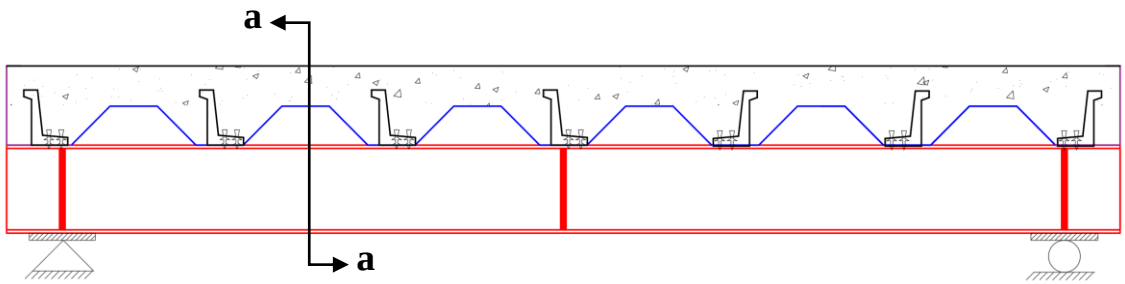


**Figure (A-2): Longitudinal Section of specimen with Decking ribs transverse to the beam axis**

**Design strength of the specimen:**

**Elastic stage:**

- Depth to the elastic neutral axis (y):

$$y = \frac{\sum A \times y}{\sum A}$$

Section a-a

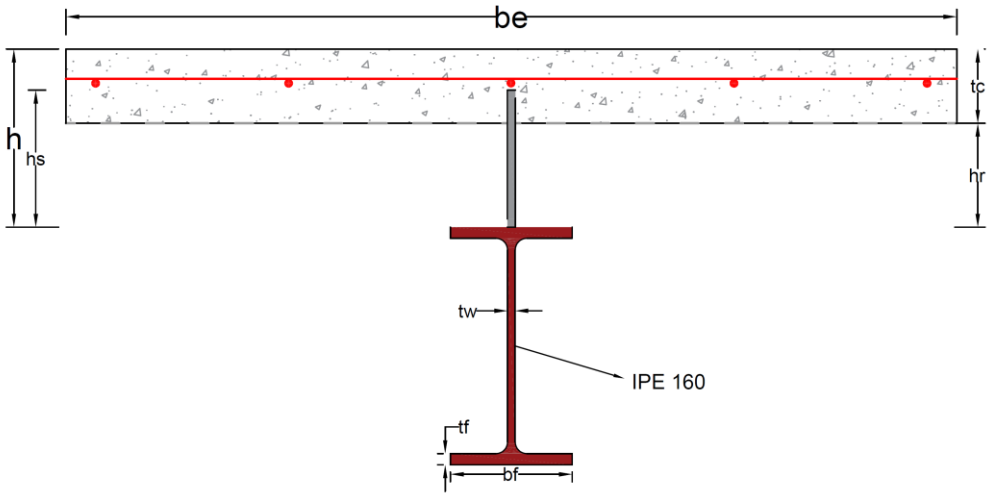


Take the datum at the top of the steel section

$$y = \frac{\frac{1}{8}[(70\times660\times105)]+(2010\times-80)}{\frac{1}{8}[(70\times660)]+2010} = 57\ mm$$

$$I_{tr} = [8.69 \times 10^6 + 2010 \times 137^2] + \left[\frac{660\times70^3}{12\times8} + \frac{660\times70}{8} \times 43.2^2\right] = 59.55 \times 10^6 mm$$

- Section modulus for the concrete and steel:

$$S_{xc} = n \times \frac{I_{tr}}{y} = 5740 \times 10^3 mm^3$$

$$S_{xs} = \frac{I_{tr}}{Ys} = 274 \times 10^3 mm^3$$

- Calculating maximum elastic moment:

$$M = f'_c \times S_{xc} = 172\ kN.m$$

$$M = F_y \times S_{xs} = 64\ kN.m\ \ (control)$$

The total applied load ($P_n$) for the beam loaded by one concentrated loads ($P_n$) applied at the third points of span;

$$p_n = \frac{4M}{L} = 142\ kN$$

**Plastic stage:**

- Tensile Yielding of the Steel Section

$$F_{s\ max.} = A_g F_y = 472\ kN$$

- Concrete Crushing

$$F_{c\ max.} = (0.85 \times f'_c \times b_e \times t_c)$$
$$= 117.8\ kN$$

$F_{c\ max.} > F_{s\ max.}$ The slab is adequate, then

Calculating maximum plastic moment:

$$Mn = F_{s\ max.} \times (h + 2h_r + h_c)/2 = = 91 kN.m$$

$p_n = \frac{4M}{L} = 182\text{kN} \quad (\text{control})$

7. Ultimate vertical shear:

The contribution of the concrete slab to the resistance to vertical shear is small and difficult to determine and is, therefore, neglected. Therefore, only the web of the steel section and adjacent parts of the steel flange are taken into account. The vertical shear resistance, is given by:

$V_s = 0.6F_y \times h \times t_w = 113\ \text{kN}$

$V_n = 2V_s = 226\ kN$

8. X-HVB shear connectors distribution:

In this study used X-HVB 95 type and its number is determining by the design longitudinal shear force of the beam divided by the design shear resistance of single shear connector

Shear resistance ($Q_n$) of this type is (28 KN) for composite beam with solid slab while for slab with corrugated sheet multiplied by reduction factor which dependent on decking orientation and profile geometry [75]:

- $k_1 = 1$, since $\frac{bo}{hp} = 2.14 > 1.8$

Longitudinal shear force; $V' = \min(F_{s\,max}, F_{c\,max}) = 472\ kN$

$\therefore No.\ of$ X-HVB shear connector $= \frac{472}{28} \cong 17$

Calculating Degree of Composite Action:

D.C. A = (Provided connectors)/(No.ofconnectors for full composite action)

D.C.A =11/17 = 65% ≥ 25%

# APPENDIX B

# MODELING OF MATERIAL PROPERTIES

## B.4 MATERIAL PROPERTIES INPUT IN THIS STUDY

### B.4.1 Concrete Material

The properties of concrete with compressive strength 30 MPa used in this study are listed in Tables B.1 to B.4.

**Table B.1: Elastic properties of concrete.**

| Elastic | Young's Modulus (Mpa) | Poisson's Ratio |
|---|---|---|
| fc'= 30 MPa | 25742.96 | 0.2 |

**Table B.2: Plastic properties of concrete.**

| Dilation angle | Eccentricity | Fb0/fc0 | k | Viscosity parameter |
|---|---|---|---|---|
| 31 | 0.1 | 1.16 | 0.667 | 0.001 |

**Table B.3: Stress-strain relationship (tensile behavior).**

| Yield stress | Cracking strain |
|---|---|
| 3.083676 | 0 |
| 2.276673 | 8.13E-05 |
| 1.764493 | 0.000151 |
| 1.403172 | 0.000215 |
| 1.132869 | 0.000276 |
| 0.923344 | 0.000334 |
| 0.757201 | 0.00039 |

**Table B.4: Stress-strain relationship (compressive behavior).**

| Yield Stress | Inelastic Strain |
|---|---|
| 10.89494 | 0 |
| 14.22907 | 6.34E-05 |
| 17.37647 | 9.11E-05 |
| 20.2684 | 0.0001288 |
| 22.84123 | 0.0001789 |
| 25.04338 | 0.0002433 |
| 26.84075 | 0.0003235 |
| 28.21951 | 0.0004199 |
| 29.18606 | 0.0005324 |
| 29.61273 | 0.0006158 |
| 30 | 0.0008346 |
| 29.24954 | 0.0010138 |
| 28.18468 | 0.0012052 |
| 26.89608 | 0.0014052 |
| 23.45777 | 0.0018888 |
| 19.98228 | 0.0023738 |
| 16.84746 | 0.0028456 |
| 14.17534 | 0.0032994 |
| 11.9592 | 0.0037354 |
| 10.14244 | 0.004156 |

| | |
|---|---|
| 8.65726 | 0.0045637 |
| 7.440646 | 0.004961 |
| 6.439317 | 0.0053499 |
| 5.610149 | 0.0057321 |
| 4.918928 | 0.0061089 |
| 4.118641 | 0.00664 |

### B.4.2 Steel beam Material

The elastic and plastic properties of IPE160 sections are shown in Table B.5.

**Table B.5: Elastic and plastic properties of unburned steel beam.**

| | | |
|---|---|---|
| **Elastic properties** | **Young's modulus (MPa)** | **Passion's ratio** |
| | 200000 | 0.3 |
| **Plastic properties** | **Yield stress (MPa)** | **Plastic strain** |
| | 224 | 0 |
| | 320 | 0.01 |

### B.4.3 Properties of Reinforcement Bar.

The elastic and plastic properties for steel reinforcement and stiffeners are shown in Tables B.6.

**Table B.6: Properties of steel reinforcement bars.**

| | | |
|---|---|---|
| **Elastic properties** | **Young's modulus (MPa)** | **Passion's ratio** |
| | 210826.39 | 0.3 |
| **Plastic properties** | **Yield stress (MPa)** | **Plastic strain** |
| | 324.5494 | 0 |
| | 350.5537 | 0.000527 |
| | 374.9264 | 0.000988 |
| | 399.3559 | 0.001482 |
| | 427.5527 | 0.002172 |
| | 451.5552 | 0.00365 |
| | 473.0197 | 0.009346 |
| | 491.0096 | 0.019898 |
| | 496.2575 | 0.025277 |
| | 425.761 | 0.035473 |
| | 406.5487 | 0.036172 |
| | 380.0659 | 0.036871 |
| | 369.0594 | 0.037062 |
| | 355.9079 | 0.037189 |
| | 252.5974 | 0.037284 |

### B.4.3 Properties of X-HVB shear connector and corrugated steel plate

The modeling of the X-HVB shear connector was based on properties determined in [14], whereas the modeling of the corrugated steel sheeting relied on properties measured in [102].

# APPENDIX C
# MODELING OF MATERIAL PROPERTIES FOR ELEVATED TEMPERATURE

## C.1 Strength Reduction of Concrete Due to Temperature

The reduction of the characteristic compressive strength of concrete as a function of temperature θ may be employed as shown in Table (C-1) represents siliceous aggregates (EN -1-2-1992, 2004) see Figure (C-1).

**Table C. 1: Reduction parameter for the stress-strain relationship of concrete under compression at elevated temperatures, according to (EN -1-2-1992, 2004).**

| **Θ(°C)** | **Stress Reduction Parameters** |
|---|---|
| 20 | 1.00 |
| 100 | 1.00 |
| 200 | 0.95 |
| 300 | 0.85 |
| 400 | 0.75 |
| 500 | 0.60 |
| 600 | 0.45 |
| 700 | 0.30 |
| 800 | 0.15 |
| 900 | 0.08 |
| 1000 | 0.04 |
| 1100 | 0.01 |
| 1200 | 0.00 |

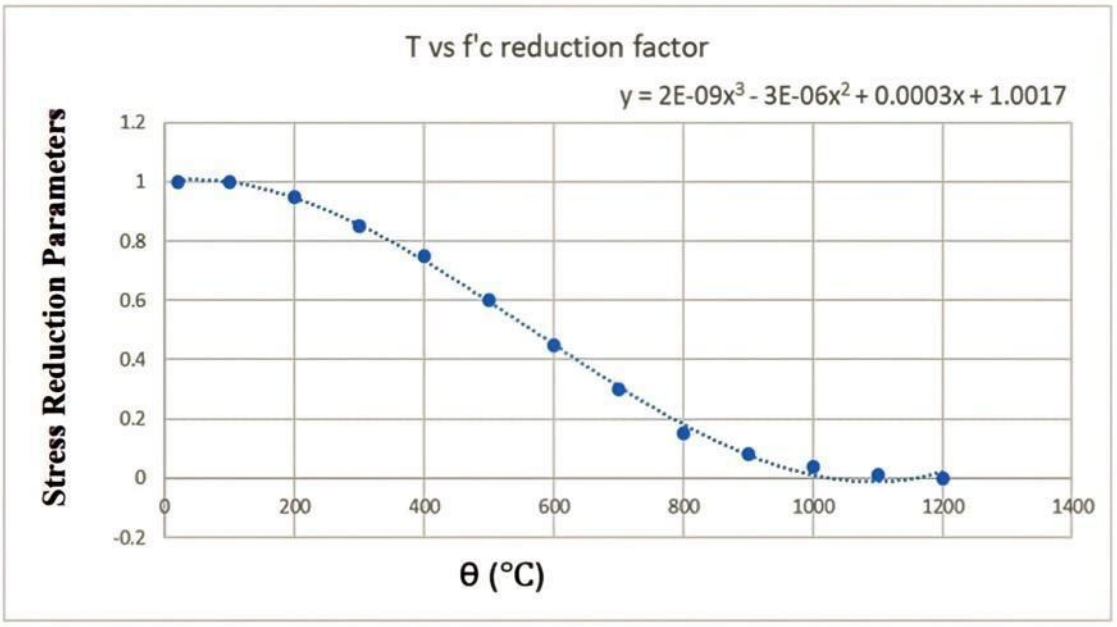


**Figure C. 1: The coefficient kc (θ) allows for a reduction in the characteristic strength (f'c) of concrete (EN -1-2-1992, 2004).**

## C.2 Stress-Strain Relationship of Concrete at Elevated Temperatures

Section 3.2.2 of Eurocode 2 Part 1.2 provides information on the mechanical characteristics of concrete at increased temperature [103].

Figure (C-2) shows the general stress-strain curve for uniaxially stressed concrete under compression, which may be constructed from the following formulas (see Table (C-2)).

**Table C. 2: Mathematical model for stress-strain relationships of concrete under compression at elevated temperatures.**

| Strain range | Stress $\boldsymbol{\sigma(\theta)}$ |
|---|---|
| $\varepsilon c,\theta \leq \varepsilon c1,\theta$ | $\sigma c,\theta = \dfrac{3.\varepsilon c,\theta.fc,\theta}{\varepsilon c1,\theta\left[2+\left(\dfrac{\varepsilon c,\theta}{\varepsilon c1,\theta}\right)^3\right]}$ |
| $\varepsilon c1,\theta \leq \varepsilon c,\theta \leq \varepsilon cu1,\theta$ | A descending branch should be used for numerical reasons. Models might be linear or non-linear. |

The compressive strength ($fc,\theta$) at a particular temperature and the strain corresponding to the peak stress ($\varepsilon c1,\theta$) are the two parameters that characterize this mathematical model. Table (C-3) of EC2 Part 1-2 Section

3.2.2.1 contains reduction factors that can be used to obtain these parameters at any given temperature Figure (C-3), where the value of the ultimate strain εcu1,θ which defines the extension of the descending branch is also included. εc,θ is the thermal strain of concrete. In ABAQUS CDPM, it is not required to define the whole behavior of concrete in compression, instead, it is required to define a point or a list of points of yield stress and inelastic strain.

By using equations in Table (C-2), it was possible to obtain full compressive behavior of concrete. However, to obtain the yield stress and inelastic strain, it was necessary to define the yield stress. Nilson et al (2016), stated that up to (50 -60) % of fc', the stress-strain curve is nearly elastic. Figure (C-4) displays the plastic stress- strain relationships of CDP model for 30 MPa compressive strength.

**Table C. 3: Values for the main parameters of the stress-strain relationships of concrete at elevated temperatures according to (EN -1-2-1992, 2004).NSC-Siliceous aggregates.**

| **Θ(°C)** | **$\varepsilon_{c1,\theta}$** | **$\varepsilon_{cu1,\theta}$** |
|---|---|---|
| 20 | 0.0025 | 0.0200 |
| 100 | 0.004 | 0.0225 |
| 200 | 0.0055 | 0.0250 |
| 300 | 0.0070 | 0.0275 |
| 400 | 0.0100 | 0.0300 |
| 500 | 0.0150 | 0.0325 |
| 600 | 0.0250 | 0.0350 |
| 700 | 0.0250 | 0.0375 |
| 800 | 0.0250 | 0.0400 |
| 900 | 0.0250 | 0.0425 |
| 1000 | 0.0250 | 0.0450 |
| 1100 | 0.0250 | 0.0475 |
| 1200 | - | - |

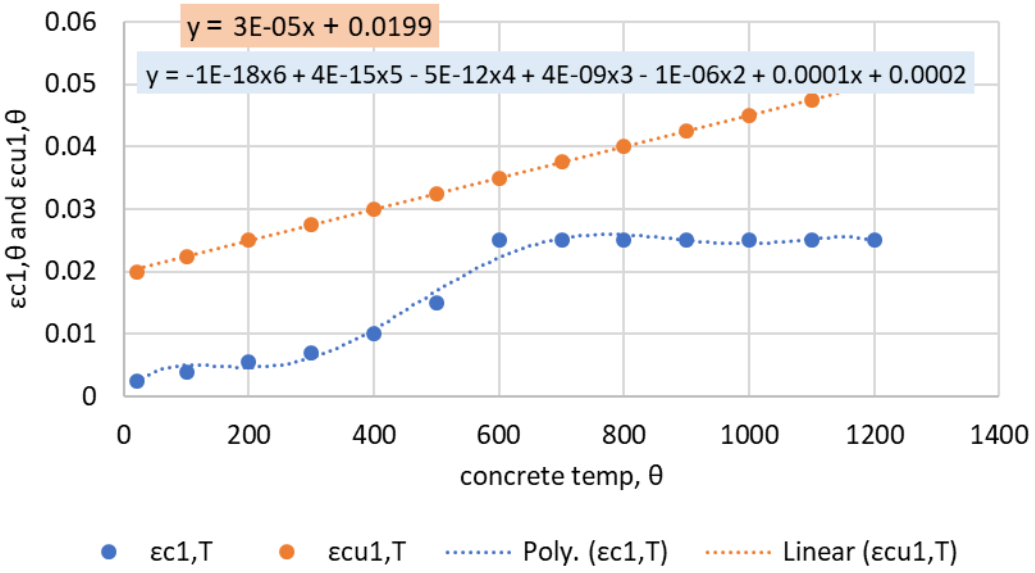


**Figure C. 2: Values for the main parameters of the stress-strain relationships of normal weight concrete at elevated temperatures (EN -1-2-1992, 2004).**

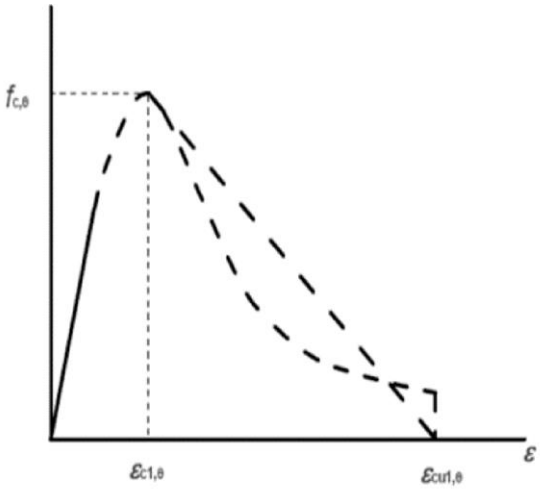


**Figure C. 3: Mathematical model for the stress-strain relationships of concrete under compression at elevated temperatures, according to (EN -1-2-1992, 2004).**

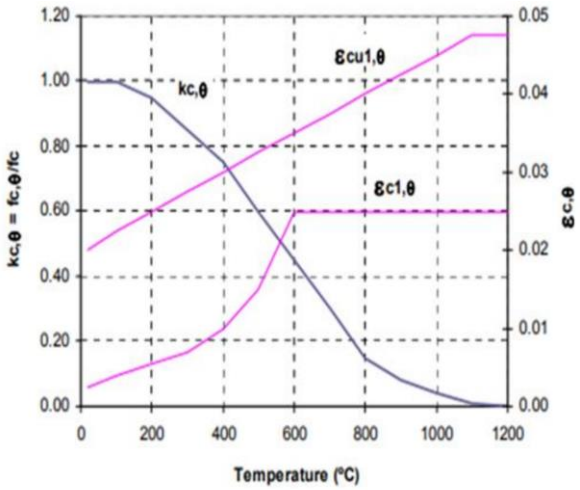


**Figure C. 4: Stress reduction parameters for the stress-strain relationships of concrete at elevated temperatures, according to (EN -1-2-1992, 2004).**

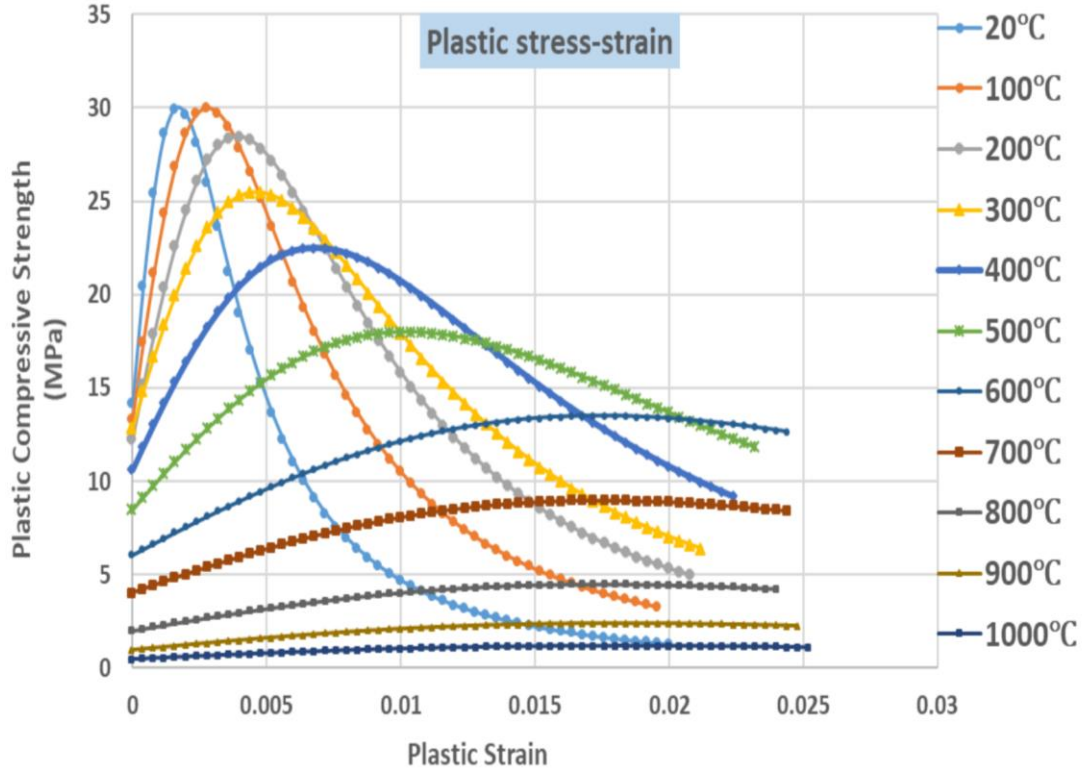


**Figure C. 5: Plastic stress-train curves for 30 MPa compressive strength of concrete at different temperatures according to (EN -1-2-1992, 2004).**

## C.3 Concrete Tensile Strength at High Temperatures

Normally, the tensile strength of concrete can be overlooked, which is a safe assumption. When tensile strength is required (i.e. in advanced models), the equations in Section 3.2.2.2 of (EN -1-2-1992, 2004) should be utilized. When concrete is exposed to high temperatures, its typical tensile strength ($f$ck, t) is lowered by a coefficient kc,t, which may be calculated as follows:

Kc,t (θc) =1.0 for 20°C ≤ θc ≤ 100°C

$$Kc,t\ (\theta c) = 1 - 1 \times \left(\frac{\theta c - 100}{500}\right)$$ for 100°C ≤ θc ≤ 600°C

being $f$ck,t (θc) =Kc,t (θc). $f$ck,t.

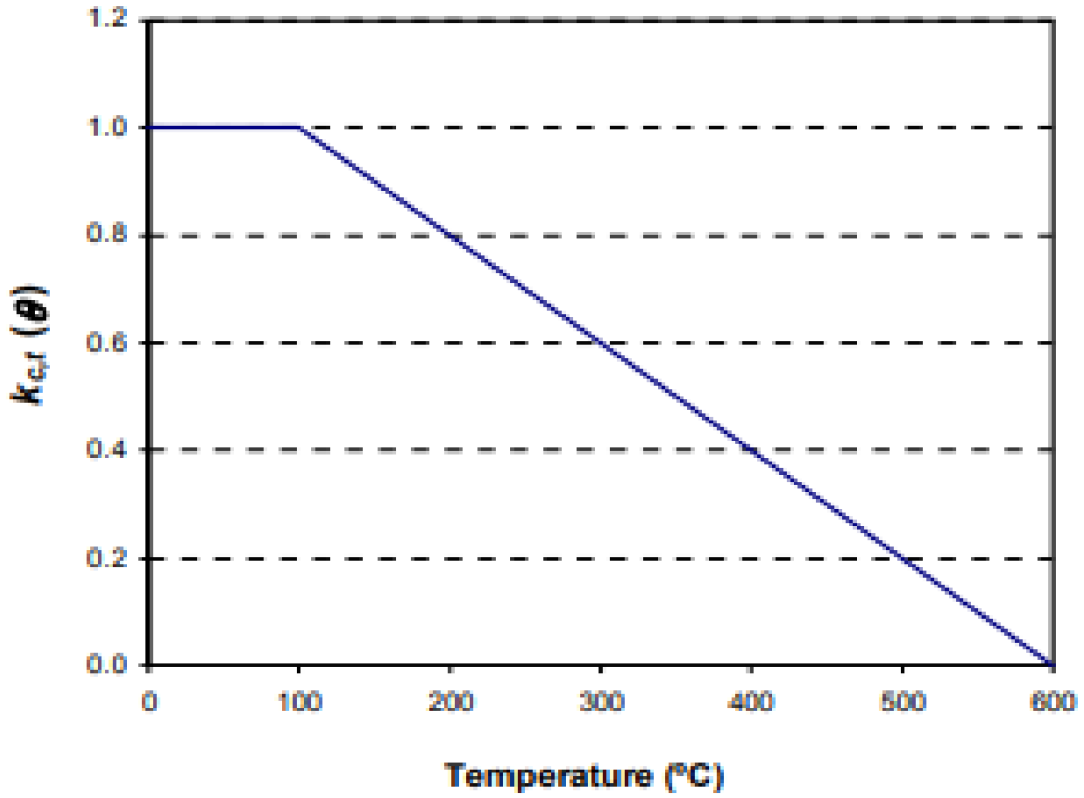


**Figure C. 6: Evolution of the tensile strength reduction coefficient for concrete, according to (EN -1-2-1992, 2004).**

## C.4 Modulus of Elasticity of Concrete

The resistance of an object or material to bend elastically (i.e. not permanently deform) when a stress is applied to it is measured by a quantity called the modulus of elasticity, which is also known an elastic modulus. The slope of an item's stress–strain curve in the elastic deformation zone may be used to determine the elastic modulus of the object. The elastic modulus of a more rigid material will be greater. A modulus of elasticity is represented by form:

$$\mathrm{E} = \frac{\text{Stress}}{\text{Strain}}$$

The modulus of elasticity of cement paste reduces with exposure to high temperatures as a result of the breakdown of bonds in the microstructure of the cement paste, with the modulus decreasing with

increasing heating rate. Normal strength concrete (fc' <60 MPa) retains its modulus better at temperature than high strength concrete.

## C.5 Thermal Properties of Concrete at Elevated Temperature

### Density

The fluctuation of the density of concrete, denoted by $\rho$c with temperature is affected by water loss, and the definition of this phenomenon is as follows:

$\rho c=\rho c(20℃)$ for $20℃ \leq \theta c \leq 115℃$

$\rho c=\rho c(20℃)*(1-\frac{0.02*(\theta c-115)}{85})$ for $115℃ < \theta c \leq 200℃$

$\rho c=\rho c(20℃)*(0.98-\frac{0.03*(\theta c-200)}{200})$ for $200℃ < \theta c \leq 400℃$

$\rho c=\rho c(20℃)*(0.95-\frac{0.07*(\theta c-400)}{800})$ for $400℃ < \theta c \leq 1200℃$

Where θc is the temperature of concrete, in ºC, and $\rho$c (20ºC) = 2400 kg/m3.

$\rho$c (θ) (kg/m3) It is shown in Figure (C-7).

### Specific Heat

The amount of heat per unit mass needed to change the temperature of a substance by one degree Celsius is referred as its thermal or heat capacity, also known as its specific heat, of a material.

$$C_c = \frac{\partial H}{\partial Tp}$$

where H represents enthalpy, T represents temperature, and p represents pressure. When measured at room temperature, the specific heat of ordinary concrete varies from 0.5 to 1.13 kJ $kg^{-1}$ $K^{-1}$ but the specific heat of hardened cement paste ranges from 0.63 to 1.72 kJ $kg^{-1}$ $K^{-1}$ [104]. The specific heat of concrete increases with increasing temperature. When the

temperature increases, concrete's specific heat value becomes more sensitive to the numerous chemical reactions that occur [105]. This includes free water vaporization occurs at around 100 degrees Celsius, Ca(OH)2 dissociation occurs at 400 to 500 degrees Celsius, and the α-β quartz transition occurs in certain aggregates. Heating of initially saturated concrete causes a rapid but temporary increase in the specific heat at about 90 degrees Celsius due to the rapid release of latent heat of vaporization.

The following formulas can be used to calculate the specific heat of calcareous or siliceous aggregates in dry concrete.

$Cc=900$ (J/kg.K) for $20°C \leq \theta c \leq 100°C$

$Cc = 900 + (\theta c - 100)$ (J/kg.K) for $100°C < \theta c \leq 200°C$

$Cc = 1000 + \frac{(\theta c - 200)}{2}$ (J/kg.K) for $200°C < \theta c \leq 400°C$

$Cc = 1100$ (J/kg.K) for $400°C < \theta c \leq 1200°C$

Where θc is the temperature of concrete, in °C.

Cc (θ) (J /kg.K) It is shown in Figure (C-8).

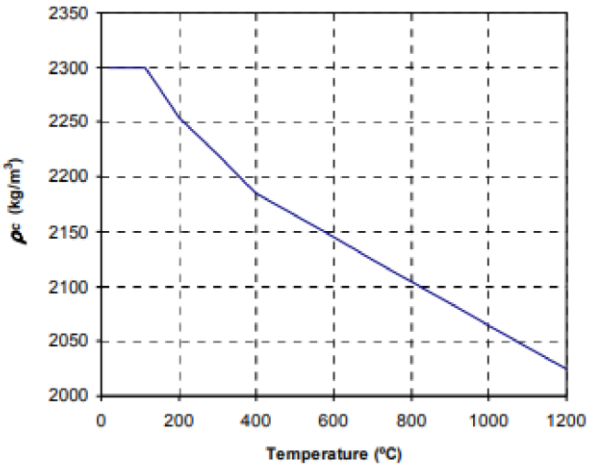


**Figure C. 7: Concrete's density when heated to a high temperature, according to (EN -1-2-1992, 2004).**

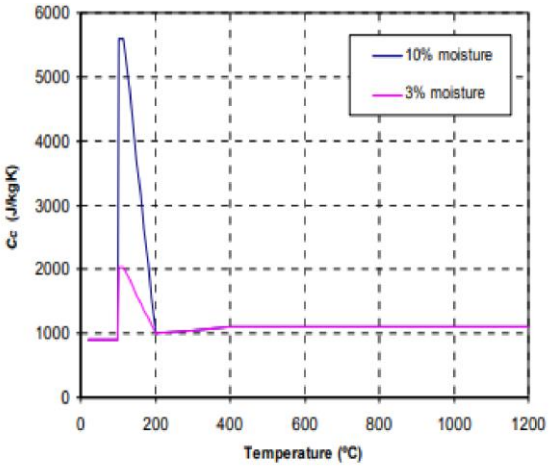


**Figure C. 8: Specific heat of concrete at elevated temperatures, according to (EN -1-2-1992, 2004).**

## C.6 Thermal Conductivity

Thermal conductivity is defined as the heat flux conducted through a unit area of a material under a unit temperature gradient (i.e., ability to conduct

heat). A concrete that has a high thermal conductivity is often preferred for prestressed pressure vessels since it will minimize temperature gradients throughout the thickness. The thermal conductivity of concrete at normal temperatures is largely determined by the thermal conductivity of the aggregate and the moisture level at the time of heating (e.g., increase in aggregate-to-cement ratio and decrease in water-cement ratio tends to increase the coefficient).

Concrete's thermal conductivity $\lambda_c$ may take on values ranging from the following lower and upper values.

Upper limit:

$$\lambda c = 2 - 0.2451 \times \left(\frac{\theta c}{100}\right) + 0.0107 \times \left(\frac{\theta c}{100}\right)^2 \left(\frac{w}{m}.k\right) \quad \text{for} \quad 20℃ \leq \theta c \leq 1200℃$$

Lower limit:

$$\lambda c = 1.36 - 0.136 \times \left(\frac{\theta c}{100}\right) + 0.0057 \times \left(\frac{\theta c}{100}\right)^2 \left(\frac{w}{m}.k\right) \quad \text{for} \quad 20℃ \leq \theta c \leq 1200℃$$

Where $\theta_c$ is the temperature of concrete, in $^{\circ}$C.

The difference in thermal conductivity between its upper limit and lower limit with temperature is shown in Figure (C-9).

## C.7 Thermal Expansion Coefficient

The change in volume due to temperature change is represented by the coefficient of thermal expansion, which is represented as a change in length for every degree that the temperature changes. The coefficient is significant because it serves as a measurement of the structural movement and thermal stresses that are brought on by variations in temperature, which may result in cracking and spalling. Due to its two primary components, cement paste and aggregate, concrete's thermal expansion is a complex phenomenon

since each has its own coefficient of thermal expansion [104] is illustrated in Table (C-5).

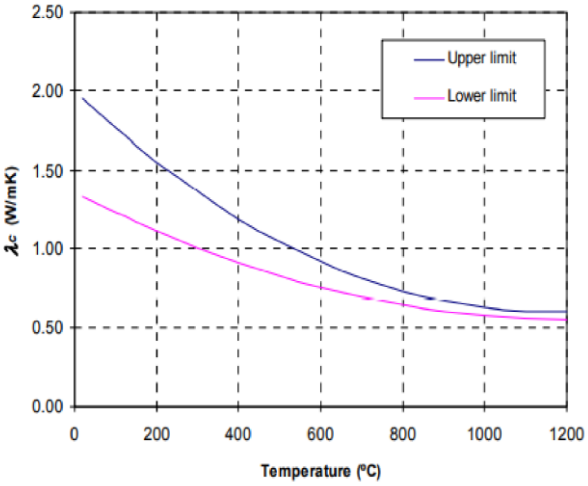


**Figure C. 9: Concrete's high-temperature thermal conductivity, as measured by (EN -1-2-1992, 2004).**

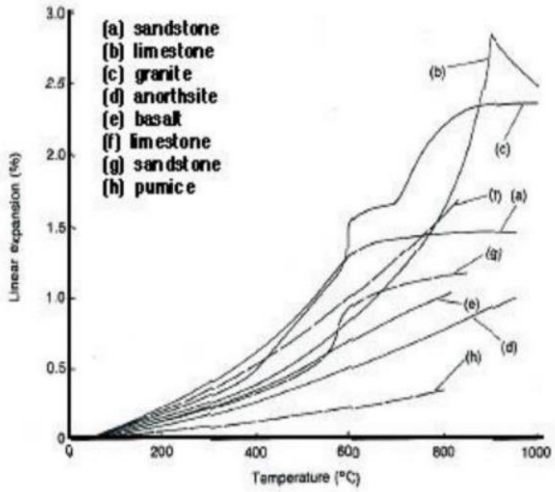


**Figure C. 10: Temperature-dependent thermal expansion of a variety of rocks, according to** [104]**.**

**Table C. 4: Thermal Properties of Concrete (EN -1-2-1992, 2004).**

| Temperature (°C) | Mass Density (ton/mm$^3$) | Specific Heat mJ/ton K | Thermal Conductivity mW/mm K |
|---|---|---|---|
| 30 | 2.4E-09 | 900000000 | 1.951 |
| 100 | 2.4E-09 | 900000000 | 1.766 |
| 200 | 2.4E-09 | 900000000 | 1.553 |
| 300 | 2.39718E-09 | 950000000 | 1.361 |
| 400 | 2.38024E-09 | 1000000000 | 1.191 |
| 500 | 2.352E-09 | 1000000000 | 1.042 |
| 550 | 2.316E-09 | 1100000000 | 0.978 |

**Table C. 5: Coefficient of Thermal Expansion of Concrete.**

| Temperature range (°C) | Thermal expansion coefficient ($10^{-6}$. °C$^{-1}$) |
|---|---|
| 20-100 | 3.0 |
| 100-300 | 9.0 |

| | |
|---|---|
| 300-500 | 17.0 |
| 500-700 | 33.0 |

## C.8 Properties of Steel

### C.8.1 Mechanical Properties of Steel at Elevated Temperatures

As previously described, T3D2 and T3D2T bar elements were used to model reinforced steel bars (longitudinal reinforcement, transverse reinforcement) for unburned and burnt samples respectively, and it is considered a bilinear isotropic material. For the linear part, the elastic relationship necessary to define (Es) representing the modulus of elasticity of steel assumed to be 200,000 MPa and the Poisson ratio ($vc$) for steel is defined as 0.3. The plastic relation can be defined for steel by introduce the yield stress ($fy$), and the steel hardening modulus required to be specified. Yield stress is 415 MPa for steel reinforcement is used. And the hardening modulus was taken to be zero.

The strength loss at 0.2% proof strain for Class N reinforcement should be utilized for compression reinforcement in columns as well as compressive zones in beams and slabs. When εs,fi < 2% this decrease in strength also applies to the tension reinforcement (see Figure (C-11), curve 3), (EN -1-2-1992, 2004).

$Ks(\theta) = 1.0$ for $20°C \leq \theta \leq 100°C$

$Ks(\theta) = 0.7 - 0.3(\theta - 400) /300$ for $100°C < \theta \leq 400°C$

$Ks(\theta) = 0.57 - 0.13(\theta - 500)/100$ for $400°C < \theta \leq 500°C$

$Ks(\theta) = 0.1 - 0.47 (\theta - 700) /200$ for $500°C < \theta \leq 700°C$

$Ks(\theta) = 0.1 (1200 - \theta) /500$ for $700°C < \theta \leq 1200°C$

As the temperature increases, the modulus of elasticity tends to decrease. The relationship of the modulus of elasticity of the structural steel

according to temperatures is shown in Table (C-6) is calculated using (EN1993-1-2, 2005).

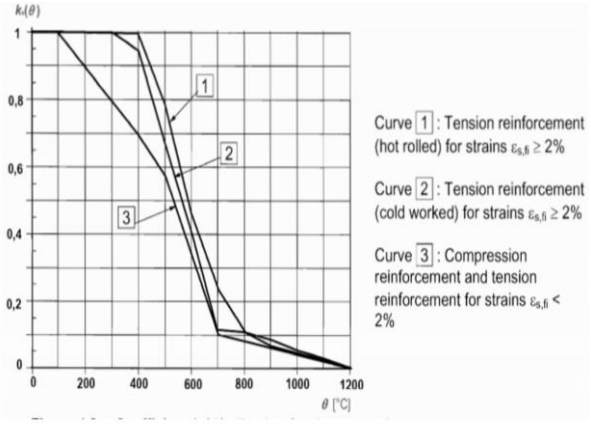


**Figure C. 11: Coefficient ks(θ) allowing for decrease of characteristic strength (fyk) of tension and compression reinforcement (Class N).**

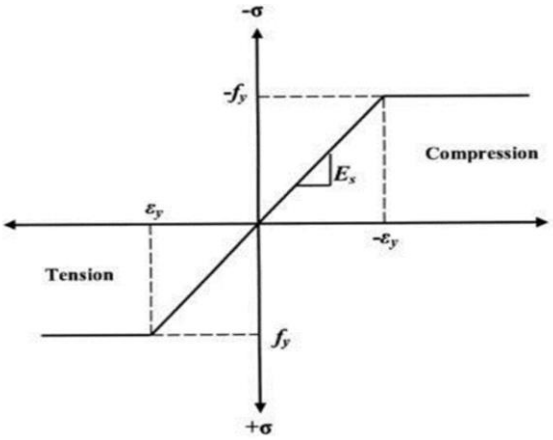


**Figure C. 12**: **Modulus of elasticity of steel.**

**Table C. 6: Elastic Properties of Steel Reinforcement (EN 1993-1-2, 2005).**

| Temperature (°C) | Poisson's Ratio | Young's Modulus (MPa) |
|---|---|---|
| 20 | 0.3 | 200000 |
| 100 | 0.3 | 200000 |
| 200 | 0.3 | 180000 |
| 300 | 0.3 | 160000 |
| 400 | 0.3 | 140000 |
| 500 | 0.3 | 120000 |
| 650 | 0.3 | 62000 |

## الخلاصة

نظراً لزيادة استخدام الأعتاب المركبة في المباني وانتشار حوادث الحريق بشكل متزايد، أصبح من الضروري فهم سلوك هذه الأعتاب أثناء الحريق. يلعب سلوك روابط القص دورًا مهمًا في الحفاظ على المقاومة المطلوبة للعتب المركب. هناك العديد من أنواع روابط القص المتاحة والمستخدمة في صناعة البناء وفقًا لاستخدامها. تعتبر روابط القص X-HVB التي تم اعتمادها من قبل شركة Hilti بديلاً مناسبًا لروابط القص التقليدية الملحومة من حيث كونها صديقة للبيئة ويمكن تثبيتها باستخدام معدات بسيطة وآمنة. تم اختبار هذه الروابط تحت أنواع مختلفة من التحميل في درجات الحرارة العادية. ومع ذلك، لم يتم دراسة سلوك هذه الروابط أثناء الحريق.

تم تقسيم الدراسة إلى ثلاثة أجزاء رئيسية. في الجزء الأول، تم إجراء اختبارات Pushout لدراسة سلوك روابط القص X-HVB تحت تأثير الحريق مختبريًا. كانت هذه الاختبارات تهدف إلى فحص قوة القص، المرونة، الصلابة، والعلاقات بين الحمل والانزلاق. تم دراسة متغيرات مختلفة، مثل التعرض لمستويات حرارة مختلفة (350، 450، و550 درجة مئوية)، اتجاه الصفيحة المموجة (موازية أو عرضية بالنسبة لطول العمود)، نسبة روابط القص، واتجاه موصل القص (للأمام أو للخلف) بالنسبة لاتجاه القوة القصية.

في الجزء الثاني، تحول التركيز إلى دراسة سلوك الأعتاب المركبة المسندة بمسندين نوع (اسناد بسيط) خلال الفحص مع الاخذ بنظر الاعتبار اختلاف اتجاه الصفيحة المموجة، سواء موازية أو عرضية بالنسبة لطول العتب، تحت اتجاهات مختلفة للتعرض للحريق، إما من الجزء العلوي للسقف أو من الجزء السفلي للعتب الفولاذي، ومستويات تعرض حرارية مختلفة عند (350، 450، و550 درجة مئوية) .أخيرًا، تضمن الجزء الثالث التحقق من نموذج عددي باستخدام ABAQUS Standard/Explicit 2017.

أظهرت نتائج اختبار Pushout أن تثبيت موصل القص نحو الأمام بالنسبة لاتجاه قوة القص يظهر مقاومة أكبر تحت تأثير الحريق مقارنة بتوجيهه إلى الوراء في ظروف الحريق. علاوة على ذلك، لوحظ أن مرونة موصل القص تتغير اعتمادًا على اتجاه الصفيحة الفولاذية المموجة (موازي أو عرضي) إلى العتب الفولاذي. بالنسبة للعينات ذات الصفيحة الفولاذية المموجة موازيًا، يؤدي زيادة نسبة روابط القص إلى زيادة الصلابة والمرونة. ومع ذلك، لا يحدث ذلك في حالة اللوح الفولاذي المموج عرضيًا، حيث تقل المرونة وتزيد الصلابة في هذه الحالة.

أما بالنسبة لنتائج اختبار العتب المركب، فقد أظهرت النتائج أن قدرة تحميل الأمثل للعينات التي تعرضت للحريق من الجزء العلوي للوح الخرسانة قليلاً بعد الاحتراق عند 400 درجة مئوية بغض النظر عن اتجاه توجيه الصفيحة الفولاذية. بينما تقل بشكل كبير بعد التعرض لدرجات حرارة الحريق (350، 450 و550 درجة مئوية) من الجزء السفلي للعتب الفولاذي بنسبة تصل إلى (20%، 29% و30%) على التوالي للعينات ذات الصفيحة الموازية، وتزيد هذه الخسائر إلى حوالي (23%، 33% و40%) على التوالي للعينات ذات الصفيحة العرضية.

كما أظهرت نتائج نموذج العناصر المحدودة توافقًا جيدًا مع النتائج المختبرية. في هذه الأطروحة، تم إجراء تحليل متغير لدراسة تأثير حجم ملف العارضة الفولاذية وتأثير التعرض للحريق من الجزء العلوي للوح الخرسانة والجزء السفلي للعارضة الفولاذية. توصل الباحث إلى أن استخدام عارضات فولاذية من نوع IPE200 بدلاً من القواعد الفولاذية IPE160 يحسن الأداء بشكل كبير، مع زيادة بنسبة 19.82% و14% في الحمولة النهائية في درجة حرارة الغرفة، وزيادة أكثر وضوحًا بنسبة 30.35% و15.37% تحت ظروف الحريق من الجزء السفلي للعارضة الفولاذية للألواح المموجة الموازية والعرضية على التوالي. أيضًا، كانت النقص في الحمولة النهائية للعينات التي تعرضت للحريق من الجزءين العلوي والسفلي 15.5% و16.25% مقارنة بالعينات التي تعرضت للحريق من الجزء السفلي فقط، و35.7% و36.5% مقارنة بالعينات التي تعرضت للحريق من الجزء العلوي للواح الموازي والعرضي على التوالي.

**جمهورية العراق**

**وزارة التعليم العالي والبحث العلمي**

**جامعة بابل/كلية الهندسة**

**قسم الهندسة المدنية**

# *سلوك البلاطة الخرسانية المركبة المكونة من صفائح فولاذية متعرجة مرتبطة ميكانيكيًا بأعتاب فولاذية معرضة للحريق*

أطروحة

مقدمة الى كلية الهندسة / جامعة بابل

كجزء من متطلبات نيل درجة الدكتوراه فلسفة في الهندسة /الهندسة المدنية/ إنشاءات

من قبل

**ميس عبد الرضا حمد موسى**

اشراف:

**الأستاذ الدكتور هيثم حسن متعب**

1445هـ 2023م